Polymer Chains with Nonlinear Interactions: Equilibrium Properties, Thermal Fragmentation, and Force-Induced Rupture

D I S S E R T A T I O N

zur Erlangung des akademischen Grades

doctor rerum naturalium
(Dr. rer. nat.)
im Fach Physik

eingereicht an der
Mathematisch-Naturwissenschaftlichen Fakultät I
Humboldt-Universität zu Berlin

von
Dipl.-Phys. Simon Martin Fugmann
geboren am 04.01.1982 in Berlin

Präsident der Humboldt-Universität zu Berlin:
Prof. Dr. Dr. h.c. Christoph Markschies

Dekan der Mathematisch-Naturwissenschaftlichen Fakultät I:
Prof. Dr. Andreas Herrmann

Gutachter:
1. Prof. Dr. Igor M. Sokolov
2. Prof. Dr. Lutz Schimansky-Geier
3. Prof. Dr. Michael Urbakh

Tag der mündlichen Prüfung: 27.10.2010

Abstract

This work intends to show how the coupled dynamics of a nonlinear polymer chain alters processes such as thermal fragmentation and force-induced rupture.

For that purpose we first examine the equilibrium relaxation properties of nonlinear polymer chains which have a distinct impact on all dynamical processes in such systems. We find that in chains with nonlinear interaction potentials the relaxation properties of the end-to-end distance and the principal components are essentially those of the harmonic chain, though with shifted correlation times. Soft nonlinear potentials increase the correlation times. While these changes are not too large for the single-well potentials, for the double-well ones they can lead to the increase in the relaxation times by orders of magnitude. Thus strong internal friction may be modeled by use of the simple double-well potential with effective parameters derived from a more complex original model. The principal components, whose directions follow the normal modes of the harmonic chain, can exhibit vastly different subdiffusive kinetics.

Concerning the thermally activated bond rupture in polymer chains we focus on two experimentally relevant situations. First, we consider the thermally activated fragmentation of a homopolymer chain. In our model the dynamics of the intact chain is a Rouse one until a bond breaks and bond breakdown is considered as a first passage problem over a barrier to an absorbing boundary. Using the framework of the Wilemski-Fixman approximation we calculate mean activation times of individual bonds for free and grafted chains. We show that these times crucially depend on the length of the chain and the location of the bond yielding a minimum at the free chain ends. In the Markovian limit of high activation barriers the distribution of the fragmentation location in the chain flattens since all activation times become equal.

Second, we study a set up corresponding to the one found in single molecule pulling experiments. A homopolymer chain is pulled at one of its ends with a force that increases monotonically in time while the opposite end is kept fixed. In addition to the influence of non-Markovian fluctuations in the coupled system the delayed force propagation into the chain has a further impact on its overall rupture dynamics. We show that the non-Markovian fluctuations play a minor role for the scaling of rupture forces in large ensembles of breakable bonds. In contrast, they have a measurable effect on the rupture forces when there is only one breakable link in a long chain of monomers. In long chains of breakable bonds the complex interplay between the force propagation into the chain and the extreme value statistics underlying rupture causes a non-monotonic scaling of the most probable rupture force f_{max} as a function of the chain length N. For short chains its decrease is proportional to $[\ln(\mathrm{const}N)]^{2/3}$ and it saturates at the value depending on the loading rate for very long ones. In between it can exhibit a non-monotonic behavior: The most probable rupture force attains its minimum for a certain intermediate chain length. We derive a theoretical model which reproduces the numerically observed non-monotonic scaling of the rupture force.

Finally we analyze experimental data of the rupture of covalent bonds in ds-DNA loops. We calculate the intrinsic activation rate of the weakest covalent bond in the repeating unit of the DNA backbone and find that this rate is by orders of magnitude larger compared to the expected activation rate of an isolated bond. This difference is attributed to an interaction with the surface and a possible force-induced catalytic reaction.

In summary, it is shown that a sensitive interplay of internal correlation times, extreme value statistics, and the timescale of external forcing can complicate the rupture kinetics even in extremely simple chain models.

Keywords:
polymers, non-Markovian dynamics, thermal fragmentation, force-induced rupture

Zusammenfassung

Ziel dieser Arbeit ist es, den Einfluss der gekoppelten Dynamik in nichtlinearen Polymerketten auf Prozesse wie den thermischen Zerfall und den kraftinduzierten Abriss zu untersuchen.

Für diesen Zweck betrachten wir zunächst die Gleichgewichtsrelaxationseigenschaften nichtlinearer Polymerketten, die einen ausgeprägten Einfluss auf alle dynamischen Prozesse in solchen Systemen haben. Es kann gezeigt werden, dass in Ketten mit nichtlinearen Wechselwirkungspotentialen die Relaxationseigenschaften des End-zu-End-Abstandes wie auch der Hauptkomponenten jene der harmonischen Kette sind. Die Korrelationszeiten weichen jedoch ab. Sogenannte weiche nichtlineare Potentiale erhöhen die Korrelationszeit. Während diese Veränderungen in Potentialen mit nur einem lokalen Minimum nicht besonders ausgeprägt sind, können sie in Doppelmuldenpotentialen zum Anwachsen typischer Korrelationszeiten um mehrere Größenordnungen führen. Das eröffnet die Möglichkeit, starke innere Reibung mittels des einfachen Doppelmuldenpotentials zu modellieren - mit effektiven Parametern, die von einem komplexeren Ausgangsmodell abgeleitet werden. Die Hauptkomponenten, deren Richtungen mit denen der Normalmoden der harmonischen Kette übereinstimmen, zeigen dabei unter Umständen eine subdiffusive Dynamik.

In Bezug auf das thermisch aktivierte Bindungsversagen gehen wir auf zwei experimentell wichtige Problemstellungen ein. Zuerst untersuchen wir den thermisch aktivierten Zerfallsprozess einer homopolymeren Kette. In unserem Modell nehmen wir an, dass die Dynamik der intakten Kette durch das Rouse Modell beschrieben wird. Bindungsversagen wird als Aktivierungsproblem über eine Barriere hin zu einem absorbierenden Rand aufgefasst. Im Rahmen der Wilemski-Fixman Näherung berechnen wir mittlere Aktivierungszeiten einzelner Bindungen für freie und befestigte Ketten. Wir können zeigen, dass diese Zeiten entscheidend von der Gesamtlänge der Kette sowie der Position der Bindung abhängen. An den freien Kettenenden weisen sie ein Minimum auf. Im Markovschen Grenzfall hoher Aktivierungsbarrieren wird die Verteilung der Abrisspositionen flach, da sich die Aktivierungszeiten angleichen.

Die zweite experimentell relevante Situation entspricht jener in Einzelmolekül-Zugexperimenten. Eine homopolymere Kette wird an einem Ende mit monoton ansteigender Kraft gezogen, während ihr anderes Ende fixiert ist. Zusätzlich zum Einfluss nicht Markovscher Fluktuationen im gekoppelten System, hat die verzögerte Kraftpropagation entlang der Kette einen weiteren Einfluss auf die Abrissdynamik. Wir zeigen, dass die nicht Markovschen Fluktuationen nur eine geringe Rolle in großen Ensembles potentiell brechbarer Bindungen spielen. Dagegen haben sie einen messbaren Einfluss auf die Abrisskräfte in langen Ketten mit nur einer brechbaren Bindung. In langen Ketten brechbarer Bindungen verursacht das komplexe Zusammenspiel zwischen Kraftpropagation und der dem Abriss zugrundeliegenden Extremwertstatistik eine nicht monotone Abhängigkeit der wahrscheinlichsten Abrisskraft f_{max} von der Kettenlänge N. Für kurze Ketten nimmt sie proportional zu $[\ln(\mathrm{const}N)]^{2/3}$ ab und saturiert für lange Ketten auf einem Wert, der von der Rate des Anwachsens der Kraft abhängt. Dazwischen ist die Abhängigkeit nicht monoton, die wahrscheinlichste Abrisskraft wird minimal für eine bestimmte Kettenlänge. Wir entwickeln ein theoretisches Modell, das dieses Verhalten reproduziert.

Zum Abschluss analysieren wir experimentelle Abrissdaten von kovalenten Bindungen in zweisträngigen DNS Ringen. Wir berechnen die intrinsische Aktivierungsrate der schwächsten Bindung in der monomerischen Einheit des DNS Rückgrats und stellen fest, dass die Rate den erwarteten Wert für eine isolierte Bindung um Größenordnungen übersteigt. Diese Abweichung wird auf die Wechselwirkung mit dem Substrat

und eine mögliche kraftinduzierte katalytische Reaktion zurückgeführt.

Insgesamt wird gezeigt, dass ein komplexes Wechselspiel von internen Korrelationszeiten, Extremwertstatistik und der Zeitskala des Anwachsens externer Kräfte zu komplizierter Dynamik selbst in einfachsten Modellsystemen führen kann.

Schlagwörter:
Polymere, nicht Markovsche Dynamik, thermischer Zerfall, kraftinduzierter Abriss

Contents

1. Introduction

Most processes in nature evolve in a complex environment and there is an apparent relation between the involved *structure* and its *function*. Important examples are the double helix structure of the DNA and its opening for transcription or the titin protein in the muscle which unfolds upon application of an external force (Kellermayer et al., 1997; Rief et al., 1997; Merkel, 2001; Kumar and Li, 2010; Samori, 2006). With growing knowledge of the basic physical and chemical mechanisms in these complex structures, furthermore, improving experimental techniques which explore structures on a nanometer length- and femtosecond timescale it became more and more evident that a function of a molecule is not solely determined by its static structure but by a complex dynamics created by a variety of intra- and intermolecular interactions.

Therefore, the dynamics of *polymers* and peptides attracted large attention in the past decade. First such interest was due to the dynamics of nonequilibrium states which is connected to the biological functioning of the proteins. Later, also the equilibrium fluctuations got into the focus of increasing interest. This interest was caused by two reasons: one has to do with the thermal stability of proteins as connected to their structures (Granek and Klafter, 2005), another one is related to the luminescent measurements of fluctuations of the distance between two groups in equilibrium (Chen et al., 2009; Kou and Xie, 2004) and the discovery of the anomalous kinetics and of extremely large characteristics times in such fluctuations which implies the existence of a strong additional internal friction mechanism slowing down the dynamics.

In most structures one encounters strong *covalent* bonds which form the relatively stable backbone of polymers and biomolecules and weak-*noncovalent* interactions which govern structural cohesion and mediate functioning in life on many length- and timescales ranging from the interior of the cell to its outer membrane surface to the muscles (Kumar and Li, 2010; Evans and Williams, 2002). These noncovalent biomolecular bonds are in the focus of growing interest especially when a huge number of weak noncovalent links assembles to form a large complex, a supramolecular polymer (Ciferri, 2000). Examples in nature are nucleic acids, polypeptides and polysaccharides and there is growing interest in applications as functional materials (Cordier et al., 2008; Mynar and Aida, 2008). A distinct feature of many important supramolecular structures is that the large number of these weak bonds contributes to the overall stability of the supramolecule. Because of this feature, the local dynamics of supramolecular bond breaking and bond making is an important aspect that allows for the rich diversity and complexity of many complex systems.

It is more and more recognized that mechanical forces play an important role at the molecular level. Functioning is mediated by the application of forces. Examples are single molecular pulling experiments (Friedsam et al., 2003; Dudko et al., 2003, 2006; Neuert et al., 2007; Evans and Williams, 2002), protein unfolding (Kellermayer et al., 1997; Kumar and Li, 2010), friction phenomena at the nanoscale (Urbakh et al., 2004; Sills and Overney,

2003; Dudko et al., 2002), or the dynamics of colloids on surfaces (Dreyer et al., 2006), to name a few. Thus the controlled application of mechanical forces to single molecules offers the possibility to probe their structure and so to understand their functioning. However, the well controlled application of a force on the molecular level is by far not limited to the investigation of biomolecular functioning. For example, the rate of cracking of long strained polymers in elongational flows may be of great importance in petrol industry. Therefore, a profound knowledge of the basic physical mechanisms is essential.

Since Kramers (Kramers, 1940) it is well established that the reaction of various bonds or molecules to an applied force can be described as a thermally activated escape (Hänggi et al., 1990). An extension to activation processes in higher dimensional energy landscapes has been given by Langer (Langer, 1969). Although in typical biomolecular bonds the interactions originate from a bunch of different atomic scale bonds which are distributed over many regions of large molecules, the bond rupture process is often assumed to exhibit first order kinetics which fits with the simplest picture.

However, for a sufficient understanding of the binding mechanism it is necessary to determine relevant length- and timescales in the molecular system. Typical timescales are those of relaxation, which can become very large due to internal friction, and thermal activation. The latter is mainly determined by the intrinsic rates of energy barrier crossings. On times which are shorter than the longest relaxation time of the polymer the motion of its monomers exhibits a strong *non-Markovian* character. Put in other words the dynamics and hence the function of a single unit in the molecule is influenced by the impact of the collective fluctuations of its neighbors. As we proceed to show this affects the monomer diffusion but also the process of thermal activation of bonds between the units since this process may become non-Markovian. Thus collectivity alters the dynamics of individual entities in the coupled system.

Soft matter motion takes place in a liquid environment and is therefore mostly assumed to be overdamped. However, on the microscopic level purely deterministic models have shown to mimic observations found in real experiments; thus the collective opening process of the DNA double helix can be described within a nonlinear chain model bearing localized breather solutions (Hennig, 2004; Hennig and Archilla, 2004; Dauxois et al., 1992; Dauxois, 1988). A worth reading introduction to the concept of nonlinear excitations in biomolecules is given in (Dauxois and Peyrard, 2006). Furthermore, as very recently published, collectivity triggers the route to escape in the purely deterministic barrier crossing process. Modulational instability causes strong energy localization in nonlinear chains and enables a few degrees of freedom to accumulate such high amounts of energy that they can overwhelm an activation barrier. This process was shown to accelerate escape in small systems as dimers (Fugmann et al., 2008a) as well as in long one- and two-dimensional chains (Hennig et al., 2007; Fugmann et al., 2008b) where an individual chain unit initially has very little energy compared to the activation barrier. Very recently, Ghosh et al. (Ghosh et al., 2010) studied the thermal breakage of an underdamped polymer chain and found that the existence of a collective unstable mode causes an inhomogeneous rupture probability distribution along a grafted chain. Thus although arising in very different physical situations, collectivity has a huge impact on the (escape and activation) dynamics in many body systems. To clarify this impact on the overdamped polymer dynamics is one of the main concerns of the thesis.

From the theoretical point of view a successful attempt to handle the coupled dynamics

of the polymer chain was given by Wilemski and Fixman (Wilemski and Fixman, 1974a,b) who introduced the concept of diffusion controlled reactions in order to solve the problem of chain closure, that is when functional groups linked to a long polymer chain react upon contact, i.e., their relative distance falls below a predefined value. This situation is omnipresent in chemistry, physics, and pharmacy. Although their ansatz, referred to as *Wilemski-Fixman approximation*, gives a satisfactory qualitative agreement with experimental findings, exact solutions for reactions in coupled systems exhibiting non-Markovian dynamics remain sparse and rely on additional assumptions. A main requirement is that the chain can be described to a good approximation as a chain of beads coupled by harmonic springs. The dynamics of the beads in the liquid environment is described by the famous *Rouse model* (Rouse, 1953). Although this model does not capture all aspects of molecular dynamics, e.g., hydrodynamic interactions are neglected, due to its simplicity and linearity it became a standard model of polymer dynamics and generalizations to arbitrary structures are in the focus of recent studies. The harmonically coupled chain will be our guide and reference mark throughout the thesis which intends to study the equilibrium relaxation behavior as well as the activation of bonds in long coupled nonlinear chains. We focus on two main questions:

1. The first question concerns the long characteristic equilibrium relaxation times observed in some polymer systems. What kind of the minimal assumptions about the intramolecular potentials have to be made to build a model mimicking the strong internal friction observed in realistic molecular dynamics simulations? In a wider sense we also intend to carry out how nonlinear interactions alter the equilibrium relaxation behavior of the polymer motion.

2. Based on the thermal activation of a single molecular bond we try to give answers to the question, how the activation dynamics is influenced in long chains of such bonds? And how is the thermal stability of a polymer chain affected by its non-Markovian dynamics? The question is of particular importance since biopolymers and supramolecular polymers possibly form functional materials and their stability properties need to be understood. Therefore, we study different experimentally relevant situations as the purely thermally activated escape in the absence of an external force, which is strongly influenced by the equilibrium relaxation properties of the system. And second we consider the force-induced rupture and study the situation when a polymer is exposed to a constant force ramp.

By taking into account the non-Markovian nature of the activation process which appears on timescales shorter than the longest relaxation time of the polymer we intend to provide new perspectives in understanding single molecule pulling experiments.

The outline of the thesis is as follows. Prior to later calculations we present in chapter 2 basic concepts and models of polymer physics. We focus on the Rouse model and its decomposition into normal modes. Furthermore, we introduce the important concept of the equilibrium correlation function. In chapter 3 we proceed and consider equilibrium relaxation properties of the end-to-end distance and of principal components in a one-dimensional polymer chain model with nonlinear interaction between the beads. While for the single-well potentials these properties are similar to the ones of a Rouse chain, for the double-well interaction potentials, modeling internal friction, they differ vastly

from those of the harmonic chain at intermediate times and intermediate temperatures. Thus, the relaxation time of the end-to-end distance may grow by orders of magnitude at intermediate temperatures. It is further shown that the principal components may display subdiffusive scaling.

The non-Markovian character of the coupled dynamics and its impact on the bond rupture process is studied in chapter 4. We consider the thermally activated fragmentation of a homopolymer chain in the absence of an external force. In our simple model the dynamics of the intact chain is a Rouse one until a bond breaks and bond breakdown is considered as a first passage problem over a barrier to an absorbing boundary. Using the framework of the Wilemski-Fixman approximation we calculate activation times of individual bonds for free and grafted chains. We show that these times crucially depend on the length of the chain and the location of the bond yielding a minimum at the free chain ends.

Going one step further we focus in chapter 5 on the rupture dynamics in the presence of a monotonically increasing force. We first present well established theoretical approaches treating the force-induced rupture of a single bond. A model-based theory is then generalized to the case of a chain of breakable bonds which is loaded with a constant force ramp at one of its terminals while the other one is grafted to a surface. On times shorter than the longest relaxation time of the polymer the forces in adjacent bonds differ and only a part of the chain accounts for the rupture process. Our aim will be to point out this impact of the chain length on the rupture force of the system and to derive a sophisticated analytical description of the numerically obtained data. Based on the results in chapter 4 we additionally take into account the non-Markovian fluctuations in the chain and show how these can affect pulling experiments.

In the concluding chapter 6 we present an experimental technique allowing for rupture experiments of long DNA chains under both dynamic and static load. We concentrate on the interpretation of the experimental data which were kindly provided by the experimentalists group of Prof. Rabe (Humboldt University Berlin). We derive intrinsic activation rates of the weakest covalent bonds in the DNA molecule and successfully extrapolate the results to those of other groups. We speculate that the rupture of covalent bonds is possibly triggered by other processes than thermal fluctuations alone. With these thoughts we conclude the main part of the thesis. Eventually we summarize all our findings and draw conclusions for possible forthcoming studies.

2. Basic concepts and definitions

2.1. Polymers

Let us start our introduction to some basic concepts in polymer physics with the etymology of the word itself: polymer. The word *polymer* is derived from the Greek words $\pi o \lambda \acute{\nu}$ (poly meaning "many") and $\mu \acute{\varepsilon} \rho o \zeta$ (meros meaning "part"). The term was first used by the Swedish chemist Jöns Jacob Berzelius (1779-1848). However, his definition of polymers as organic compounds which share identical empirical formulas but different overall molecular weight (the larger of the compounds being described as "polymers" of the smallest) is obsolete (Morawetz, 1987). A present-day definition of polymers was given by Carothers: A polymer is matter whose "structure may be represented by -R-R-R- where '-R-' are bivalent radicals which, in general, are not capable of independent existence." (Morawetz, 1987; Carothers, 1929). Thus, a polymer is synthesized by chemically joining together many small molecules into a single giant one. This idea of polymers as long chains of atoms held together by covalent bonds was first proposed by Hermann Staudinger in 1922 and honored in 1953 with the Nobel Prize in chemistry.

The small molecules used to synthesize polymers are called *monomers*. The *repeat unit* which is derived from the monomer is the simplest repeating entity of a polymer chain. The number of repeat units is specified by the *degree of polymerization*. If it is the same for the whole ensemble of polymer chains the chains are called *monodisperse*, otherwise *polydisperse*. The repeat unit can consist of more than one *structural unit* in cases when it is derived from more than one monomeric reactant (Flory, 1953). Polymers which are synthesized from more than one monomeric species are called *copolymers* or *heteropolymers*; in contrast to *homopolymers* for which the structural and repeat unit is identical.

The units may be connected together in an arbitrary pattern. They can be connected in a linear sequence forming a *linear polymer* or in such way that they form a *branched* structure. Repeating units are not necessarily connected by covalent chemical bonds. Contrary to conventional covalent polymers prepared by the polymerization of low molar mass reactive compounds supramolecular polymers are arrays of low or high molar mass molecules reversibly self-assembled through noncovalent interactions. There exists a wide range of supramolecular polymers where the repeat units are held together by noncovalent forces such as coordination, $\pi - \pi$ charge transfer interaction, and hydrogen bonding (Ciferri, 2000). Since our work is of theoretical origin and we do not specify the interaction between repeating units, we will refer to the term monomer as the monomeric repeat unit throughout the text. So, loosely speaking, a polymer is taken as a long chain molecule that is made up of a large number of monomeric repeat units.

If one wished to have a complete description of the chain, one would have to take into account all microscopic degrees of freedom of the system. Due to the immense number of degrees of freedom this would be a mathematically and also numerically difficult task.

Therefore, it is usual to pass to a coarse grained simplified description. In such a picture the monomeric repeat unit can incorporate a huge number of molecules, interactions between the repeat units are then described by effective potentials and the individual interactions with the solvent molecules are included by independent Gaussian white noise terms.

The ideas presented in this thesis can find their application in all kinds of thermally activated processes in coupled systems and go beyond solely describing rupture processes in coupled polymer systems neglecting the impact of the coupled dynamics of the chain.

2.2. Polymer chain models

In order to introduce some basic models and concepts which we will make use of in the following chapters, we present some discrete polymer chain models, which are of importance for the present work and their basic results. Of special interest is the Rouse model (Rouse, 1953), a coarse grained description of a polymer chain consisting of $N+1$ monomers (also referred to as beads) connected by N harmonic springs. Although in the original Rouse model all restoring forces are of entropic nature we can apply the main concept to the description of series of energetic bonds which in thermal equilibrium—under some conditions—can be approximated as Hookean springs. Eventually we discuss interaction potentials and their applicability for the description of breakable bonds in polymers. It is worth to remark that our brief presentation of polymer models is far away from being complete. For a comprehensive overview on polymer modeling we refer to the standard literature (Flory, 1953, 1969; de Gennes, 1979; Doi and Edwards, 1986; Lin, 2003)

2.2.1. The freely jointed chain model

The freely jointed chain model is the most simple model for a single polymer in solution (Lin, 2003; Doi and Edwards, 1986; de Gennes, 1979). The freely jointed chain (FJC) consists of N links, each of length l_0 which can point in any direction independently of each other. Its conformation is given by the set of $(N+1)$ position vectors $\{\mathbf{R}\} \equiv (\mathbf{R}_0 \dots \mathbf{R}_N)$ of the joints or equivalently by the set of N bond vectors $\{\mathbf{r}\} \equiv (\mathbf{r}_1 \dots \mathbf{r}_N)$ with $\mathbf{r}_n = \mathbf{R}_n - \mathbf{R}_{n-1}$ for $n = 1, 2, \dots, N$. The conformations of the FJC are essentially N step random walks with step lengths equal to the bond length l_0. A schematic picture of the FJC is shown in Fig. 2.1.

The distribution function for the polymer conformation factorizes into the distribution functions of individual links

$$\Psi(\{\mathbf{r}\}) = \prod_{n=1}^{N} \psi(\mathbf{r}_n) \,, \tag{2.1}$$

with the normalized distribution function

$$\psi(\mathbf{r}_n) = \frac{1}{4\pi l_0^2} \delta(|\mathbf{r_n}| - l_0) \,. \tag{2.2}$$

The characteristic length of a polymer can be deduced from the end-to-end vector $\mathbf{r}_{ete}$ of the chain, defined as

$$\mathbf{r}_{ete} = \mathbf{R}_N - \mathbf{R}_0 = \sum_{n=1}^{N} \mathbf{r}_n \,. \tag{2.3}$$

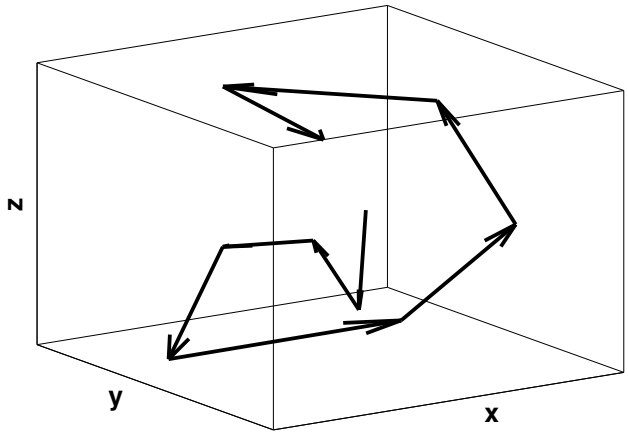

Figure 2.1.: The freely jointed chain. The chain is formed as a sequence of N links which can point in any direction independently of each other. Its mean squared end-to-end distance grows linearly with N. A conformation is a N step random walk with a step length equal to the bond length.

Since there is no preferred direction for any bond, the average vector for each bond is zero, i.e., $\langle \mathbf{r}_n \rangle = 0$, and thus the mean end-to end vector is zero, too, i.e.,

$$\langle \mathbf{r}_{ete} \rangle = \sum_{n=1}^{N} \langle \mathbf{r}_n \rangle = \mathbf{0} \,. \tag{2.4}$$

However, $\langle \mathbf{r}_{ete}^2 \rangle$ attains a non-zero value giving the characteristic length of the coupled chain system as follows

$$\left\langle \mathbf{r}_{ete}^2 \right\rangle = \sum_{n,m=1}^{N} \langle \mathbf{r}_n \cdot \mathbf{r}_m \rangle = \sum_{n=1}^{N} \left\langle \mathbf{r}_n^2 \right\rangle + 2 \sum_{n>m} \langle \mathbf{r}_n \cdot \mathbf{r}_m \rangle = N l_0^2 \,. \tag{2.5}$$

All cross terms vanish because the distributions of the bonds are statistically independent. The root mean squared displacement grows as

$$\sqrt{\langle \mathbf{r}_{ete}^2 \rangle} \propto \sqrt{N} \,. \tag{2.6}$$

This result holds true in a much more general scope and follows essentially from the central limit theorem in statistical mechanics (Lin, 2003). One of the important characteristics of polymers which is not described by the FJC model is the stiffness of the chain. The worm-like chain model (Flory, 1969), being an extension of the FJC, is most commonly used to describe the elastic response of polymers.

2.2.2. The Gaussian chain

The Gaussian chain model describes a polymer as a chain with a bond length distributed as a Gaussian (Lin, 2003; Doi and Edwards, 1986)

$$\psi\left(\mathbf{r}_n\right) = \left(\frac{3}{2\pi l_0^2}\right)^{3/2} \exp\left(-\frac{3\mathbf{r}_n^2}{2l_0^2}\right) , \tag{2.7}$$

with $\left\langle \mathbf{r}_n^2 \right\rangle = l_0^2$. The conformational distribution function of the whole chain becomes

$$\Psi\left(\{\mathbf{r}\}\right) = \prod_{n=1}^{N} \psi\left(\mathbf{r}_n\right) = \left(\frac{3}{2\pi l_0^2}\right)^{3N/2} \exp\left(-\sum_{n=1}^{N} \frac{3\left(\mathbf{R}_n - \mathbf{R}_{n-1}\right)^2}{2l_0^2}\right) . \tag{2.8}$$

Thus the distribution given in Eq. (2.8) corresponds to the Boltzmann distribution of a chain of $N+1$ monomers (beads) connected by harmonic springs with an interaction energy

$$U_H\left(\{\mathbf{R}_n\}\right) = \frac{3k_BT}{2l_0^2} \sum_{n=1}^{N} \left(\mathbf{R}_n - \mathbf{R}_{n-1}\right)^2 , \tag{2.9}$$

with the Boltzmann constant k_B and the temperature T.

Since a harmonic spring allows for an infinite extensibility, the Gaussian chain is not expected to reproduce experimental observations for large deformations. As a consequence of the properties of Gaussian integrals it follows that the distributions of all vectors between any two beads n and m are Gaussians (Wang and Uhlenbeck, 1945), i.e.,

$$\psi\left(\mathbf{R}_n - \mathbf{R}_m\right) = \left(\frac{3}{2\pi l_0^2 \left|n-m\right|}\right)^{3/2} \exp\left(-\frac{3\left(\mathbf{R}_n - \mathbf{R}_m\right)^2}{2l_0^2 \left|n-m\right|}\right) . \tag{2.10}$$

In the limit of large N the probability distribution of the end-to-end vector in the Gaussian chain model coincides with the one in the FJC model. In fact, both models equally describe long sections of a polymer chain. However, the distance distribution given in Eq. (2.10) for the Gaussian chain model can be used between any two beads of the chain.

2.2.3. The Rouse chain

The above described models can represent the static properties of a polymer chain consisting of beads and links as shown in Fig. 2.2. The dynamics of the polymer can be modeled by the Brownian motion of the beads. This was first done by Rouse (Rouse, 1953)[1]. He assumed a coarse grained description of a polymer with local interaction. Excluded volume interactions are disregarded as well as hydrodynamic interactions. Furthermore, the solvent is replaced by a continuum description in terms of viscous friction and thermal noise.

The equations of motion of the beads can either be casted in the form of the Smolu-

[1] A *bead and spring* model for linear polymers was published before by the Soviet physicists Kargin and Slonimskii. Their model did not include fluctuations and was published solely in Russian, therefore, the international impact remained limited (Gurtovenko and Blumen, 2005)

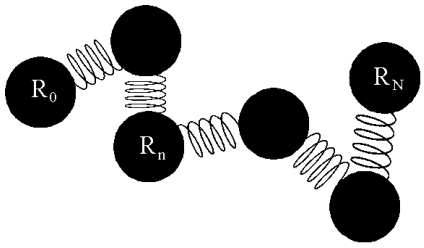

Figure 2.2.: The Rouse chain. $N+1$ beads are coupled by N harmonic links. Hydrodynamic interactions are disregarded as well as excluded volume effects.

chowski equation

$$\frac{\partial \psi}{\partial t} = \sum_n \frac{\partial}{\partial \mathbf{R}_n} \mathbb{M}_{nm} \left(k_B T \frac{\partial \psi}{\partial \mathbf{R}_m} + \frac{\partial U_H}{\partial \mathbf{R}_m} \psi \right) \tag{2.11}$$

or in the form of a set of overdamped Langevin equations

$$\frac{\partial}{\partial t} \mathbf{R}_n(t) = \sum_m \mathbb{M}_{nm} \left(-\frac{\partial U_H}{\partial \mathbf{R}_m} + \boldsymbol{\xi}_m(t) \right) + \frac{k_B T}{2} \sum_m \frac{\partial}{\partial \mathbf{R}_m} \mathbb{M}_{nm} \,, \tag{2.12}$$

with the harmonic interaction potential U_H given in Eq. (2.9) and a diagonal mobility tensor

$$\mathbb{M}_{nm} = \frac{\mathbf{1}}{\gamma} \delta_{nm} \,, \tag{2.13}$$

with a friction coefficient γ. The Langevin equations are linear equations for the beads

$$\gamma \frac{d\mathbf{R}_n}{dt} = -\kappa \left(2\mathbf{R}_n - \mathbf{R}_{n+1} - \mathbf{R}_{n-1} \right) + \boldsymbol{\xi}_n \,, \quad n = 0, \ldots N \,, \tag{2.14}$$

with δ-correlated Gaussian white noise terms

$$\left\langle \xi(t)_{ni} \xi(t')_{mj} \right\rangle = 2\gamma k_B T \delta_{nm} \delta_{ij} \delta(t - t') \,, \quad (i, j = x, y, z) \,, \tag{2.15}$$

and $\kappa = 3k_B T / l_0^2$ for the three-dimensional polymer chain, cf., Eq. (2.9). Eq. (2.14) can be casted in the more convenient form

$$\gamma \frac{d\mathbf{R}_n}{dt} = -\kappa \sum_m \mathbb{W}_{nm} \mathbf{R}_m + \boldsymbol{\xi}_n \,. \tag{2.16}$$

$\mathbb{W}$ is the connectivity matrix governing the interaction strength between connected beads

$$\mathbb{W} = \begin{pmatrix} (2-\epsilon_1) & -1 & & & 0 \\ -1 & 2 & \ddots & & \\ & \ddots & \ddots & \ddots & \\ & & \ddots & 2 & -1 \\ 0 & & & -1 & (2-\epsilon_2) \end{pmatrix} . \tag{2.17}$$

The values of ϵ_1 and ϵ_2 put constraints on the chain ends. For $\epsilon_1 = \epsilon_2 = 1$ the chain is free, for $\epsilon_1 = 0$ and $\epsilon_2 = 1$ one end is fixed, and for $\epsilon_1 = \epsilon_2 = 0$ both ends are fixed resembling

a closed loop. In the course of this work we will consider the first two situations.

The linear system of equations of motion (2.16) can be decoupled by transformation to normal coordinates what is done in Sec. 2.3.

The Rouse chain as a linear model of the dynamics of coupled harmonic springs immersed in a liquid environment will be used frequently in this thesis, either as a reference mark when comparing with the dynamics of chains made up of nonlinear springs or as an approximative description of these nonlinear springs in the small amplitude limit.

To conclude, we remark that the concept of generalized Gaussian structures (GGS) originates from the Rouse chain model. In the framework of the GGS, a polymer system is modeled as a collection of beads connected to each other by means of elastic springs in a system-specific way (to describe e.g. hierarchically built structures). For a comprehensive review see (Gurtovenko and Blumen, 2005).

2.2.4. The Zimm model

For the sake of completeness we briefly present the Zimm model (Zimm, 1956). In addition to the Rouse model it takes into account hydrodynamic interactions. The mobility matrix is given by the Oseen tensor which reads

$$\begin{aligned} \mathbb{M}_{nn} =& \frac{\mathbf{1}}{\gamma}\,, \\ \mathbb{M}_{nm} =& \frac{1}{8\pi\eta\,|\mathbf{r}_{nm}|}\left(\mathbf{1}+\frac{\mathbf{r}_{nm}\mathbf{r}_{nm}}{|\mathbf{r}_{nm}|^2}\right)\,, \end{aligned} \tag{2.18}$$

with $\mathbf{r}_{nm} = \mathbf{R}_n - \mathbf{R}_m$ and the fluid viscosity η. Following Zimm one can introduce a pre-averaged version of the mobility matrix $\langle\mathbb{M}_{nm}\rangle_{eq}$. Assuming that all monomer distances are Gaussian distributed in the thermal equilibrium the pre-averaged Oseen tensor is

$$\langle\mathbb{M}_{nm}\rangle_{eq} = \frac{\mathbf{1}}{\sqrt{6\pi^3\,|n-m|}\eta l_0}\,. \tag{2.19}$$

On this level of approximation the equations of motion for the beads are linear and a decoupling through transformation to normal coordinates is possible

$$\frac{\partial}{\partial t}\mathbf{R}_n(t) = \sum_m \langle\mathbb{M}_{nm}\rangle_{eq}\left(-\frac{\partial U}{\partial \mathbf{R}_m}+\boldsymbol{\xi}_m(t)\right)\,. \tag{2.20}$$

In addition to the harmonic interaction the potential U can contain further contributions, e.g., a term taking into account the excluded volume interactions.

2.3. Normal modes of the Rouse chain

The set of equations (2.16) can be decoupled by transformation to normal coordinates (Doi and Edwards, 1986). While in the continuous limit the transformation is straight forward, it is a little more involved for the discrete Rouse chain. A detailed derivation using the recursion formulas for Chebyshev polynomials is presented in App. A. In the following we present the results of the transformation for the free and for the grafted chain.

The free chain

First we consider the freely diffusing chain. Following the derivation in App. A the normalized eigenvectors of the connectivity matrix $\mathbb{W}$ (see Eq. (2.17)) with $\epsilon_1 = \epsilon_2 = 1$ are

$$\mathbf{u}_k(n) = \sqrt{\frac{2}{N+1}} \cos\left(\left(n+\frac{1}{2}\right)\frac{k\pi}{N+1}\right), \tag{2.21}$$

for $k = 1, ..., N$. The corresponding eigenvalues read

$$\lambda_k^f = 4\sin\left(\frac{\pi}{2}\frac{k}{N+1}\right)^2. \tag{2.22}$$

They are inverse proportional to the relaxation times of single modes. Furthermore, the zero mode eigenvector corresponding to the translational mode of the whole system is

$$\mathbf{u}_0 = \sqrt{\frac{1}{N+1}}\,(1,1,\ldots,1)_{N+1}\,. \tag{2.23}$$

Representing the monomer motion with respect to the normal modes, the monomer coordinate is given by

$$\mathbf{R}_n(t) = \mathbf{X}_0 + 2\sum_{k=1}^{N}\mathbf{X}_k(t)\cos\left(\left(n+\frac{1}{2}\right)\frac{k\pi}{N+1}\right), \tag{2.24}$$

with $\mathbf{X}_k(t)$ being the new coordinates

$$\mathbf{X}_k(t) = \frac{1}{N+1}\sum_{n=0}^{N}\mathbf{R}_n(t)\cos\left(\left(n+\frac{1}{2}\right)\frac{k\pi}{N+1}\right). \tag{2.25}$$

The normalization of the coordinate transformation is chosen such that the dynamics of $\mathbf{X}_0$ represent the time-evolution of the chain's center of mass. In the new coordinates, the equations of motions describe independent Ornstein-Uhlenbeck processes

$$\gamma\dot{\mathbf{X}}_k = -\kappa\lambda_k^f\mathbf{X}_k + \tilde{\boldsymbol{\xi}}_k\,, \tag{2.26}$$

with

$$\left\langle\tilde{\boldsymbol{\xi}}_{0i}(t)\tilde{\boldsymbol{\xi}}_{0j}(t')\right\rangle = \frac{2\gamma k_BT}{N+1}\delta_{ij}\delta\left(t-t'\right), \quad (i,j=x,y,z)\,, \tag{2.27}$$

and

$$\begin{aligned}\left\langle\tilde{\boldsymbol{\xi}}_{ki}(t)\tilde{\boldsymbol{\xi}}_{k'j}(t')\right\rangle &= \frac{2\gamma k_BT\delta_{ij}\delta(t-t')}{(N+1)^2}\sum_{n=0}^{N}\cos\left(\left(n+\frac{1}{2}\right)\frac{k\pi}{N+1}\right)\cos\left(\left(n+\frac{1}{2}\right)\frac{k'\pi}{N+1}\right)\\ &= \frac{\gamma k_BT}{N+1}\delta_{ij}\delta(t-t')\delta_{kk'}\,, \quad k\neq 0\,.\end{aligned} \tag{2.28}$$

We refer to the relaxation times of the normal modes of the free chain as

$$\tau_k^f = \frac{\gamma}{\lambda_k^f \kappa}\,, \tag{2.29}$$

with $k = 1, ..., N$.

The grafted chain

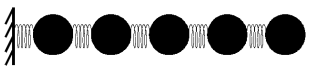

The grafted chain is fixed at one of its ends. The remaining second terminal is free. The normalized eigenvectors of the connectivity matrix (2.17) with $\epsilon_1 = 0$ and $\epsilon_2 = 1$ are found to be (for details see App. A)

$$\mathbf{u}_k(n) = \frac{2}{\sqrt{2N+1}} \sin\left(n\pi \frac{2k-1}{2N+1}\right)\,, \tag{2.30}$$

and the corresponding eigenvalues are

$$\lambda_k^g = 4 \sin\left(\frac{\pi}{2}\frac{2k-1}{2N+1}\right)^2\,. \tag{2.31}$$

Since one end of the chain is fixed there is no translational mode of the whole system. Representing the monomer motion with respect to the normal modes, the monomer coordinate is given by

$$\mathbf{R}_n(t) = \frac{2}{\sqrt{2N+1}} \sum_{k=1}^{N} \mathbf{X}_k(t) \sin\left(n\pi \frac{2k-1}{2N+1}\right)\,, \tag{2.32}$$

with $\mathbf{X}_k(t)$ being the corresponding transformed coordinates

$$\mathbf{X}_k(t) = \frac{2}{\sqrt{2N+1}} \sum_{n=1}^{N} \mathbf{R}_n(t) \sin\left(n\pi \frac{2k-1}{2N+1}\right)\,. \tag{2.33}$$

The decoupled equations of motions describe independent Ornstein-Uhlenbeck processes

$$\gamma \dot{\mathbf{X}}_k = -\kappa \lambda_k^g \mathbf{X}_k + \tilde{\boldsymbol{\xi}}_k\,. \tag{2.34}$$

Due to the choice of normalization the diffusion coefficient of the coordinates remains unchanged, i.e.,

$$\tilde{\boldsymbol{\xi}}_k = \frac{2}{\sqrt{2N+1}} \sum_{n=1}^{N} \boldsymbol{\xi}_n \sin\left(n\pi \frac{2k-1}{2N+1}\right) \tag{2.35}$$

and thus

$$\begin{aligned} \left\langle \tilde{\boldsymbol{\xi}}_{ki}(t) \tilde{\boldsymbol{\xi}}_{k'j}(t') \right\rangle &= 2\gamma k_B T \delta_{ij} \delta(t-t') \frac{4}{2N+1} \sum_{n=1}^{N} \sin\left(n\pi \frac{2k-1}{2N+1}\right) \sin\left(n\pi \frac{2k'-1}{2N+1}\right) \\ &= 2\gamma k_B T \delta_{ij} \delta(t-t') \delta_{kk'}\,, \quad (i,j = x,y,z)\,. \end{aligned} \tag{2.36}$$

Finally, we define the relaxation times of the grafted normal modes of the chain as

$$\tau_k^g = \frac{\gamma}{\lambda_k^g \kappa}\,, \tag{2.37}$$

with $k = 1, ..., N$.

To conclude, we have presented some simple polymer chain models. We will make use of these in the proceeding chapters. Especially the harmonically coupled Rouse chain will play a key role in understanding the equilibrium relaxation properties of chains with beads that are coupled via nonlinear interactions (chapters 3, 4, and 5) or in the description of tension propagation in pulled polymer chains (chapter 5). The important feature of the harmonic chain is that its equations of motion are uncoupled in the representation of its normal modes and are solvable explicitly. Although the Zimm model was presented only for illustration it is worth to remark that—in the pre-averaged form—its equations of motion can be decoupled, too and the theoretical framework developed in this thesis can in principle be applied.

2.4. Binding potentials

In the previous section we presented some simple chain models aiming to mimic polymers in solution. Their object is to describe well the polymer scaling properties with changing system size and its response to an external forcing. Although these models do not allow for bond failure, they help us to understand the chain dynamics. However, in order to study bond rupture in the framework of energetic bonds we have to define an activation barrier which separates the bounded from the unbounded state.

The simplest description of a breakable bond is a Hookean spring with a cut-off at some predefined value of its elongation. For an overcritical elongation of the bond the restoring force drops to zero and the bond is assumed to be broken. We will make use of such a simplified description in chapter 4. The interaction energy (with the potential defined along a reaction coordinate x) reads

$$U_H(x) = \begin{cases} \frac{\kappa}{2}(x - l_0)^2 & , x \leq x_+ \\ -\infty & , x > x_+ \end{cases}\,. \tag{2.38}$$

The local minimum representing the metastable bound state is given by

$$\frac{dU_H}{dx}|_{x=x_-} = 0 \quad \text{and} \quad \frac{d^2U_H}{dx^2}|_{x=x_-} > 0\,, \tag{2.39}$$

and situated at $x_- = l_0$. A schematic representation of this cusp potential is given in panel (a) of Fig. 2.3 (solid line). Superimposed is the full harmonic potential (dashed line).

A more realistic binding potential is the Morse potential named after Philip M. Morse (Morse, 1929). It accounts for the anharmonicity of real bonds and offers the possibility of unbound states for values of the energy which are larger than the dissociation energy D_0. The potential has the form

$$U_M(x) = D_0 \left(1 - \mathrm{e}^{-\alpha(x-l_0)}\right)^2\,, \tag{2.40}$$

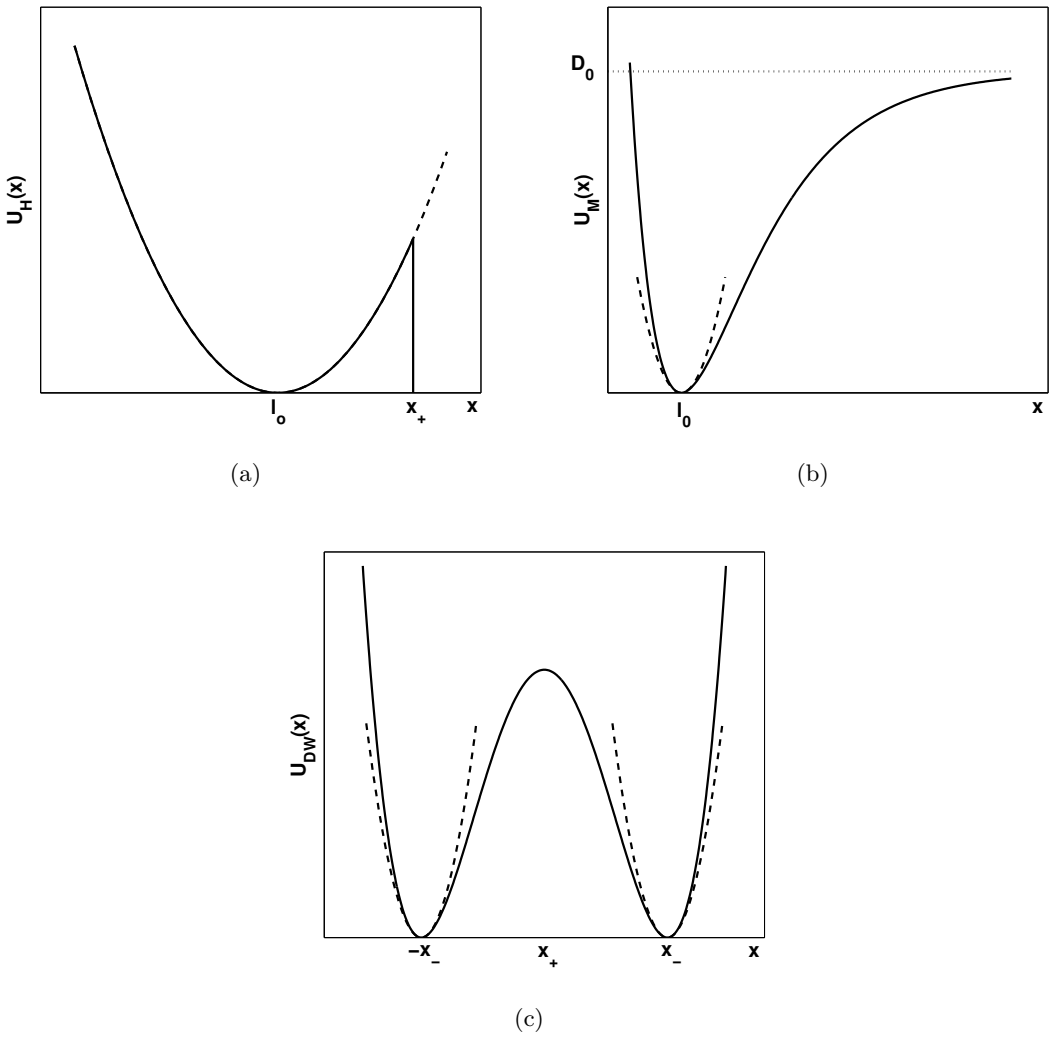

Figure 2.3.: Schematic representation of different binding potentials. Panel (a): The cusp-shaped potential defined in Eq. (2.38) representing a breakable harmonic spring (solid line). Superimposed is the full harmonic potential well (dashed line). Panel (b): The Morse potential defined in Eq. (2.39) (solid line). Superimposed is the harmonic approximation at the potential minimum with a curvature derived from Eq. (2.41) (dashed line) and the value of the dissociation energy D_0 (dotted line). Panel (c): The double-well interaction potential defined in Eq. (2.42) (solid line) and the harmonic approximations at the potential minima (dashed lines) with a value of the curvature $\kappa_{DW} = 2b$.

with the dissociation energy D_0 and a parameter α controlling the width of the potential well. The corresponding harmonic force constant is given by the potential curvature at its minimum (the latter obeys Eq. (2.39))

$$\kappa_M = \frac{d^2U_M(x)}{dx^2}|_{x=x_-} = 2D_0\alpha^2\,. \tag{2.41}$$

The potential (solid line) and the corresponding approximation for small elongations from its minimum (dashed line) are presented in panel (b) of Fig. 2.3. Note that in the absence of an external force the maximum of the Morse potential is situated at infinity.

Apart from these two binding potentials which are used in this thesis for modeling the rupture processes in polymer systems there are other interaction potentials, for example the Lennard-Jones interaction (Lennard-Jones, 1924) or the finitely extensible nonlinear elastic (FENE) potential (Bird et al., 1977) to name only two. However, the behavior of breakable bonds close to the point of rupture is rather universal and it is sufficient to have one convenient parameterization in terms of dissociation energy and stiffness. This will be discussed in detail in chapter 5.

The simplest way to mimic the switching between two distinct states of a bond along its reaction coordinate is given by a double-well potential (DW-potential)

$$U_{DW}(x) = \frac{a}{4}x^4 - \frac{b}{2}x^2\,. \tag{2.42}$$

Its barrier is located at $x_+ = 0$ and the minima are found at $|x_-| = \sqrt{b/a}$. The curvature at the potential minima is $\kappa_{DW} = 2b$. The DW-potential (solid line) and the harmonic approximations at its minima (dashed lines) are depicted in panel (c) of Fig. 2.3.

As we will show in chapter 3 the double-well interaction—as the simplest version of a multistable interaction landscape—can provide an explanation for the observation of strong internal friction found in polymeric solutions (Tang and Lin, 2006; Neusius et al., 2008). Furthermore, the DW-potential may represent a model for protein unfolding as it is found in titin (Staple et al., 2008; Makarov et al., 2001; Hummer and Szabo, 2003; Oberhauser et al., 2001).

2.5. Time correlation function

A practical measure to gain insight into the equilibrium dynamics of a polymer is the equilibrium correlation function and its relaxation properties. Considering the physical quantities $A(t)$ and $B(t)$ the equilibrium correlation function is given by

$$\phi_{AB}(t) = \langle A(t)B(0)\rangle \ . \tag{2.43}$$

If A and B are the same, the function expressed in Eq. (2.43) is called autocorrelation function (ACF). Strictly speaking the above definition gives the equilibrium covariance function. If the definition is done in this way, the normalized function with $\phi_{AB}(t=0)=1$ is called the correlation function. However, except when stated differently, we will refer to the expression in Eq. (2.43) as correlation function and indicate when it is normalized.

Based on a microscopic description of the dynamics we can derive an expression for the time correlation function. Let $\mathcal{G}$ be the conditional probability that given the system was in state x' at time $t=0$ it is observed in state x at time t. According to Bayes formula the two-point joint probability can be expressed as

$$\psi(x,t;x',0) = \mathcal{G}(x,t|x',0)\psi_{eq}(x') \, . \tag{2.44}$$

Then, the time correlation function reads

$$\langle A(t)B(0)\rangle = \int dx \int dx' A(x)B(x')\mathcal{G}(x,t|x',0)\psi_{eq}(x') \, , \tag{2.45}$$

where $A(x)$ and $B(x')$ denote the values of the measured quantity in the states x at time t and x' at $t=0$, respectively.

For a coupled chain system on the microscopic level the conditional probability can be derived from the corresponding Smoluchowski equation (compare Eq. (2.11))

$$\frac{\partial}{\partial t}\mathcal{G}(\mathbf{x},t|\mathbf{x}',0) = \sum_{n,m}\frac{\partial}{\partial x_n}\mathbb{M}_{nm}\left(k_BT\frac{\partial\mathcal{G}}{\partial x_m}+\frac{\partial U}{\partial x_m}\mathcal{G}\right) \, , \tag{2.46}$$

together with the initial condition

$$\mathcal{G}(\mathbf{x},0|\mathbf{x}',0) = \delta(\mathbf{x}-\mathbf{x}') = \prod_n \delta(x_n - x_n') \, . \tag{2.47}$$

Let us illustrate the solution of Eq. (2.45) with an important example: the time correlation of the Brownian motion in a harmonic potential, that is the Ornstein-Uhlenbeck process (Uhlenbeck and Ornstein, 1930). We remark that (as presented in Sec. 2.3) the equations of motion of linearly coupled monomers can be decoupled into a set of independent equations, each describing an Ornstein-Uhlenbeck process.

Eq. (2.45) for the displacement ACF of the Ornstein-Uhlenbeck process reads

$$\langle x(t)x(0)\rangle = \int dx \int dx' x x' \mathcal{G}(x,t|x',0)\psi_{eq}(x') \, . \tag{2.48}$$

The Green's function $\mathcal{G}$ is so far unknown. The equilibrium distribution $\psi_{eq}(x)$ is a Gaus-

sian

$$\psi_{eq}(x) = \sqrt{\frac{\kappa}{2\pi k_B T}} \exp\left(-\frac{kx^2}{2k_B T}\right) . \tag{2.49}$$

The ACF can be derived without explicit knowledge of the Green's function. Using the time derivative of Eq. (2.48) together with Eq. (2.46) we obtain

$$\frac{\partial}{\partial t}\langle x(t)x(0)\rangle = \int dx \int dx' x x' \left\{\frac{1}{\gamma}\frac{\partial}{\partial x}\left(k_B T \frac{\partial \mathcal{G}}{\partial x} + \kappa x \mathcal{G}\right)\right\} \psi_{eq}(x') . \tag{2.50}$$

Integration by parts immediately shows

$$\frac{\partial}{\partial t}\langle x(t)x(0)\rangle = -\frac{\kappa}{\gamma}\langle x(t)x(0)\rangle . \tag{2.51}$$

The equilibrium distribution is known and therefore $\langle x(0)^2\rangle = k_B T/\kappa$. Eventually the ACF of a Brownian particle in a harmonic potential reads

$$\langle x(t)x(0)\rangle = \frac{k_B T}{\kappa} \exp\left(-\frac{\kappa}{\gamma}t\right) . \tag{2.52}$$

The Green's function of this special problem can be found using the eigenfunction expansion of the Fokker-Planck operator (Risken and Frank, 1996) in the Smoluchowski equation

$$\frac{\partial}{\partial t}\mathcal{G} = \mathcal{L}\mathcal{G} = \left(\frac{k_B T}{\gamma}\frac{\partial^2}{\partial x^2} + \frac{k}{\gamma}\frac{\partial}{\partial x}x\right)\mathcal{G} . \tag{2.53}$$

In terms of the eigenfunctions $\hat{\phi}_i(x)$ and eigenvalues $\hat{\lambda}_i$ the Green's function reads (Jacobsen, 1996)

$$\mathcal{G}(x,t|x',0) = \sum_i \hat{\phi}_i(x)\hat{\phi}_i(x')\psi_{eq}(x)\,\mathrm{e}^{-\hat{\lambda}_i t} . \tag{2.54}$$

The eigenfunctions of the Fokker-Planck operator $\mathcal{L}$ are the Hermite polynomials (Spanier et al., 2008; Gardiner, 2004)

$$\hat{\phi}_i(x) = \frac{1}{\sqrt{2^i i!}} H_i\left(\sqrt{\frac{\kappa}{2k_B T}}x\right) , \tag{2.55}$$

together with the eigenvalues

$$\hat{\lambda}_i = \frac{i\kappa}{\gamma} . \tag{2.56}$$

Using Mehler's formula (Mehler, 1866) one finally derives

$$\mathcal{G}(x,t|x',0) = \frac{\sqrt{\kappa}}{\sqrt{2\pi k_B T\left(1-\mathrm{e}^{-2t/\tau}\right)}}\,\mathrm{e}^{-\frac{\kappa\left(x-x'\,\mathrm{e}^{-t/\tau}\right)^2}{2k_B T\left(1-\mathrm{e}^{-2t/\tau}\right)}} , \tag{2.57}$$

with $\tau = \gamma/\kappa$. In the limit $t \to \infty$ the propagator becomes the Gaussian equilibrium distribution $\psi_{eq}(x)$ in the harmonic potential well.

With the above example one can now easily calculate the autocorrelation function of

the normal modes of a harmonic chain. For the free chain we obtain

$$\begin{aligned}\left\langle X_{ki}(t)X_{k'j}(0)\right\rangle &= \left\langle X_{ki}(0)^2\right\rangle \delta_{ij}\exp\left(-\frac{t}{\tau_k^f}\right)\\ &= \frac{k_BT}{2(N+1)\gamma}\tau_k^f\exp\left(-\frac{t}{\tau_k^f}\right)\end{aligned} \tag{2.58}$$

and for the grafted chain

$$\begin{aligned}\left\langle X_{ki}(t)X_{k'j}(0)\right\rangle &= \left\langle X_{ki}(0)^2\right\rangle \delta_{ij}\exp\left(-\frac{t}{\tau_k^g}\right)\\ &= \frac{k_BT}{\gamma}\tau_k^g\exp\left(-\frac{t}{\tau_k^g}\right).\end{aligned} \tag{2.59}$$

Note that in the case of a single grafted bond $\tau_1^g = \gamma/\kappa$ and Eq. (2.52) is recovered.

Relation to the mean squared displacement

In general the correlation function of a physical quantity with zero mean is related to its mean squared displacement. The mean squared displacement can be rewritten as follows

$$\begin{aligned}\left\langle x^2(t)\right\rangle &= \left\langle \left(x(t+t') - x(t')\right)^2\right\rangle\\ &= \left\langle x^2(t+t') - 2x(t+t')x(t') + x^2(t')\right\rangle\\ &= 2\sigma^2\left(1-\phi(t)\right).\end{aligned} \tag{2.60}$$

Thus the values of $1-\phi(t)$ and $\langle x^2(t)\rangle$ contain the same information and differ only in normalization. σ denotes the variance.

Discrete set of data

Computer simulations as well as real experiments involve the measurement of a discrete sample of data points rather than continuous trajectories. In such cases the unbiased normalized autocorrelation function of $\phi(t)$ $(t \in 0, ..., M-1)$ is given by

$$\phi(t) = \frac{1}{(M-t)\sigma_{\mathfrak{X}}^2}\sum_{n=0}^{M-t-1}\left(\mathfrak{X}(n+t) - \mu_{\mathfrak{X}}\right)\left(\mathfrak{X}(n) - \mu_{\mathfrak{X}}\right), \tag{2.61}$$

with the sample trajectory $\mathfrak{X}(t)$ (coordinate, end-to-end distance, etc.), the sample mean $\mu_{\mathfrak{X}}$, and sample variance $\sigma_{\mathfrak{X}}^2$. A fast numerical algorithm evaluating $\phi(t)$ usually involves the calculation of the Fourier transform of $\mathfrak{X}(t)$ since the expression in Eq. (2.61) is essentially a convolution.

2.6. Summary

In the present chapter we have introduced the polymer chain as a system of repeating units synthesized from monomers. We presented important static polymer models. A famous model describing the chain dynamics is the Rouse model which is a linear one and therefore is exactly solvable in the representation of the normal modes. Based on such a description, the equilibrium relaxation properties of the polymer can be determined. The corresponding relaxation times of internal modes will play an important role in understanding the fragmentation kinetics of polymer chains which are discussed in chapter 4. Since the purely harmonic description of the interaction potential between adjacent monomers does not allow for fragmentation, we introduced interaction potentials which mimic breakable bonds with at least one metastable state and an activation barrier. Eventually we introduced the definition of the time correlation function and calculated the latter exemplary for the Ornstein-Uhlenbeck process. Furthermore, we have shown how the correlation function of a physical quantity is related to its mean squared displacement. Based on this introduction we will concentrate in the following chapter 3 on the equilibrium relaxation properties in polymer chains with nonlinear interactions. The linear Rouse model will be our reference mark we compare all our results with.

3. Correlations in simple polymer chain models

3.1. Introduction

In the previous chapter we presented important polymer chain models and introduced the concept of the correlation function to gain insight into their dynamics. In this chapter we study the equilibrium relaxation properties of the correlations of the dynamical quantities of polymer chains (Fugmann and Sokolov, 2009b). Special interest is paid to the impact of nonlinearities and barriers in the free energy landscape. Although, at a first glance, seemingly not directly related to the fragmentation dynamics of bonds in the chain, we will show in the following chapters 4 and 5 that the breakup of bonds in a chain is crucially affected by the overall motion of all beads in the system which is correlated on a timescale given by the chain's longest relaxation time.

The dynamics of polymers and peptides attracted large attention in the past decade, mostly due to the relations of such dynamics to biological function. First such interest was due to the dynamics of nonequilibrium states (connected with the folding problem and with the biological functioning of the proteins), and only later some interest to equilibrium fluctuations in proteins arose. This interest was caused by two reasons: one has to do with the thermal stability of proteins as connected to their structures (Granek and Klafter, 2005), another one is related to the luminescent measurements of fluctuations of the distance between two groups in equilibrium (Chen et al., 2009; Kou and Xie, 2004) and the discovery of the anomalous kinetics and extremely large characteristic times in such fluctuations. The results of these investigations, put together, lead to an enigma: On the one hand, the thermal stability and many other properties of proteins can be well-described within simple bead-spring models of such systems (Togashi and Mikhailov, 2007; Cressman et al., 2008), which for small deviations from equilibrium can be reduced to a standard picture of normal modes in a generalized Gaussian structure (GGS). The evaluation of the characteristic times in such systems, however, leads to results being off by orders of magnitudes when compared to the observed times (Tang and Lin, 2006). The strong discrepancy in correlation times implies the existence of a strong additional *internal friction* mechanism slowing down the dynamics compared to the linear Rouse one.

Recently, the anomalous kinetics, which is expressed in a power-law decay of correlations, was observed even in single modes and even in relatively short and flexible peptides, i.e., linear chains lacking secondary structure (Neusius et al., 2008)[1], and the behavior found here is very close to the one observed in protein simulations (Senet et al., 2008). Therefore

[1] *Secondary structure*: It is formally defined by the hydrogen bonds of the biopolymers. Since hydrogen bonding is related to other structural features of the polymer there are less formal definitions applying the concepts of curvature and torsion. For comparison, the *Primary structure* is the specification of the atomic composition and the chemical bonds. For a linear chain the primary structure coincides with the monomeric repeat unit.

such kinetics probably is an intrinsic property of a large class of polymers and is not connected to the specific properties of the secondary structure of proteins. Furthermore, it has been shown that trap models cannot account for the anomalous dynamics (Neusius et al., 2008). Therefore, it is necessary to analyze what kind of the minimal assumptions about the intramolecular potentials have to be made to build a model mimicking the behavior observed in realistic molecular dynamics simulations.

We study the equilibrium relaxation properties in one-dimensional coupled chain systems. We focus on models which are sufficiently simple to understand their underlying dynamics in very detail but are able to reproduce the most important features found in much more complex models mimicking realistic polymer behavior. A number of calculations in the proceeding parts of the thesis are based on the results obtained in this chapter.

We consider a one-dimensional chain of beads, similar to the Rouse model of the polymer dynamics, with the only difference being an exchange of the harmonic interaction between the beads for a nonlinear one. We discuss the end-to-end distance of the chain and the relaxation properties of the principal components[2] (PCs) (Kitao and Go, 1999) of the system. While for the single-well potentials these properties are similar to the ones of a Rouse chain, for the double-well interaction potentials, modeling internal friction, they differ vastly from those of the harmonic chain at intermediate times and intermediate temperatures. The description within our minimal framework mimics the relaxation properties found in much more complex polymer systems. Thus, the relaxation time of the end-to-end distance may grow by orders of magnitude at intermediate temperatures. The principal components not only display larger relaxation times but also subdiffusive scaling. Their directions are shown to coincide with the normal modes of the harmonic chain, whatever interaction potential is assumed.

Typical mechanisms of internal friction involve the existence of barriers in the free energy landscape of the system, being of entropic or of enthalpic nature (de Gennes, 1979; Khatri and McLeish, 2007). The necessity to overcome such barriers slows down the overall dynamics by the Arrhenius factor which might be quite large (Fixman, 1978). However, the existence of a complex, nonlinear energy landscape may lead to a strong mixing of modes appearing in the linearized description, and make the whole analysis based on such a picture problematic. As we proceed to show, this is not the case: Although the dynamics of modes is strongly influenced, the directions of the PCs in configuration space follow those of the normal modes.

The multiwell intramolecular potentials appear at different scales and are ubiquitous in polymers (Ryckaert and Bellemans, 1975; Binder and Paul, 1997). They appear quite naturally e.g. within the valent-angle model (Rigby and Roe, 1987; Binder and Paul, 1997). The anomalous behavior is present within the finite temperature range which may be relevant for the biological functioning. It disappears both for low and for high temperatures, where the dynamics can therefore be described by an effective harmonic model, albeit with the values of parameters strongly different from the microscopic ones. This property can explain why the GGS work quite well in predicting thermal stability properties while failing to mimic the temporal fluctuation behavior at moderate temperatures.

The chapter is structured as follows: In the next section we introduce our one-dimensional minimal chain model and present the different types of nonlinear interaction po-

[2] the outcome of the principal component analysis which is introduced in Sec. 3.4

tentials. In Sec. 3.3 we consider the correlation function of the end-to-end vector of the polymer chain. As a reference we calculate the latter for the harmonic Rouse chain and compare the results with those obtained from numerical simulations of chains with nonlinear interactions. In Sec. 3.4 we have a closer look at the principal components of the polymer chain and their relaxation dynamics. First we introduce the concept of principal component analysis and proof that their directions follow those of the normal modes of the harmonic chain whatever interaction potential is assumed. We proceed and study the relaxation behavior of the correlation function of the PCs for different nonlinear interactions. In Sec. 3.5 we compare our results with those of a realistic chain model mimicking a polyethylene molecule and find a qualitative agreement. Eventually we draw the conclusions and discuss implications of our findings for the proceeding chapters.

3.2. Minimal chain model

We consider a one-dimensional chain of $N+1$ monomers, similar to the Rouse model introduced in chapter 2, with the only difference being an exchange of the harmonic interaction between the beads for a nonlinear one. Thus, the interaction potential as a function of the monomer distances $r_n = x_n - x_{n-1}$ $(n = 1, \dots N)$ is given by $U(r_n)$ which we specify below. We consider freely diffusing chains, hence $U(r_{n+1}) = U(r_1) = 0$. For small elongations from the equilibrium position the interaction potential U is assumed to yield a harmonic approximation with a corresponding coupling strength κ_h. The coupled system of equations of motion is given by the following set of overdamped Langevin equations

$$\gamma \dot{x}_n = -\frac{d\left(U(r_{n+1}) + U(r_n)\right)}{dx_n} + \sqrt{2\gamma k_B T}\xi_n \,, \tag{3.1}$$

with friction coefficient γ and δ-correlated Gaussian white noise. We pass to a dimensionless time $\tilde{t} = t\kappa_h/\gamma$ and omit the tilde in our notation. Furthermore, we introduce the noise strength $D = k_B T/\kappa_h$. Lengths are given in arbitrary units. Note, that for $U(r_n) = U_H(r_n)$ with $U_H(r_n)$ introduced in Eq. (2.9) the equations of motion (3.1) are those of a one-dimensional Rouse chain.

In the following we focus on three types of coupling functions U, either single-well or double-well. For the single-well coupling potentials we consider the soft and asymmetric Toda interaction (T-potential) and a hard and symmetric quartic interaction (Q-potential). The Toda potential reads

$$U_T(r_n) = \kappa_h \left(r_n + \exp(-r_n) - 1\right) \,. \tag{3.2}$$

For small elongations from the minimum the potential can be approximated by

$$U_T(r_n) = \frac{\kappa_h}{2}\left(r_n^2 - \frac{1}{3}r_n^3\right) \,. \tag{3.3}$$

Thus the potential exhibits a soft nonlinear correction to the harmonic term. The local curvature of the potential decreases with increasing value of r_n and for very small elongations from its rest state, i.e., $|r_n| \ll 1$, the potential can be described by a harmonic one with a coupling constant $\kappa = \kappa_h$. Since the potential is asymmetric its mean $\langle r_n \rangle$ differs

from zero. The stationary probability density function is

$$\psi(r_n) = \frac{1}{\psi_{norm}} \exp\left(-\frac{\kappa_h \left(r_n + \mathrm{e}^{-r_n} - 1\right)}{k_B T}\right) , \tag{3.4}$$

with the normalization

$$\psi_{norm} = \int_{-\infty}^{\infty} \exp\left(-\frac{\kappa_h \left(r_n + \mathrm{e}^{-r_n} - 1\right)}{k_B T}\right) dr_n = \left(\frac{k_B T}{\kappa_h}\right)^{\kappa_h / k_B T} \Gamma\left(\frac{\kappa_h}{k_B T}\right) , \tag{3.5}$$

with the Gamma function Γ. The mean bond length is given by

$$\langle r_n \rangle = \left(\ln\left(\frac{\kappa_h}{k_B T}\right) - \beta\left(\frac{\kappa_h}{k_B T}\right)\right) , \tag{3.6}$$

with the digamma function $\beta(x)$ (exemplary, $\beta(1) = \gamma_{EM}$ and $\beta(2) = \gamma_{EM} + \ln(2)$, $\gamma_{EM} \simeq 0.577216$ is the Euler-Mascheroni constant).

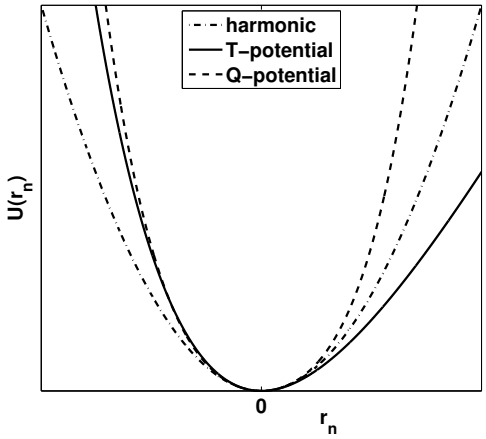

Figure 3.1.: Different types of single-well interaction potentials, the harmonic potential (dashed-dotted line), the Toda potential (T-potential, solid line), and the quartic interaction (Q-potential, dashed line). The latter exhibits a hard nonlinearity while the T-potential has a soft cubic nonlinearity for positive elongations.

The Q-potential reads

$$U_Q(r_n) = \frac{\kappa_h}{2}\left(r_n^2 + \frac{1}{2} r_n^4\right) . \tag{3.7}$$

Here the local curvature is

$$\frac{d^2 U_Q(r_n)}{dr_n^2} = \kappa_h \left(1 + 3 r_n^2\right) \geq \kappa_h \, , \tag{3.8}$$

thus the potential obeys a hard nonlinearity. Again, for small elongations from its rest

state the coupling strength is given by the corresponding value κ_h of the harmonic chain. The single-well potentials are sketched for illustration in Fig. 3.1. The T-potential shows a pronounced asymmetry. In the one-dimensional chain the location of the potential minimum can be set to zero, i.e., the equations of motion (3.1) describe the evolution of deviations from the zero temperature bond length.

The double-well coupling potential (DW-potential) is given by

$$U_{DW}(r_n) = \kappa_h \left(\frac{a}{4} r_n^4 - \frac{b}{2} r_n^2 \right) , \tag{3.9}$$

with a barrier height

$$\Delta E = \frac{\kappa_h b^2}{4a} , \tag{3.10}$$

and the curvature close to the two potential minima

$$\kappa_{DW} = 2b\kappa_h . \tag{3.11}$$

On short times the motion proceeds in the vicinity of one of the two quasiharmonic minima and on a timescale given by the Arrhenius law large jumps occur.

3.3. Relaxation of the end-to-end distance

First, we consider the ACF of the end-to-end distance $r_{ete} = x_N - x_0$. Its correlation time is a measure for the reorientation motion of the polymer molecule (Lin, 2003). The unnormalized ACF is referred to as $\tilde{\phi}_{ete} = \phi^0_{ete}\phi_{ete}(t)$ with the normalized ACF $\phi_{ete}(t)$. Before studying the impact of nonlinearity and internal friction on the chain dynamics we calculate $\tilde{\phi}_{ete}$ for the free harmonic chain. Therefore, we make use of the normal modes of the chain (Doi and Edwards, 1986; Lin, 2003). Using Eq. (2.24) r_{ete} is given by

$$\begin{aligned} r_{ete} = x_N - x_0 &= 2\sum_{k=1}^{N} X_k(t) \left\{ \cos\left(\left(N + \frac{1}{2} \right) \frac{k\pi}{N+1} \right) - \cos\left(\frac{1}{2} \frac{k\pi}{N+1} \right) \right\} \\ &= 2\sum_{k=1}^{N} X_k(t) \left((-1)^k - 1 \right) \cos\left(\frac{k\pi}{2(N+1)} \right) \\ &= -4{\sum_{k=1}^{N}}' X_k(t) \cos\left(\frac{k\pi}{2(N+1)} \right) , \end{aligned} \tag{3.12}$$

where the sum with the prime denotes that we sum over odd values of k only. Its autocorrelation function is thus

$$\langle r_{ete}(t) r_{ete}(0) \rangle = 16{\sum_{k=1}^{N}}' \langle X_k(t) X_k(0) \rangle \cos\left(\frac{k\pi}{2(N+1)} \right)^2 . \tag{3.13}$$

In chapter 2 we calculated the ACF of the normal modes of the free chain and obtained

$$\langle X_k(t) X_k(0) \rangle = \frac{k_B T}{2(N+1)\gamma} \tau_k^f \exp\left(-\frac{t}{\tau_k^f} \right) . \tag{3.14}$$

Hence we have

$$\begin{aligned}\tilde{\phi}_{ete} &= 8\frac{k_BT}{\gamma(N+1)}{\sum_{k=1}^{N}}' \tau_k^f \exp\left(-\frac{t}{\tau_k^f}\right)\cos\left(\frac{k\pi}{2(N+1)}\right)^2 \\ &= \frac{2k_BT}{\kappa(N+1)}{\sum_{k=1}^{N}}' \exp\left(-\frac{t}{\tau_k^f}\right)\cot\left(\frac{k\pi}{2(N+1)}\right)^2 .\end{aligned} \tag{3.15}$$

Finally, the normalized ACF reads

$$\phi_{ete}(t) = \frac{2}{N(N+1)}{\sum_{k=1}^{N}}' \exp\left(-\frac{t}{\tau_k^f}\right)\cot\left(\frac{k\pi}{2(N+1)}\right)^2 . \tag{3.16}$$

In the limit of large chain lengths, $N \gg 1$, the relaxation times of the normal modes are

$$\tau_k^f \simeq \frac{N^2}{\pi^2}\frac{1}{k^2} = \frac{\tau_1^f}{k^2} , \tag{3.17}$$

and the normalized ACF can be written as

$$\phi_{ete}(t) \simeq \frac{8}{\pi^2}{\sum_{k=1}^{N}}' \frac{1}{k^2}\exp\left(-\frac{t}{\tau_1^f}k^2\right) . \tag{3.18}$$

Following Eq. (2.60) in chapter 2 the mean squared displacement $\langle r_{ete}(t)^2\rangle$ and $1-\phi_{ete}(t)$ contain the same information and differ only in normalization. For times $t < \tau_1^f$ and long chains, the mean squared displacement of r_{ete} is thus given by (Doi, 1975)

$$\begin{aligned}1-\phi_{ete}(t) &= \frac{8}{\pi^2}{\sum_{k=1}^{N}}' \frac{1}{k^2}\left(1-\exp\left(-\frac{t}{\tau_1^f}k^2\right)\right) \\ &\simeq \frac{4}{\pi^2}\int_0^\infty dk \frac{1}{k^2}\left(1-\exp\left(-\frac{t}{\tau_1^f}k^2\right)\right) \\ &= \frac{4}{\pi^{3/2}\sqrt{\tau_1^f}}\sqrt{t} ,\end{aligned} \tag{3.19}$$

and hence $1-\phi_{ete} \propto \sqrt{t}$. We remark that for short chains the scaling breaks down for small t.

In the following we compare the scaling of chains with different interaction potentials and the scaling of the harmonic chain which is our reference mark for the typical timescale of relaxations.

3.3.1. Nonlinear single-well potentials

In the first part of this section we consider the relaxation properties of r_{ete} for chains of monomers coupled via nonlinear single-well interaction potentials. Therefore, we numerically recorded trajectories of polymer motion and deduced the end-to-end distance and eventually its unbiased ACF according to Eq. (2.61). The simulation time was chosen such that $\tau_{sim} \gg \tau_1^f$, τ_1^f being the longest relaxation time of the freely diffusing chain. Note that for the symmetric interaction potentials the sample mean is expected to be zero while for the asymmetric T-potential it coincides with $N\langle r_n\rangle$ (the mean bond length $\langle r_n\rangle$ is given in Eq. (3.6)) and has to be taken into account in the calculation of the unbiased ACF, see Eq. (2.61).

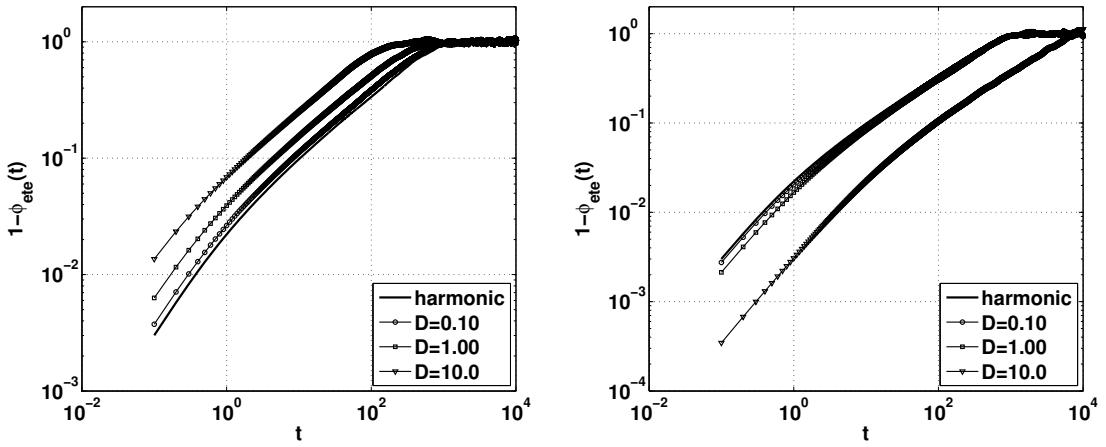

Figure 3.2.: $1 - \phi_{ete}(t)$ for different values of the noise strength D as given in the legend. The chain has $N = 31$ bonds. In panel (a) the bead interaction is described by the Q-potential while in panel (b) it is the T-potential. Superimposed is the scaling of the corresponding harmonic chain.

For small bond elongations the interactions are linear. With increasing noise strength the mean squared bond elongation grows and the impact of nonlinearity on the dynamics of r_{ete} becomes more pronounced. In contrast it is expected to vanish in the limit $D \to 0$. Therefore, we study the scaling of the ACF as a function of the noise strength D. In Fig. 3.2 we present the temporal evolution of $1 - \phi_{ete}(t)$ for different values of D. Panel (a) shows the results for the Q-potential and panel (b) for the asymmetric T-potential. It is clearly visible that the curves (thin lines with symbols) are shifted to shorter times in the first case and to later times in the second. For $D = 0.10$ (circles) the curves follow very close the solid line describing the relaxation behavior of the corresponding harmonic chain. For $D = 1.00$ (squares) the curves lie still close to the solid line. The distance becomes larger for $D = 10.0$ (triangles) . Thus, compared to the corresponding harmonic chain, the autocorrelation time reduces for the Q-potential while it grows for the T-potential, and this effect is stronger for higher temperatures (larger values of D).

An illustrative explanation is as follows: The relaxation time of r_{ete} is to a good approxi-

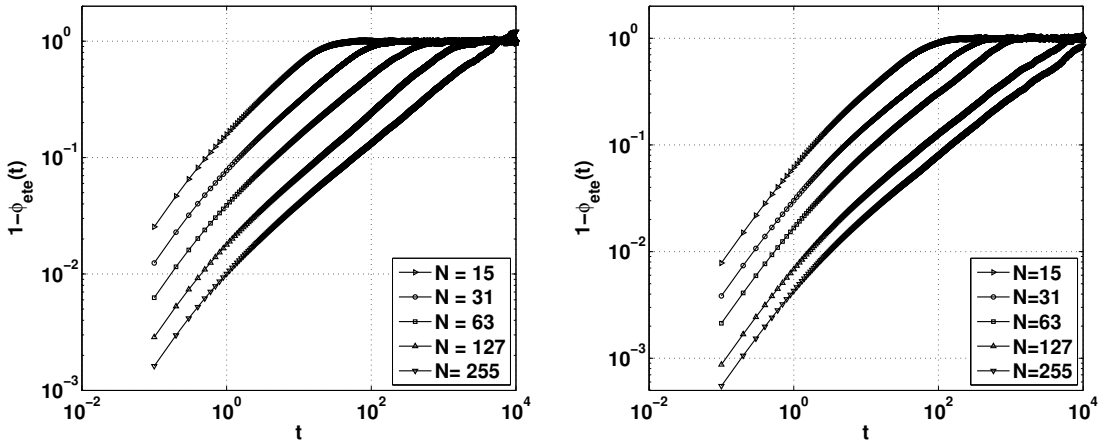

(a) (b)

Figure 3.3.: $1 - \phi_{ete}(t)$ for different values of the chain lengths N as given in the legend. The value of the noise strength is $D = 1$. In panel (a) the bead interaction is described by the Q-potential while in panel (b) it is the T-potential.

mation the longest relaxation time of the normal modes of the harmonic chain (Lin, 2003). This one behaves as $\tau_1^f \propto 1/\kappa_h$. For any nonlinear potential the curvature (the effective coupling strength) is a function of the elongation from its rest state. The mean squared bond elongation grows with the noise strength and causes a growing effective value of κ_h for a hard Q-potential, while for the soft nonlinearity of the T-potential the opposite is true. Hence, τ_1^f is expected to be smaller for the Q-potential and larger for the T-potential. However, the scaling of all presented curves follows the one of the corresponding harmonic chain (solid black lines in Fig. 3.2). Hence introducing nonlinear single-well potentials does not change the scaling of the relaxation properties of the polymer chain.

Having studied the impact of the noise strength D on the relaxation behavior of the ACF of r_{ete} we now consider its dependence on the system size. In Fig. 3.3 we present $1 - \phi_{ete}(t)$ for different values of the chain length N. As in Fig. 3.2, in panel (a) the beads are coupled by the Q-potential while in panel (b) they interact through the T-potential. Compared to the harmonic chain the ordering of the curves as a function of the overall number of beads remains the same, i.e., $1-\phi_{ete}(t)$ is shifted to larger times with increasing chain length.

Hence the scaling of $\phi_{ete}(t)$ of a nonlinear single-well interaction potential may be well described within an effective harmonic model with parameter values depending on the noise strength (corresponding, e.g., to the temperature in real experiments) and the number of bonds in the chain.

3.3.2. Double-well potential

Now we consider the double-well coupling potential. It is the simplest representation of a complex interaction energy landscape allowing for different structural configurations. The transitions between the two states may be described by a rate process and in equilibrium

the transition rates are governed by the Arrhenius law. Thus by establishing a potential barrier and multiple minima in the free energy landscape we introduce further timescales which affect the dynamical properties of the system. In the long time domain the kinetics are dominated by the rare fluctuations following the Arrhenius law. Therefore, the characteristic relaxation times are shown to increase drastically when the typical transition times are large compared to the relaxation times of the lowest modes of the corresponding harmonic chain. However, for very large transition times, which might overcome the observation time in the experiment, hardly no transitions happen and the relaxation behavior of the corresponding harmonic chain is recovered.

In Fig. 3.4 we show the ACF of r_{ete} for different chain lengths and two values of the temperature. We observe an interesting behavior. First, for a high barrier height as presented in panel (a), i.e., $\Delta E/k_BT = 10$, at small times the scaling of $1 - \phi_{ete}(t)$ is comparable with the one of a harmonic chain, i.e., $1 - \phi_{ete}(t) \propto \sqrt{t}$. For larger times the scaling changes, the exponent becomes larger, and the curves for different chain lengths come closer.

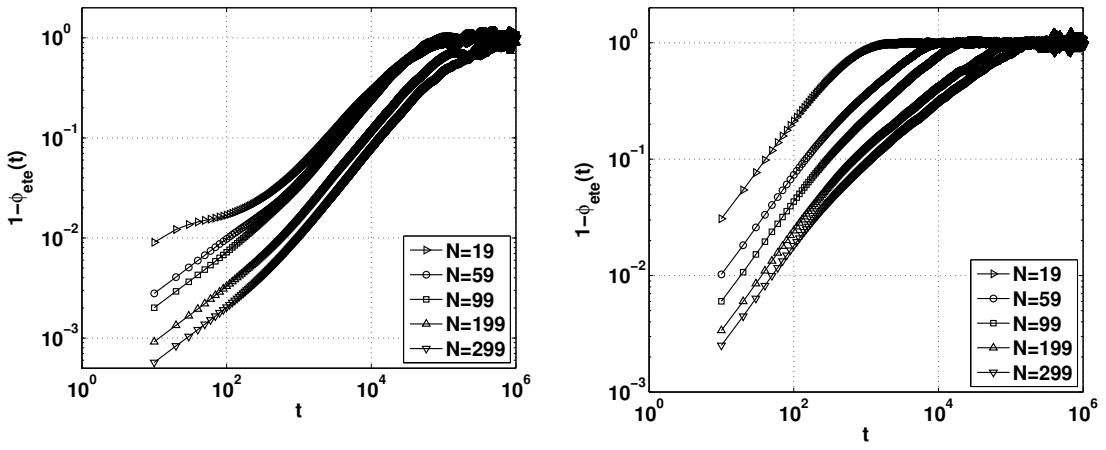

Figure 3.4.: $1 - \phi_{ete}(t)$ as a function of the time for different values of the length of chains with DW interaction between the beads (as given in the legends) and two values of the barrier height (panel (a): $\Delta E/k_BT = 10$ and panel (b): $\Delta E/k_BT = 5$). The remaining parameter values are $a = 1$ and $b = 2$.

As it was first noticed by Kuhn and Kuhn (Kuhn and Kuhn, 1945, 1946), the chain end-to-end internal friction should vary inversely with the number of monomers N. This is due to the fact that the dynamics of conformational change from internal barrier hopping depends on any one of N bonds flipping states. Thus for long chains their end-to-end friction due to internal barriers is expected to be negligible when compared to solvent friction (de Gennes, 1979; Manke and Williams, 1985; Khatri and McLeish, 2007). Thus for the short chains in Fig. 3.4 the non-monotonic scaling due to internal friction is more pronounced. Passing to $\Delta E/k_BT = 5$ the overall picture changes. The scaling differs only slightly from the corresponding harmonic one, however the huge increase of relaxation times for the smaller chains (which would result from strong internal friction) disappears.

We conclude that since the barrier height defines the timescale of rare barrier crossings it should be possible to change the scaling by varying the height of the activation barrier.

Thus we studied the scaling of the ACF for different values of the barrier height. In realistic polymers there may be found many bonds with different barrier heights. Therefore, we also considered a case when the barrier heights are randomly distributed with the density $\rho(e) \sim \exp(\lambda_e(e - e_{min}))$, $\Delta E/k_BT = e \geq e_{min} = 5$, $\lambda_e = 0.1$ with a cut-off at $e_{max} = 11$ to avoid freezing. The results are depicted in Fig. 3.5. Let us first discuss the case of fixed barrier heights (black symbols). For different values of $\Delta E/k_BT$ the curves strongly differ. At a low temperature ($\Delta E/k_BT = 20$, black circles) the curve coincides with the one of the corresponding harmonic chain (solid black line) for a finite simulation time (as expected the beads hardly jump between the two minima of the coupling potential): This is exactly what should be observed when such a conformation change mechanism is frozen out (Tournier and Smith, 2003). For intermediate barrier heights ($\Delta E/k_BT = 10$, black triangles) the behavior of the ACF is strongly different. It shows distinctly diverse behavior for short and long times interpolated by a plateau. The characteristic relaxation time in the long-time domain (where the kinetics is dominated by rare fluctuations following the Arrhenius law) is by about four orders of magnitude larger than for the harmonic chain. For high temperatures ($\Delta E/k_BT = 1$, black upturned triangles) the correlation time is much smaller compared to the previous case (but still larger than in the harmonic case due to the softer effective potential) and its scaling follows the one of the harmonic chain. We conclude that the increase of the correlation time (related to the timescale of rare barrier crossings) becomes large at intermediate temperatures. For very low and very high temperatures the scaling of r_{ete} may be described by the one of an effective harmonic potential. In the case of randomly distributed barrier heights (gray squares) the plateau observed for the intermediate value of $\Delta E/k_BT = 10$ is smoothed out, but the increase of characteristic relaxation time persists.

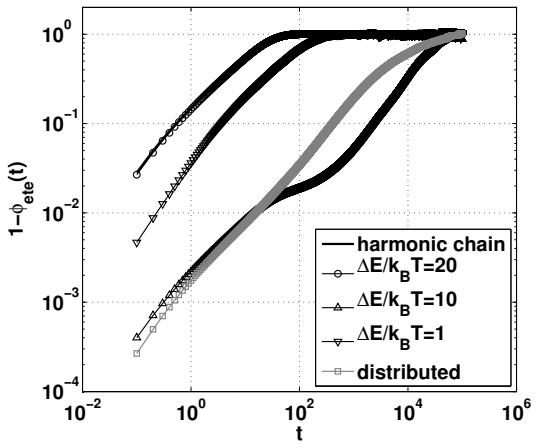

Figure 3.5.: ACF of the end-to-end distance r_{ete}. Shown is $1 - \phi_{ete}(t)$. DW-potential. The barrier heights are given in the legend and the remaining parameter values are $b = 2$ and $N = 25$. Superimposed is the scaling of the corresponding harmonic chain with $\kappa = 2b\kappa_h$ (solid line).

To summarize, we have shown that internal friction introduced by the simplest representation of a multi-well free energy surface in configuration space, i.e., a DW-potential, may cause a drastic change of the relaxation behavior of the end-to-end distance of a polymer chain. The characteristic relaxation times may be enlarged by many orders of magnitude. For both low and high temperatures (or high and low barrier barrier heights, respectively) the scaling of a harmonic chain is recovered, albeit with effective parameter values depending on the temperature. This is also true for the nonlinear single-well potentials, which however show a harmonic relaxation behavior of r_{ete} for all values of D.

3.4. Principal components

To gain more insight into the chain dynamics we study the PCs of the one-dimensional polymer chain. Therefore, we first introduce the concept of principal component analysis (PCA) and discuss their scaling for the harmonic chain which again—as for the end-to-end distance—provides a reference mark for our further studies.

3.4.1. Principal component analysis

In real experiments or in numerical simulations, the complete dynamical information (e.g. trajectories of atoms) is stored in a huge amount of data . Based on these raw data a physical interpretation of the underlying processes is often involved. However, it has been shown that the essential dynamics can be mapped on lower-dimensional subspaces via PCA, see (Cohen and Moerner, 2007; Kitao and Go, 1999) and references therein. Therefore, PCA is a powerful tool for the analysis of complex measured data.

Mathematically, PCA is defined as an orthogonal linear transformation that maps the data to a new coordinate system such that the greatest variance by any projection of the data comes to lie on the first coordinate (the first principal component), the second greatest variance on the second coordinate and so on. In the following we will briefly describe how PCA works.

1. Suppose you have measured a set of data, comprising observations of N variables. Each variable has been measured M times. Then the data can be arranged as a matrix $\mathbb{X}$. Each row corresponding to one particular variable and a column to one grouped observation of all N variables. The matrix $\mathbb{X}$ has thus a dimension $N \times M$.

2. Next, subtract the empirical mean

$$\mu\,(1 \leq n \leq N) = \frac{1}{M} \sum_{m=1}^{M} \mathbb{X}\,[n, m] \tag{3.20}$$

   of each row of $\mathbb{X}$ and derive $\tilde{\mathbb{X}}$.

3. Continue and calculate the covariance matrix

$$\mathbb{C}_{XX} = \frac{1}{M-1} \tilde{\mathbb{X}} \tilde{\mathbb{X}}^T\,. \tag{3.21}$$

4. The eigenvectors of $\mathbb{C}_{XX}$ are the PCs of $\tilde{\mathbb{X}}$, see App. B. They are grouped according to the values of their eigenvalues in decreasing order.

5. Eventually the coordinates in the space of the PCs are obtained by the projection of the original data on the new basis.

With regard to polymer physics (the data are supposed to be measured trajectories of particle coordinates, distances and so on) lower PCs contain most of the diffusive dynamics of the whole polymer while higher PCs represent the local dynamics of the beads.

For the Rouse chain the distribution of coordinates is a multivariate Gaussian. Thus the connectivity matrix given in Eq. (2.17) is proportional to the inverse of the covariance matrix $\mathbb{C}_{XX}$. Since a matrix shares the eigenvectors with its inverse—for the harmonic chain—the PCs coincide with the normal modes.

We denote the unbiased ACF of the $k-$th PC by ϕ_k. For the harmonic chain, which is our reference system, it follows from Eq. (2.59) that the normalized ACF of the $k-$th mode reads

$$\phi_k(t) = \exp\left(-\frac{t}{\tau_k^f}\right), \quad k = 1, \ldots, N\,. \tag{3.22}$$

Hence the mean squared displacement which is proportional to $1 - \phi_k(t)$ scales for times $t \ll \tau_k^f$ as

$$1 - \phi_k(t) \simeq \frac{t}{\tau_k^f} \propto t^1\,. \tag{3.23}$$

3.4.2. Principal components and normal modes

Let us now turn to the behavior of the principal components. We proceed to show that in a homogeneous linear chain with symmetric interaction potentials $U(r_n)$ between the beads, with the overall potential energy given by $\tilde{U} = \sum_n U(r_n)$, the PCs follow the directions of the normal modes of the harmonic chain, independent of the exact form of the potential $U(r_n)$. This is due to the fact that the directions of PCs are essentially thermodynamical quantities.

The proof of this fact involves the following steps. Consider a grafted chain of $N+1$ beads, whose first bead is attached to the origin of coordinates by a weak spring, with the small elastic constant ε (an "asymptotically free" chain). Let $\mathbf{X}$ be the vector of the coordinates, and $\mathbf{r}$ be the vector with components $r_0 = x_0$ and $r_n = x_n - x_{n-1}$ for $n \geq 1$. For a given interaction potential the distribution of $\mathbf{r}$ is given by

$$\Psi(r_0, ..., r_n) = \frac{1}{\Psi_{norm}} \exp\left[-\frac{1}{k_B T}\left(\frac{\varepsilon}{2} r_0^2 + \sum_n U(r_n)\right)\right]. \tag{3.24}$$

This overall canonical distribution factorizes in the product of the distributions of single r_n-components, which means that the corresponding random variables are independent. Due to the symmetry of all interaction potentials, the mean values of r_n are all zero. Hence, the corresponding variables are uncorrelated too:

$$\left\langle r_0^2 \right\rangle = r_0^2 = k_B T/\varepsilon\,, \tag{3.25}$$

$$\left\langle r_n^2 \right\rangle = r^2 \quad \text{for} \quad n = 1, \ldots, N\,, \tag{3.26}$$

and

$$\langle r_n r_m \rangle = 0 \quad \forall n \neq m\,. \tag{3.27}$$

The variables x_n are obtained through r_n via linear transformation, $x_n = \sum_{j=0}^{n} r_j$, so that their correlator is given by

$$\mathbb{C}_{nm} = \langle x_n x_m \rangle = r_0^2 + \min\{n, m\} r^2\,. \tag{3.28}$$

The matrix $\mathbb{C}$ can be diagonalized. Its eigenvectors are the PCs of the grafted chain, whether harmonic or not. The normalized PCs cannot depend on r^2 or r_0^2 independently, but only on their ratio $r^2/r_0^2 = r^2\varepsilon/(k_B T)$. Note that for the free chain, $\varepsilon \to 0$, $r_0 \to \infty$, the PCs of a harmonic and anharmonic chain coincide. The same is true also for asymmetric interaction potentials, where the lengths r_n have to be corrected for thermal expansion.

Turning to a harmonic chain, we can change r_n for x_n in Eq. (3.24), which now reads

$$\Psi(x_0, ..., x_N) = \frac{1}{\Psi'_{norm}} \exp\left[-\frac{\kappa}{2k_B T}\left(\mathbf{X}^T \mathbb{W} \mathbf{X}\right)\right], \tag{3.29}$$

where $\mathbb{W}$ is the tridiagonal force matrix similar to the one defined in Eq. (2.17), whose elements are: $w_{00} = 1 + \varepsilon$, $w_{NN} = 1$, the rest of diagonal elements $w_{nn} = 2$, the elements on the sub- and super-diagonals are equal to -1. Since the corresponding distribution is a multivariate Gaussian, the elements of the correlation matrix $\mathbb{C}$ are proportional to the ones of the inverse of the matrix $\mathbb{W}$. The eigenvectors of the matrix $\mathbb{W}$ are the normal modes of the harmonic chain. Since the matrix $\mathbb{W}$ and its inverse $\mathbb{C}$ share the eigenvectors, those are also the PCs of the harmonic chain. The idea of considering the grafted chain is connected to the wish to have $\mathbb{W}$ invertible. Finally for $\varepsilon \to 0$ $\mathbb{W}$ becomes the connectivity matrix of the free chain with the corresponding eigenvectors calculated in App. A.

Thus assuming whatever interaction potential between neighboring beads, the PCs follow the directions of the normal modes of the harmonic chain. However, as we proceed to show, the dynamical properties of each single mode can be drastically different from those of a harmonic chain.

Projection of the PCs on the normal modes

In order to illustrate that indeed the PCs point into the directions of the normal modes we calculate the projections of the PCs on the harmonic normal modes. It is given by

$$\mathbb{P}_{kk'} = \left| \sum_{n=0}^{N} X_k(n)\, X_{k'}^{harm}(n) \right|. \tag{3.30}$$

We present in Fig. 3.6 the projections of the normalized PCs on the normal modes of a harmonic chain of the same length. The panels (a) and (b) show the projection for the chain with Q- and T-potential, respectively. The remaining panels (c) to (f) show the projection for a chain with DW-interaction and different values of the barrier height

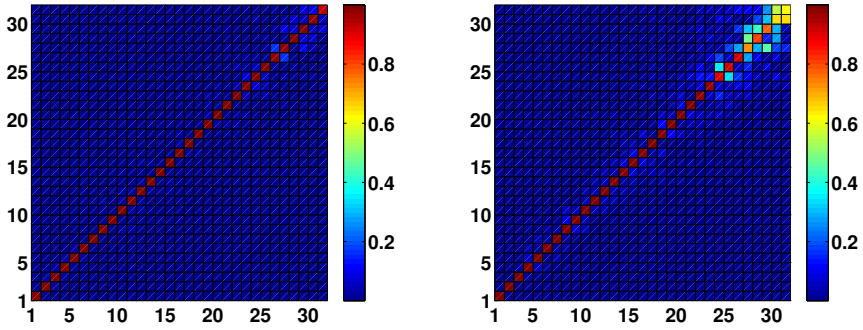

(a)

(b)

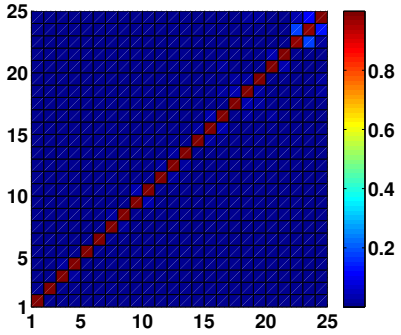

(c)

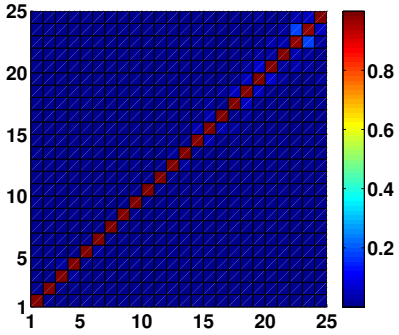

(d)

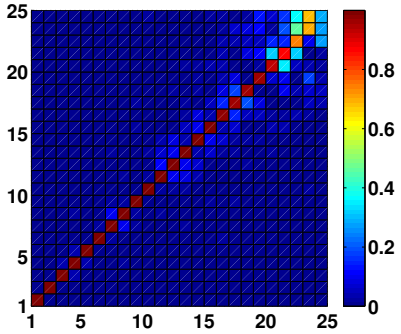

(e)

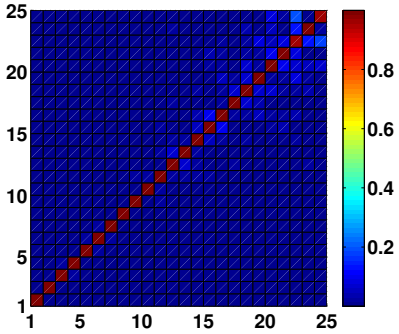

(f)

Figure 3.6.: Projections of the PCs on the harmonic normal modes. Panels (a) and (b): nonlinear single-well potentials. Panel (a): Q-potential, panel (b): T-potential. The parameter values are $D = 5$ and $N = 31$. Panels (c) to (f): the nonlinear DW-potential with different values of the barrier height. From (c) to (f): $\Delta E/k_BT = 100$, $\Delta E/k_BT = 20$, $\Delta E/k_BT = 20/3$ and $\Delta E/k_BT = 2$. The remaining parameter values are $a = 1$, $b = 2$, and $N = 25$.

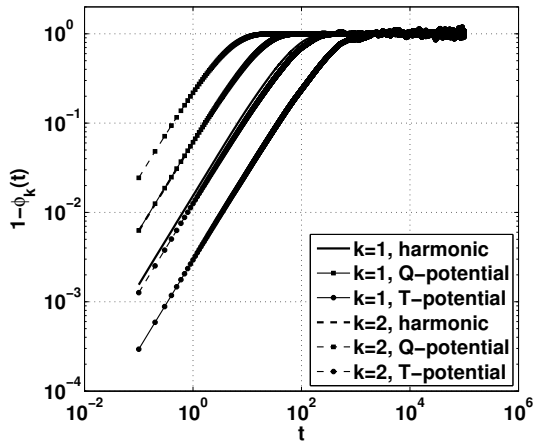

Figure 3.7.: The ACFs of the lowest two PCs ($k = 1$ and $k = 2$) and the different single-well coupling potentials. The parameter values are $D = 5$ and $N = 25$.

as given in the caption. All the projections indicate that the directions of the PCs of the chains with nonlinear interaction and those of the harmonic normal modes coincide. Small deviations appear for higher values of k which tend to disappear with increasing measurement time.

3.4.3. Nonlinear single-well potentials

Having analyzed the directions of the PCs we now turn to their relaxation properties. As in the study of the relaxation behavior of r_{ete} let us first concentrate on nonlinear single-well potentials. In Fig. 3.7 we depict $1 - \phi_k(t)$ for the lowest two PCs ($k = 1$ and $k = 2$) for the Q-potential (squares) and the T-potential (circles), respectively. Superimposed is the scaling of the lowest two normal modes of the corresponding harmonic chain (solid, $k = 1$, and dashed line, $k = 2$). In analogy to the scaling behavior found for $1 - \phi_{ete}(t)$ the introduction of nonlinearity causes a shift in the correlation times but does not change the overall scaling. Qualitatively the shift is the same as for the relaxation of r_{ete}, i.e., to longer times for the T-potential and to shorter times for the Q-potential.

Let us have a closer look at the typical correlation times. For a discrete set of measurements we define a typical correlation time τ_k following (Cohen and Moerner, 2007) as

$$\frac{1}{\tau_k} = \frac{1}{\Delta t} \frac{\phi_k(1) - \phi_k(2)}{\phi_k(1)} , \tag{3.31}$$

with the size of a single lag Δt and the value of the ACF of the k-th PC $\phi_k(i)$ at lag i[3].

From the normal mode analysis of a harmonic chain it is known that in the limit $N \gg 1$ the autocorrelation time of its k-th normal mode scales as

$$\tau_k \propto \frac{N^2}{k^2} . \tag{3.32}$$

[3]Note that this definition implies an exponentially decaying correlation function. A more general definition is given in chapter 4, Eq. (4.69), for the continuous correlation function.

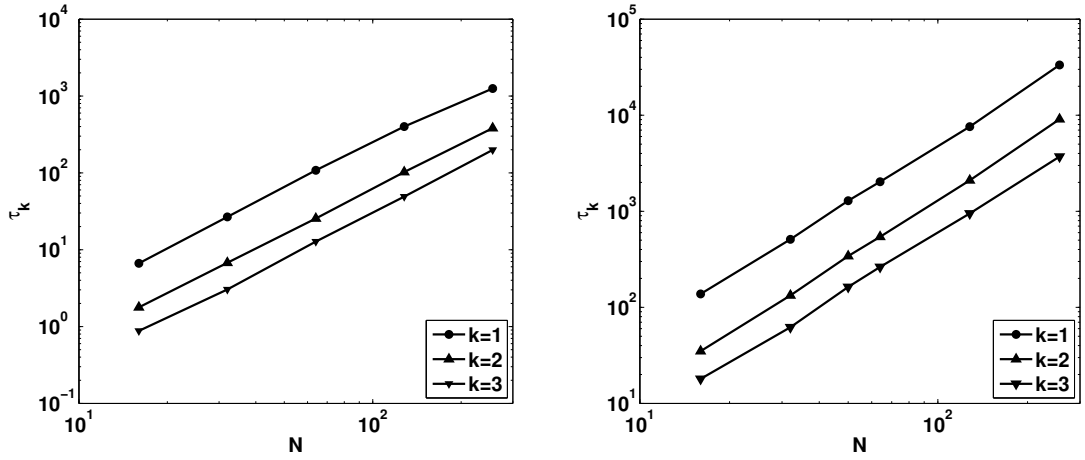

(a) (b)

Figure 3.8.: Correlation times τ_k of the lowest three PCs as a function of the chain length N for a fixed value of the noise strength. Panel (a): Q-potential and panel (b): T-potential. The value of the noise strength is $D = 5$. The scaling obeys $\tau_k \propto N^2$.

Next we show that this scaling with respect to N and k persists also in the nonlinear chains, however τ_k becomes D-dependent. In Fig. 3.8 the correlation time of the lowest three PCs ($k = 1, 2, 3$) as a function of the chain length N is shown. The noise strength D is fixed. It is found that the correlation time scales as $\tau_k \propto N^2$ for the Q-potential (panel (a)) as well as for the T-potential (panel (b)). Thus we obtain the same N dependence of τ_k as in the harmonic chain.

Now we consider the dependence on the mode index k. In panel (a) of Fig. 3.9 the correlation time vs. k is shown for the lowest ten PCs. The noise strength D and the number of bonds N are fixed. The correlation time scales as $\tau_k \propto 1/k^2$ for the Q-potential (lower straight line, upturned triangles) as well as for the T-potential (upper straight line, triangles). Again, the scaling is the same as the one found in the harmonic chain.

Since the time evolution of the autocorrelation function of r_{ete} of a nonlinear chain strongly depends on the noise strength D, the PCs are expected to exhibit a similar dependence. In Fig. 3.9, panel (b), we present the τ_k of the lowest three PCs as a function of the noise strength D for the Q-potential (upturned triangles) and the T-potential (triangles). As a reference, the noise strength independent values of τ_k for each normal mode are superimposed. The slope of the curves representing the nonlinear interaction potentials deviates from this straight line, positive in the case of the T-potential and negative in the case of the Q-potential. The trend of the deviations is nonexponential and it exhibits no power-law behavior. It is worth to underline that the observed behavior stems solely from the nonlinearity of the interaction potentials.

To preliminary summarize, it was found that a nonlinear interaction in a one-dimensional chain system can change the correlation times in this system. In contrast to the harmonic system, the correlation time τ_k becomes dependent on the noise strength (the temperature). Nevertheless, typical scaling properties (with N, κ, and time t) remain the same. Thus the experimentally observed different scaling cannot solely arise from existing nonlinearities.

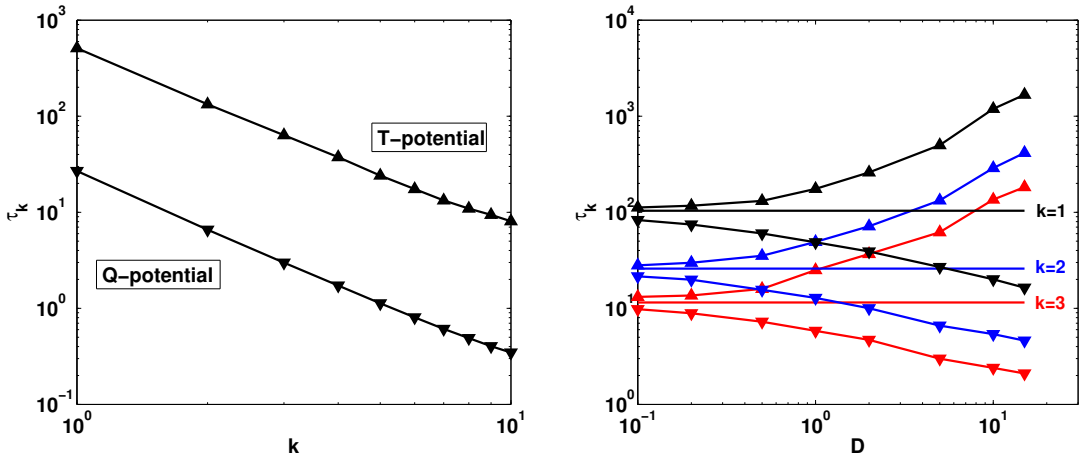

(a) (b)

Figure 3.9.: Panel (a): Correlation times τ_k of the lowest ten PCs in a chain of $N = 31$ bonds. The value of the noise strength is $D = 5$. Triangles: T-potential (upper straight line), upturned triangles: Q-potential (lower straight line). The scaling follows $\tau_k \propto k^{-2}$. Panel (b): Correlation times τ_k of the lowest three PCs ($k = 1, 2, 3$) as a function of the noise strength D. The chain has $N = 31$ bonds. Shown are the curves for the Q-potential (upturned triangles) and the T-potential (triangles). Superimposed are the straight lines of the corresponding normal modes. Equal colors belong to the same value of k.

3.4.4. Double-well potential

Let us now turn to the mode relaxation in the chain with DW interaction. For the DW-potential with intermediate barrier height of $\Delta E/k_BT = 10$, Fig. 3.10 panel (a), the relaxation times of the lowest three modes are almost equal: The corresponding curves merge for $t > 10^2$. The overall shape of the curves is similar to the one for r_{ete} (see Fig. 3.4). For a harmonic chain the scaling is given by t^α with $\alpha = 1$ (corresponding to the solid line in the plot). For small times $1 - \phi_k(t)$ still follows this scaling, but at longer time it crosses over to anomalous, subdiffusive behavior with $\alpha \approx 0.82$ over two orders of magnitude in time. The case of distributed barrier heights (see explanation in Sec. 3.3.2) is shown in panel (b). Here we observe again a subdiffusive scaling of the ACF. Interestingly the shown curves for different values of k do not merge at longer times and their slope is mode dependent with smaller α for higher values of k ($k = 1$: $\alpha \approx 0.79$, $k = 2$: $\alpha \approx 0.72$, $k = 3$: $\alpha \approx 0.68$). For modes $k \geq 4$ the slope changes only slightly (not shown). Thus the relaxation scaling of the PCs shows a pronounced difference compared to the harmonic one. At intermediate times it is subdiffusive. Therefore, a chain build of DW-bonds might be a minimal model explaining the long relaxation times and the subdiffusive scaling found in realistic simulations and experiments.

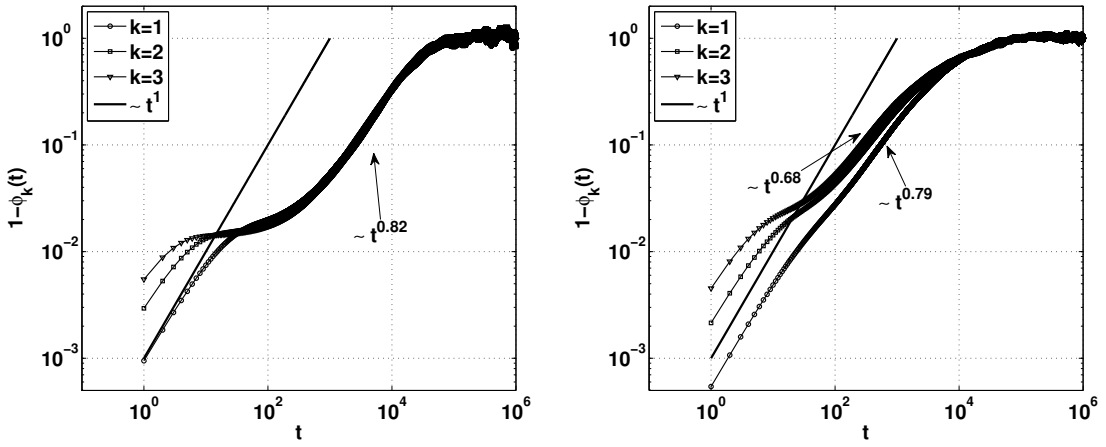

(a) (b)

Figure 3.10.: ACFs of the lowest three PCs ($k = 1, 2, 3$). Panel (a): DW-potential with the parameter values $a = 1$, $b = 2$, and $\Delta E/k_BT = 10$; panel (b): DW-potential with barrier heights distributed as described in the text. The chain length is $N = 25$. The solid lines indicate a slope of unity.

3.5. Internal friction in a three-dimensional chain model

One might argue that the one-dimensional model studied so far is rather artificial and the results may hardly be observed in realistic molecular dynamics simulations. Therefore, we consider briefly a more general polymer chain model and compare the scaling of its PCs with the one found in the much more simple one-dimensional chain model.

In what follows we consider the Brownian dynamics of a three-dimensional polymer chain, as applied e.g. for simulating a polyethylene molecule within the valent-angle model (Ryckaert and Bellemans, 1975; Rigby and Roe, 1987; Binder and Paul, 1997) and show that it follows slow kinetics at intermediate times, provided that the temperature is low enough. On the other hand, at high temperatures the typical Rouse dynamics sets on.

The model equations can be found in (Ryckaert and Bellemans, 1975; Rigby and Roe, 1987; Binder and Paul, 1997). They include valence bond-, valence angle- and torsional angle-interactions. For our purpose we neglect the Lennard-Jones interactions and focus on the influence of the angle interactions which follow a multistable potential energy landscape. The chain consists of N beads, labeled consecutively by an index $n = [0, N-1]$.

The interaction potential of the chain reads

$$U = \sum_{n=1}^{N-1} U_{VB}(r_n) + \sum_{n=1}^{N-2} U_{VA}(\Theta_n) + \sum_{n=2}^{N-2} U_{TA}(\Xi_n)\,, \tag{3.33}$$

with r_n being the bond length between two consecutive beads, the bond angle Θ_n, defined by three successive beads $(n-1, n, n+1)$ and the torsional angle Ξ_n, defined by four successive beads $(n-2, n-1, n, n+1)$, i.e., the angle between the plane spanned by the beads $(n-2, n-1, n)$ and $(n-1, n, n+1)$. A detailed description can be found for example

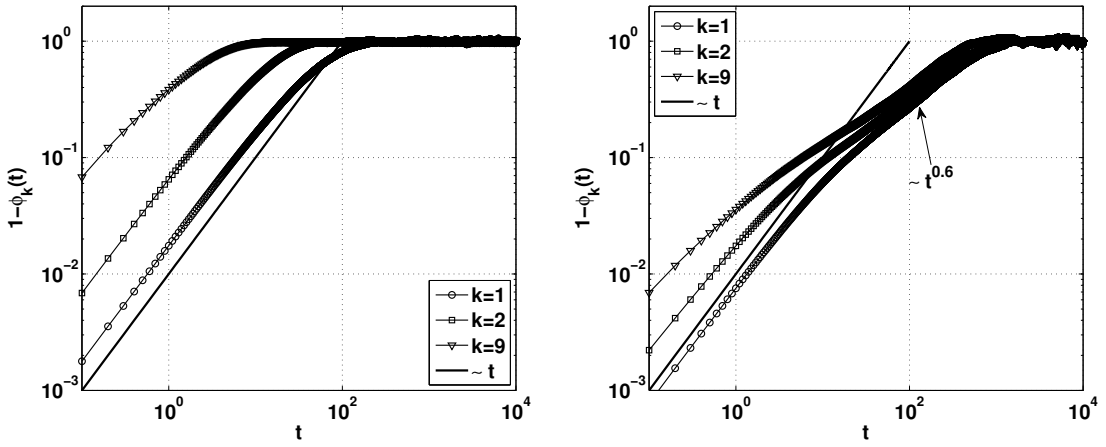

(a) (b)

Figure 3.11.: $1 - \phi_k(t)$ of some of the PCs. Panel (a): High temperature value. Panel (b): Intermediate temperature value for which strong internal friction is observed. The parameter values are given in Rigby and Roe (1987) and in the text. The chain length is $N = 25$.

in (Binder and Paul, 1997). The potentials are

$$U_{VB}(r_n) = \frac{\kappa_b}{2} (r_n - l_0)^2 \ , \tag{3.34}$$

$$U_{VA}(\Theta_n) = \frac{\kappa_\Theta}{2} (\cos(\Theta_n) - \cos(\Theta_0))^2 \ , \tag{3.35}$$

and

$$U_{TA}(\Xi_n) = \kappa_\Xi \sum_{i=0}^{5} a_i \cos^i(\Xi_n) \, . \tag{3.36}$$

All parameter values are the same as in (Rigby and Roe, 1987) except for the bond length $l_0 = 1.$ and the constants $\kappa_b = 3.$, $\kappa_\Theta = 3.$, and $\kappa_\Xi = 0.1$ which only set the timescale of simulation. We perform Brownian dynamics simulations[4] and study the relaxation properties of the PCs and their autocorrelation functions. Therefore, the equations of motion given in Eq. (3.1) are formulated in Cartesian coordinates.

In Fig. 3.11 we show the scaling of $1 - \phi_k(t)$ for some of the PCs. In panel (a) we have chosen a high value of the temperature yielding a trans-gauche barrier height of $\Delta E_{tg}/k_B T = 0.66$, a cis barrier height of $\Delta E_c/k_B T = 2.4$ and $\Delta E_{t\to g}/k_B T = 0.16$[5]. All PCs show a scaling t^α with $\alpha = 1$, which is the same as for the relaxation of single modes in the Rouse chain (Doi, 1996). The scaling for a lower value of the temperature with $\Delta E_{tg}/k_B T = 7.6$, a cis barrier height of $\Delta E_c/k_B T = 27.6$ and $\Delta E_{t\to g}/k_B T = 1.8$ is presented in panel (b). The relaxation behavior strongly differs compared to the previous

[4]The valence- and torsional angles can be expressed in terms of Cartesian coordinates. The Brownian dynamics simulations are then performed in Cartesian space.

[5]cis ($\Xi_n = 0$), trans ($\Xi_n = \pi$), and gauche ($\Xi_n = \pi/3$) denote different configurations of the torsion angle.

case. For small times $1 - \phi_k(t)$ still follows the t^1 scaling (solid line); but at longer times it crosses over to anomalous, subdiffusive behavior. The curve's slope is slightly higher for the first mode. Compared to the high temperature case, the typical relaxation times are shifted to longer times. Thus the existence of barriers in the free energy landscape at intermediate temperatures slows down the dynamics.

The relaxation behavior of the realistic chain presented in Fig. 3.11 is similar to the one found in the much more simple one-dimensional chain with DW-potential interaction, albeit with somewhat different exponents. However, the exponents are expected to depend crucially on the choice of parameter values and the ratio of different timescales in the system. The proposed minimal model is able to mimic qualitatively the relaxation behavior of a much more complex structure and therewith it helps to understand the underlying mechanisms of internal friction and subdiffusive kinetics.

3.6. Summary

We studied the equilibrium relaxation properties of the correlations of the end-to-end vector and the PCs within a simple polymer chain model. It was found that for nonlinear interaction potentials the scaling of the end-to-end ACF is essentially the one of the harmonic chain, though with shifted correlation times. Soft nonlinearities in the binding potential cause an increase of the correlation times while hard nonlinearities shrink the latter. The changes were found to depend on the temperature and to be the more pronounced for the higher temperature values. Since most breakable bonds (for example the Morse potential) exhibit a soft cubic nonlinearity we expect their typical relaxation times to be larger than those of the corresponding harmonic chain. However, while these changes are not too large for the single-well potentials at intermediate temperatures, for the double-well ones (describing internal friction) they can lead to the increase in the relaxation times by orders of magnitude. Turning to the principal components we have shown that for homogeneous chains they follow the normal modes of the harmonic chain, but can exhibit vastly different kinetics, both with respect to the characteristic times and to the overall scaling. For the double-well potentials the last can correspond to subdiffusion. We compared the outcome of our simple model with the one of a more realistic polymer model mimicking the behavior of polyethylene and found qualitatively the same behavior. Therefore, a one-dimensional chain of beads connected with springs described by a double-well potential might be a possible minimal model describing the similar observations of anomalous kinetics in realistic molecular dynamics simulations and experiments.

In the next chapter we show the important impact of the correlation times in the chain on the thermal activation of individual bonds, especially when the correlation times have the same order of magnitude as the typical activation times. Moreover, in chapter 5 the force mediated activation in nonlinear potentials will be analyzed and our results concerning the relaxation behavior of the chain dynamics will help us to understand the observed behavior.

4. Thermal fragmentation

4.1. Introduction

In the previous chapter we studied the equilibrium relaxation properties in a one-dimensional as well as in a more complex three-dimensional polymer chain system. We observed that the relaxation times of internal modes can be drastically increased due to the existence of barriers in the free energy interaction potential landscape. Furthermore, especially soft nonlinear interactions may cause an increase of the typical correlation timescale. In general the dynamics on timescales which are shorter or comparable with these correlation times exhibits a non-Markovian character. Since especially binding potentials often show a soft nonlinearity, the behavior of long chains of breakable bonds is probably non-Markovian on the timescale of interest, i.e., the timescale of activation. The question arises, how the thermal stability of a polymer chain is affected by its non-Markovian fluctuations? The question is the more important since biopolymers and supramolecular polymers possibly form functional materials and therefore their stability properties need to be understand (Cordier et al., 2008; Mynar and Aida, 2008). Thus, the problem of thermally activated chain fragmentation (thermolysis) is of fundamental interest in understanding the degradation and stabilization properties of such polymers (Allen and Edge, 1966). In the present chapter we study the simplest realization of a breakable polymer, being a chain of harmonic springs, each with a sharp cut-off at some pre-defined value of the bond elongation. The interaction potential is thus linear until rupture happens. We assume that no external force is applied to the system. However, the application of a static force to the grafted linear chain can be described by the same harmonic chain with lower activation barrier. In chains consisting of nonlinear bonds also the effected curvature in the vicinity of the metastable state of each bond changes upon application of the force. We have shown in the previous chapter that the correlation functions of the system still follow those of the harmonic chain and therefore the qualitative behavior of the chain fragmentation is expected to be the same. The situation when the external force increases linearly with time is more involved and will be treated in chapter 5.

Whenever the corresponding *fragmentation kernel* is known as the function of the breakdown position, time, chain's length etc., the overall fragmentation process is well-described. For illustration we show in Fig. 4.1 a schematic representation of the fragmentation process of an initially monodisperse ensemble of polymers. As time goes on the polymers break into smaller fragments conserving thereby the total mass. The fragmentation kernel is the probability per unit time for a bond at a given position to break. The distribution of fragments at whatever time can be obtained by the solution of the corresponding kinetic equation (Simha, 1941; Ziff, 1986; McGrady and Ziff, 1987; Cheng and Redner, 1988). Here the fragmentation kernel is the input into the universal theory, and many mathematical expressions for such kernels were formulated on the basis of parameterizing experimental observations or simply as analytical examples. However, the question of how

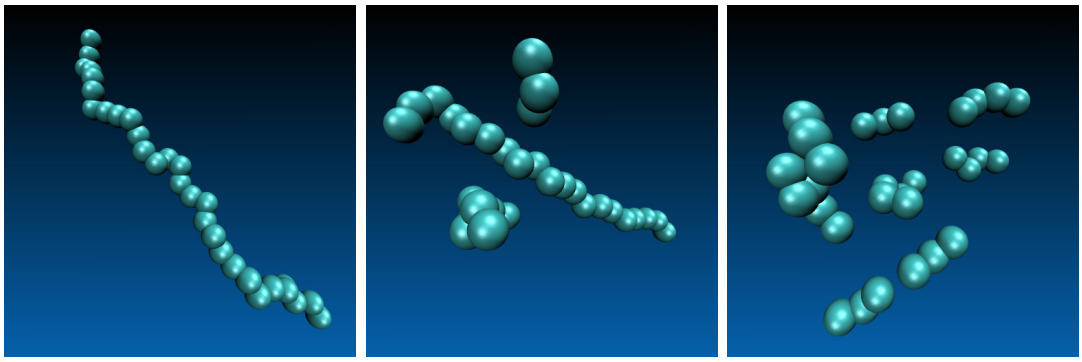

(a) (b) (c)

Figure 4.1.: Schematic representation of the fragmentation process. Panel (a): Initially at time $t_0 = 0$ the ensemble of chains is monodisperse, i.e., solely N-mers are present. As time goes on, smaller fragments with $N' < N$ are formed, panel (b): $t_1 > t_0$. Panel (c): $t_2 > t_1 > t_0$. The evolution of the fragment size distribution is governed by the fragmentation kernel.

does the corresponding kernel follow from the single polymer chain dynamics was hardly considered. One example is contained in (Hathorn et al., 2001) which however deals with a model whose relation to the standard polymer dynamics ones is not quite evident.

In what follows we discuss the thermally activated breakdown within a model which assumes that the dynamics of the chain is—as long as it does not break—a Rouse one, i.e., we disregard excluded volume effects, which is a reasonable assumption in the case of chains in melts and concentrated solutions, as well as hydrodynamical interactions. The breakdown of a bond is represented as a breakable harmonic spring, which is a harmonic spring with a sharp cut-off at some predefined value of its elongation. Activation takes place as soon as the elongation of the bond achieves the preassigned value, which is assumed to be equal for all bonds in the chain. The possibility of reestablishing the bond after breakdown (defect healing) is neglected. We consider the relevant situations of free and grafted chains.

Although the formulation of the overall problem is extremely simple, its solution is not, since the projection of the overall chain motion onto the reaction coordinate makes the corresponding diffusion strongly non-Markovian (Szabo et al., 1980). This non-Markovian nature of the problem involving multiple characteristic timescales reflects the fact that the reaction essentially takes place in a many-particle system.

Let us give an outline of the chapter: In Sec. 4.2 we present different approaches to treat Markovian escape processes and to calculate mean first passage times and activation rates for a single bond. In Sec. 4.3 we introduce the one-dimensional chain model and discuss the overall fragmentation behavior. The simplicity of our model allows for an analytical calculation of the mean first passage times of the bonds within the Wilemski-Fixman approximation. This is done in Sec. 4.4. The analytical results are compared with the outcome of numerical simulations for one-dimensional free and grafted chains in Sec. 4.5. Going beyond the Wilemski-Fixman approximation we present in Sec. 4.6 analytical results obtained using a generalized version of the renewal equation for barrier crossings. Our

model is then generalized to the case of a three-dimensional chain. Eventually in Sec. 4.8 we use the obtained fragmentation kernel to predict the evolution of the mass distribution of an initially monodisperse polymer solution. At the end we summarize our results.

4.2. Markovian escape process of a single reaction coordinate

Before studying the activation of individual links in a chain we give a brief overview over some approaches to calculate activation rates and first passage times for Markovian escape processes of a single reaction coordinate. The first passage time τ_{fp} is defined as the time t, when a stochastic process $\mathfrak{X}(t)$ leaves a domain of its phase space Ω for the first time, assuming that the process started at $t = t_0 = 0$ from given initial conditions within Ω. A large variety of processes in a wide spread field of science areas demand the knowledge of the average time the process once generated needs to reach a certain target. Examples are chemical reactions and nucleation (Hänggi et al., 1990) or the diffusion controlled reactions of reactive groups attached to polymers (de Gennes, 1982; Srinivas et al., 2002) to name some of which have a direct relation to the present work. There is a huge literature on first passage time problems and a review can be found in (Hänggi et al., 1990). Furthermore, the reader is advised to the very intuitive summary in the thesis of Tatiana Engel (Engel, 2006).

In this section we focus solely on the escape process in the overdamped (Smoluchowski) limit. For the Markovian escape process the mean first passage time does not depend on initial conditions almost everywhere in Ω. Prior to escape an equilibrium distribution is formed and the first passage times are exponentially distributed at times exceeding the local relaxation time τ_{relax}. The probability to escape in a unit timestep (the escape rate) is then independent of the age of the decaying state. Hence the first passage time problem for Markovian models reduces to the calculation of a constant escape rate. In polymers with a huge number of degrees of freedom N the longest relaxation time is of the order of the Rouse time $\tau_1 \propto N^2$ and can become very large. Therefore, due to the polymer connectivity the diffusion of a reaction coordinate in the chain reveals a strong non-Markovian character. The dynamics is non-Markovian on timescales ranging over many orders of magnitude and one has to check carefully the validity of a Markovian description of the escape process.

4.2.1. Fokker-Planck equation with an absorbing boundary

As introduced above the first passage time τ_{fp} is defined as the time t, when a stochastic process $\mathfrak{X}(t)$ leaves a domain of its phase space Ω for the first time. The process itself is stochastic and therefore τ_{fp} is a random variable. We denote the probability density distribution of first passage times $\mathcal{F}(t)$. The survival probability, i.e., the probability of remaining inside Ω until t follows

$$\Phi(t) = 1 - \int_0^t \mathcal{F}(t')dt' \tag{4.1}$$

and

$$\mathcal{F}(t) = -\frac{d\Phi(t)}{dt}\,. \tag{4.2}$$

The mean first passage time is thus given by

$$\tau_{mfp} = \int_0^\infty t\mathcal{F}(t)dt = \int_0^\infty \Phi(t)dt\,. \tag{4.3}$$

The change in the survival probability per unit timestep is governed by an escape rate ν, which is in general time-dependent. The corresponding kinetic equation is

$$\frac{d\Phi(t)}{dt} = -\nu(t)\Phi(t)\,, \tag{4.4}$$

with the solution

$$\Phi(t) = \exp\left(-\int_0^t \nu(t')dt'\right)\,, \tag{4.5}$$

and with Eq. (4.2) we have

$$\mathcal{F}(t) = \nu(t)\exp\left(-\int_0^t \nu(t')dt'\right)\,. \tag{4.6}$$

For a process whose probability to escape does not depend on the time spent in Ω, the escape rate is independent of the time t and the integrals in the two previous equations are solved immediately. Furthermore, it follows the important result that the mean first passage time is equal to the inverse constant escape rate

$$\tau_{mfp} = \frac{1}{\nu}\,. \tag{4.7}$$

The transition probability $\mathcal{G}(x,t|x',0)$ is the conditional probability of visiting a point $x \in \Omega$ at time t provided that the process was at $t = 0$ in $x' \in \Omega$ and did not leave Ω in the meantime. The survival probability is then simply

$$\Phi(x',t) = \int_\Omega \mathcal{G}\left(x,t|x',0\right)dx\,, \tag{4.8}$$

and thus the mean first passage time, which in general will depend on the initial position x', is given by

$$\tau_{mfp}(x') = \int_0^\infty dt \int_\Omega \mathcal{G}\left(x,t|x',0\right)dx\,. \tag{4.9}$$

$\mathcal{G}$ satisfies the Fokker-Planck equation with the appropriate boundary conditions[1] (Risken and Frank, 1996; Hänggi et al., 1990)

$$\begin{aligned} \partial_t\mathcal{G}\left(x,t|x',0\right) &= \mathcal{L}_x\mathcal{G}\left(x,t|x',0\right)\,, \quad x \in \Omega \\ \mathcal{G}\left(x,t|x',0\right) &= 0\,, \quad x \in \partial\Omega\,, \end{aligned} \tag{4.10}$$

with the Fokker-Planck operator $\mathcal{L}_x$ (Risken and Frank, 1996). The conditional probability also obeys the backward equation, thus

$$\begin{aligned} \partial_t\mathcal{G}\left(x,t|x',0\right) &= \mathcal{L}^+_{x'}\mathcal{G}\left(x,t|x',0\right)\,, \quad x' \in \Omega \\ \mathcal{G}\left(x,t|x',0\right) &= 0\,, \quad x' \in \partial\Omega\,, \end{aligned} \tag{4.11}$$

[1] for a Fokker-Planck process it is sufficient to demand that the boundary $\partial\Omega$ of Ω is absorbing

and with Eq. (4.9) one obtains

$$\begin{aligned} \mathcal{L}^{+}_{x'}\tau_{mfp}(x') &= -1\,, \quad x' \in \Omega \\ \tau_{mfp}(x') &= 0\,, \quad x' \in \partial\Omega\,. \end{aligned} \tag{4.12}$$

Let us specify the adjoint Fokker-Planck operator $\mathcal{L}^{+}_{x'}$ for the one-dimensional overdamped motion of a Brownian particle in a potential $U(x)$. The corresponding Langevin equation reads

$$\dot{x} = -\frac{1}{\gamma}U'(x) + \sqrt{2\frac{k_BT}{\gamma}}\xi(t)\,. \tag{4.13}$$

The adjoint Fokker-Planck operator thus becomes

$$\mathcal{L}^{+}_{x'} = -\frac{1}{\gamma}U'(x')\partial_{x'} + \frac{k_BT}{\gamma}\partial^2_{x'}\,. \tag{4.14}$$

Assuming that the domain Ω is given by the semiinfinite interval $(-\infty, x_a)$, the solution of Eq. (4.12) together with the operator given in Eq. (4.14) is (Pontryagin et al., 1933)

$$\tau_{mfp}(x') = \frac{\gamma}{k_BT}\int_{x'}^{x_a} dy\, \mathrm{e}^{\frac{U(y)}{k_BT}} \int_{-\infty}^{y} \mathrm{e}^{-\frac{U(z)}{k_BT}}\, dz\,. \tag{4.15}$$

Let us consider two situations which are of relevance in this thesis. First, the escape over a barrier situated at x_+ with $-\infty < x_+ < x_a$. The metastable potential minimum is supposed to be situated at $-\infty < x_- < x_+$. Using the approximation of steepest descent in the limit of a large barrier, i.e., $U(x_+) - U(x_-) = \Delta E \gg k_BT$, the mean first passage time can be calculated in the following way: The main contribution to the outer integral originates from two regions, $y \simeq x_+$ and $y < -x_+$. Since the inner integral vanishes for $y < -x_a$, the only remaining contribution to the outer integral comes from the vicinity of the potential maximum situated at x_+. The contribution to the inner integral originates mainly from the vicinity of the metastable potential well located at x_-. Thus for the inner integral the potential can be written as

$$U(z) \simeq U(x_-) + \frac{1}{2}U''(x_-)(z - x_-)^2\,. \tag{4.16}$$

The same can be done for the outer integral where we approximate the potential in the vicinity of the barrier top x_+

$$U(y) \simeq U(x_+) - \frac{1}{2}\left|U''(x_+)\right|(y - x_+)^2\,. \tag{4.17}$$

Eventually the mean first passage time is given by

$$\tau_{mfp} = \frac{2\pi\gamma}{\sqrt{U''(x_-)|U''(x_+)|}}\,\mathrm{e}^{\frac{U(x_+)-U(x_-)}{k_BT}}\,, \tag{4.18}$$

and it is independent of the initial position x' of the trajectory.

Following the same reasoning we can deduce the mean first passage time for the second relevant situation, the escape to an absorbing boundary in the harmonic cusp-shaped

potential. The potential is

$$U_H(x) = \begin{cases} \frac{\kappa}{2}x^2 & , x \leq x_+ \\ -\infty & , x > x_+ \end{cases} . \tag{4.19}$$

In contrast to the previous case the barrier coincides with the absorbing boundary and the potential is approximated linearly close to it, thus

$$U_H(y) \simeq U_H(x_+) - \kappa x_+(x_+ - x) . \tag{4.20}$$

Evaluating the integrals in Eq. (4.15) in the limit of a high barrier finally gives

$$\tau_{mfp} = \frac{\gamma}{\kappa}\sqrt{\frac{\pi k_B T}{U_H(x_+)}}\, \mathrm{e}^{\frac{U_H(x_+)}{k_B T}} . \tag{4.21}$$

For smaller values of the barrier height (or in turn high temperatures) the mean first passage time becomes a function of the initial position x'. The cusp potential is somewhat special since one can calculate the mean first passage time for any given initial condition. The inner integral in Eq. (4.15) becomes

$$\int_{-\infty}^{y} dz\, \mathrm{e}^{\frac{U(z)}{k_B T}} = \sqrt{\frac{\pi k_B T}{2\kappa}} \left(1 + \mathrm{erf}\left(\sqrt{\frac{\kappa y^2}{2k_B T}}\right)\right) , \tag{4.22}$$

and the mean first passage time reads

$$\tau_{mfp} = \gamma\frac{\sqrt{\pi}}{\kappa}\int_{z(x')}^{z(x_a)} dz\; \mathrm{e}^{z^2}\left(1 + \mathrm{erf}\,(z)\right) , \tag{4.23}$$

with $z(y) = \sqrt{\kappa y^2/(2k_B T)}$. The solution of Eq. (4.23) is given in terms of the generalized hypergeometric function. For a comprehensive discussion see (Engel, 2006).

4.2.2. Kramers escape rate

If the condition of timescale separation ($\tau_1 \ll \tau_{mfp}$) is fulfilled, i.e., the process can be described as a Markovian escape process, the mean first passage time is equal to the inverse of a time-independent constant escape rate. The theory of calculating rates goes back to Svante Arrhenius who discussed various reaction-rate data and showed that the rate governing thermal activation follows the Van't Hoff-Arrhenius law (Hänggi et al., 1990).

Kramers idea was to suppose that the dissociation of a chemical molecule can be described as the Brownian motion of a reaction coordinate (Kramers, 1940). The probability flux J through $\partial\Omega$ is given as the product of pop, the population inside Ω, and the probability of leaving Ω in a unit timestep which is the escape rate ν. Therefore, the rate can be calculated as the ratio of quasistationary flux through the potential barrier and the population in the domain Ω

$$\nu = \frac{J}{\mathrm{pop}} , \tag{4.24}$$

and the approach is thus referred to as *flux-over-population method*. An important assumption is a stationary probability flux. A particle once reaching the boundary $\partial\Omega$ is reinjected into Ω guaranteeing a stationary probability current J.

The overdamped dynamics described by the Langevin equation given in Eq. (4.13) obeys the Smoluchowski equation with the probability density of the Brownian particle $\psi(x,t)$

$$\partial_t \psi(x,t) = \mathcal{L}_x \psi(x,t) = \partial_x \left(\frac{U'(x)}{\gamma} + D\partial_x \right) \psi(x,t) = -\partial_x J(x,t)\,. \tag{4.25}$$

Under the assumption of stationarity the probability current is

$$J(x) = -\frac{k_B T}{\gamma}\, \mathrm{e}^{-\frac{U(x)}{k_B T}}\, \frac{\partial}{\partial x} \left(\psi(x,t)\, \mathrm{e}^{\frac{U(x)}{k_B T}} \right) . \tag{4.26}$$

Since the probability vanishes at the absorbing boundary $\partial\Omega$ (located at x_a in the one-dimensional system), i.e., $\psi(x_a,t) = 0$, the stationary probability distribution is given by

$$\psi(x) = \frac{J\gamma}{k_B T}\, \mathrm{e}^{-\frac{U(x)}{k_B T}} \int_x^{x_a} \mathrm{e}^{\frac{U(y)}{k_B T}}\, dy\,. \tag{4.27}$$

Further integration over the domain Ω yields the population $\mathrm{pop} = \int_{-\infty}^{x_a} \psi(x)dx$. Following the same reasoning of large energy barriers (or in turn low temperatures) as it was done above, the rates in the cases of the escape over a smooth and a cusp-shaped barrier are obtained and coincide with the inverse mean first passage times, respectively.

4.2.3. The renewal approach

The renewal approach reduces the solution of a problem with absorbing boundary condition to the one of the free problem, using the assumption that the trajectory is continuous and the physical process has a Markovian description.

The renewal approach can be understood as follows (Ebeling and Sokolov, 2005): A particle is at time $t = 0$ at $x = 0$ (initial condition) and evolves until it reaches a point x_a at time t_a. A boundary is situated at $0 < x_+ < x_a$. Since the trajectory is continuous the particle has crossed the boundary at least one time. The probability density of times when the particle crossed the boundary for the first time is denoted by $\mathcal{F}(x_+,t)$. Since the process is a Markovian one, the probability density of reaching x_a at t_a provided it crossed the barrier at some time t is independent of its initial condition and is given by the product $\mathcal{G}(x_a,t_a|x_+,t)\mathcal{F}(x_+,t)$. Demanding stationarity of the process in the absence of the boundary the conditional probability $\mathcal{G}$ is a propagator. Taking furthermore the limit $x_a \to x_+$ and integrating over all possible times $t \le t_a$ we obtain a convolution equation

$$\mathcal{G}(x_+,0;t_a) = \int_0^{t_a} \mathcal{G}(x_+,x_+;t_a - t)\mathcal{F}(x_+,t)dt\,, \tag{4.28}$$

which can be solved in Laplace space. We get

$$\tilde{\mathcal{F}}(x_+,s) = \frac{\tilde{\mathcal{G}}(x_+,0;s)}{\tilde{\mathcal{G}}(x_+,x_+;s)}\,, \tag{4.29}$$

from which the mean first passage time can be derived since

$$\tau_{mfp} = \int_0^\infty dt\, t\mathcal{F}(x_+, t) = -\frac{d}{ds}\tilde{\mathcal{F}}(x_+, s)|_{s=0}\,. \tag{4.30}$$

For stationary non-Markovian processes the renewal approximation might still hold and is equivalent to the Wilemski-Fixman approximation (Sokolov, 2003; Ebeling and Sokolov, 2005). The latter approximation is used in the proceeding sections. Sokolov (Sokolov, 2003) has introduced a generalized renewal equation, which we are going to present later in this chapter. It takes into account non-Markovian behavior.

4.3. Fragmentation in a simple chain model

Having presented different approaches which are appropriate to describe Markovian escape processes of a single reaction coordinate we now turn to a chain of breakable bonds with a priori non-Markovian dynamics.

The thermally activated bond breakdown is essentially an example of an intrachain reaction. However, contrary to e.g. polymer cyclization which was considered in quite a detail (Doi, 1975; Likthman and Marques, 2006; Das and Sabhapandit, 2008; Kolb et al., 1997; Moreira and Marques, 2004; Pastor et al., 1996; Sokolov, 2003) and is still under consideration, this one was hardly tackled. The assumption that the bond breaks when achieving a given elongation simplifies the description and corresponds to assume that the reaction is a purely diffusion-controlled reaction on a contact. Such a problem can be casted into the mathematical form of a first passage problem over a barrier to an absorbing boundary.

In recent years theoretical methods have emerged to treat the diffusion-controlled reactions among sites attached to polymers. Pioneering works go back to Wilemski and Fixman (Wilemski and Fixman, 1974a,b) and conceptual advances were made by Doi (Doi, 1975), de Gennes (de Gennes, 1982), and others (Szabo et al., 1980). But for all that, except for some special cases (Likthman and Marques, 2006), the analytical theories of reaction diffusion in polymer physics fail to give an exact description of the reaction rates and rely on additional assumptions (Pastor et al., 1996). However, as we proceed to show, the outcome of theoretical considerations within the framework of Wilemski and Fixman agrees qualitatively very well with the results obtained in Brownian dynamics simulations. Distinct from numerous studies on chain end reactions (Doi, 1975; Likthman and Marques, 2006; Das and Sabhapandit, 2008; Kolb et al., 1997; Moreira and Marques, 2004; Pastor et al., 1996; Sokolov, 2003) or the studies on interior loop forming reactions (Sung et al., 2003), we focus on the related but somewhat different problem of thermal activation of bonds, i.e., the first passage problem of nearest neighbor monomer distances.

As we proceed to show the dissociation dynamics of a bond strongly depends on its location within the chain and the size of the system. Although the equilibrium distributions and activation barriers are the same for all the bonds, their activation times are not. At the free ends of the chain the first passage times are substantially lower compared to bonds in the middle of the chain (for a free chain) or at its grafted end (for a grafted one). Thus, the thermally activated fragmentation is expected to happen with higher probability at the chain ends. A similar behavior was found experimentally (Madras et al., 1996a,b), though

the underlying mechanism of chain-end scission differs. Moreover, our findings differ from observations in experiments on polymer solutions in elongational flows, where fragmentation happens mostly at the center of the chain where the tensile force has a maximum (de Gennes, 1974; Odell et al., 1988). Furthermore, our prediction of location-dependent breakdown probability for the activation of a free chain is opposite to what was predicted by Lee (Lee, 2009) for the similar model. However, the analysis developed by the author applies solely in the Markovian limit, but it is the many-body dynamics causing the interesting behavior. In the same realm it was shown that the forced rupture of adhesive contacts is strongly influenced by chain dynamics for undercritical forcing (Barsegov et al., 2008).

We consider a one-dimensional chain of $N+1$ monomers (Fugmann and Sokolov, 2010) with coordinates $\mathbf{X} = (x_0, ..., x_N)$. The interaction potential is given by

$$U_H(x_0, ..., x_N) = \frac{\kappa}{2} \sum_{n,m} \mathbb{W}_{n,m} x_n x_m \,, \tag{4.31}$$

with the connectivity matrix $\mathbb{W}$. The overdamped dynamics of the beads follow the Langevin equations

$$\gamma \dot{x}_n = -\frac{\partial U_H}{\partial x_n} + \sqrt{2\gamma k_B T}\xi_n \,, \tag{4.32}$$

with ξ_n being independent δ-correlated Gaussian white noise, damping coefficient γ, and thermal energy $k_B T$. We consider the cases of a free chain as well as of a grafted chain with $x_0(t) \equiv 0$. The connectivity matrix was first given in chapter 2, Eq. (2.17), and reads

$$\mathbb{W} = \begin{pmatrix} (2-\epsilon_1) & -1 & & & 0 \\ -1 & 2 & \ddots & & \\ & \ddots & \ddots & \ddots & \\ & & \ddots & 2 & -1 \\ 0 & & & -1 & 1 \end{pmatrix} . \tag{4.33}$$

with $\epsilon_1 = 1$ for the free chain and $\epsilon_1 = 0$ for the grafted one. We pass to a dimensionless time, $\tilde{t} = t\,\kappa/\gamma$, and neglect in the following the tilde in our notation. As long as the chain is intact, it is described by the Rouse model introduced in Sec. 2.2.3.

The system of coupled monomers is sketched in Fig. 4.2 for a free chain. Superimposed is the equilibrium distribution of the r_n,

$$\psi_{eq}(r_n) = \frac{1}{\sqrt{2\pi\phi_0}} \exp\left[-\frac{r_n^2}{2\phi_0}\right] \quad \text{with} \quad \phi_0 = \langle r_n^2 \rangle = \frac{k_B T}{\kappa} \,, \tag{4.34}$$

which is the same for all n. ϕ_0 is the mean squared bond length in the one-dimensional chain (in arbitrary units). Later we will generalize our study to the in real experiments relevant three-dimensional case.

The problem of thermally activated breakdown can be casted into a first passage problem of a reaction coordinate $r_n = x_n - x_{n-1}$ to a barrier of height $\Delta E = U_H(r_+) - U_H(0)$ situated at r_+. In our harmonic model the reaction is assumed to be irreversible and to take place once the reaction coordinate reaches r_+ in the harmonic potential well. Thus

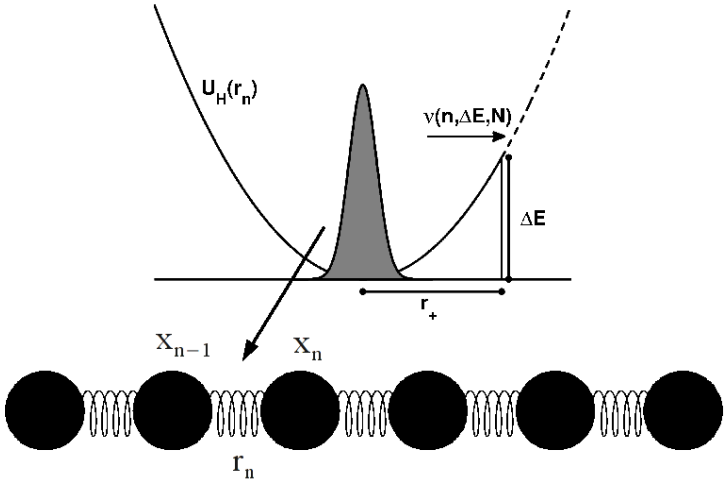

Figure 4.2.: One-dimensional chain of $N+1$ monomers connected by harmonic springs. Superimposed is the interaction potential with a barrier of height ΔE at $r_n = x_n - x_{n-1} = r_+$. The activation rate is assumed to depend on the barrier height, the position of the bond in the chain, and the system size.

the absorbing boundary at r_+ introduces a sharp cut-off of the harmonic potential. The advantage of this simple model is that as long as the chain is intact, it is described by the standard Rouse model of polymer dynamics, and therefore it represents sufficiently well what happens in melts and concentrated solutions.

In order to study the thermolysis of the chain, all N bonds are assumed to have a cut-off at r_+ and the chain is broken as soon as the first r_n reaches the barrier. For the systematic study of the mean first passage times (the inverse activation rates) $\tau_{mfp}(n)$ of individual bonds only one of them is breakable (the one under study, with a cut-off at r_+), the remaining $N-1$ bonds are described by perfect harmonic springs[1].

First, we consider numerically the thermolysis of the whole chain. Let us assume that the activation barrier is sufficiently large and the survival probability of the bonds only slightly deviates from an exponential (what has been shown by Sokolov (Sokolov, 2003)); the latter is given by

$$\Phi_n(t) = \exp\left[-\nu(n)t\right] , \tag{4.35}$$

with the breakdown rate $\nu(n)$ equal to the activation rate of the bond n over the barrier, which on its turn is assumed to be proportional to the inverse mean first passage time to r_+, i.e., $\nu(n) \simeq 1/\tau_{mfp}(n)$. The survival probability of the whole chain (under the

[1]The set of coupled equations (4.32) was integrated by use of a Heun integration scheme (Mannella, 2000). The timestep was chosen as follows: For bond elongations away from r_+ it was set to $\Delta t = 5\times10^{-4}$ and reduced to $\Delta t = 10^{-6}$ for $r_+ - r_n < 0.1$. A further decrease of the timestep did not cause a noticeable change of the numerical results. Furthermore, for $N=1$, the obtained first passage times (both for the free and the grafted chain) agreed with the available exact analytical results. The location of the absorbing boundary was given by $r_+ = \sqrt{2\phi_0 \Delta E/k_B T}$ and we fixed $\phi_0 = 0.02$ without loss of generality. Averages were performed over an ensemble of at least 10000 trajectories. Initial configurations were generated using the equilibrium distribution of r_n.

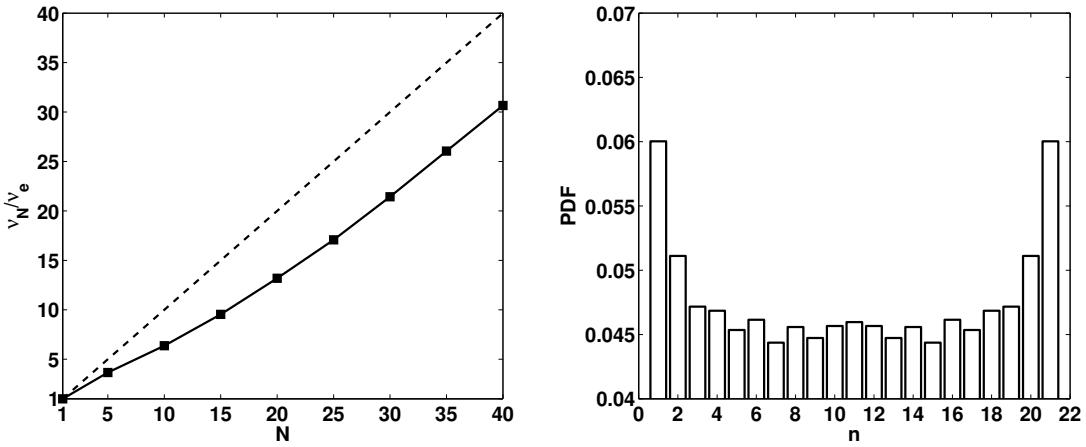

(a) (b)

Figure 4.3.: Panel (a): The numerically obtained fragmentation rate of the chain as a function of its length (squares). Shown is ν_N/ν_e. The dashed line corresponds to a chain of bonds with equal activation rate and a scaling $\nu_N/\nu_e = N$. Panel (b): Probability distribution of the broken bond position for a free chain with $N = 22$ bonds. The barrier height is $\Delta E/k_BT = 5$.

assumption of uncooperative activation of the bonds) is thus

$$\Phi_N(t) = \prod_{n=1}^{N} \Phi_n(t) = \exp\left[-\nu_N t\right] , \tag{4.36}$$

with the total fragmentation rate of the chain

$$\nu_N = \sum_{n=1}^{N} \nu(n) . \tag{4.37}$$

For a set of N bonds with equal activation rates $\nu(n) = \nu_e$ we have $\nu_N/\nu_e = N$. Due to the coupled dynamics this scaling with N is shown not to hold true. In Fig. 4.3 we depict the numerically obtained activation rates for free chains of different length. The scaling differs drastically from the linear one for small chains and approaches asymptotically a slope of almost one in the limit of long chains. The rate is always below its value for the case of identically activated bonds (dashed line). We conclude, that in longer chains especially the inner bonds have lower activation rates, or—in turn—larger mean first passage times (or mean lifetimes). Hence a chain is expected to be activated with higher probability close to its ends. This is shown in panel (b) of Fig. 4.3 where we present the probability density distribution of activation as a function of the location of the bond in the free chain. Note that our findings differ from observations in experiments on polymer solutions in elongational flows, see e.g. Fig. 7 in (Cascales and de la Torre, 1992), where the tensile force exhibits a maximum at the chain's center and hence fragmentation happens mostly there.

4.4. Thermolysis as diffusion-controlled reaction

In order to calculate the mean first passage times we recall an approach put forward by de Gennes (de Gennes, 1982), based on the pioneering work of Wilemski and Fixman (Wilemski and Fixman, 1974a,b). The probability distribution function of the monomer coordinates $\mathbf{X}$ is $\psi(\mathbf{X}, t)$. Its dynamics follows the generalized reaction-diffusion equation

$$\frac{\partial \psi}{\partial t} = \mathcal{L}\psi - \mathcal{Q}\psi \,, \tag{4.38}$$

with $\mathcal{L}$ being the diffusion operator in the absence of reaction, i.e., the Fokker-Planck-operator (Risken and Frank, 1996)

$$\mathcal{L}\psi = \phi_0 \Delta\psi + \nabla\left(\psi \mathbb{W}\mathbf{X}\right) \,. \tag{4.39}$$

$\mathcal{Q}$ is the sink operator describing the reaction. Choosing the δ-function sink (the Smoluchowski sink)

$$\mathcal{Q}(r_n) = K\delta(r_n - r_+) \tag{4.40}$$

we have in the limit of infinite sink strength, i.e., $K \to \infty$, an absorbing boundary at r_+. Note, that especially when considering the polymer cyclization reaction other sink terms can be applied, most prominent being the Heaviside and the Gaussian sink.

The aim is now to derive an expression for the mean first passage time to a barrier corresponding to the energy growth towards r_+ into an infinitely deep and steep "adhesion well". Eq. (4.39) can be formally solved using the Green's function method. Introducing the probability density of the r_n ($\psi(r_n, t) = \int d\mathbf{X}\psi(\mathbf{X}, t)\delta(r_n - (x_n - x_{n-1}))$) and assuming that the presence of reaction does not affect the distribution of all other variables r_m, $m \neq n$, the formal solution of Eq. (4.39) for the probability density $\psi(r_n, t)$ reads (Wilemski and Fixman, 1974a; Likthman and Marques, 2006)

$$\psi(r_n, t) = \psi_{eq}(r_n) - \int_0^t dt_0 \int dr_n^0 \mathcal{G}(r_n, t|r_n^0, t_0)\mathcal{Q}(r_n^0)\psi(r_n^0, t_0) \,. \tag{4.41}$$

The propagator $\mathcal{G}$ is the conditional probability of finding the bond n with elongation r_n at time t provided that it was at r_n^0 at t_0. We remark that Eq. (4.41) applies to the situation when activation happens with initial conditions following the equilibrium distribution $\psi_{eq}(r_n)$ in the absence of reaction.

The fraction of bonds that have not crossed the barrier at r_+ is given by $\Phi(t)$, being the survival probability of an unreacted bond, and obeys the following relation

$$\begin{aligned} -\frac{d\Phi(t)}{dt} &= \int dr_n \mathcal{Q}(r_n)\psi(r_n, t) \\ &= K\psi(r_+, t) \\ &= K\psi_{eq}(r_+) - K^2 \int_0^t dt_0 \mathcal{G}(r_+, t - t_0|r_+, 0)\psi(r_+, t_0) \,. \end{aligned} \tag{4.42}$$

The single-point propagator $\mathcal{G}(t) = \mathcal{G}(r_+, t|r_+, 0)$ is often called the memory function. Taking the Laplace transform of Eq. (4.42) together with $\Phi(0) = 1$ (meaning that initially

the bonds are intact), we have

$$1 - s\tilde{\Phi}(s) = \frac{K\psi_{eq}(r_+)}{s\left(1 + K\tilde{\mathcal{G}}(s)\right)}\,, \tag{4.43}$$

what reduces in the limit of $K \to \infty$ to

$$1 - s\tilde{\Phi}(s) = \frac{\psi_{eq}(r_+)}{s\tilde{\mathcal{G}}(s)}\,. \tag{4.44}$$

For times exceeding the longest relaxation time the memory function approaches the equilibrium distribution $\psi_{eq}(r_+)$. Thus, one usually introduces a function which vanishes when $t \to \infty$

$$h(t) = \frac{\mathcal{G}(t)}{\psi_{eq}(r_+)} - 1\,. \tag{4.45}$$

Eq. (4.44) then reads

$$\tilde{\Phi}(s) = \frac{\tilde{h}(s)}{1 + s\tilde{h}(s)}\,. \tag{4.46}$$

In general the mean first passage time is given by

$$\tau_{mfp} = \int_0^\infty \Phi(t)dt = \lim_{s\to 0}\tilde{\Phi}(s)\,. \tag{4.47}$$

Using the small s expansion of the memory function

$$\lim_{s\to 0}\tilde{\mathcal{G}}(s) = \frac{\psi_{eq}(r_+)}{s} + \int_0^\infty dt\,(\mathcal{G}(t) - \psi_{eq}(r_+)) \tag{4.48}$$

in the Laplace transform of Eq. (4.45) we obtain

$$\tilde{h}(s \to 0) = \int_0^\infty dt\left(\frac{\mathcal{G}(t)}{\psi_{eq}(r_+)} - 1\right)\,. \tag{4.49}$$

Combining the Laplace transform of Eq. (4.45) and the expansion given in (4.48) one can easily show that in the limit of vanishing s we have $sh(s) \to 0$. Hence, the mean first passage time reads

$$\begin{aligned}\tau_{mfp} &= \tilde{\Phi}(0) = \tilde{h}(0)\\ &= \int_0^\infty dt\left(\frac{\mathcal{G}(t)}{\psi_{eq}(r_+)} - 1\right)\,.\end{aligned} \tag{4.50}$$

It was shown (Doi, 1975; Moreira and Marques, 2004), that the long-time rate constant s^* can be obtained by finding the pole of Eq. (4.46). Furthermore, in the limit of large characteristic activation timescales (when the potential barrier height is much larger than k_BT), s^* is close to zero and the mean first passage time τ_{mfp} is approximately given by

$$\tau_{mfp} \simeq \frac{1}{|s^*|}\,. \tag{4.51}$$

Following Bayes formula the propagator $\mathcal{G}$ is related to the two-point joint probability distribution of r_n via

$$\mathcal{G}(r_n, t|r_n^0, 0) = \frac{\psi_n(r_n, t; r_n^0, 0)}{\psi_{eq}(r_n^0)} \,. \tag{4.52}$$

The mean first passage time becomes

$$\tau_{mfp}(n) = \int_0^\infty \left(\frac{\psi_n(r_+, t; r_+, 0)}{\psi_{eq}^2(r_+)} - 1 \right) dt \,. \tag{4.53}$$

Introducing the deviations of the sink function from its equilibrium average as

$$\delta\mathcal{Q} = \mathcal{Q} - \langle \mathcal{Q} \rangle \tag{4.54}$$

one finds another equivalent representation of the mean first passage time

$$\tau_{mfp}(n) = \int_0^\infty \frac{\langle \delta\mathcal{Q}(t)\delta\mathcal{Q}(0) \rangle}{\langle \mathcal{Q} \rangle^2} dt \tag{4.55}$$

as the integral over the equilibrium sink-sink correlation function (which was introduced in Eq.(2.43)).

For any one-dimensional harmonic chain the two-point joint probability distribution is a bivariate Gaussian and, like all multivariate Gaussian distributions, fully determined by its covariance matrix $\mathbb{C}$

$$\psi_n(r_n, t; r_n^0, 0) = \frac{1}{2\pi\sqrt{\det \mathbb{C}}} \exp\left(-\frac{1}{2} \mathbf{R}^T \mathbb{C}^{-1} \mathbf{R} \right) \,, \tag{4.56}$$

with $\mathbf{R}^T = \{R_i\}$ being a 2-component vector $(r_n(t), r_n(0))$. The covariance matrix $\mathbb{C}_{ij} = \langle R_i R_j \rangle$ has equal elements on its diagonal line $\mathbb{C}_{ii} = \langle R_i^2 \rangle = \phi_0$. The off-diagonal elements correspond to correlations at different times $\langle r_n(t) r_n(0) \rangle = \phi_0 \phi_n(t)$. The covariance matrix reads

$$\mathbb{C} = \phi_0 \begin{pmatrix} 1 & \phi_n(t) \\ \phi_n(t) & 1 \end{pmatrix} \,. \tag{4.57}$$

Note that in the three-dimensional case the cross-correlations of different coordinates all vanish in the Rouse chain and the 6×6 covariance matrix has a block-diagonal form. The two-point joint probability distribution is given by

$$\psi_n(r_n, t; r_n^0, 0) = \frac{1}{2\pi\phi_0\sqrt{1 - \phi_n(t)^2}} \exp\left[-\frac{r_n^2 + (r_n^0)^2 - 2\phi_n(t) r_n r_n^0}{2\phi_0(1 - \phi_n(t)^2)} \right] \,, \tag{4.58}$$

with the normalized autocorrelation function $\phi_n(t)$ which depends on the location in the chain and which we will specify in the next section for the cases of the free and the grafted chain. r_+ is related to a barrier height via

$$\Delta E = \frac{\kappa}{2} r_+^2 \,. \tag{4.59}$$

Inserting Eqs. (4.34), (4.58), and (4.59) into Eq. (4.53) we finally derive

$$\tau_{mfp}(n) = \int_0^\infty \left(\frac{\exp\left[\frac{\Delta E}{k_B T}\frac{2\phi_n(t)}{1+\phi_n(t)}\right]}{\sqrt{1-\phi_n(t)^2}} - 1 \right) dt\,. \tag{4.60}$$

It is worth to mention that for a system with only a single reaction coordinate (one grafted monomer or a free dimer), the ACF is a single exponential, the escape process is Markovian for $\Delta E \gg k_B T$, and Eq. (4.60) becomes exact. This can be shown as follows: The main contribution to the integral in Eq. (4.60) comes from short times. For a single grafted monomer the correlation function at short times is approximately given by $\phi(t) \simeq 1 - t/\tau_1^g$. Rewriting Eq. (4.60) in a somewhat different form

$$\tau_{mfp} = \exp\left[\frac{\Delta E}{k_B T}\right] \int_0^\infty \left(\frac{\exp\left[-\frac{\Delta E}{k_B T}\frac{1-\phi(t)}{1+\phi(t)}\right]}{\sqrt{1-\phi(t)^2}} - \exp\left[-\frac{\Delta E}{k_B T}\right] \right) dt\,. \tag{4.61}$$

Using the short time expansion of the correlation function as well as considering the limit $\Delta E \gg k_B T$, further setting the upper limit of the integration to $t'_{max} = \tau_1^g/2$, we obtain

$$\begin{aligned} \tau_{mfp} &= \tau_1^g \exp\left[\frac{\Delta E}{k_B T}\right] \int_0^{t'_{max}} \frac{\exp\left[-\frac{\Delta E}{k_B T}\frac{t'}{2\tau_1^g}\right]}{\sqrt{2t'}} dt' \\ &= \tau_1^g \sqrt{\frac{\pi k_B T}{\Delta E}} \exp\left[\frac{\Delta E}{k_B T}\right] \operatorname{erf}\left(\sqrt{\frac{\Delta E}{k_B T}\frac{t'_{max}}{2\tau_1^g}}\right) \to \tau_1^g \sqrt{\frac{\pi k_B T}{\Delta E}} \exp\left[\frac{\Delta E}{k_B T}\right]\,. \end{aligned} \tag{4.62}$$

Essentially, the result coincides with the expression given in Eq. (4.21) derived from the Pontryagin equation which is equal to the inverse Kramers escape rate. In the more general case of an arbitrary sink function there is no immediate counterpart within a first-passage-time formalism.

4.5. Results

4.5.1. The free chain

Let us first consider the free one-dimensional chain. In terms of the normal modes given in Eq. (2.25) the bond lengths $r_n = x_n - x_{n-1}$ in such a chain read

$$\begin{aligned} r_n(t) &= 2\sum_{k=1}^{N} X_k(t) \left\{ \cos\left(\left(n+\frac{1}{2}\right)\frac{k\pi}{N+1}\right) - \cos\left(\left(n+\frac{1}{2}\right)\frac{k\pi}{N+1}\right)\right\} \\ &= -4\sum_{k=1}^{N} X_k(t) \sin\left(\frac{k\pi}{2(N+1)}\right) \sin\left(\frac{nk\pi}{N+1}\right)\,. \end{aligned} \tag{4.63}$$

In chapter 2 we calculated the ACF of the corresponding normal modes

$$\langle X_k(t) X_k(0)\rangle = \frac{k_B T}{2(N+1)\gamma} \tau_k^f \exp\left(-\frac{t}{\tau_k^f}\right)\,. \tag{4.64}$$

Hence, the time correlation functions of the r_n are

$$\langle r_n(t) r_n(0) \rangle = \frac{2}{N+1} \phi_0 \sum_{k=1}^{N} \mathrm{e}^{-t/\tau_k^f} \sin\left[\frac{k\pi n}{N+1}\right]^2 , \tag{4.65}$$

where we have used the fact that different modes are orthogonal. The normalized correlation functions $\phi_n(t)$ are

$$\phi_n(t) = \frac{2}{N+1} \sum_{k=1}^{N} \mathrm{e}^{-t/\tau_k^f} \sin\left(\frac{k\pi n}{N+1}\right)^2 , \tag{4.66}$$

with the correlation times

$$\tau_k^f = \frac{1}{\lambda_k^f} , \tag{4.67}$$

for $k = 1, ..., N$.

For $N \gg 1$ the sum in Eq. (4.66) can be replaced by an integral and $N + 1 \simeq N$. Substituting k by $k' = k\pi/N$ we have

$$\phi_n(t) \simeq \frac{2}{\pi} \int_0^{\pi} dk' \, \mathrm{e}^{-t(k')^2} \sin\left(k'n\right)^2 . \tag{4.68}$$

Thus for $N/2 \gg n$ (and $N \geq n \gg N/2$ for reasons of symmetry), i.e., for bonds close to the chain ends, the correlation function $\phi_n(t)$ is independent of the system size N. The integral in Eq. (4.68) can be solved in terms of error functions.

Since the mean first passage time is a functional of the correlation function, which by itself depends on the location of the bond in the chain, strong differences in the scaling of the correlation function might cause drastic differences of the activation rates (times) for bonds with different localization. Thus we first present in Fig. 4.4, panel (a), the normalized autocorrelation function of a free chain of $N = 99$ bonds. Depicted are the temporal correlation functions for a bond at one of the terminals of the chain ($n = 1$, dashed line) and for a bond at the center of the chain ($n = 50$, dashed-dotted line). Superimposed is the correlation function of a single bond, i.e., a dimer (solid line). At short times ($t \ll \tau_1^f$) all curves coincide, while for longer times the correlations decrease much slower at the chain's center compared to the terminal where the correlation time is also larger than for the dimer.

Let us have a closer look at the correlation function. A widely used definition of the correlation time is

$$\tau_c(n) = \int_0^{\infty} \phi_n(t) dt = \frac{1}{2(N+1)} \sum_{k=1}^{N} \frac{\sin\left(k\frac{\pi n}{N+1}\right)^2}{\sin\left(k\frac{\pi}{2(N+1)}\right)^2} . \tag{4.69}$$

For an odd number of bonds the central bond is situated at $n = (N+1)/2$ and evaluating the sum in the previous equation its correlation time is given by

$$\tau_c^{central} = \frac{N+1}{4} , \tag{4.70}$$

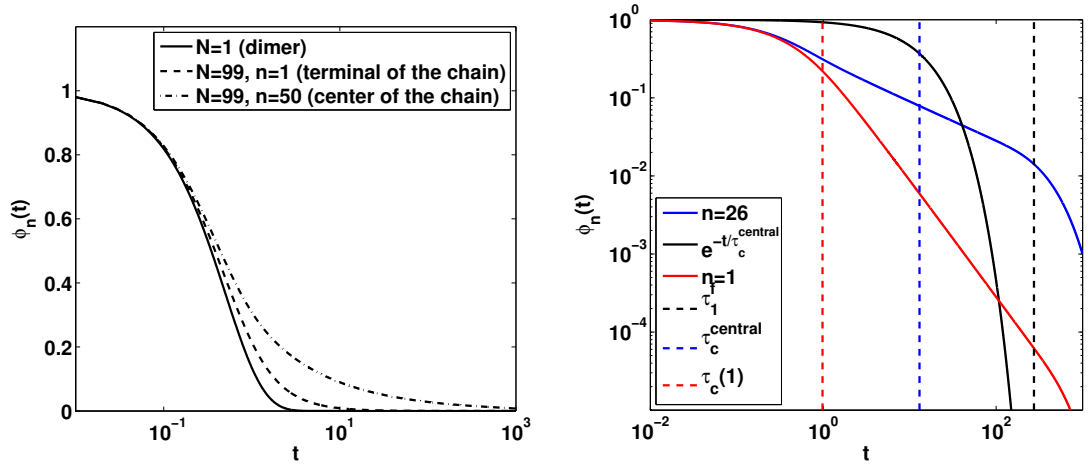

(a) (b)

Figure 4.4.: Panel (a): Normalized autocorrelation function $\phi_n(t)$ in a free chain with $N = 99$ bonds. The correlation function is shown for $n = 1$ (dashed line, terminal of the chain) and $n = 50$ (dashed-dotted line, center of the chain). Superimposed is the correlation function of a dimer, i.e., a chain consisting of only one bond. Panel (b): Double-logarithmic plot of the ACF for the bond elongation at $n = 1$ (solid red line) and $n = 26$ (solid blue line) in a chain of $N = 51$ bonds. Superimposed are the correlation times derived from Eq. (4.69) ($\tau_c(1)$, dashed red line) and Eq. (4.70) ($\tau_c^{central}$, dashed blue line). Furthermore, depicted is the ACF corresponding to a single exponential with relaxation time $\tau_c^{central}$ and the longest relaxation time of the whole chain $\tau_1^f = 1/\lambda_1^f$ (dashed black line).

and $\tau_c(n) < \tau_c^{central}, \quad \forall n \neq (N+1)/2$. Seemingly the longest relaxation time grows linearly with the system size. However, the intrinsic timescale of relaxations is given by $\tau_1^f = 1/\lambda_1^f$ which grows with N^2. In the double-logarithmic plot in Fig. 4.4, panel (b), we show the ACF of the elongation of a bond at the free terminal of a chain (solid red line) and a bond at the center of the chain (solid blue line). The dashed lines mark the corresponding correlation times derived from Eq. (4.69) (dashed red line) and Eq. (4.70) (dashed blue line). Superimposed is an exponentially decaying function with relaxation (decay) time $\tau_c^{central}$ and the longest correlation time in the chain $\tau_1^f = 1/\lambda_1^f$ (dashed black line). Notably the latter is approximately one order of magnitude larger compared to the correlation time at the chain center derived from Eq. (4.70) which itself is much larger than the one at the free terminal. Furthermore, although the ACF of a bond at the free terminal decays much faster compared to the ACF of a bond at the center of the chain, in both cases there is a power-law decay for times smaller than $1/\lambda_1^f$. Thus the decrease of correlations on an intermediate timescale is weaker compared to an exponential decay and the dynamics is non-Markovian. However, for each given instant in time, the ACF itself is smaller for bonds close to the chain ends. Since the analytical expression of the mean first passage time given by Eq. (4.60) is exact in the limit of timescale separation, the theory is expected to work more accurate in predicting the times close to the chain's

ends where the correlations are smaller at long times.

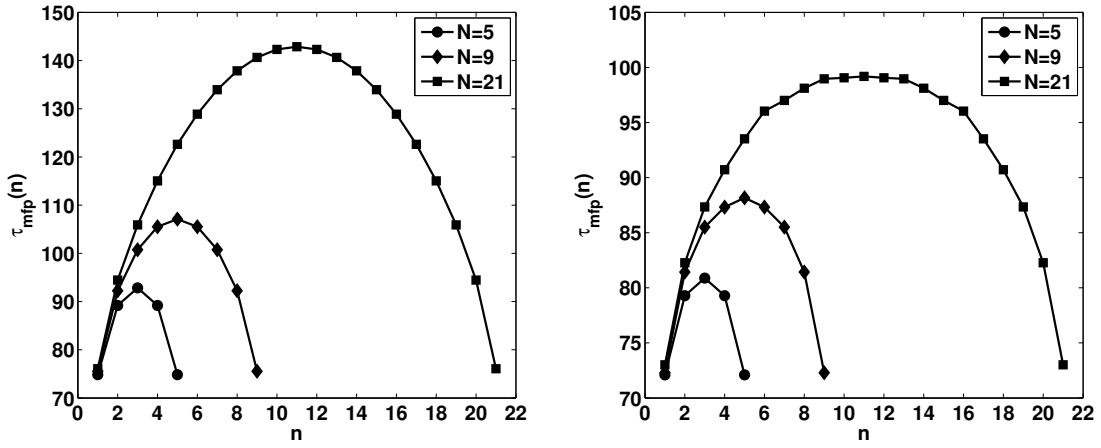

Figure 4.5.: Mean first passage time as a function of the bond position in the free chain for three different chain lengths as given in the legend. Panel (a): Mean first passage times obtained from Eq. (4.60) with the correlation function given in Eq. (4.66). Panel (b): Numerically obtained mean first passage times. The barrier height is $\Delta E = 5k_BT$.

As shown in Fig. 4.5, our analytical approach offers a qualitative picture that can explain observations in numerical simulations, i.e., it works qualitatively well in the whole range of n, which is typical for the Wilemski-Fixman approximation. In panel (a) we present the mean first passage times derived analytically from Eq. (4.60) (with $\phi_n(t)$ taken from Eq. (4.66)) for three chain lengths ($N = 5, 9, 21$) and a barrier height of $\Delta E = 5k_BT$. In panel (b) we show the outcome of Brownian dynamics simulations for the same set of parameter values. The general picture is the following: τ_{mfp} is minimized at the chain ends and grows towards the center of the chain. The increase of the mean first passage times is the stronger the longer the chains are. Qualitatively the outcome of the numerical simulations agrees very well with the theoretical prediction. Both, theory and numerical simulations, show that for bonds at the ends of the chain the mean first passage times are smaller compared to the activation times of the inner bonds. For these outer bonds the theory is also quantitatively in good agreement with the numerical simulations. As expected the agreement becomes worse with enlarging distance from the terminals of the chain. Nevertheless, unisonous, the theory as well as the numerical simulations predict an increase of the activation time with increasing system size, even for the bonds located at $n = 1$ and $n = N$. The observed effect is large already in relatively small systems (see panel (b) for $N = 21$: $\tau_{mfp}(10)$ is about 40% larger than $\tau_{mfp}(1)$) and becomes even larger in longer chains. Thus our study of the mean first passage times of individual bonds reveals that the activation times are smaller towards the chain ends and cause there a higher probability of fragmentation.

Furthermore, the fragmentation kernel depends on the barrier height which defines the intrinsic timescale of activation. In Fig. 4.6 we depict the numerically obtained mean first passage times over barriers of different height for a fixed chain length. The values of τ_{mfp}

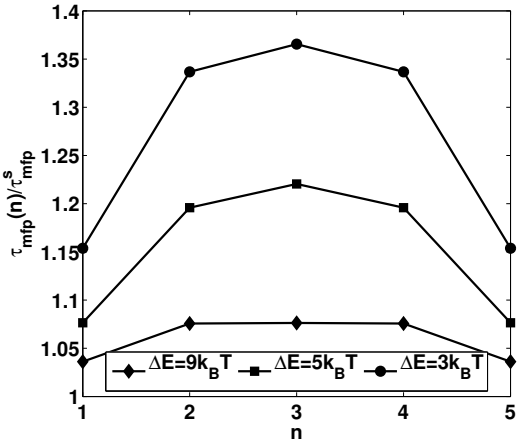

Figure 4.6.: Mean first passage times for different values of the barrier height. Mean first passage times as a function of the position of the bond in the free chain for different values of the barrier height as given in the legend. The times are given in multiples of the first passage time in a single bond system (dimer). The chain has $N = 5$ bonds.

are given in multiples of the first passage time in a single bond system τ^s_{mfp}. The higher is the potential barrier the weaker is the increase of the times for the bonds at the center of the chain. This illustrates that the observed effect of the dependence of the dissociation time on the bond location is of highly non-Markovian nature. For lower barriers the activation times are comparable with the timescale of correlations in the chain and the activation process is non-Markovian. We can conclude that the growth of activation times with enlarging distance from the chain's ends is the larger, the longer the chain and the lower the activation barrier is. In the contrary limit of very high activation barriers all activation times $\tau_{mfp}(n)$ are expected to be the same and thus the probability of breakage becomes homogeneous along the chain. This coincides with the predictions made by Lee (Lee, 2009). The activation rate of the individual bonds in the chain is simply given by the inverse mean first passage time for single bond rupture, given in Eq. (4.21).

4.5.2. The grafted chain

In most pulling experiments a polymer is grafted to a surface and then pulled away. Therefore, it is necessary to understand the activation kinetics of bonds in such chains. In the free chain we observed an increase of the activation times towards the central bond of the system. In the grafted chain there is also one free end, but another end is fixed. It was mentioned in the beginning that the longest relaxation time in the grafted chain (corresponding to the first normal mode) is four times longer compared to this time in the free chain. Thus we may expect that the non-Markovian aspect (induced by long correlation times) plays an even more important role in the barrier crossing dynamics.

In the grafted chain the bond elongation $r_n = x_n - x_{n-1}$ is given by

$$r_n(t) = \frac{4}{2N+1} \sum_{k=1}^{N} X_k(t) \left\{ \sin\left(n\pi \frac{2k-1}{2N+1} \right) - \sin\left((n-1)\pi \frac{2k-1}{2N+1} \right) \right\} , \qquad (4.71)$$

and using Eq. (2.59) the normalized ACF reads

$$\begin{aligned}\phi_n(t) &= \frac{4}{2N+1}\sum_{k=1}^{N}\frac{1}{\lambda_k^g}\,\mathrm{e}^{-t\lambda_k^g}\left(\sin\left(n\pi\frac{2k-1}{2N+1}\right)-\sin\left((n-1)\pi\frac{2k-1}{2N+1}\right)\right)^2 \\ &= \frac{4}{2N+1}\sum_{k=1}^{N}\mathrm{e}^{-t\lambda_k^g}\cos\left(\left(\frac{1}{2}-n\right)\pi\frac{2k-1}{2N+1}\right)^2,\end{aligned} \tag{4.72}$$

with λ_k^g taken from Eq. (2.37).

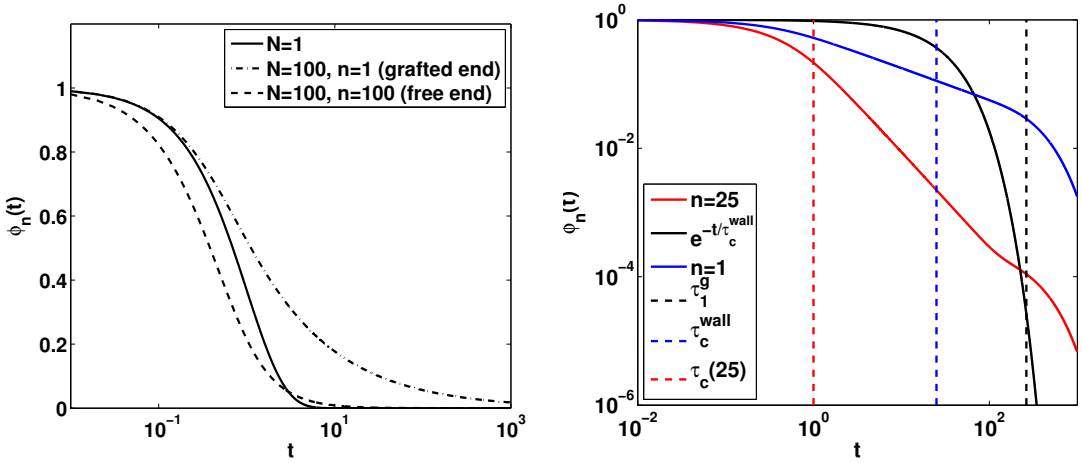

(a) (b)

Figure 4.7.: Panel (a): Normalized autocorrelation function $\phi_n(t)$ in a grafted chain with $N = 100$ bonds. The correlation function is shown for $n = 1$ (dashed-dotted line, grafted terminal of the chain) and $n = 100$ (dashed line, free end of the chain). Superimposed is $\phi_1(t)$ for a single grafted monomer. Panel (b): Double-logarithmic plot of the ACF for the bond elongation at $n = 1$ (solid blue line) and $n = 25$ (solid red line) in a chain of $N = 25$ bonds. Superimposed are the correlation times derived from Eq. (4.74) (τ_c^{wall}, dashed blue line) and Eq. (4.73) ($\tau_c(1)$, dashed red line). In addition, depicted are the exponential decay corresponding to τ_c^{wall} and the longest relaxation time of the whole chain $\tau_1^g = 1/\lambda_1^g$ (dashed black line).

In Fig. 4.7, panel (a), we show the normalized autocorrelation function as given in Eq. (4.72) of a grafted chain of $N = 100$ bonds. We depict the temporal evolution of $\phi_n(t)$ for $n = 1$, i.e., the bond at the grafted end (dashed-dotted line), and for $n = 100$, i.e., the bond at the free terminal (dashed line). Superimposed is the correlation function for a single grafted bond. At short times the correlations drop down earlier compared to the single bond situation and the bond at the grafted end. Note that the dashed line coincides with the solid line in Fig. 4.4, panel (a). Thus we conclude that for short times the dynamics of the bond at the free end resembles the dynamics of a dimer. We can infer, that for short times the dynamics of a bond at the chain's free terminal is the same, no matter whether the chain is fixed or not. As it is possible in the free chain, we are able to

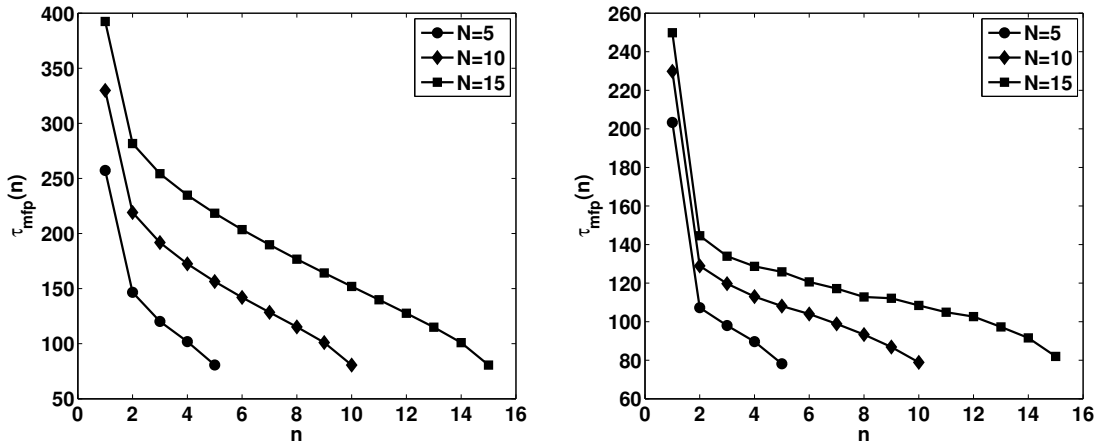

Figure 4.8.: Mean first passage time as a function of the bond position in the grafted chain for different chain lengths as given in the legend. Panel (a): Mean first passage times obtained from Eq. (4.60) with the correlation function given in Eq. (4.72). Panel (b): Numerically obtained mean first passage times. The barrier height is $\Delta E = 5k_BT$.

study the scaling of the correlation times of the bonds. In general it is given by

$$\tau_c(n) = \int_0^\infty \phi_n(t)dt = \frac{1}{2N+1} \sum_{k=1}^{N} \frac{\cos\left(\left(\frac{1}{2} - n\right)\pi \frac{2k-1}{2N+1}\right)^2}{\sin\left(\frac{\pi}{2}\frac{2k-1}{2N+1}\right)^2} \,. \tag{4.73}$$

For the bond at the wall it becomes

$$\tau_c^{wall} = N \,. \tag{4.74}$$

Interestingly $\tau_c(1) = 1$ independent of the number of bonds in the system. However, the correlation function itself differs in the long-time limit since the typical timescale is given by the relaxation time of the lowest mode which is a functional of N.

In the double-logarithmic plot in Fig. 4.7, panel (b), we show the ACF of the elongation of a bond at the grafted terminal of a chain (solid blue line) and a bond at the opposite end of the chain (solid red line). The dashed lines mark the corresponding correlation times derived from Eq. (4.74) (dashed blue line) and Eq. (4.73) (dashed red line). Superimposed is an exponentially decaying function with correlation time τ_c^{wall} and the longest correlation time in the chain $\tau_1^g = 1/\lambda_1^g$ (dashed black line). The ACF of a bond at the free terminal decays much faster compared to the ACF of the grafted bond. Nevertheless, as in the free chain, in both cases there is a power-law decay for times smaller than $\tau_1^g = 1/\lambda_1^g$. Thus the decrease of correlations on an intermediate timescale is weaker compared to an exponential decay and the activation process is non-Markovian. Interestingly, for the curve which corresponds to the bond at the free terminal, at the end of the power-law tail the decrease of the ACF becomes weaker before becoming an exponential.

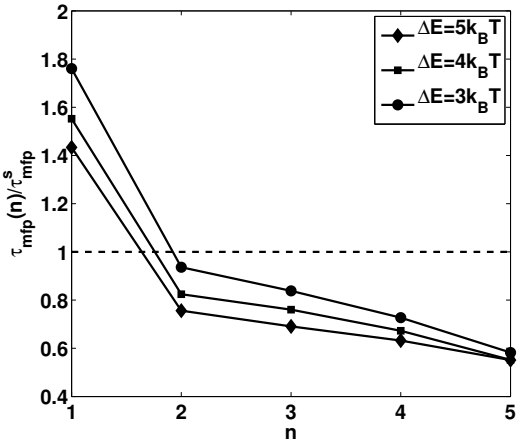

Figure 4.9.: Mean first passage times as a function of the position of the bond in the grafted chain for different values of the barrier height as given in the legend. The times are given in multiples of the first passage time in a single bond system. The chain consists of $N = 5$ bonds.

In Fig. 4.8, panel (a), we present the mean first passage times derived from Eq. (4.60) with the ACF given in Eq. (4.72) for three chain lengths ($N = 5, 10, 15$) and a barrier height of $\Delta E = 5k_BT$. In panel (b) we show the outcome of Brownian dynamics simulations for the same set of parameter values. As in the free chain, for bonds at the loose terminal the mean first passage times are smaller compared to those of the inner bonds. For these bonds the theory is also quantitatively in good agreement with the numerical simulations. The mean first passage times gradually increase with growing distance from the free end of the chain and grow substantially at the grafted terminal. The growth of τ_{mfp} towards the grafted terminal is the more pronounced the longer the chains are. The effect is overestimated by the theory. However, theory and numerical simulation are in good qualitative agreement.

As for the free chain we study the impact of the activation barrier height on the chain fragmentation kinetics. In Fig. 4.9 we depict the numerically obtained mean first passage times over barriers of different height and a fixed chain length. Mean first passage times are given in multiples of the value for a single grafted bond τ^s_{mfp}. The lower is the potential barrier, the stronger is the increase of the dissociation time along the chain. In the opposite limit $\Delta E \gg k_BT$ we have $\tau_{mfp}(1) \to \tau^s_{mfp}$ while $\tau_{mfp}(n \neq 1) \to \tau^s_{mfp}/2$ (the value expected for a free dimer). Thus in this limit at the grafted end the value of the activation rate is half of the value of a bond situated at $n \neq 1$. This has also been shown by Lee (Lee, 2009).

Let us briefly sum up the results we found so far. Bond breakage happens with higher probability at the free chain ends. Towards the center of the free chain as well as towards the grafted terminal of the fixed chain the activation times increase substantially. In the limit of high activation barriers the mean first passage times become equal along the chain and hence the distribution of the fragmentation location in the chain flattens. In the opposite limit of low activation barriers the mean first passage times markedly differ with

varying location of the breakable bond in the chain.

4.6. Non-Markovian generalization of the renewal equation

Let us now apply a somewhat different theoretical approach proposed by Sokolov (Sokolov, 2003). It is a modification of the renewal equation Eq. (4.28) for non-Markovian escape problems. Sokolov showed that in the Markovian case his approach is equivalent to the Wilemski-Fixman approximation with a Smoluchowski sink term. It was argued by Likthman et al. (Likthman and Marques, 2006) that Sokolov's calculation does not fully capture the non-Markovian dynamics. In the next paragraph we will shortly outline why the approach involves an approximation[2]. In fact, as we are going to show, there is a mismatch between the analytically predicted mean first passage times and the outcome of numerical simulations. However, we show that the correction to the Wilemski-Fixman approximation tends towards the numerical results. The approach proposed by (Likthman and Marques, 2006) may yield a better agreement with numerical simulations, but the calculation effort is huge and we do not expect qualitatively different results.

We start with a generalized version of the renewal equation (4.28). The conditional probability to be at r_n at time t, provided the elongation has been $r_n(0) = r_n^0$ at time $t = 0$, $\mathcal{G}(r_n, t|r_n^0, 0)$, is given by (Sokolov, 2003)

$$\mathcal{G}(r_n, t|r_n^0, 0) = \delta(r_n - r_n^0)\delta(t) + \int_0^t \mathcal{F}(r_n, t'|r_n^0, 0)\mathcal{G}(r_n, t|r_n, t'; r_n^0, 0)dt' \,, \tag{4.75}$$

where $\mathcal{G}(r_n, t|r_n, t'; r_n^0, 0)$ is the conditional probability to be at r_n at time t, provided r_n was visited earlier at time t' and that the particle started at r_n^0 at $t = 0$. $\mathcal{F}(r_n, t'|r_n^0, 0)$ is the distribution of first passage times. If $r_n^0 \neq r_n$ the δ term can be omitted. The approximation made in the formula is the following. The Green's function in (4.75) is the propagator of the equilibrium system in the absence of the boundary. Thus it includes trajectories that evolve behind the absorbing boundary and should not contribute to the first passage time distribution. Therefore, the approach yields only an approximative solution of the full non-Markovian problem.

For a Markovian process $\mathcal{G}(r_n, t|r_n, t'; r_n^0, 0) = \mathcal{G}(r_n, t|r_n, t')$ and Eq. (4.75) reduces to the usual renewal equation given in Eq. (4.28). According to Bayes formula,

$$\mathcal{G}(r_n, t|r_n^0, 0) = \frac{\psi(r_n, t; r_n^0, 0)}{\psi_{eq}(r_n^0, 0)} \tag{4.76}$$

and

$$\mathcal{G}(r_n, t|r_n, t'; r_n^0, 0) = \frac{\psi(r_n, t; r_n, t'; r_n^0, 0)}{\psi(r_n, t'; r_n^0, 0)} \,, \tag{4.77}$$

where $\psi_{eq}(r_n^0, 0)$, $\psi(r_n, t; r_n^0, 0)$, and $\psi(r_n, t; r_n, t'; r_n^0, 0)$ are the joint probability distributions at one, two, and three different times, respectively. Eq. (4.75) now reads

$$\frac{\psi(r_n, t; r_n^0, 0)}{\psi_{eq}(r_n^0, 0)} = \int_0^t \mathcal{F}(r_n, t'|r_n^0, 0)\frac{\psi(r_n, t; r_n, t'; r_n^0, 0)}{\psi(r_n, t'; r_n^0, 0)}dt' \,, \tag{4.78}$$

[2]I gratefully acknowledge the discussion with Prof. Sokolov who pointed this out in detail.

which can be put in the following form

$$\int_0^t \mathcal{F}(r_n, t'|r_n^0, 0)\hat{\mathcal{Q}}(t, t', r_n^0)dt' = 1\,, \tag{4.79}$$

with the kernel

$$\hat{\mathcal{Q}}(t, t', r_n^0) = \frac{\psi(r_n, t; r_n, t'; r_n^0, 0)\psi_{eq}(r_n^0, 0)}{\psi(r_n, t'; r_n^0, 0)\psi(r_n, t; r_n^0, 0)}\,. \tag{4.80}$$

The three-point joint probability distribution is given by

$$\psi(r_n, t; r_n, t'; r_n^0, 0) = \frac{(2\pi)^{-3/2}}{\sqrt{\det \mathbb{C}}} \exp\left(-\frac{1}{2}\mathbf{R}^T\mathbb{C}^{-1}\mathbf{R}\right)\,, \tag{4.81}$$

with the three-component vector $\mathbf{R}^T = (r_n(t), r_n(t'), r_n^0)$ and the covariance matrix

$$\mathbb{C} = \phi_0 \begin{pmatrix} 1 & \phi_1 & \phi_2 \\ \phi_1 & 1 & \phi_3 \\ \phi_2 & \phi_3 & 1 \end{pmatrix}\,, \tag{4.82}$$

with $\phi_1 = \phi_n(t - t')$, $\phi_2 = \phi_n(t)$ and $\phi_3 = \phi_n(t')$. Thus the three-point joint probability distribution reads

$$\begin{aligned}\psi(r_n, t; r_n, t'; r_n^0, 0) = &\frac{1}{(2\pi\phi_0)^{3/2}} \frac{1}{\sqrt{1 - \phi_1^2 - \phi_2^2 - \phi_3^2 + 2\phi_1\phi_2\phi_3}} \\ &\exp\left[-\frac{r_n^2\left(2 - 2\phi_1 - (\phi_2 - \phi_3)^2\right) + (r_n^0)^2(1 - \phi_1^2) + 2\left(\phi_2 + \phi_3\right)\left(\phi_1 - 1\right) r_n r_n^0}{2\phi_0\left(1 - \phi_1^2 - \phi_2^2 - \phi_3^2 + 2\phi_1\phi_2\phi_3\right)}\right]\,.\end{aligned} \tag{4.83}$$

The solution of Eq. (4.79) can be found numerically; passing to a discrete time Eq. (4.79) becomes a linear system of equations and its solution is found by matrix inversion. There we encounter some difficulties: In order to sample the continuous distribution accurately the timestep needs to be sufficiently small increasing the rank of the matrix and therewith the computational time and accuracy. Therefore, we recover only a part of the distribution for times $0 < t \leq t_{max}$. Since the solution is exponentially decaying for long times (corresponding to the long time rate constant) we accordingly fit the long-time tail of the distribution. The distribution of the first passage times is depicted in Fig. 4.10, panel (a), for the bond with index $n = 3$ in a free chain of $N = 5$ bonds. The initial elongation was set to $r_n^0 = 0$. The deviations from an exponential distribution at short times are rather small. For larger times the distribution decays exponentially. In Fig. 4.10, panel (b), we present the distribution of the first passage times of the bonds $n = 1, 2, 3$ in a free chain of $N = 5$ bonds (for symmetry reasons in the free chain the distributions for $n = 1, 2$ are the same as those for $n = 5, 4$, respectively). With increasing distance from the free terminal ($n = 1$) the exponential tail flattens and the peak becomes more pronounced; the mean first passage time grows. An inset shows the distributions obtained via direct Brownian dynamics simulations of the coupled chain system. Qualitatively the order and shape of the distributions coincide with those derived from the analytical approach but the peak is located at slightly larger times and the exponential decay at long times is somewhat

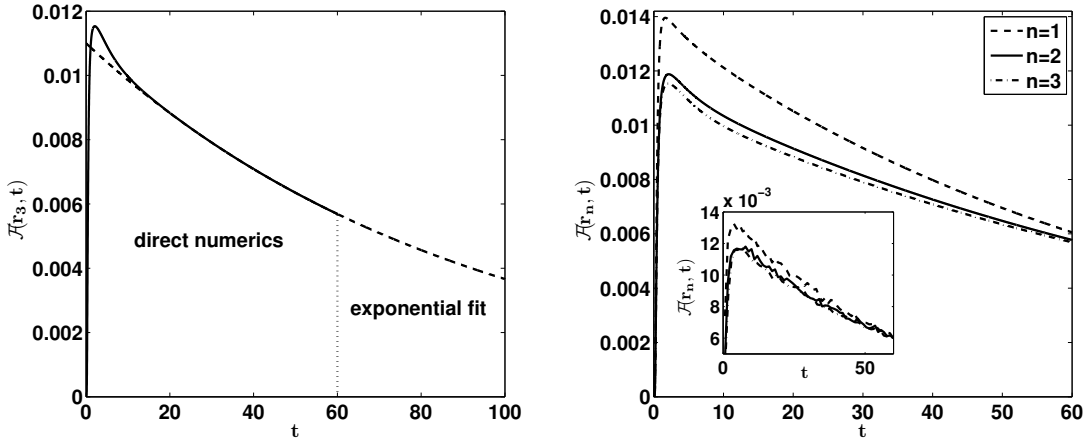

(a) (b)

Figure 4.10.: Panel (a): Distribution of first passage times for the bond with index $n = 3$ (solid line). The barrier height is $\Delta E = 5k_BT$. The chain consists of $N = 5$ bonds. The rank of the matrix is 10000 and the numerical resolution given by the timestep is $\Delta t = 0.006$ corresponding to $t_{max} = 60$. Superimposed is the exponential fit of the long-time tail (dashed line). Panel (b): Numerically obtained distribution of the first passage times for the different bonds in a chain of $N = 5$ bonds. The barrier height is $\Delta E = 5k_BT$. The rank of the matrix is 10000 and the timestep is $\Delta t = 0.006$ corresponding to $t_{max} = 60$. The inset shows the distributions obtained via direct Brownian dynamics simulations of the coupled chain system.

stronger.

Using the data obtained via direct numerics (dn) and the exponential fitting procedure the mean first passage time is given by

$$\begin{aligned}\tau_{mfp}(r_0) &= \int_0^\infty t\mathcal{F}(r_n,t)dt = \int_0^{t_{max}} t\mathcal{F}(r_n,t)dt + \int_{t_{max}}^\infty t a_f \,\mathrm{e}^{-t/b_f}\,dt \\ &= \langle t\rangle_{dn}(r_n) + a_f b_f\,(b_f + t_{max})\,\mathrm{e}^{-t_{max}/b_f}\,,\end{aligned} \tag{4.84}$$

where we replace the integral by a sum in order to calculate $\langle t\rangle_{dn}(r_n)$. Since the result may sensitively depend on the timestep in the discrete description, we repeated the calculations for different values of Δt and checked that the mean first passage time becomes independent of Δt for $\Delta t \to 0$. The results of numerical simulations (initially the bond elongations are either taken from an equilibrium distribution or zero) are depicted in Fig. 4.11 and compared with both the prediction of the Wilemski-Fixman approximation and the mean first passage time given by Eq. (4.84). It is clearly visible that the latter is shifted towards the numerical simulation curve. There remains a difference and its elimination requires a more sophisticated mathematical treatment as proposed by (Likthman and Marques, 2006). Though, we do not expect surprising new results. Note, that the Wilemski-Fixman approximation works sufficiently well in the whole range of n.

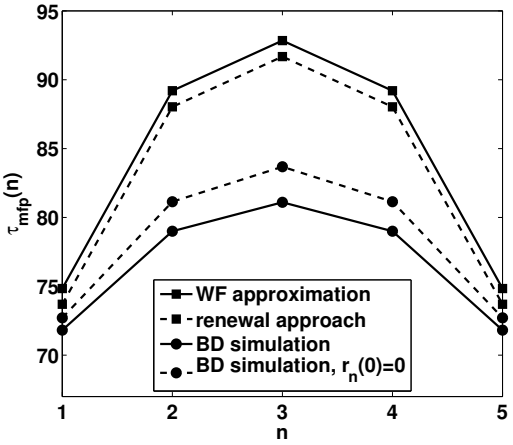

Figure 4.11.: Mean first passage times to a barrier of height $\Delta E/k_BT = 5$. The chain has $N = 5$ bonds. We compare the outcome of Brownian dynamics simulations ($r_n^0 = 0\,\forall n$ (circles, dashed line) and initial values taken from the bond equilibrium distribution (circles, solid line)) with the Wilemski-Fixman approximation (squares, solid line) and the values given by Eq. (4.84) (squares, dashed line).

4.7. The free 3D Rouse chain

Let us now turn to the free three-dimensional harmonic chain. $N+1$ beads are connected by N harmonic springs. The ends are free and the chain's center of mass diffuses with an effective friction constant $\sim N$. We restrict ourselves to the calculations within the framework of the Wilemski-Fixman approximation. In the three-dimensional chain system the two-point joint probability distribution of a distance vector $\mathbf{r}_n$ is given by

$$\psi_n(\mathbf{r}_n, t; \mathbf{r}_n^0, 0) = \left(\frac{1}{2\pi\phi_0}\right)^3 \frac{1}{(1-\phi_n(t)^2)^{3/2}} \exp\left[-\frac{1}{2\phi_0}\frac{\mathbf{r}_n^2 + (\mathbf{r}_n^0)^2 - 2\phi_n(t)\mathbf{r}_n\cdot\mathbf{r}_n^0}{1-\phi_n(t)^2}\right]. \tag{4.85}$$

Since the absorbing boundary for the bond elongation is a sphere, the problem of activation reduces to a one-dimensional one. After averaging over angles

$$\psi_n(r_n, t; r_n^0, 0) = \int_{\delta\mathbb{S}}\int_{\delta\mathbb{S}^0} d\mathbf{s}d\mathbf{s}^{\mathbf{0}}\psi_n(\mathbf{r}_n, t; \mathbf{r}_n^0, 0)\,, \tag{4.86}$$

where we integrate over the surfaces $\mathbb{S}$ and $\mathbb{S}^0$ with radii r_n and r_n^0, respectively, the distribution has the following form

$$\psi_n(r_n, t; r_n^0, 0) = \frac{2r_nr_n^0}{\pi\phi_0^2\phi_n(t)\sqrt{1-\phi_n(t)^2}} \sinh\left[\frac{\phi_n(t)r_nr_n^0}{\phi_0\left(1-\phi_n(t)^2\right)}\right] \exp\left[-\frac{r_n^2+(r_n^0)^2}{2\phi_0\left(1-\phi_n(t)^2\right)}\right]. \tag{4.87}$$

Together with Eq. (4.60) the mean first passage time reads

$$\tau_{mfp}(n) = \int_0^\infty \left(\frac{\phi_0}{r_+^2 \phi_n(t) \sqrt{1-\phi_n(t)^2}} \sinh\left[\frac{\phi_n(t) r_+^2}{\phi_0 \left(1-\phi_n(t)^2\right)} \right] \exp\left[-\frac{r_+^2 \phi_n(t)^2}{\phi_0 \left(1-\phi_n(t)^2\right)} \right] - 1 \right) dt \,, \tag{4.88}$$

with $\phi_n(t)$ taken from Eq. (4.66).

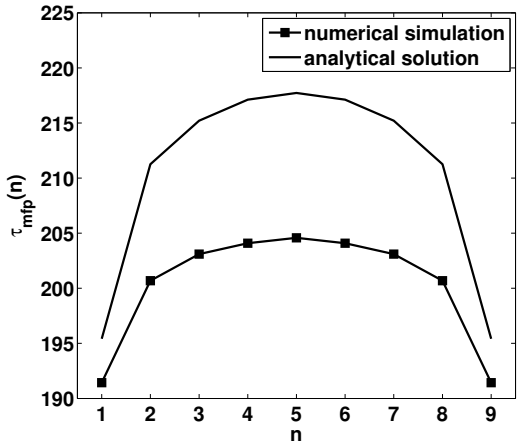

Figure 4.12.: Mean first passage times as a function of the position of the bond in the chain. The barrier height is $\Delta E/k_BT = 10$. The chain length is $N = 9$. Results obtained via Brownian dynamics simulations (squares) are compared with those derived from Eq. (4.88) (solid line).

In Fig. 4.12 we compare the mean first passage times of $|\mathbf{r}_n|$ derived from Eq. (4.88) and from Brownian dynamics simulations for a barrier height of $\Delta E/k_BT = 10$. As in the one-dimensional system, there is a qualitative agreement between theory and numerical simulations. Even for a relatively short chain consisting of $N = 9$ bonds, there is an increase of the activation time towards the center of the chain of about 8%, which will be even larger for longer chains and/or lower activation barriers which are of relevance in biological systems.

4.8. Fragmentation kinetics

Eventually we describe the fragmentation kinetics based on the location dependent mean first passage times in the chain. Our intention is to illustrate the evolution of the fragment size distribution with time. For high enough activation barriers the mean first passage time of a bond in the coupled chain system is approximately inverse proportional to its long time reaction rate constant. Based on this assumption we studied the scaling of the decrease of the inverse mean first passage times (being the probabilities per unit time for a bond to break, and thus being the fragmentation kernel) towards the chain ends and found neither a power law nor an exponential scaling. Thus we cannot map the obtained

fragmentation kernel on an existing standard class of kernels (Ziff, 1986; McGrady and Ziff, 1987; Cheng and Redner, 1988) and therewith no immediate analytical prediction of the distribution of fragments at a given instant in time is available. However, in principle the corresponding kinetic equation governing the fragmentation can be solved numerically. This was done as follows: The kinetic equations for the concentration of n-mers ρ_n have the general form (Ziff, 1986)

$$\frac{d\rho_n}{dt} = -\nu_n \rho_n + 2 \sum_{j=n+1}^{\infty} \nu_{n,j} \rho_j \,, \tag{4.89}$$

with the breakdown rate $\nu_{n,j}$, i.e., the probability per unit time for a j-mer to break at bond n into a n-mer and a $(j-n)$-mer. The factor 2 in front of the sum reflects the fact, that for the symmetric free chain we may also write $\nu_{n,j} = \nu_{j-n,j}$. Here we study solely the case of having a solution of free chains; including also the situation with grafted chains is straight forward. The total breakdown rate of a n-mer is

$$\nu_n = \sum_{i=1}^{n-1} \nu_{i,n} \,. \tag{4.90}$$

We consider a monodisperse system of M-mers at time $t = 0$. Then it is possible to solve the system of kinetic equations (4.89). The kinetic equation for the density of M-mers reads (no gain, only a loss term)

$$\frac{d\rho_M}{dt} = -\nu_M \rho_M \,, \tag{4.91}$$

with the solution

$$\rho_M = \exp\left(-\nu_M t\right) \,. \tag{4.92}$$

The density of $(M-1)$-mers satisfies

$$\frac{d\rho_{M-1}}{dt} = -\nu_{M-1}\rho_{M-1} + 2\nu_{M-1,M}\rho_M \,. \tag{4.93}$$

Such equations have the general solutions

$$\rho_n = \sum_{i=n}^{M} \hat{C}_{ni} \exp\left(-\nu_i t\right) \,, \tag{4.94}$$

with numerical coefficients $\hat{C}_{ni}$. Putting (4.94) into (4.89) one finds

$$\hat{C}_{ni} = \frac{2}{\nu_n - \nu_i} \sum_{j=n+1}^{i} \hat{C}_{ji} \nu_{n,j} \,, \quad (n < i < M) \,. \tag{4.95}$$

Furthermore, $\hat{C}_{MM} = 1$ and since $\rho_n(0) = 0$ for $n < M$

$$\hat{C}_{nn} = -\sum_{i=n+1}^{M} \hat{C}_{ni} \,. \tag{4.96}$$

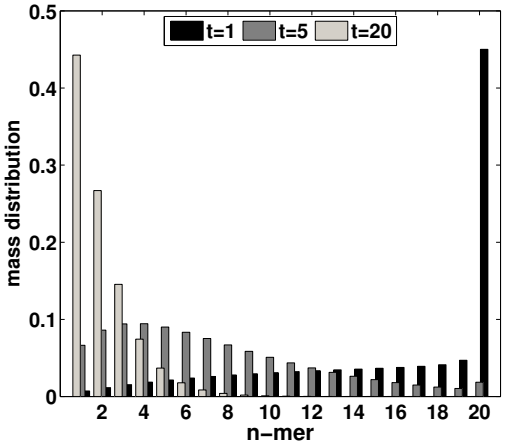

Figure 4.13.: Numerically obtained mass distribution for different values of the time as given in the legend. The barrier height of the bonds is $\Delta E/k_BT = 7$. At time $t = 0$ the chain length is $N = 19$.

Thus starting with $\hat{C}_{MM}$ and $\nu_{M-1,M}$ all coefficients $\hat{C}_{ni}$ and therewith the concentrations $\rho_n(t)$ can be found recursively. This was done exemplary for a solution of polymers in three dimensions consisting initially ($t = 0$) of chains with $N = 19$ bonds (20-mers). The fragmentation kernel has been derived from Eq. (4.88). The mass distribution, which is $n\rho_n(t)$, is shown in Fig. 4.13 for three different values of the time. In the beginning the distribution is sharply peaked at the initial chain length (not shown). Within time the larger polymers split into smaller ones and eventually only monomers remain (again not shown). The total mass is conserved during the fragmentation process.

4.9. Summary

Let us summarize our findings. We have studied the thermally activated fragmentation of a homopolymer chain, which can exhibit strongly non-Markovian behavior on the timescale of interest. We first presented different approaches to calculate first passage times and activation rates for Markovian escape processes of a single reaction coordinate. Concerning the chain fragmentation these rates are obtained in the limiting case when the activation time becomes much longer than the longest relaxation time in the chain. Our study of the polymer fragmentation was mainly grounded on a simple one-dimensional chain model with beads coupled by harmonic springs having a sharp cut-off for overcritical elongations. The model has the advantage that—as long as the chain is intact—its dynamics is described by the usual Rouse model. This enabled us to apply a well-established approximation for reaction-diffusion processes in polymers, which is the Wilemski-Fixman approximation, to calculate the mean first passage times of bonds in the chain as a function of their location and the lengths of the polymer. It was shown that the overall fragmentation rate follows a nonlinear scaling as a function of the number of breakable bonds in the chain. Bond breakage happens with higher probability at the free chain ends. Studying the activation times of individual bonds, it was found that towards the center of the free chain as well as towards the grafted terminal of the fixed chain the activation times increase substantially.

In the limit of high activation barriers the distribution of the fragmentation location in the chain flattens, since the activation rates become equal along the chain. The dynamics on the timescale of interest becomes Markovian.

Going beyond the Wilemski-Fixman approximation we have shown that a generalized form of the renewal equation for barrier crossings serves to improve our analytical predictions for the mean first passage times when comparing them with the outcome of numerical simulations. Furthermore, we extended our model to a three-dimensional chain which might be of importance for the application of our theory to realistic experiments. Eventually we considered the evolution of the mass distribution of an initially monodisperse polymer solution. Therefore, we presented the numerical scheme which solves the corresponding kinetic equations. We remark that the fragmentation kernel crucially depends on the height of the activation barrier, the location of the breakable bond in the chain, and the total length of the latter.

Exchanging the harmonic potential with a sharp cut-off for a nonlinear binding potential is expected to show qualitatively the same fragmentation behavior. Our study of equilibrium relaxation times in chapter 3 revealed that nonlinear chain models may be approximated by harmonic chains with effective coupling strength. The same might also be true when a static force is applied to a chain. In contrast, loading the chain at a constant rate, i.e., increasing an external force with time, will significantly alter the rupture process of a polymer as we will see in the next chapter.

5. Bond rupture in the presence of a time-dependent force

5.1. Introduction

In the previous chapter we studied the thermally activated fragmentation in a simple polymer chain model in the absence of an external force. However, a variety of chemical and biological processes require the reaction of various bonds or molecules to an applied time-dependent force (Evans and Ritchie, 1997; Dudko et al., 2003, 2006).

It is well established that such a reaction can be described as thermally activated escape. There it is assumed that an abstract reaction coordinate exists, which evolves from a metastable initial state to a final equilibrium. Along the reaction pathway at least one energetic barrier has to be overcome. In the commonly used most simple picture there exists a unique pathway and a single energy barrier. Although in typical biomolecular bonds the interactions originate from a bunch of different atomic scale bonds which are distributed over many regions of large molecules, the bond rupture process is often assumed to exhibit first order kinetics which fits with the simplest picture.

We focus on the rupture dynamics in the presence of a monotonically increasing force. The thermally activated escape from a metastable state in the presence of an increasing force—in other words—in the presence of a time varying energy barrier is omnipresent in numerous physical, biological, and chemical systems. Examples are single molecular pulling experiments (Friedsam et al., 2003; Dudko et al., 2003, 2006; Neuert et al., 2007; Kumar and Li, 2010; Evans and Williams, 2002), protein unfolding (Kellermayer et al., 1997; Kumar and Li, 2010), friction phenomena at the nanoscale (Urbakh et al., 2004; Sills and Overney, 2003; Dudko et al., 2002), or the dynamics of colloids on surfaces (Dreyer et al., 2006), to name only a few.

Regarding the pulling experiments of weak bonds the dynamic force spectroscopy (DFS) (Evans, 2001; Dudko et al., 2003, 2006; Strunz et al., 1999) offers a powerful tool to probe the internal dynamics of the structure under study. A complete spectrum of the rupture force versus loading rate can be derived and the strength of a weak bond can be characterized by the relation between these two quantities (Garg, 1995; Dudko et al., 2003, 2006; Chen and Chu, 2005; Dias et al., 2005).

Experimentally, measurements of single bond strengths are usually performed with one of the following techniques (Merkel, 2001; Evans and Williams, 2002): First, the atomic force microscope (AFM), where the force is sensed by the deflection of a thin cantilever (Binnig et al., 1986; Florin et al., 1994; Rief et al., 1997). A second technique is biomembrane force probe (BFP). Here the force is sensed by the axial displacement of a glass microsphere glued to the pole of a micropiped pressurized blood cell (Evans et al., 1995). Another method to apply a force load uses laser optical tweezers where the force is sensed by the displacement of a microsphere trapped in a narrowly focused beam of laser light

(Ashkin, 1997; Smith et al., 1996). A comprehensive review on technical aspects of pulling experiments including also the application of magnetic forces was given by Merkel (Merkel, 2001). A very recent review focusing on the force-induced unfolding of polymers and stretching of DNA was given by Kumar et al. (Kumar and Li, 2010). A novel example of an experimental set up for rupture under a constant force ramp as well as constant force is given and discussed in the proceeding chapter 6.

Except for the last the above mentioned techniques act to a good approximation as soft harmonic springs. In general, for low probe stiffness the sensitivity in force measurements is high, but one encounters large thermal fluctuations in the position of the order of $\delta x^2 \sim k_B T/\kappa_p$ with κ_p being the spring constant of the probe. In the contrary limit of high probe stiffness the sensitivity in force is low and large fluctuation in the force are observed. However, even if the probe stiffness is well defined, the effective spring that pulls the bond may be different. This can be the case when the bond under study is linked to the substrate and/or the tip by flexible polymer linkers. They alter the bond strength under constant loading detachments in ways that are particularly important at low pulling speeds (Evans and Ritchie, 1999; Tshiprut et al., 2008). Let us consider for example the case when the bond is linked to a polymer which may be described as a soft harmonic spring with a stiffness κ_{poly}. Then, the combined effective spring that pulls the bond is

$$\frac{1}{\kappa_{eff}} = \frac{1}{\kappa_{poly}} + \frac{1}{\kappa_p}\,. \tag{5.1}$$

For highly flexible polymers, i.e., $\kappa_{poly} \ll \kappa_p$, their stiffness governs the effective spring constant and therewith dominates the rupture dynamics. Moreover, the effective stiffness can become a function of the applied force itself. Thus the existence of a polymer chain which is always present in such single molecule experiments, both as linker or as object of the study, has a distinct impact on the dynamics of the rupture process, and therefore, has to be taken into account when formulating a reasonable physical model.

In contrast to the huge amount of literature on the rupture of polymers, studies of force-induced bimolecular reactions are found only rarely (Beyer and Clausen-Schaumann, 2005). There, upon application of an external mechanical force, a strong covalent chemical bond is activated. The bond breakdown is referred to as mechanochemical rupture. In this realm the unbinding of biomolecules is sometimes called "noncovalent mechanochemistry" (Beyer and Clausen-Schaumann, 2005). In a mechanochemical reaction force causes a geometry change and may allow for a variety of reaction pathways. Consequently the validity of the idea of having only a single escape path is rather limited there.

From the theoretical point of view the rupture of a single bond under load can be mapped on the thermally activated escape process of a Brownian particle in a time-varying potential well. Albeit very rarely, excitations in the liquid environment occasionally contribute large transient impulses of force which added to an external force enable an escape of the confining potential barrier. Assuming first order kinetics, the survival probability of the bond follows

$$\frac{d\Phi_1(t)}{dt} = -\nu(f(t))\Phi_1(t)\,, \tag{5.2}$$

which has the formal solution

$$\Phi_1(t) = \mathrm{e}^{-\int_0^t \nu(t')dt'}\,. \tag{5.3}$$

The probability density of bond failure in a time interval $[t, t+dt]$ is thus

$$\mathcal{F}_1(t) = -\frac{d\Phi_1(t)}{dt}\,. \tag{5.4}$$

Since the force changes with time, i.e., $f = f(t)$, the probability density as a function of the force reads

$$\mathcal{F}_1(f) = \frac{\nu(f)}{\dot{f}(f)}\,\mathrm{e}^{-\int_0^f \frac{\nu(y)}{\dot{f}(y)}dy}\,. \tag{5.5}$$

Eq. (5.5) is also referred to as Kurkijärvi-Fulton-Dunkelberger formula (Garg, 1995) and can hardly be solved without any approximating assumptions on the unbinding dynamics. In the following we will confine ourself to the case of a constant loading rate, i.e., $\dot{f}(f) = \dot{f} = \text{const}$.

When the loading rate is very small there is sufficient time for rupture caused by thermal activation and low rupture forces are expected. On the other hand, if the loading rate is very high thermally activated escape is unlikely to happen and the rupture is mechanically induced. The typical rupture force approaches the maximum intrinsic binding force. Interestingly, in such situations, the activation barrier height is rather unimportant since the maximum intrinsic force is solely determined by the steepest gradient of the binding potential. However, for very high loading rates the crucial assumption which guarantees the validity of the kinetic equation (5.2) is not fulfilled, that is the adiabatic assumption that at each instant in time the density distribution within the metastable potential well is quasistatic. Therefore, we will refer to a loading rate as high, if it is high compared to an average loading rate in a real experiment but still such low that the kinetic equation (5.2) is valid and the rupture is thermally activated. Friddle (Friddle, 2008) calculated that for reasonable parameter values of loading rate and friction constant (of the order of those which we used in our simulations, see below) the mean position of the probability density distribution has a negligible lag of $\delta x = 10\,\mathrm{fm}$ compared to the static one. Thus the assumption of having a quasistatic distribution is fulfilled.

We remark that a more general approach would be

$$\frac{d\Phi_1(t)}{dt} = -\nu(t)\Phi_1(t) + \nu_{on}(t)\,(1-\Phi_1(t))\,, \tag{5.6}$$

with $\nu_{on}(t)$ taking into account the rate of re-crossing the potential barrier. It was discussed by Evans (Evans, 2001) that rebinding is especially important for stiff probe linkage. Furthermore, as shown by Dudko et al. (Dudko et al., 2003), rebinding is less important at higher loading rates. For some additional theoretical works which discuss the effects of rebinding on the rupture dynamics see (Tshiprut and Urbakh, 2009; Tshiprut et al., 2008; Friddle et al., 2008; Chen and Chu, 2005; Tang et al., 2007). Since we later work in a regime of higher loading rates we can neglect ν_{on}.

It was mentioned by Dudko et al. (Dudko et al., 2006) that in the validity region of the adiabatic assumption there is a relation between the outcome of experiments performed at a constant force ramp (measuring the probability density of rupture events $\mathcal{F}_1$), i.e., $f = \dot{f}t$, and those performed under a constant force (measuring the rate $\nu(f = \text{const})$).

From Eq. (5.2) one obtains the general relation

$$\nu(f) = \frac{\dot{f}\mathcal{F}_1(f)}{1 - \int_0^f \mathcal{F}_1(f')df'} \quad \forall \dot{f}\,. \tag{5.7}$$

Based on their simulations Dudko et al. showed the remarkably validity of the latter relation over 7 orders of magnitude of loading rates $\dot{f}$.

In the next section we present an approximate solution of the rupture problem which assumes that the energy barrier for bond dissociation along the reaction pathway decreases linearly with the applied force. As a result of this phenomenological theory, the most probable rupture force scales like $\ln(\dot{f})$, (Bell, 1978; Evans and Ritchie, 1997; Evans, 2001).

Based on the pioneering work of Garg (Garg, 1995) Dudko et al. (Dudko et al., 2003) approximated the free energy profile of a Morse binding potential close to its point of steepest descent up to the third order. This model-based ansatz revealed that the rupture force scales like $(\ln \dot{f})^{2/3}$. Later (2006), Dudko et al. generalized their approach and showed that the model-based theory can also be applied to cusp-shaped free energy profiles. In (2007), Lin et al. pointed out that both approaches, the phenomenological and the model-based theory, are valid in two asymptotic limits; the first one in the slow pulling regime while the second one is valid in the fast loading regime. One year later, in (2008), Friddle presented a unified model of dynamic rupture yielding in the asymptotic limiting regimes the corresponding well known expressions. However, all these approaches concentrate on the breakage of a single bond and neglect the collective fluctuations arising due to the coupled dynamics of a huge ensemble of monomers.

In contrast, we focus our interest on the dissociation process in chains of breakable bonds. Rings of identical bonds, i.e., a chain with periodic boundary conditions, have been studied theoretically in (Dias et al., 2005) as well as experimentally in (Severin et al., 2006). There, all bonds experience the same pulling force. Distinct to that we apply a constant loading at one of the terminals of the chain while the other end is grafted to a surface. For sufficiently small loading and short chains all bonds experience the same force and rupture can occur at an arbitrary bond with almost equal probability. For a longer chain or a high loading rate a force profile along the chain has to be taken into account (Lee and Thirumalai, 2004). Hence the tension in adjacent bonds differs. A few recent studies have theoretically treated tension propagation in stiff polymers under constant external fields (Hallatschek et al., 2005) and in semiflexible polymers under the application of a pulling force (Seifert et al., 1996). A rough description can be given in terms of the Rouse model. When pulling one terminal of the chain a force front propagates through the latter on a timescale of the order of the Rouse time. If bond rupture occurs on a timescale shorter than the Rouse time, only a part of the chain accounts for the rupture process. Thus the rupture force will be crucially affected by the number of monomers in the chain. Our aim is to point out this impact of the chain length on the rupture force of the system and to derive a sophisticated analytical description of the numerically obtained data. Furthermore, we intend to clarify how the non-Markovian fluctuations in the coupled chain system alter the rupture dynamics of the breakable bonds.

This chapter is structured as follows: In Sec. 5.2 we briefly present the theoretical description of the rupture dynamics of a single bond. In particular we focus on the

regime of high loading rates where the model-based approximation is valid. In Sec. 5.3 we pass to chains of coupled bonds and consider the cases of either one or all bonds being breakable. Although the non-Markovian influence of the coupled dynamics plays not the most dominant role in large ensembles of breakable bonds, it has a measurable effect on the rupture forces when there is only one breakable link in a long chain of monomers. This effect is studied in Sec. 5.4 numerically and qualitatively confirmed by theoretical considerations based on the results derived in the preceding chapter 4. In the following Sec. 5.5 we focus on chains which consist solely of breakable links. Especially for higher loading rates the force propagation is shown to play a dominant role in the rupture process and an analytical expression for the survival probability of the chain is given. Finally we summarize our results.

5.2. Single bond rupture

5.2.1. Bell's model

As mentioned in the introduction the Bell model (Bell, 1978) applies in the slow pulling regime. The interaction potential associated with $U(x)$ is characterized by three parameters: the distance from the metastable well (the potential minimum) to the barrier top $\Delta x_{\pm}^0 = x_+^0 - x_-^0$, the intrinsic energy barrier ΔE_0, and the steepest slope of the potential, i.e., the critical force associated with x_c, $f_c = U'(x_c)$. The schematic view of the free energy landscape is given in Fig. 5.1, panel (a). A rate $\nu(f = 0) = \nu_0$ determines the decay of the survival probability of the bond in the absence of the external force.

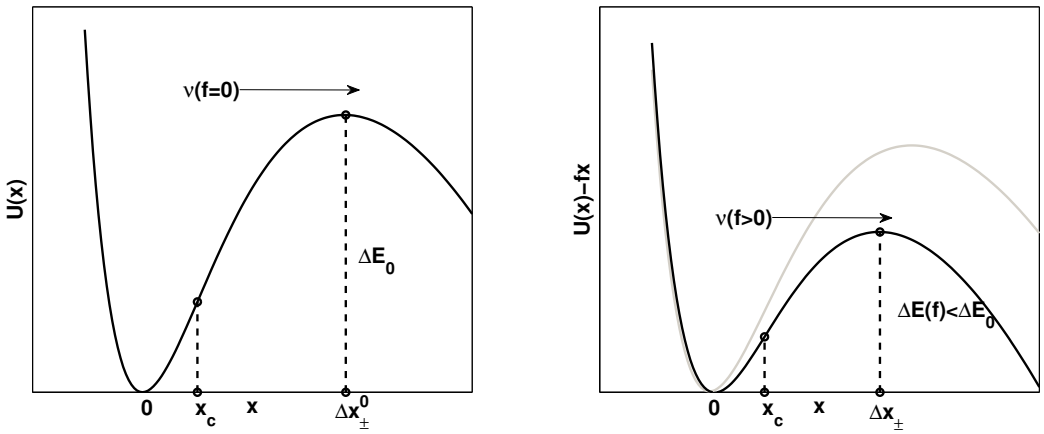

(a) (b)

Figure 5.1.: Schematic view of the single-well free energy landscape. Panel (a): Intrinsic free energy surface $U(x)$ with an activation barrier ΔE_0 situated at $\Delta x_{\pm}^0$ and the inflection point at x_c. Panel (b): Combined free energy surface $U(x) - fx$ with a decreased activation barrier $\Delta E(f) < \Delta E_0$. The location of the barrier is shifted towards the unchanged inflection point x_c.

In the presence of an external force the combined free energy surface

$$U_f(x) = U(x) - fx \tag{5.8}$$

is modified. As presented in Fig. 5.1, panel (b), the activation barrier is decreased and $\Delta x_\pm < \Delta x_\pm^0$ while x_c remains unchanged. Bell's assumption was, that for small forces, i.e., $f/f_c \ll 1$, the intrinsic well-to-barrier distance $\Delta x_\pm^0$ is only slightly perturbed. Hence, the main contribution to the change in the rate comes from the decrease of the activation barrier. Expanding the intrinsic potential $U(x)$ near $x_\pm^0$ we have

$$U(x) \simeq U(x_\pm^0) + \frac{1}{2}U''(x_\pm^0)\left(x - x_\pm^0\right)^2 . \tag{5.9}$$

The shifted well and barrier locations are determined by $U_f'(x_\pm) = 0$. They read

$$x_\pm = x_\pm^0 + \frac{f}{U''(x_\pm^0)} . \tag{5.10}$$

The activation barrier height is given by

$$\Delta E(f) = U_f(x_+) - U_f(x_-) = \Delta E_0 + \frac{f^2}{2}\left(\frac{1}{U''(x_-^0)} - \frac{1}{U''(x_+^0)}\right) . \tag{5.11}$$

Furthermore, $U''(x_\pm) \simeq U''(x_\pm^0)$ and we have in the leading order of f an expression for the rupture rate

$$\nu(f) = \nu_0 \, \mathrm{e}^{\frac{f\Delta x_\pm^0}{k_B T}} . \tag{5.12}$$

A generalization of the latter equation is the following (Dudko et al., 2008): Starting from the Pontryagin equation (4.15) in the limit of high barrier the mean first passage time to the barrier is given by

$$\tau(f) = \frac{\gamma}{k_B T}\int_{\text{barrier}} \mathrm{e}^{\frac{U_f(x)}{k_B T}}\, dx \int_{\text{well}} \mathrm{e}^{-\frac{U_f(x')}{k_B T}}\, dx' . \tag{5.13}$$

Taking the derivative of the logarithm of $\tau(f)$ with respect to f one has

$$\frac{d\ln(\tau(f))}{df} = \frac{1}{k_B T}\left(\langle x\rangle_{\text{well}} - \langle x\rangle_{\text{barrier}}\right) = -\frac{\langle \Delta x_\pm(f)\rangle}{k_B T} , \tag{5.14}$$

where the averages are performed with respect to all realizations of forces f. Integrating both sides of Eq. (5.14) with respect to f the force-dependent lifetime is

$$\tau(f) = \tau(0)\exp\left(-\frac{1}{k_B T}\int_0^f \langle \Delta x_\pm(f')\rangle\, df'\right) , \tag{5.15}$$

what reduces to the inverse rate given in Eq. (5.12) under the assumption that $\langle \Delta x_\pm(f)\rangle \simeq \Delta x_\pm^0$.

The bond is characterized by the most probable rupture force f_{max}. It is given by

$$\frac{d}{df}\left(\frac{d\Phi_1}{df}\right)_{f=f_{max}} = 0\,, \tag{5.16}$$

with the survival probability Φ_1 introduced in Eq. (5.3). If the loading rate $\dot{f}$ is a constant, the most probable rupture force can immediately be calculated and follows a logarithmic scaling as a function of the loading rate

$$f_{max} = \frac{k_B T}{\Delta x_\pm^0} \ln\left(\dot{f}\frac{\Delta x_\pm^0}{k_B T \nu_0}\right)\,. \tag{5.17}$$

Thus, from the experimental point of view, measurements at low forces, i.e., at very small loading rates, offer the possibility to derive the zero force rate ν_0 and the intrinsic well-to-barrier distance $\Delta x_\pm^0$. However, at larger loading rates and thus higher force values the validity of Eq. (5.17) is questionable and a model-based approach was shown to work accurately (Friddle, 2008; Dudko et al., 2006). Furthermore, in a later part of the chapter we study the impact of force propagation in a chain of breakable bonds which plays a remarkable role especially at higher loading rates.

5.2.2. Model-based approach

At higher forces all smooth combined free energy profiles can be represented by a cubic polynomial. Let us expand U_f around the inflection point x_c, $U''(x_c) = 0$. In the deterministic limiting case the bond would exactly break when the external force f approaches the value of the largest restoring potential force $f_c = U'(x_c)$.

Since the system is in contact to a heat bath bond rupture will occur at random and typically before f approaches f_c. Under the assumption that the rupture force f is close to f_c, we can expand the combined potential around the inflection point x_c to the third order in deviations from x_c

$$\tilde{U}_f(x) \simeq U_f(x_c) + \left(U'(x_c) - f\right)(x - x_c) + \frac{1}{2}U''(x_c)\,(x - x_c)^2 + \frac{1}{6}U'''(x_c)\,(x - x_c)^3\,. \tag{5.18}$$

Since $U'''(x_c) < 0$ we introduce $U_3 = -U'''(x_c)$. Furthermore, we use $U''(x_c) = 0$ and $U'(x_c) = f_c$ to obtain

$$\tilde{U}_f(x) \simeq U_f(x_c) + (f_c - f)\,(x - x_c) - \frac{1}{6}U_3\,(x - x_c)^3\,. \tag{5.19}$$

The local extrema are given by $\tilde{U}_f'(x_\pm) = 0$ and located at

$$x_\pm = x_c \pm \sqrt{\frac{2f_c}{U_3}}\sqrt{1 - \frac{f}{f_c}}\,, \tag{5.20}$$

and therewith the distance from the metastable well to the barrier top obeys

$$\Delta x_\pm = 2\sqrt{\frac{2f_c}{U_3}}\sqrt{1 - \frac{f}{f_c}}\,. \tag{5.21}$$

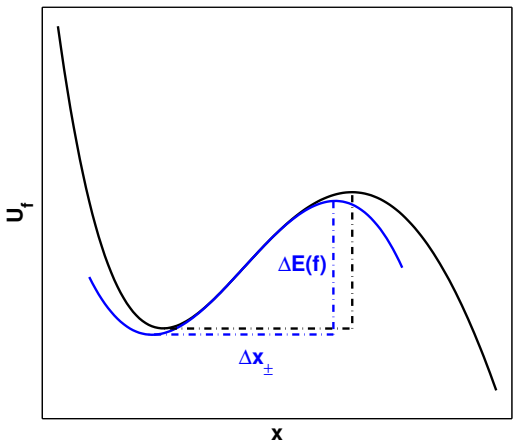

Figure 5.2.: Schematic representation of the cubic approximation of a free energy landscape. The solid black line corresponds to a combined energy profile of an intrinsic (Morse) potential and an additive force. The solid blue line corresponds to the cubic approximation. The horizontal dashed lines show the well-to-barrier distances for the true (black) and the approximated potential (blue). The vertical lines give the height of the activation barriers for the both cases, respectively.

The activation barrier height is

$$\Delta E = \frac{2}{3}\frac{(2f_c)^{3/2}}{\sqrt{U_3}}\left(1-\frac{f}{f_c}\right)^{3/2} . \tag{5.22}$$

Furthermore, the absolute value of the curvature at the extremal positions $x_\pm$ is given by

$$\omega = (2f_cU_3)^{1/4}\left(1-\frac{f}{f_c}\right)^{1/4} . \tag{5.23}$$

Note that the critical force f_c is related to the intrinsic barrier height $\Delta E(f\to 0)=\Delta E_0$ and the zero force value of $\Delta x_\pm(f\to 0)=\Delta x_\pm^0$ via

$$f_c = \frac{3\Delta E_0}{2\Delta x_\pm^0} . \tag{5.24}$$

A schematic representation of the cubic approximation is given in Fig. 5.2. Upon application of the external force the well-to-barrier distance shrinks and the activation barrier is lowered. In the case of a constant loading rate $\dot f = \text{const}$, the survival probability (5.2) obeys

$$\Phi_1(f) = \exp\left(-\frac{1}{\dot f}\int_0^f \nu(f')df'\right) , \tag{5.25}$$

with the Kramers escape rate $\nu(f)$ (being the inverse first passage time introduced in

Eq. (4.18))

$$\nu(f) = \frac{\sqrt{2f_c U_3}}{2\pi\gamma}\sqrt{1-\frac{f}{f_c}}\exp\left(-\frac{\Delta E_0}{k_B T}\left(1-\frac{f}{f_c}\right)^{3/2}\right). \tag{5.26}$$

Since

$$\nu(f\to 0) = \nu_0 = \frac{\sqrt{2f_c U_3}}{2\pi\gamma}\exp\left(-\frac{\Delta E_0}{k_B T}\right), \tag{5.27}$$

the rupture rate for a given force f is

$$\nu(f) = \nu_0\sqrt{1-\frac{f}{f_c}}\exp\left(\frac{\Delta E_0}{k_B T}\left(1-\left\{1-\frac{f}{f_c}\right\}^{3/2}\right)\right). \tag{5.28}$$

Note that the rate incorrectly tends to approach 0 as $f \to f_c$. This is due to the fact that the Kramers rate is solely valid in the high barrier limit. With this expression for the rate the integral in Eq. (5.25) can be solved explicitly yielding

$$\Phi_1(f) = \exp\left(-\frac{2f_c k_B T}{3\Delta E_0 \dot{f}}\nu_0\exp\left(\frac{\Delta E_0}{k_B T}\right)\exp\left\{-\frac{\Delta E_0}{k_B T}\left(1-\frac{f}{f_c}\right)^{3/2}\right\} + \frac{2f_c k_B T}{3\Delta E_0 \dot{f}}\nu_0\right). \tag{5.29}$$

We define

$$w = \frac{\Delta E_0}{k_B T} \quad \text{and} \quad v = \frac{2f_c}{3w}\nu_0\exp\left(\frac{\Delta E_0}{k_B T}\right). \tag{5.30}$$

With these abbreviations the survival probability reads

$$\Phi_1(f) = \exp\left(-\frac{v}{\dot{f}}\exp\left(-w\left(1-\frac{f}{f_c}\right)^{3/2}\right) + \frac{v}{\dot{f}}\,\mathrm{e}^{-w}\right). \tag{5.31}$$

The probability density of bond failure in a force interval $[f, f+df]$ is then

$$\mathcal{F}_1(f) = \frac{3vw}{2f_c\dot{f}}\sqrt{1-\frac{f}{f_c}}\exp\left[-w\left(1-\frac{f}{f_c}\right)^{\frac{3}{2}} - \frac{v}{\dot{f}}\left(\exp\left[-w\left(1-\frac{f}{f_c}\right)^{\frac{3}{2}}\right] - \mathrm{e}^{-w}\right)\right]. \tag{5.32}$$

Following (Garg, 1995) the asymptotic expression for the mean rupture force is

$$\langle f\rangle \simeq f_c\left(1-\left(\frac{\ln\left(v/\dot{f}\right)+\gamma_{EM}}{w}\right)^{2/3}\right), \tag{5.33}$$

with the Euler-Mascheroni constant $\gamma_{EM} \simeq 0.577216$. The most probable rupture force is to a good approximation given by the above expression with γ_{EM} set to zero, thus

$$f_{max} \simeq f_c\left(1-\left(\frac{\ln\left(v/\dot{f}\right)}{w}\right)^{2/3}\right). \tag{5.34}$$

Note that based on this expression f_{max} becomes negative for $\dot{f} < \nu_0 k_B T/\Delta x_{\pm}^0$. Thus the model based approach turns out to be inappropriate in the limit of small loading rates.

In order to compare this expression with the corresponding one for the Bell model we give f_{max} in terms of the intrinsic parameters of the free energy landscape

$$f_{max} \simeq f_c \left(1 - \left(\frac{k_B T}{\Delta E_0} \ln\left(\frac{k_B T \nu_0}{\Delta x_\pm^0 \dot{f}} \, \mathrm{e}^{\Delta E_0 / k_B T}\right)\right)^{2/3}\right) . \tag{5.35}$$

In contrast to the logarithmic scaling predicted by the Bell model, the model based approach predicts that the most probable rupture force of the bond scales as $f_{max} \propto \left[\ln(\mathrm{const}/\dot{f})\right]^{2/3}$. This scaling was experimentally verified in the higher loading rate limit. From the experimentalist's point of view the ultimate goal is to derive the intrinsic parameter values of the free energy landscape under study. In this realm it was remarked by Dudko et al. that the barrier height and well-to-barrier distance appearing in Eq. (5.35) are only apparent parameters and do not necessarily coincide with the true ones.

Let us briefly consider the cusp-shaped potential and finally derive more general expressions for the mean and most probable rupture forces, which were first given by Dudko et al. (Dudko et al., 2006). Distinguished to the cubic energy profile the cusp-shaped potential given in Eq. (2.38) does not possess a smooth barrier and no inflection point x_c. Upon applying an external force the potential minimum $x_-(f)$ approaches the fixed position of the barrier x_+. The curvature at the potential well remains unchanged, i.e., $U_f'' = \kappa = \mathrm{const}$. Thus, one easily finds $f_c = \kappa x_+$ and an expression for the distance from the metastable well to the barrier top

$$\Delta x_\pm = \frac{f_c}{\kappa}\left(1 - \frac{f}{f_c}\right) . \tag{5.36}$$

The activation barrier height is

$$\Delta E(f) = \frac{f_c^2}{2\kappa}\left(1 - \frac{f}{f_c}\right)^2 . \tag{5.37}$$

The Kramers escape rate is equal to the inverse mean first passage time given in Eq. (4.21).

$$\nu(f) = \nu_0 \left(1 - \frac{f}{f_c}\right) \exp\left(\frac{\Delta E_0}{k_B T}\left(1 - \left\{1 - \frac{f}{f_c}\right\}^2\right)\right) , \tag{5.38}$$

with

$$\nu_0 = \frac{\kappa}{\gamma}\sqrt{\frac{\Delta E_0}{\pi k_B T}} \exp\left(-\frac{\Delta E_0}{k_B T}\right) . \tag{5.39}$$

It is now straightforward to derive the appropriate expressions for the survival probability $\Phi_1(f)$ and the rupture probability density $\mathcal{F}_1(f)$.

Moreover, there exists a unified form of these expression for both the cubic and cusp-shaped energy profiles. Exchanging the v in Eq. (5.30) for

$$v = b_m \frac{f_c}{w} \nu_0 \exp\left(\frac{\Delta E_0}{k_B T}\right) , \tag{5.40}$$

with $b_m = 1/2$ for the cusp potential and $b_m = 2/3$ for the cubic one, the survival

probability reads

$$\Phi_1(f) = \Phi_0 \exp\left(-\frac{v}{\dot{f}} \exp\left(-w\left(1-\frac{f}{f_c}\right)^{1/b_m}\right)\right), \tag{5.41}$$

with

$$\Phi_0 = \exp\left(\frac{v}{\dot{f}}\,\mathrm{e}^{-w}\right). \tag{5.42}$$

The probability density of bond failure in a force interval $[f, f+df]$ is

$$\mathcal{F}_1(f) = \Phi_0 \frac{vw}{b_m f_c \dot{f}} \left(1-\frac{f}{f_c}\right)^{1/b_m-1} \exp\left[-w\left(1-\frac{f}{f_c}\right)^{1/b_m} - \frac{v}{\dot{f}}\,\mathrm{e}^{-w\left(1-\frac{f}{f_c}\right)^{1/b_m}}\right]. \tag{5.43}$$

Hence the asymptotic expression for the mean rupture force is

$$\langle f \rangle \simeq f_c \left(1-\left(\frac{\ln\left(v/\dot{f}\right)+\gamma_{EM}}{w}\right)^{b_m}\right). \tag{5.44}$$

The most probable rupture force is to a good approximation given by

$$f_{max} \simeq f_c \left(1-\left(\frac{\ln\left(v/\dot{f}\right)}{w}\right)^{b_m}\right). \tag{5.45}$$

In the following we will consider the rupture of a single bond described by either a Morse or a double-well potential (DW-potential) in more detail. When we pass to the description of the rupture process of multiple bonds in series these two potentials will hold as parameterizations of the binding potentials. Since we will come back to the cusp-shaped potential in a later part of this chapter it was presented here for completeness.

Example 1: The Morse potential

Let us now derive expressions for the Morse potential introduced in Eq. (2.40). The combined free energy profile reads

$$U_f(x) = D_0\left(1-\mathrm{e}^{-\alpha(x-l_0)}\right)^2 - \dot{f}tx\,. \tag{5.46}$$

The inflection point is found at $x_c = l_0 + \ln(2)/\alpha$ and the critical force is $f_c = D_0\alpha/2$. For an external force growing linearly in time it is possible to deduce the well-to-barrier distance and activation barrier height in a closed form being

$$\Delta x_\pm = \frac{2}{\alpha}\ln\left(1 \pm \sqrt{1-\frac{f}{f_c}}\right) \tag{5.47}$$

and

$$\Delta E_{full}(f) = U_f(x_+) - U_f(x_-) = D_0\sqrt{1-\frac{f}{f_c}} + \frac{f}{\alpha}\ln\left(\frac{1-\sqrt{1-\frac{f}{f_c}}}{1+\sqrt{1-\frac{f}{f_c}}}\right), \tag{5.48}$$

respectively. However, only the cubic approximation in the vicinity of the inflection point allows for the explicit calculation of the survival probability of the bond. We derive

$$\Delta x_\pm = \frac{2}{\alpha}\sqrt{1-\frac{f}{f_c}} \tag{5.49}$$

and

$$\Delta E(f) = \frac{2}{3}D_0\left(1-\frac{f}{f_c}\right)^{\frac{3}{2}}. \tag{5.50}$$

Note that for $f \to 0$ the values of ΔE_0 in Eqs. (5.48) and (5.50) differ by a factor of 2/3. Therefore, the apparent barrier height ΔE_0 deduced from a hypothetical experiment does not coincide with the true dissociation energy D_0.

From Eq. (5.27) we obtain (with $U_3 = D_0\alpha^3$) the intrinsic Arrhenius prefactor

$$\nu_0 \exp\left(\frac{\Delta E_0}{k_B T}\right) = \frac{D_0\alpha^2}{2\pi\gamma}, \tag{5.51}$$

and finally

$$v = \frac{D_0\alpha^3 k_B T}{4\pi\gamma} \quad \text{and} \quad w = \frac{2D_0}{3k_B T}. \tag{5.52}$$

Together with the Eqs. (5.31), (5.32), and (5.34) the survival probability $\Phi_1(f)$, the rupture force probability density $\mathcal{F}_1(f)$, and the most probable rupture force are fully determined.

We compare the predictions of the model based approach with the outcome of Brownian dynamics simulations. The corresponding overdamped Langevin equation for the reaction coordinate x of a single bond reads

$$\gamma\dot{x} = -\frac{\partial U_f(x)}{\partial x} + \sqrt{2\gamma k_B T}\xi(t), \tag{5.53}$$

with U_f being the combined free energy potential, γ the constant friction parameter, k_B the Boltzmann constant and ξ Gaussian white noise with zero mean, hence

$$\langle\xi(t)\rangle = 0 \quad \text{and} \quad \langle\xi(t)\xi(t')\rangle = \delta(t-t'). \tag{5.54}$$

Bond rupture was considered as have taken place when the reaction coordinate x passed the location of the activation barrier of the breakable bond x_+[1]. The range of chosen parameter values covers covalent to noncovalent bonds, i.e., $D_0 \propto o(10^{-19})$ J and $\alpha \propto o(10)$ 1/nm.

[1] For numerical simulations it is important to bypass stiff terms in Eq. (5.53) which might appear depending on the values of D_0 and α. Thus the equation of motion can be casted in a dimensionless rescaled form. With $x \to \alpha x$, $t \to 2\alpha^2 D_0/\gamma t$, $\dot{f} \to \gamma/(4D_0^2\alpha^3)\dot{f}$, and $D = k_B T/(2D_0)$ the Langevin equation reads $\dot{x} = -(1-\exp(-x))\exp(-x) + \dot{f}t + \sqrt{2D}\xi(t)$. The overdamped Brownian dynamics simulations were performed using a Heun integration scheme.

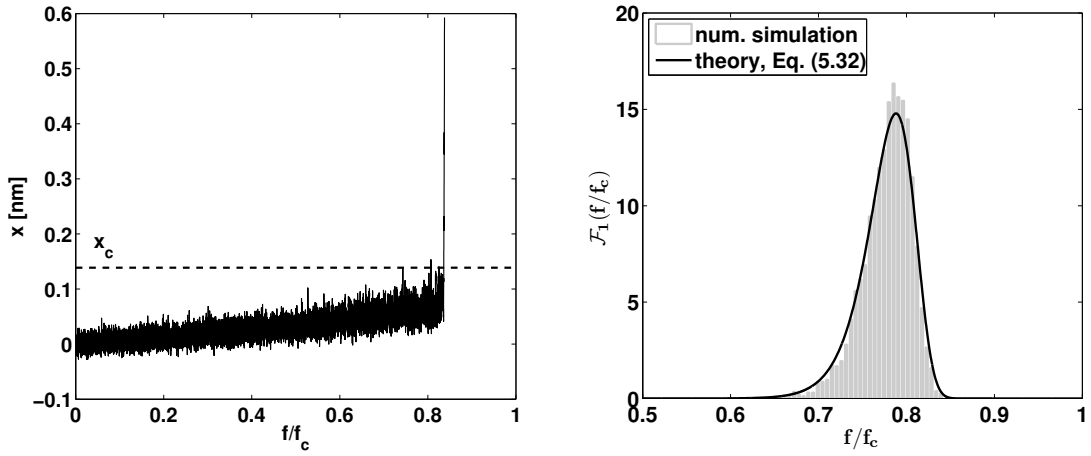

(a) (b)

Figure 5.3.: Panel (a): Trajectory of one realization of a Morse bond rupture. Superimposed is the location of the inflection point x_c (dashed line). The parameter values are $D_0 = 800\,\mathrm{pNnm}$, $\alpha = 5\,\mathrm{nm}^{-1}$, $k_BT = 4\,\mathrm{pNnm}$, $\gamma = 2\times10^{-6}\,\mathrm{kg/s}$ and $\dot{f} = 2\times10^{-6}\,\mathrm{N/s}$. Panel (b): Probability density distribution $\mathcal{F}_1(f/f_c)$. Gray bars represent the outcome of numerical simulations while the solid black line is derived from Eq. (5.32) with values of v and w taken from Eq. (5.52). The parameter values are $D_0 = 350\,\mathrm{pNnm}$, $\alpha = 10\,\mathrm{nm}^{-1}$, $k_BT = 4\,\mathrm{pNnm}$, $\gamma = 2\times10^{-6}\,\mathrm{kg/s}$, and $\dot{f} = 2\times10^{-7}\,\mathrm{N/s}$.

Furthermore, the solvent friction lies in the range of $\gamma = 2\times10^{-8}\,\mathrm{kg/s}$ to $\gamma = 2\times10^{-6}\,\mathrm{kg/s}$. These values are comparable with those in the literature (Evans and Ritchie, 1997; Marrink et al., 1998; Kühner and Gaub, 2006; Friddle, 2008; Izrailev et al., 1997; Friedsam et al., 2003; Cui et al., 2006; Berger et al., 1997).

In Fig. 5.3 we present the typical rupture dynamics of a Morse bond loaded under a force ramp with $\dot{f} = \mathrm{const}$. In panel (a) we depict a trajectory of one particular realization of rupture. Due to the impact of the external forcing the coordinate evolving most of the time in the close vicinity of the potential minimum x_- moves towards the inflection point x_c. Eventually the trapped Brownian coordinate escapes from the bounded state. Apparently, rupture happens when x_- is close to x_c. Thus the extrema are close to the inflection point what substantiates the assumptions made in the derivation of the model based approach. In panel (b) we depict $\mathcal{F}_1(f/f_c)$, that is the probability density distribution of rupture forces. Gray bars represent the outcome of numerical simulations while the solid black line is derived from Eq. (5.32) with values of v and w taken from Eq. (5.52). Both theory and simulations agree very well. The distribution is skewed to the left, hence $f_{max} > \langle f \rangle$.

The scaling of the most probable rupture force with changing $\dot{f}$ is shown in Fig. 5.4. The solid line represents the prediction of Eq. (5.34) and the symbols were obtained in Brownian dynamics simulations. There are deviations in the limit of small loading rates. For these loading rates the cubic approximation becomes worse since the rupture forces become smaller. However, the numerically obtained overall scaling is well described by the theory. In the opposite limit of very large $\dot{f}$ and thus low activation energy barriers the validity of the Kramers rate approach becomes questionable and deviations appear,

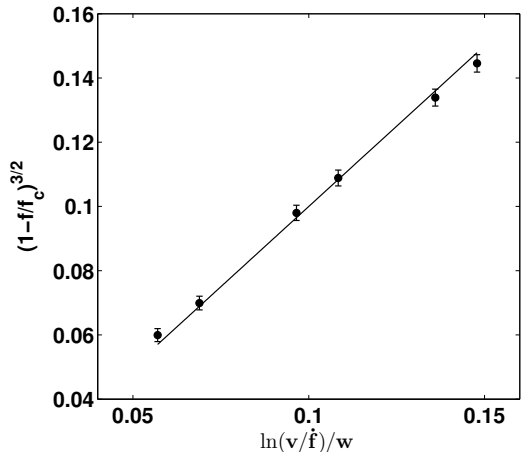

Figure 5.4.: The most probable rupture force f_{max} as a function of the loading rate $\dot{f}$. The solid line is calculated using Eq. (5.34). Symbols represent the outcome of numerical simulations. The parameter values are the same as in Fig. 5.3, panel (b), except for $\dot{f}$. $\dot{f}$ ranges from $2 \times 10^{-9}\,\mathrm{N/s}$ to $2 \times 10^{-6}\,\mathrm{N/s}$.

too.

Since the escape rate for a given force f depends exponentially on the barrier height we have a look at the ratio of the barrier height calculated from Eq. (5.48) (ΔE_{full}, being the true one) and the approximated one following Eq. (5.50), both calculated at $f = f_{max}$. So we can predict parameter value regions in which the theory and the numerical simulations are expected to agree. A ratio far away from unity will necessarily cause an inappropriate description of the rupture dynamics. The ratio reads

$$\frac{\Delta E_{full}}{\Delta E} = \frac{3}{4}\left[2\left(\frac{\ln(\tilde{v})}{w}\right)^{-2/3} + \left(\frac{w}{\ln(\tilde{v})} - \left(\frac{\ln(\tilde{v})}{w}\right)^{-\frac{1}{3}}\right)\ln\left(\frac{1-\left(\frac{\ln(\tilde{v})}{w}\right)^{1/3}}{1+\left(\frac{\ln(\tilde{v})}{w}\right)^{1/3}}\right)\right]. \qquad (5.55)$$

In Fig. 5.5 we present the relative error $\Delta E_{full}/\Delta E$ of the barrier height at f_{max} as a function of the parameters $\tilde{v} = v/\dot{f}$ and w. For small values of w, that means low intrinsic activation barriers, and growing value of $\tilde{v}$, i.e., for smaller values of the loading rate $\dot{f}$, the ratio becomes large. In the opposite limit the ratio is close to unity and the analytical theory presented in this section is expected to work accurately.

Example 2: The double-well potential

A mathematical model proposed to describe a binding potential in a real experiment relies on additional assumptions and can at best be a sufficient parameterization of the bond under study. Therefore, our intention is to show that the model based approach enables us to predict the outcome of numerical simulations at least for one other binding potential. We chose the DW-potential which was introduced in Eq. (2.42) and has the following

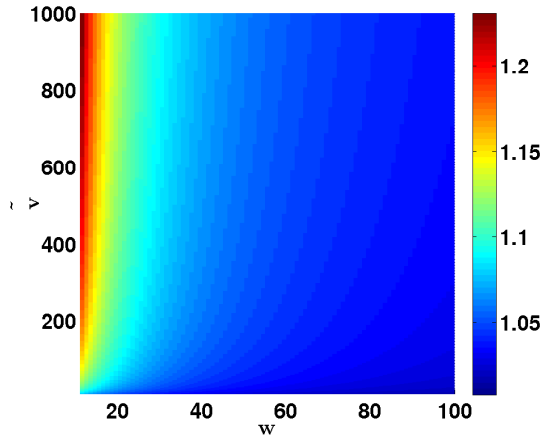

Figure 5.5.: The relative error $\Delta E_{full}/\Delta E$ of the barrier height at f_{max} as a function of the parameters $\tilde{v} = v/\dot{f}$ and w for a Morse potential.

combined free energy profile

$$U_f(x) = \frac{a}{4}x^4 - \frac{b}{2}x^2 - \dot{f}tx\,. \tag{5.56}$$

For zero force the extremal points are situated at

$$x_+^0 = 0 \quad \text{and} \quad x_-^0 = \pm\sqrt{b/a}\,. \tag{5.57}$$

The inflection points are found at $x_c = \pm\sqrt{b/(3a)}$.

Within the cubic approximation using Eqs. (5.21), (5.22), and (5.23) we derive for the combined free energy profile $U_f(x) = U_{DW}(x) - fx$ the well-to-barrier distance

$$\Delta x_\pm = 2\sqrt{\frac{2b}{9a}\left(1 - \frac{f}{f_c}\right)}\,, \tag{5.58}$$

the effective barrier height

$$\Delta E(f) = \frac{b^2}{a}\left(\frac{2}{3}\right)^{\frac{7}{2}}\left(1 - \frac{f}{f_c}\right)^{3/2}\,, \tag{5.59}$$

as well as the critical force

$$f_c = \sqrt{\frac{4b^3}{27a}}\,, \tag{5.60}$$

respectively. Solving the Kramers rate equation we obtain the parameters v and w as

$$v = \frac{\sqrt{3ab}k_BT}{2\pi\gamma\dot{f}} \quad \text{and} \quad w = \frac{b^2}{ak_BT}\left(\frac{2}{3}\right)^{7/2}\,. \tag{5.61}$$

The double-well interaction does not allow for a complete rupture of the bond. However,

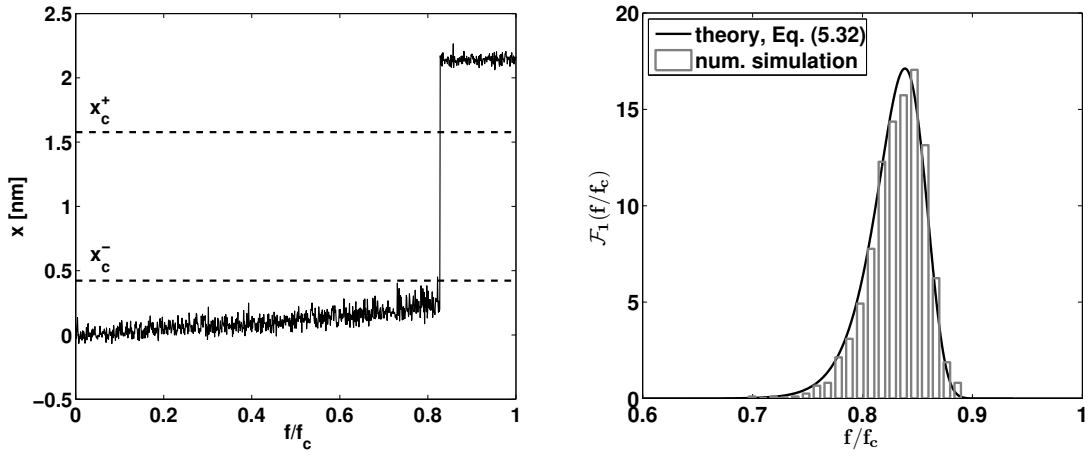

(a) (b)

Figure 5.6.: Panel (a): Trajectory of one realization of a DW bond rupture. Superimposed are the locations of the two inflection points x_c (dashed lines). The parameter values are $a = 1.28\,\mathrm{nNnm}^{-3}$, $b = 1.28\,\mathrm{nNnm}^{-1}$, $k_BT = 4\,\mathrm{pNnm}$, $\gamma = 1 \times 10^{-8}\,\mathrm{kg/s}$, and $\dot{f} = 1 \times 10^{-6}\,\mathrm{N/s}$. Panel (b): Probability density distribution $\mathcal{F}_1(f/f_c)$. Gray bars represent the outcome of numerical simulations while the solid black line is derived from Eq. (5.32) with values of v and w taken from Eq. (5.61). The parameter values are the same as in panel (a).

it mimics the change of state of a hypothetical bond (when initially situated in one of the two minima) or the rupture dynamics when the energy landscape of the bond under study is well described by such potential in the vicinity of the activation barrier.

We compare the predictions made by the theory with the outcome of Brownian dynamics simulations of the overdamped Langevin equation (5.53)[2]. In Fig. 5.6 we present the typical rupture dynamics of a DW bond loaded under a force ramp with $\dot{f} = \text{const}$. In panel (a) we depict a trajectory of one particular realization of rupture. One well is initially located at zero and the force is applied in positive x-direction. Due to the impact of the external forcing the coordinate evolving most of the time in the close vicinity of the potential minimum x_- moves towards the left inflection point x_c^-. Eventually the trapped Brownian coordinate jumps from the bounded state in the vicinity of x_- to the other minimum. A jump back is rather unlikely to happen since the activation barrier in the backward direction is much higher due to the bias introduced by the external force. In panel (b) we depict $\mathcal{F}_1(f/f_c)$, that is the probability density distribution of the activation forces. Gray bars represent the outcome of numerical simulations while the solid black line is derived from Eq. (5.32) with values of v and w taken from Eq. (5.61). Both theory and simulations agree very well. Again, as for the Morse bond, the distribution is skewed

[2]The equation of motion can be casted in a dimensionless rescaled form. With $x \to x\sqrt{a/b}$, $t \to t\,b/\gamma$, $\dot{f} \to \dot{f}\,\gamma\sqrt{a}/b^{5/2}$, and $D = k_BTa/b^2$ the Langevin equation reads $\dot{x} = -x^3 + x + \dot{f}t + \sqrt{2D}\xi(t)$. Bond rupture was considered as have taken place when the reaction coordinate x passed the location of second inflection point x_c^+. The overdamped Brownian dynamics simulations were performed using a Heun integration scheme.

to the left, hence $f_{max} > \langle f \rangle$.

5.3. New aspects arising from the chain dynamics

In application to polymers the theoretical description of bond failure concentrates on breaking of one bond (presumably the weakest one) and fully disregards the chain structure of the system. On the other hand, the situation of breaking of a more or less homogeneous chain has hardly been considered. Thus, Ref. (Dias et al., 2005) discusses breaking of a ring of identical bonds, i.e., of a chain with periodic boundary conditions. An experimental realization of such a set up is possible (Severin et al., 2006) and discussed in chapter 6. However, the typical case corresponds to a linear chain pulled at one of its ends with another end kept fixed. The case of having a chain of breakable bonds was realized experimentally by Embrechts et al. (Embrechts et al., 2008). As discussed in the beginning polymer linker molecules may drastically affect the rupture dynamics since they cause a loading rate $\dot{f} \neq$ const. Although a number of studies focus on the impact of these linker molecules describing their force-extension characteristics by using those of the wormlike chain or the FJC (freely jointed chain), they concentrate on the breakage of a single bond, see (Evans and Ritchie, 1999) and references therein.

Compared to this single bond breaking, the existence of the chain introduces two new aspects into rupture dynamics: the non-Markovian fluctuations in the barrier crossing and the slow-down of the force propagation to the breakable bond. The relative impact of both these processes is investigated, and the second one is found to be the most important at higher loading rates $\dot{f}$. The most probable rupture force is found to decrease with the number of bonds as $f_{max} \propto -\left[\ln(\text{const}N/\dot{f})\right]^{2/3}$ for short chains and finally for longer ones to approach a saturation value independent of N. In between these limiting cases we observe a non-monotonic scaling of the most probable rupture force which attains a minimal value depending on the loading rate.

In the common literature, the non-Markovian fluctuations in the coupled chain system have so far been neglected in describing the failure of bonds when linked in series. We show that especially for soft bonds and long chains with long correlation times the non-Markovian dynamics may affect the rupture of bonds.

The aim of our work is to investigate the impact of the chain length on the rupture force both numerically and analytically. Except for the binding potentials our model will correspond to a chain of monomers which is closely related to the Rouse one introduced in chapter 2: We disregard hydrodynamical interactions and describe the interaction of the monomers with the heat bath via independent white noises.

To get insight into the role of the chain we consider first the situation when only one bond is breakable and take this bond to be either at the fixed or at the pulled end of the chain. Therefore, we study numerically a chain with one breakable Morse bond; all the other bonds are considered as perfect harmonic springs with a coupling constant corresponding to $U''(x_-^0) = \kappa = 2D_0\alpha^2$. The system of coupled overdamped Langevin equations is either

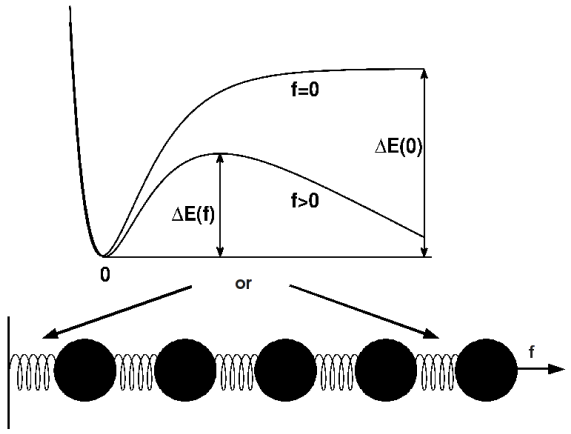

Figure 5.7.: Rupture of a single breakable bond within a chain of $N-1$ harmonic springs. Schematic sketch of the grafted chain with one breakable bond either situated at the pulled terminal ($n = N$) or close to the fixed end ($n = 1$) of the chain.

$$\begin{aligned}
\gamma\dot{x}_1 &= -2D_0\alpha\left(1-e^{-\alpha x_1}\right)e^{-\alpha x_1} + \kappa\left(x_2 - x_1\right) + \sqrt{2\gamma k_B T}\xi_1 \\
\gamma\dot{x}_n &= \kappa\left(x_{n+1} + x_{n-1} - 2x_n\right) + \sqrt{2\gamma k_B T}\xi_n\,, \quad 1 < n < N \\
\gamma\dot{x}_N &= -\kappa\left(x_N - x_{N-1}\right) + \sqrt{2\gamma k_B T}\xi_N + \dot{f}t\,,
\end{aligned} \tag{5.62}$$

when the breakable bond is situated at the grafted terminal, or

$$\begin{aligned}
\gamma\dot{x}_1 &= \kappa\left(x_2 - 2x_1\right) + \sqrt{2\gamma k_B T}\xi_1 \\
\gamma\dot{x}_n &= \kappa\left(x_{n+1} + x_{n-1} - 2x_n\right) + \sqrt{2\gamma k_B T}\xi_n\,, \quad 1 < n < N-1 \\
\gamma\dot{x}_{N-1} &= \kappa\left(x_{N-2} - x_{N-1}\right) + 2D_0\alpha\left(1-e^{-\alpha(x_N - x_{N-1})}\right)e^{-\alpha(x_N - x_{N-1})} + \sqrt{2\gamma k_B T}\xi_{N-1} \\
\gamma\dot{x}_N &= -2D_0\alpha\left(1-e^{-\alpha(x_N - x_{N-1})}\right)e^{-\alpha(x_N - x_{N-1})} + \sqrt{2\gamma k_B T}\xi_N + \dot{f}t\,,
\end{aligned} \tag{5.63}$$

when the force is applied directly to the Morse bond. The polymer chain defined in this way is sketched in Fig. 5.7.

The influence of the chain on the breaking properties of the bond is twofold: First, due to the coupled dynamics, the overall noise force acting on the monomer stems from the whole rest of the chain and is non-Markovian on timescales shorter than the longest relaxation time of the chain which is of the order of the Rouse time of a grafted chain τ_1^g given in Eq. (2.37)[3]. Second, since the force does not propagate immediately through the chain, a bond at the grafted end of the chain experiences at the beginning the force smaller than the one that is applied at the pulled terminal. The rupture of a single breakable Morse

[3] Although nonlinear binding potentials may alter the correlation times, their scaling properties remain unchanged. Therefore, especially at low temperatures when the motion of the monomers proceeds most of the time close to the quadratic minima of the bond energies, τ_1^g gives the timescale of relaxations also in the chain with nonlinear interactions. This was shown in chapter 3.

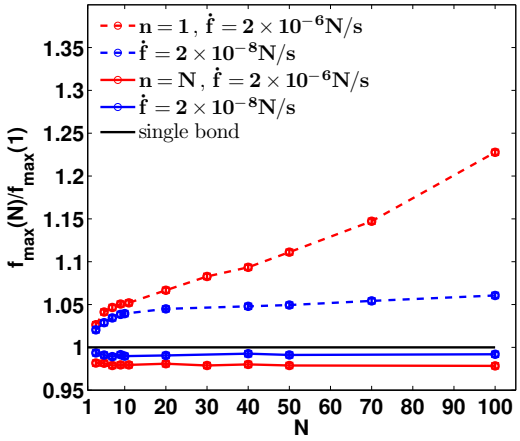

Figure 5.8.: Rupture of a single breakable bond within a chain of $N-1$ harmonic springs. Most probable rupture force f_{max} for a single breakable Morse bond situated at the fixed (dashed lines) or at the pulled end (solid lines) of a chain of $N-1$ harmonic springs as a function of N. Red lines correspond to $\dot{f} = 2\times10^{-6}\,\mathrm{N/s}$ while the blue lines correspond to $\dot{f} = 2\times10^{-8}\,\mathrm{N/s}$. The solid black line shows the value of f_{max} for a single bond. The parameter values are $D_0 = 350\,\mathrm{pNnm}$, $k_BT = 4\,\mathrm{pNnm}$, and $\alpha = 10^{10}\,\mathrm{m}^{-1}$, giving the parameter values $v = 7/(4\pi)\times10^{-4}\,\mathrm{s/N}$ and $w = 175/3$. Error bars indicate the uncertainty due to the binning of numerical data.

bond at the fixed wall is affected both by the non-Markovian fluctuations and by the force profile propagation. In contrast, a bond situated at the pulled terminal of the chain feels the instantaneous force, and the deviations from the single-bond rupture statistics are solely due to the non-Markovian character of the noise. In Fig. 5.8 we present the most probable rupture force f_{max} as a function of the number of bonds in the chain N for both situations, revealing quite different behavior. Thus, for a breakable bond at a wall f_{max} (dashed lines) lies well above the reference value for a single bond (solid black line), while for the breakable bond at a pulled terminal f_{max} lies slightly below the value for the single bond (colored solid lines).

We conclude that non-Markovian fluctuations have a distinct influence on the rupture dynamics of bonds at different locations in the chain. Seemingly these fluctuations slightly accelerate the bond breakage at the pulled chain end and cause a delay for the bond at the grafted terminal. This is in agreement with our observation in chapter 4 where we found that the mean first passage times of chain fragmentation were substantially higher at the grafted chain end. However, since the delay of rupture at this terminal is the stronger the higher is the loading rate $\dot{f}$, our observation for the longer chains, i.e., $N > 20$ for $\dot{f} = 2\times10^{-6}N/s$, is expected to be mostly caused by the retarded force propagation.

Let us specify how the regimes of short and long chains can be distinguished. Concerning the force propagation, for sufficiently small loading rates and/or short chains, i.e., $f/\dot{f} < \tau_1^g$, each bond experiences the same force and the rupture can occur at an arbitrary bond. To a good approximation the longest relaxation time of the chain is $\tau_1^g \simeq 4\gamma N^2/(\kappa\pi^2)$ (compare Eq. (2.37)). Thus assuming the rupture force to be of the order of f_{max} the

force propagation will play a minor role for chain lengths $N^2 \ll \kappa\pi^2 f_{max}/(4\gamma\dot{f})$ or loading rates $\dot{f} \ll \kappa\pi^2 f_{max}/(4\gamma N^2)$. In the contrary situation, for a longer chain and/or for a high loading rate, i.e., $f/\dot{f} \gg \tau_1^g$, the actual force profile along the chain has to be taken into account. When pulling at one terminal of the chain the time of the order of the longest relaxation time of the grafted chain τ_1^g is necessary for the tension to propagate through the chain; hence the forces in adjacent bonds differ. If bond rupture occurs on a timescale shorter than this relaxation time, only a part of the chain is under tension and accounts for the rupture process. Thus the rupture force will be crucially affected by the number of monomers in the chain. Depending on the system parameters this is the case when $N^2 \gtrsim \kappa\pi^2 f_{max}/(4\gamma\dot{f})$ or $\dot{f} \gtrsim \kappa\pi^2 f_{max}/(4\gamma N^2)$.

5.4. Chain with a single breakable bond

In order to gather deeper insight into the role of the non-Markovian fluctuations in the chain rupture kinetics we study in this part of the chapter chains with a single breakable bond situated at one of the two terminals of the grafted chain. Later we consider chains consisting solely of breakable bonds.

Above we have shown that non-Markovian fluctuations slightly accelerate the bond breakage at the pulled chain end and cause a delay for the bond at the grafted terminal. Additionally the rupture force there is increased due to the retarded force propagation. For very long chains the force propagation into the chain is such dominant that one may neglect the collective fluctuations. However, in short chains these fluctuations are expected to alter the rupture kinetics of the breakable bond noticeably.

In what follows we develop a theory for experiments performed with a constant force ramp. Our study is based on the results presented in chapter 4. First we consider the thermal activation at zero loading rate (vanishing force) in a chain with a single cusp-shaped interaction potential. The theory predicting the activation times (the inverse rates) has been developed in the previous chapter. Next, we pass to the case with $\dot{f} \neq 0$, still considering a chain with a single cusp-shaped binding potential. Exchanging this potential for a Morse one we recover the chain system described in the Eqs. (5.62) and (5.63). We study how the loading rate alters the impact of the coupled dynamics on the overall rupture process and consider eventually the force propagation into the chain. Furthermore, we discuss when the non-Markovian fluctuations can be neglected in chains consisting of a large number of breakable bonds.

We start with a grafted chain of N bonds consisting of $N-1$ perfect harmonic springs and one breakable bond. This one is either located at the grafted terminal or at the pulled terminal of the chain. Thus our model is closely related to the one introduced in Sec. 4.3. The schematic picture is identical to the representation in Fig. 5.7 with the breakable Morse bond exchanged for a harmonic cusp-shaped potential. In order to carry out our analysis we need to know two special correlation functions, the one of the relative distance of the first monomer to the wall and the one of the bond elongation at the pulled end. These correlation functions were given in Eq. 4.72. For easier readability we rewrite them here

$$\phi_1(t) = \frac{4}{2N+1} \sum_{k=1}^{N} \mathrm{e}^{-t/\tau_k^g} \cos\left(\frac{\pi}{2}\frac{2k-1}{2N+1}\right)^2 \tag{5.64}$$

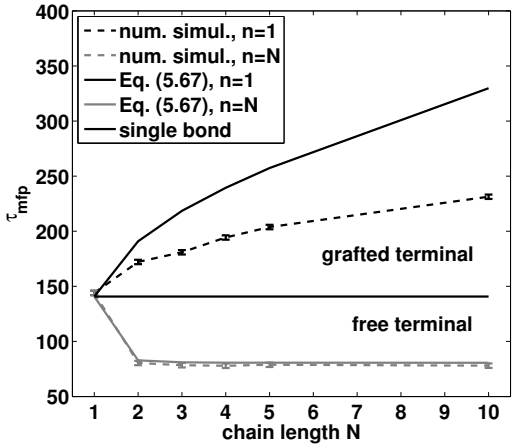

Figure 5.9.: Mean first passage times for a bond either situated at the grafted or at the free terminal of a grafted chain as a function of its length. Comparison between numerical simulation (dashed lines, symbols) and theory (solid lines). The time is scaled in dimensionless units, i.e., $t \to t\kappa/\gamma$. The barrier height is $\Delta E/k_BT = 5$.

and

$$\phi_N(t) = \frac{4}{2N+1} \sum_{k=1}^{N} \mathrm{e}^{-t/\tau_k^g} \cos\left(\left(N - \frac{1}{2}\right)\pi \frac{2k-1}{2N+1}\right)^2 . \tag{5.65}$$

The mode relaxation times derived in Sec. 2.3 are

$$\tau_k^g = \gamma \left(4\kappa \sin\left(\frac{\pi}{2}\frac{2k-1}{2N+1}\right)^2\right)^{-1} . \tag{5.66}$$

Then, within the framework of the Wilemski-Fixman approximation the mean first passage time is given as

$$\tau_{mfp}(n,f) = \int_0^\infty \left(\frac{1}{\sqrt{1-\phi_n(t)^2}} \exp\left[\frac{2\phi_n(t)}{1+\phi_n(t)}\frac{\Delta E(f)}{k_BT}\right] - 1\right) dt\,, \tag{5.67}$$

with $n \in \{1, N\}$. Since the ACF depends on the total system size N, τ_{mfp} will be a function of N, too. Moreover, the effective free energy landscape alters upon application of an external force f, therefore, the mean first passage time is also a function of the applied force f.

In order to gather a comprehensive knowledge of the underlying dynamics we first study the mean first passage times in the absence of any pulling, i.e., $\dot{f} = 0$, for an intrinsic barrier height of $\Delta E/k_BT = 5$. In Fig. 5.9 we show the results of Brownian dynamics simulations vs. the prediction of Eq. (5.67). Similar results may be deduced from Fig. 4.8 in chapter 4. The overall picture is as follows: For a bond situated at the grafted end of the chain the mean first passage time grows with increasing chain length. In contrast, the time shrinks for the bond at the free terminal. In the latter case the chain length is rather unimportant as long as it contains more than one bond. With increasing value of N the

mean first passage time remains almost constant. The independence of $\tau_{mfp}(N \gg 1)$ of N can be shown analytically in a same way as it has been done for the terminals of a free chain in chapter 4. Furthermore, the theory predicts the mean first passage times with high accuracy. For the bond close to the wall the theory only qualitatively predicts the outcome of the simulations. However, both curves (numerics and theory) have the same shape and both continue growing with enlarging value of N.

Having represented some results which have been originally shown in chapter 4 we now take the next step towards the understanding of the breakage of the chain with a single breakable bond and assume $\dot{f} \neq 0$. In order to carry out a detailed analysis of the impact of the non-Markovian fluctuations on the rupture dynamics we first consider short chains and neglect the force propagation. Below we account for this effect in longer chains.

Considering the rupture of a bond we assumed so far that the survival probability follows

$$\Phi_1(f) = \exp\left(-\frac{1}{\dot{f}}\int_0^f \nu(f')df'\right) . \tag{5.68}$$

The mean rupture force (which we focus on in the following since it allows for a higher numerical accuracy compared to the most probable rupture force and can be easily deduced from the survival probability) is given by

$$\langle f\rangle = \int_0^\infty \Phi_1(f')df' . \tag{5.69}$$

In order to have an estimate for this mean force we make the ansatz that

$$\nu(f) \simeq \frac{1}{\tau_{mfp}(n,f)} , \tag{5.70}$$

with the mean first passage time taken from Eq. (5.67). Eventually the mean rupture force is given by

$$\langle f\rangle_n = \int_0^\infty df' \exp\left[-\frac{1}{\dot{f}}\int_0^{f'} df''\Big/ \int_0^\infty dt\left\{\frac{\exp\left(\frac{2\phi_n(t)}{1+\phi_n(t)}\frac{\Delta E(f'')}{k_BT}\right)}{\sqrt{1-\phi_n(t)^2}} - 1\right\}\right] , \tag{5.71}$$

with $n = 1$ for the breakable bond at the grafted terminal and $n = N$ for the one at the opposite pulled end.

Chain with a single breakable bond represented by a cusp-shaped potential

Let us first consider the case when the breakable bond is a harmonic bond with a sharp cut-off. Upon application of a static force f, the well-to-barrier distance (the x_+ in Eq. (4.53)) changes to

$$\Delta x_\pm = x_+ - \frac{f}{\kappa} , \tag{5.72}$$

and the combined activation energy barrier is

$$\Delta E(f) = \frac{\kappa x_+^2}{2}\left(1 - \frac{f}{\kappa x_+}\right)^2 . \tag{5.73}$$

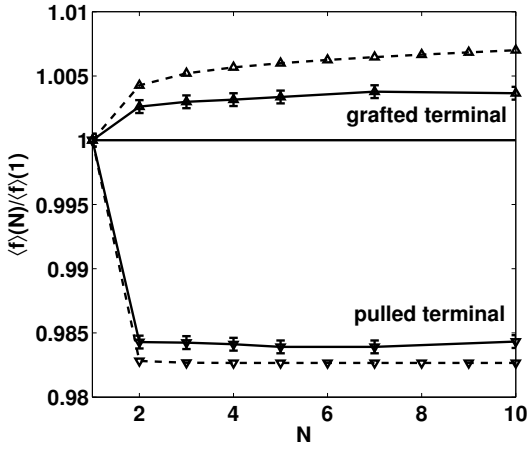

Figure 5.10.: Mean rupture force $\langle f\rangle(N)$ as a function of the chain length N. The chain consists of $N-1$ perfect harmonic springs and one breakable bond modeled by the cusp-shaped potential, either situated at the grafted terminal (upper curves) or at the free one (lower curves). Dashed lines represent the values derived from Eq. (5.71) and solid lines those from numerical simulations. Superimposed is the horizontal line corresponding to the rupture of a single grafted bond. The parameter values are $\kappa = 70\,\mathrm{N/m}$ $k_BT = 4\,\mathrm{pNnm}$, $\gamma = 2\times10^{-6}\,\mathrm{kg/s}$, and $\dot{f} = 2\times10^{-6}\,\mathrm{N/s}$.

Putting this expression into Eq. (5.71) we calculate (the integrals are evaluated numerically) the mean rupture force.

In Fig. 5.10 we compare the numerically obtained mean rupture forces (symbols) for bonds either situated at the grafted or at the free terminal of the chain with the prediction of Eq. (5.71). The parameter values are chosen such that they correspond to the harmonic approximation of the chain in Fig. 5.8. Theory and numerical simulations agree qualitatively quite well. Quantitative differences are typical for the approach based on the Wilemski-Fixman approximation as discussed in chapter 4. The mean forces $\langle f\rangle(N)$ are, compared to the case of the single bond rupture $\langle f\rangle(1)$, lowered at the pulled terminal and increased at the opposite end of the chain. The lowering is more pronounced, however, it is in the range of only a few percent. The opposite has been observed in Fig. 5.8 for a single breakable Morse bond where the increase of the force at the grafted terminal is stronger.

Chain with a single breakable Morse bond

Let us now consider the rupture dynamics of a single Morse bond loaded at a constant force ramp. We rewrite the combined free energy profile

$$U_f(x) = D_0\left(1-\mathrm{e}^{-\alpha(x-l_0)}\right)^2 - \dot{f}tx\,. \tag{5.74}$$

The inflection point is found at $x_c = l_0 + \ln(2)/\alpha$ and the critical force is $f_c = D_0\alpha/2$. The well-to-barrier distance and activation barrier height are

$$\Delta x_\pm = \frac{2}{\alpha}\ln\left(1 \pm \sqrt{1 - \frac{f}{f_c}}\right) \tag{5.75}$$

and

$$\Delta E(f) = D_0\sqrt{1 - \frac{f}{f_c}} + \frac{f}{\alpha}\ln\left(\frac{1 - \sqrt{1 - \frac{f}{f_c}}}{1 + \sqrt{1 - \frac{f}{f_c}}}\right) , \tag{5.76}$$

respectively. The latter equation is the input into Eq. (5.71) which gives the mean rupture force. The remaining $N - 1$ harmonic springs have a coupling constant $\kappa = 2D_0\alpha^2$.

In Fig. 5.11 we compare the outcome of Brownian dynamics simulations with the predictions of Eq. (5.71) with $\Delta E(f)$ given in Eq. (5.76) for two values of the coupling strength κ. Panel (a) presents the results of our numerical simulations while panel (b) shows the theoretical results. Compared to the outcome of the numerical simulations the analytical result predicts qualitatively the observed behavior. For a chain of $N > 1$ beads the mean force at the pulled terminal is lowered to a chain length independent value while it increases with growing chain length at the grafted terminal. The increase tends to weaken in the limit of longer chains. Furthermore, the effect is the more pronounced the softer the bonds are. The theoretical description based on Eq. (5.71) fails quantitatively. The decrease of the mean force is overestimated while the increase is drastically underestimated. This seems to be an intrinsic feature of the theoretical approach since the same has been observed for the cusp-shaped potential, see Fig. 5.10. Note, that—compared to the harmonic cusp-shaped potential, the nonlinear Morse potential seems to alter the rupture dynamics in such a way that now the decrease of the rupture force at the pulled terminal is less pronounced compared to its increase at the opposite polymer chain end.

The agreement between theory and simulations is qualitatively good but systematic quantitative differences are observed. Therefore, we attempt to modify the theory. Since the mean first passage time in Eq. (5.67), which is the inverse activation rate in our theory, is the average time of a reaction coordinate to reach a sharp barrier top it does not account for the curvature of the latter. For a single Brownian particle we have shown in chapter 4 that in the Markovian limit of timescale separation the inverse first passage time to a cusp-shaped barrier is given by

$$\nu_{cusp} = \frac{\kappa}{\gamma}\sqrt{\frac{\Delta E}{\pi k_B T}}\,\mathrm{e}^{-\frac{\Delta E}{k_B T}} . \tag{5.77}$$

The mean first passage time was derived in the limit of high activation barriers and under the assumption that the potential close to the barrier can be approximated by a linear function. On the other hand for the escape of a Brownian particle over a curved barrier we got

$$\nu_{curved} = \frac{\sqrt{|U''(x_+)|}\sqrt{U''(x_-)}}{2\pi\gamma}\,\mathrm{e}^{-\frac{\Delta E}{k_B T}} . \tag{5.78}$$

We thus write

$$\nu_{curved}(f) = q(f)\nu_{cusp}(f) , \tag{5.79}$$

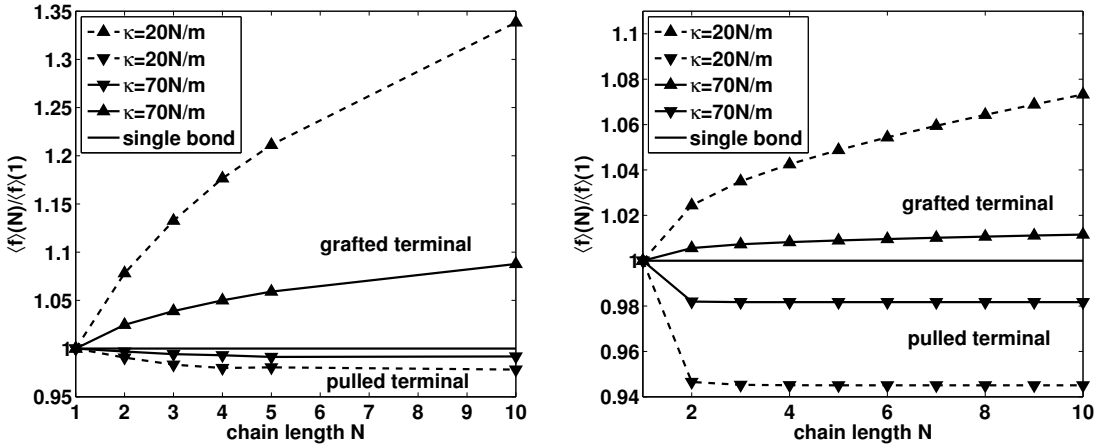

Figure 5.11.: Panel (a): Numerically obtained mean rupture force $\langle f\rangle(N)$ for two values of the coupling strength κ as given in the legend. Panel (b): Analytically obtained mean rupture force $\langle f\rangle(N)$. Except for the value of κ the parameter values are the same as in Fig. 5.10. The breakable bond is described by a Morse potential with $\kappa = 2D_0\alpha^2$ and $\alpha = 10\,\mathrm{nm}^{-1}$.

with $q(f)$ being a force-dependent prefactor. First, we assume that the curvatures at the top and bottom of the potential well do not depend on the external force and can be approximately set to $\sqrt{\kappa}$. Then, the prefactor becomes

$$q_1(f) = \frac{1}{2}\sqrt{\frac{k_BT}{\pi\Delta E(f)}}\,. \tag{5.80}$$

Putting the modified rate into Eq. (5.68), we obtain different values of the mean rupture force which are shown in Fig. 5.12, panel (a). Taking into account the curvatures (which are deduced from the combined free energy profile given in Eq. (5.76)) at x_- and x_+

$$U''(x_-) = D_0\alpha^2\sqrt{1-\frac{f}{f_c}}\left(1+\sqrt{1-\frac{f}{f_c}}\right)\,, \tag{5.81}$$

$$|U''(x_+)| = D_0\alpha^2\sqrt{1-\frac{f}{f_c}}\left(1-\sqrt{1-\frac{f}{f_c}}\right)\,, \tag{5.82}$$

we obtain

$$q_2(f) = \frac{1}{4}\sqrt{\frac{k_BT}{\pi\Delta E(f)}}\sqrt{\left(1-\frac{f}{f_c}\right)\frac{f}{f_c}}\,. \tag{5.83}$$

The corresponding results are shown in Fig. 5.12, panel (b). Compared to the analytical prediction shown in panel (b) of Fig. 5.11 the modified theory fits much better to the numerical simulations (panel (a) of Fig. 5.11). We remark that not only the relative forces agree better with the numerical simulations, but also their absolute values. To show this

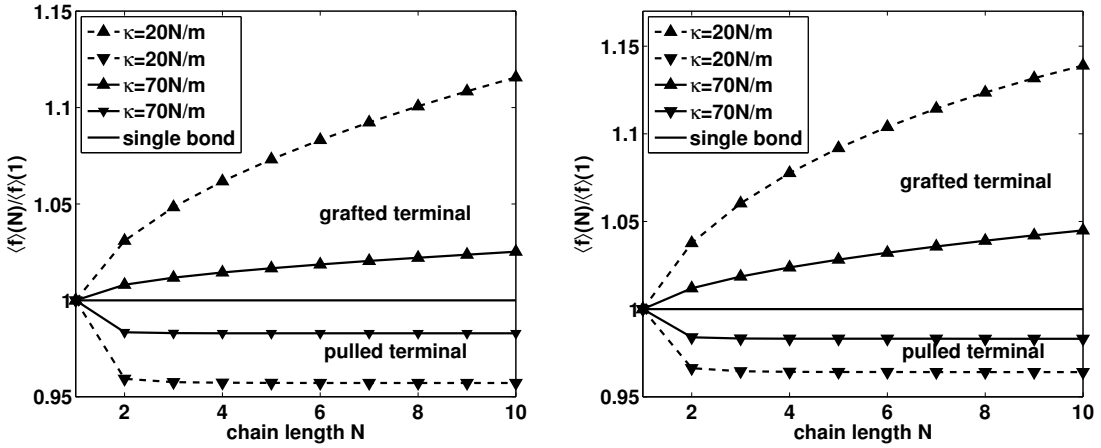

(a) (b)

Figure 5.12.: Analytically obtained mean rupture force $\langle f \rangle(N)$ for two values of the coupling strength κ as given in the legend. Panel (a): The rate has been multiplied with $q_1(f)$. Panel (b): The rate has been multiplied with $q_2(f)$. The parameter values are the same as in Fig. 5.11

we present in Tab. 5.1 the analytically obtained values for $\langle f \rangle(1)/f_c$. Since the analytical prediction taking into account the prefactor q_2 fits better than the one with q_1 we conclude that, in fact, the change of the curvature at the extremal points of the binding potential as a function of the force modifies the dynamics.

κ [N/m]	num. simul.	theory	$q_1(f)$	$q_2(f)$
20	0.768	0.556	0.664	0.752
70	0.848	0.757	0.808	0.848

Table 5.1.: Comparison of the numerically obtained values of the mean rupture force of a single loaded bond with the predictions of the theory without correcting prefactor, with $q_1(f)$, and with $q_2(f)$. Presented is $\langle f \rangle(1)/f_c$.

The method presented here can be adopted without restrictions to any other bond location in the chain, i.e., $1 < n < N$, with the appropriate $\tau_{mfp}(n)$. In Fig. 5.13 we depict the mean rupture forces $\langle f \rangle$ of breakable Morse bonds located at $n \in N$ in a chain whose remaining bonds are harmonic springs with a coupling constant corresponding to the harmonic approximation of the breakable bond for two different values of the loading rate as given in the legend. Dashed lines show the outcome of numerical simulations while solid lines represent the calculations based on Eq. (5.71) with the correlation function according to the bond's position. The theoretical prediction underestimates the rupture force quantitatively but shows the correct qualitative behavior. The rupture forces gradually increase from the pulled end to the grafted one. The increase is the stronger the higher the loading rate is.

Let us summarize our preliminary results. Starting from the thermally activated chain

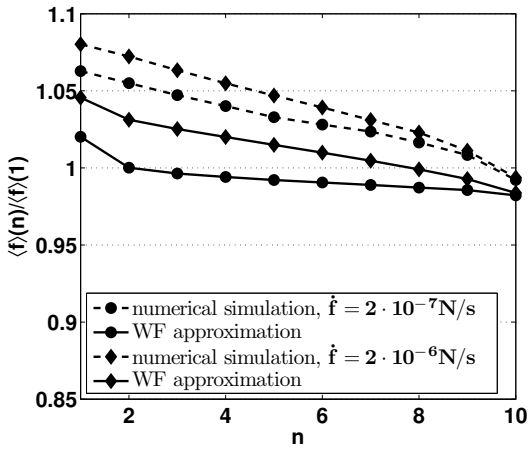

Figure 5.13.: Mean rupture forces in chains of $N = 10$ monomers with a single breakable bond at n. We compare the results of the WF approximation (solid lines) with the outcome of numerical simulations (dashed lines) for two values of the loading rate (as given in the legend). The parameter values are the same as in Fig. 5.11. The breakable bond is modeled by a Morse potential and the corresponding harmonic coupling strengths is $\kappa = 2D_0\alpha^2 = 70\,\mathrm{N/m}$.

fragmentation in the absence of an external force we have developed a theoretical framework which enables us to predict the mean rupture force of a single breakable bond in a chain when its terminal is loaded under a constant force ramp, i.e., $\dot{f} = \text{const}$. We concentrated on the bonds either situated at the grafted or at the pulled terminal and found a good qualitative agreement between the theory and numerical simulations. First, we studied a breakable bond represented by a cusp-shaped potential and later a more realistic Morse bond. The involved curvature at the activation barrier top noticeably changes the observed rupture forces. Introducing correcting prefactors we were able to account for these influences and to get a satisfactory agreement between theory and simulations.

Impact of the loading rate

In the following we study how the loading rate affects the impact of the non-Markovian fluctuations. Since a higher loading rate causes larger rupture forces (since there is rather little time for large thermal fluctuations which trigger the rupture process) the activation barrier heights are smaller compared to the ones obtained for the smaller values of $\dot{f}$ and the dynamics evolves on a timescale shorter than the relaxation time τ_1^g of the system. Hence we expect a more pronounced impact of the non-Markovian fluctuations for larger values of $\dot{f}$.

In order to establish a more sound explanation we depict in Fig. 5.14 the rupture rates as a function of an applied external force calculated with Eq. (5.67) (panel (a)) and the corresponding survival probability as given by Eq. (5.68) (panel (b)). The chain length is $N = 10$. The curves representing the situation with a breakable bond at the grafted end are drawn in dashed style while the behavior of the bond at the pulled terminal is depicted with solid lines. In panel (a) the rates for a single bond (simple OU process)

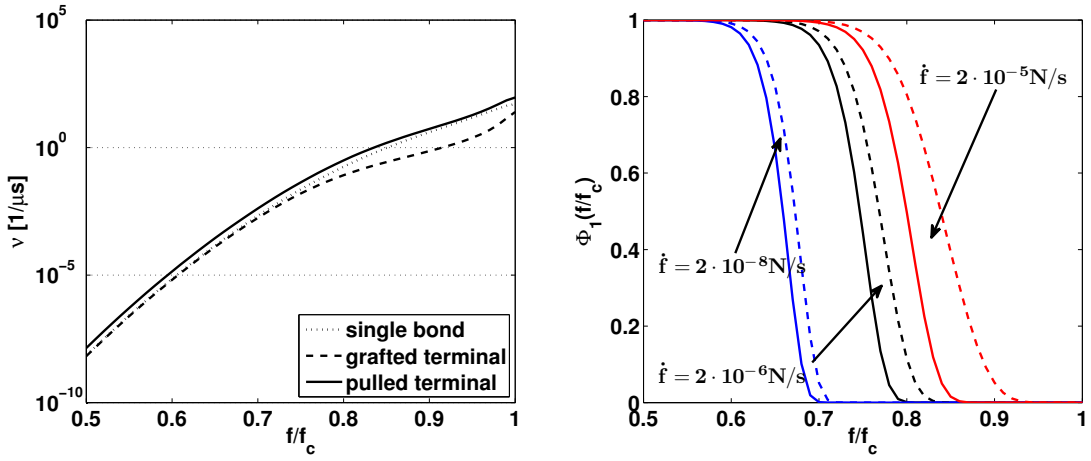

(a) (b)

Figure 5.14.: The influence of collective noise on the rupture dynamics of chains with a single weak link. The curves representing the situation with a breakable bond at the grafted end are drawn in dashed style while the behavior of the bond at the pulled terminal is depicted with solid lines. Panel (a): Rupture rate calculated from Eq. (5.67) for a chain with $N = 10$ bonds. The weak link is either situated at the grafted end or at the pulled terminal. Panel (b): Survival probability calculated from Eq. (5.68). The parameter values are the same as in Fig. 5.11.

are superimposed in dotted style. Although we now know, that the theory based on the Wilemski-Fixman approximation deviates quantitatively from the numerically obtained data, the qualitative agreement helps us to understand the behavior of the system under study. Therefore, we focus on the results given by the theoretical approach. Let us first discuss the rates, i.e., panel (a). Over a wide range of forces, far away from the critical force f_c for which the activation barrier vanishes, the presented rates (dotted, dashed, and solid line) run side by side, the dotted line closer to the dashed line. For higher forces the dotted line merges with the solid one and the distance to the dashed line becomes larger. This means, that for smaller forces (higher activation barriers) the rupture rates at the chain's ends are close to each other and correspond to the Markovian limiting value of a single breakable bond at the grafted terminal and half of that value at the opposite terminal. At high forces they differ by a factor of about 10. Together with Eq. (5.68) we are able to understand panel (b). The survival probability as given in Eq. (5.68) drops from one to zero depending on the force. The exponent scales with $1/\dot{f}$ and the integral over the rates is essentially the area under the curves in panel (a). We can expect that the typical timescale of rupture will be given by the value of the force for which the exponent becomes -1. Thus we have

$$\dot{f} = \int_0^f \nu(f')df' \,. \tag{5.84}$$

Following this idea we can almost directly deduce from panel (a) the importance of the collective effects as a function of the loading rate. For very very small loading rates the

drop down of the survival probability will happen at small forces where the collective fluctuations are negligible. In contrast, for a very high value of the loading rate the drop down of the survival probability appears at large forces (low activation barriers) where the rupture rates at different bonds in the chain differ. The survival probability for different values of the loading rate (derived from Eq. (5.68)) is shown in panel (b). With decreasing loading rate the differences between the dashed line and the solid line become smaller. The delay of the rupture at the grafted end weakens.

Thus in summary, we observed that in the limit of vanishing loading rates, where rupture happens at very low forces, the impact of the collective effects disappears almost completely. For the rupture dynamics of a chain of N breakable bonds this means—since there will also be no effect of the force propagation—that the extreme value statistics of multiple bond rupture in series fully describes the breakdown kinetics.

5.4.1. Long chains and the influence of the force propagation

In the preceding paragraphs we have shown that the non-Markovian fluctuations cause an increase of the rupture force of a grafted bond when the force is applied via a chain of monomers. For small chains and loading rates the force propagation will for sure be negligible. However, for longer chains this propagation will delay the application of force. Since both effects, the non-Markovian fluctuations and the force propagation, cause an increase of the rupture force, one may ask the question, which effect is the predominant one? By passing to the limit of infinite chains one can show two things. First, the timescale of force propagation which is proportional to the longest relaxation time of the grafted chain diverges as $\propto N^2$. Second the correlation function of the grafted bond saturates and becomes independent of the chain length N. Therewith the activation rate becomes independent of the value of N and consequently the survival probability, too. The correlation function was given in Eq. (5.64). We have

$$\phi_1(t) = \frac{4}{2N+1} \sum_{k=1}^{N} \mathrm{e}^{-t/\tau_k^g} \cos\left(\frac{\pi}{2}\frac{2k-1}{2N+1}\right)^2 . \tag{5.85}$$

For large N we have $2N \pm 1 \to 2N$ and

$$\tau_k^g \simeq \frac{\gamma(2N)^2}{\kappa\pi^2(2k-1)^2} . \tag{5.86}$$

We obtain

$$\phi_1(t) = \frac{2}{N} \sum_{k=1}^{N} \mathrm{e}^{-\frac{t\kappa\pi^2(2k-1)^2}{4N^2\gamma}} \cos\left(\frac{\pi}{2}\frac{2k-1}{2N}\right)^2 . \tag{5.87}$$

Furthermore, we can replace the sum by an integral and write

$$\begin{aligned} \phi_1(t) &\simeq \frac{1}{N} \int_1^{2N} \mathrm{e}^{-\frac{t\kappa\pi^2 x^2}{4N^2\gamma}} \cos\left(\frac{\pi x}{4N}\right)^2 dx \\ &= 2\int_{1/(2N)}^{1} \mathrm{e}^{-\frac{t\kappa\pi^2}{\gamma}y^2} \cos\left(\frac{\pi}{2}y\right)^2 dy . \end{aligned} \tag{5.88}$$

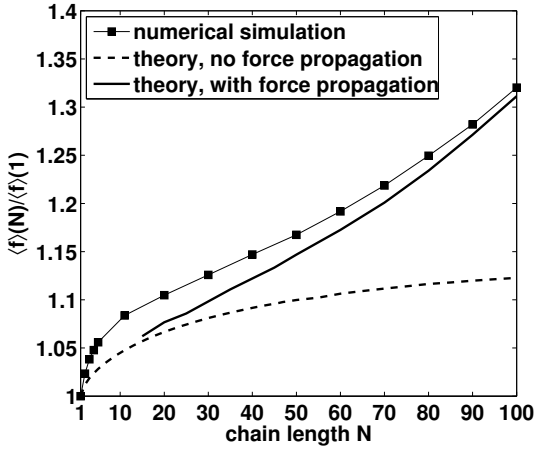

Figure 5.15.: Mean rupture force $\langle f \rangle(N)$ as a function of the chain length N. The results obtained via numerical simulations (symbols) are compared with the analytically calculated mean forces neglecting the force propagation (dashed line) and those taking it into account (solid line). The parameter values are the same as in Fig. 5.11 with $\kappa = 70\,\mathrm{N/m}$.

For large N the lower limit of the integration tends to zero and the correlation function becomes independent of the number of bonds. Since then the mean first passage time (which is the inverse rate in the calculation of the survival probability, see Eq. (5.68)) becomes independent of N while the typical time of force propagation to the grafted end grows as N^2 we deduce that the latter effect completely dominates the rupture dynamics.

Since the force propagation will not affect the rupture process at the pulled end of the chain we focus solely on the dynamics at the opposite terminal. In the next section we will derive the time-dependent force profile of a grafted chain pulled at one terminal at a constant rate. Anticipating this calculation one can show that the force at the grafted terminal ($n = 1$) is given by the following expression

$$\tilde{f}(1,t) = \frac{4\kappa\dot{f}\tau_1^g}{N\gamma}\sum_{k=1}^{\infty}\sin\left(\frac{k\pi}{2}\right)\cos\left(\frac{k\pi}{2N}\right)\sin\left(\frac{k\pi}{4N}\right)\left(\frac{t}{k^2}-\frac{\tau_1^g}{k^4}\left(1-\exp\left[-\frac{k^2 t}{\tau_1^g}\right]\right)\right), \tag{5.89}$$

with t related to the applied force at the pulled end of the chain via $t = f/\dot{f}$ and

$$\tau_1^g = \frac{4\gamma N^2}{\kappa\pi^2}\,. \tag{5.90}$$

Putting (5.89) into the expression for the barrier height (5.76) and the correcting prefactor (5.83) we are able to calculate the modified survival probability of the bond using expression (5.68). In Fig. 5.15 we show our results. Those obtained via numerical simulations (symbols) are compared with the analytically calculated mean forces neglecting the force propagation (dashed line) and those taking it into account (solid line). In the latter case the calculated modified mean rupture force agrees well will the outcome of numerical simulations. We remark that the upper limit of the sum in Eq. (5.89) was set to 1500. It

has been checked that an increase of this number did not lead to a change in our results. To conclude, taking into account the impact of non-Markovian fluctuations on the barrier crossing process as well as the delayed force propagation to the breakable bond we can nicely predict the outcome of the numerical simulations.

5.5. Chains of breakable bonds

Having studied the rupture of a single breakable bond in a polymer chain we now pass to a chain build only of breakable bonds. We first estimate the impact of the non-Markovian fluctuations on its rupture process. Therefore, we have to remember how the mean activation times in a coupled chain system depend on the activation barrier height. For the case of the grafted chain this was discussed in chapter 4. We showed in Fig. 4.9 that at the grafted terminal the ratio $\tau_{mfp}(1)/\tau^s_{mfp}$ is always larger than one while for the other bonds it changes gradually to values below one. For $\Delta E \gg k_B T$ we found $\tau_{mfp}(1) \to \tau^s_{mfp}$ while $\tau_{mfp}(n \neq 1) \to \tau^s_{mfp}/2$. For lower barriers the times may reach a few times the value of the corresponding single bond. Thus we may substitute the activation rate of a bond in the chain $\nu(f)$ (which is the basic input into the calculation of the survival probability, see Eq. (5.25)) by $\varepsilon\nu(f)$ with ε being a number of the order of $o(1)$ which accounts for the impact of the non-Markovian fluctuations.

In order to estimate the influence of the non-Markovian fluctuations in long chains of breakable bonds we anticipate a results which we will derive below. In the limit of negligible force propagation the most probable rupture force scales with the number of breakable bonds in the chain as

$$\frac{f_{max}}{f_c} = 1 - \left(\frac{\ln(vN/\dot{f})}{w} \right)^{b_m} . \tag{5.91}$$

The derivation of the latter equation is analog to the one of (5.34) with Nv substituted for v. Changing in this derivation the instantaneous activation rate of the bond to $\varepsilon\nu(f)$ we get

$$\frac{f_{max}}{f_c} = 1 - \left(\frac{\ln(vN/\dot{f})}{w} + \frac{\ln(\varepsilon)}{w} \right)^{b_m} . \tag{5.92}$$

Since w is the apparent barrier height in multiples of $k_B T$, the fraction $\ln(\varepsilon)/w$ will usually be very small while $(v/\dot{f}) \times N \geq o(10^2) \times N$ for reasonable loading rates. Although this is only a rough estimation, we may conclude that the change of the rupture force due to long-time correlations in the chain is rather small. Especially for high values of the loading rate we expect that the major impact on the rupture dynamics originates from the delayed force propagation. Thus we can neglect the impact of the non-Markovian character of the fluctuations as well as correlations introduced by noise by assuming that the rupture of different bonds is independent and this is how we proceed in the following.

5.5.1. Analytical description

Let N be the number of breakable bonds in the chain and let $\Phi_1(f_n(t))$ be the survival probability of the bond $n \in [1, N]$. The chain is grafted at $n = 0$ and pulled at $n = N$

with a force $f_N(t) = \dot{f}t \equiv f$. Then, assuming that the rupture processes of different bonds are independent, the survival probability of the whole chain is given by

$$\begin{aligned}\Phi_N(f) &= \prod_{n=1}^{N} \Phi_1(f_n(t)) = \exp\left\{\ln\left(\prod_{n=1}^{N} \Phi_1(f_n(t))\right)\right\} \\ &= \exp\left\{\sum_{n=1}^{N} \ln\left(\Phi_1(f_n(t))\right)\right\} .\end{aligned} \tag{5.93}$$

We pass to the continuum limit and obtain

$$\Phi_N(f) = \exp\left\{\int_0^N \ln\left(\Phi_1(\tilde{f}(n, t = f/\dot{f}))\right) dn\right\} , \tag{5.94}$$

with N being the length of the chain. The continuum approximation is justified as long as the function $\tilde{f}(n,t)$ is smooth, i.e., as long as the loading rate $\dot{f}$ is sufficiently small. A schematic representation of the rupture process of the chain is given in Fig. 5.16.

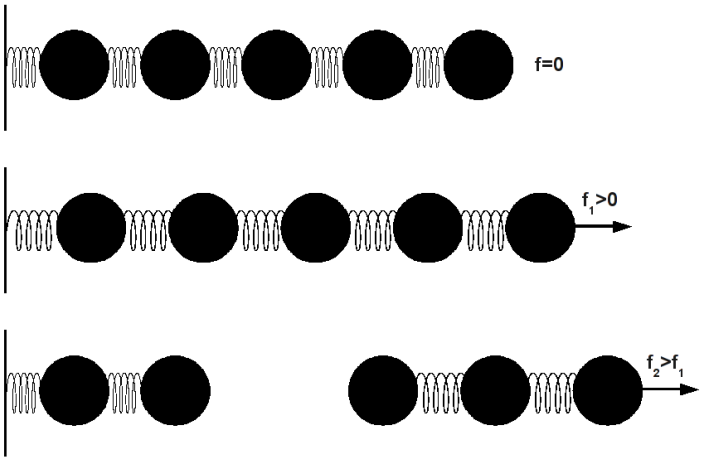

Figure 5.16.: Schematic representation of the rupture of a grafted chain of breakable bonds loaded at a constant rate $\dot{f}$.

The unknown function in Eq. (5.94) is the force profile $\tilde{f}(n,f)$, which we will specify as follows. Since barrier crossing events are very rare the motion of the monomers proceeds mostly close to the quadratic minima of the bond energies. Therefore, we can calculate the force profile $\tilde{f}(n,f)$ in the chain of monomers by considering a chain of harmonic bonds with the corresponding harmonic spring constant κ given by the curvature of the intrinsic free energy profile in the vicinity of its minimum. Then, the force propagation is governed by the following continuum equation for the scalar field $x(n,t)$

$$\dot{x}(n,t) = \frac{\kappa}{\gamma}\Delta_n x(n,t) + \frac{\dot{f}}{\gamma} t\delta(n - n_0) , \tag{5.95}$$

together with appropriate boundary conditions. The discrete coupling term is replaced by a Laplacian. Eq. (5.95) is a nonhomogeneous heat equation with a source located at

n_0. We will solve this equation assuming different boundary conditions, but for reasons of mathematical simplicity the source term is always located in middle between the boundaries. In the original coupled chain system the Laplacian (and thus the coupling) vanishes for $n > n_0$. Integrating (5.95) over a small $\epsilon-$interval around n_0 we have

$$\int_{n_0-\epsilon}^{n_0+\epsilon} \dot{x}(n',t)dn' = \frac{\kappa}{\gamma}\int_{n_0-\epsilon}^{n_0+\epsilon} \Delta_n x(n',t)dn' + \frac{\dot{f}}{\gamma}t\,. \tag{5.96}$$

Taking the limit $\epsilon \to 0$ this becomes

$$-(\kappa\nabla_n x(n_0^+,t) - \kappa\nabla_n x(n_0^-,t)) = 2\tilde{f}(n_0,t) = \dot{f}t\,. \tag{5.97}$$

Thus since the central bead is coupled to two chain strands each of them experiences only half of the force. Therefore, we introduce a correction prefactor 2 to recover the single-sided grafted chain model. The force is then given by

$$\tilde{f}(n,t) = -2\kappa\nabla_n x\,. \tag{5.98}$$

The linear equation Eq. (5.95) can be solved using the appropriate Green's function of the corresponding homogeneous problem. This will be done explicitly for two different boundary conditions below.

Anticipating that we are able to derive the force profile $\tilde{f}(n,t)$ we further simplify the calculations in order to derive a closed form expression of the survival probability. We linearize the force profile close to the pulled end, yielding

$$\begin{aligned}\tilde{f}(n,f) &\simeq \tilde{f}(n_0,f) - \nabla_n\tilde{f}|_{n=n_0}(n_0-n)\\ &= f\left(1-g(f)(N-n)\right)\,,\end{aligned} \tag{5.99}$$

where we set $n_0 = N$. We will later show that a linearly decreasing force properly describes $\tilde{f}(n,f)$ for $N \geq n \gg 1$.

At the pulled terminal the force follows $f = \dot{f}t$. Since the force propagates into the chain the force $\tilde{f}$ experienced at a location n inside the chain will be a function of n and f. Furthermore, the loading rate $\dot{f}$ for bonds far away from the pulled terminal will be in general a nonlinear function of the force. The force $\tilde{f}(n,f)$ itself will be smaller compared to its maximum value f at the pulled terminal. As shown in the previous section the most probable rupture force scales on a logarithmic scale with changing value of $\dot{f}$ while the force lowering the activation barrier increases exponentially the rate of rupture. We expect that the exponential change of the rupture rate of a bond n in the chain as a result of the force profile will dominate the rupture dynamics compared to the impact of $\dot{f} \neq$ const.

Therefore, in order to evaluate the integral in Eq. (5.94), we make the assumption that the survival probability for each bond located at $1 \leq n \leq N$ is given by the survival probability of a single loaded bond Φ_1, given in Eq. (5.41). Its derivation is based on the assumption that the bond is loaded under a constant force ramp with $\dot{f} =$ const. To make this clear let us explain this assumption in more detail: The force needs a typical time of the order of the longest relaxation time in the chain to propagate through the latter. After this characteristic time the bonds which have the longest distance to the pulled end start to experience tension. Our assumption corresponds to the approximation, that at

each instant in time the force at a certain bond n corresponds to a force caused by pulling with the rate $\dot{f}$ for a time which is given by $\tilde{f}(n)/\dot{f}$. However, we underline that assuming a constant loading rate $\dot{f}$ along the chain can only be an approximation, however, as we proceed to show, a very well working one. In a later part of this section we compare our approximation (which leads to a closed expression of the survival probability of the chain) with a calculation taking into account the force dependence of the loading rate (which, in contrast, leads to an integral expression that has to be solved numerically) and find practically no difference what justifies our assumptions.

Putting the linearized force profile given in (5.99) into the expression for the survival probability of a single bond (5.41) and finally into (5.94) we obtain an expression for the survival probability of the chain

$$\Phi_N(f) = \Phi_0^N \exp\left\{-\frac{v}{\dot{f}}\int_0^N \exp\left\{-w\left(1-\frac{f}{f_c}\left(1-g(f)(N-n)\right)^{1/b_m}\right)\right\}dn\right\}, \tag{5.100}$$

with $b_m = 1/2$ for a cusp-shaped potential and $b_m = 2/3$ for a smooth cubic one, respectively.

The integral in Eq. (5.100) can be solved as follows: Introducing $n' = N - n$ we rewrite the integral in the following form

$$I = \int_0^N \exp\left(-w\left(\left[1-\frac{f}{f_c}\right]\left[1+\frac{fg(f)}{f_c-f}n'\right]\right)^{1/b_m}\right)dn'\,. \tag{5.101}$$

Further, introducing the abbreviation

$$S(n', f) = y = \frac{fg(f)}{f_c - f}n' \tag{5.102}$$

and the effective barrier height of a bond

$$e(f) = w\left(1-\frac{f}{f_c}\right)^{1/b_m}, \tag{5.103}$$

we obtain

$$I = \frac{b_m}{e(f)^{b_m}}\frac{f_c-f}{fg(f)}\left(\Gamma\left(b_m, e(f)\right) - \Gamma\left(b_m, e(f)(1+S(N,f))^{1/b_m}\right)\right), \tag{5.104}$$

with the upper incomplete gamma function $\Gamma(m, x)$. Eventually the survival probability is

$$\Phi_N(f) = \Phi_0^N \exp\left[-\frac{b_m v f_c}{\dot{f} f g(f) w^{b_m}}\left(\Gamma\left(b_m, e(f)\right) - \Gamma\left(b_m, e(f)\left(1+S(N,f)\right)^{1/b_m}\right)\right)\right]. \tag{5.105}$$

Let us further introduce

$$d(f) = \frac{dg(f)}{df}\,. \tag{5.106}$$

Then the probability density distribution of rupture forces reads

$$\begin{aligned}\mathcal{F}_N(f) = &- \Phi_N(f) \\ &\left\{ \frac{b_m v f_c}{\dot{f} w^{b_m}} \left(\frac{1}{f^2 g(g)} + \frac{d(f)}{f g(f)^2} \right) \left(\Gamma\left(b_m, e(f)\right) - \Gamma\left(b_m, e(f)\left(1 + S(N,f)\right)^{1/b_m}\right)\right) \right. \\ &\left. - \frac{v}{f g(f)} \left[\mathrm{e}^{-e(f)} - \left(1 - g(f)N - f d(f) N\right) \mathrm{e}^{-e(f)(1+S(N,f))^{1/b_m}} \right] \right\} .\end{aligned} \tag{5.107}$$

Since no closed analytical expressions for the mean and most probable rupture forces of the chain are available, these values are deduced numerically from Eq. (5.105) and (5.107), respectively. We recall, that for any smooth activation barrier within the cubic approximation around the inflection point of the single bond energy landscape we set $b_m = 2/3$.

One might doubt the accuracy of these results based on the linearization assumption, Eq. (5.99), since for $1/g(f) < N - n$ the force $\tilde{f}(n, f)$ becomes negative in the region where it essentially has to vanish, which is an unphysical result. However, this property of Eq. (5.99) has no impact on the rupture kinetics. A negative force exponentially suppresses the rate of escape, see Eq. (5.28), leading to the fact that the corresponding bonds simply do not break. For the rupture kinetics there is therefore no difference between getting negative forces or setting the force to zero, as it is the situation in the physical experiment. To prove this we also performed calculations with a modified profile $\tilde{f}(n, f) = f(1 - g(f)(N - n))\Theta(1 - g(f)(N - n))$ instead of Eq. (5.99). The calculations are given in App. C. Evaluating the equations presented there we found practically no difference in the outcome of the theory.

Limit of vanishing loading rates

Let us now discuss two limiting cases. Let the loading rate $\dot{f}$ be very small, thus for a typical rupture force it holds that $f/\dot{f} \gg \tau_1^g \propto N^2$. Then we can assume that the force acting on each spring along the chain of coupled bonds is virtually the same. In the limit of vanishing decrease of the force along the chain we have $S(N, f) \to 0$ in Eq. (5.102) as well as in Eq. (5.105) and Eq. (5.107). A first order series expansion of the incomplete gamma function gives ($S(N, f)$ being a small parameter)

$$\Gamma\left(b_m, e(f)\right) - \Gamma\left(b_m, e(f)(1 + S(N,f))^{1/b_m}\right) \simeq \frac{1}{b_m} e(f)^{b_m} \mathrm{e}^{-e(f)} S(N,f) + o(S(N,f)^2) . \tag{5.108}$$

Putting this expansion into Eq. (5.105) for the survival probability we obtain the limiting expression

$$\Phi_N(f) = \Phi_1(f)^N . \tag{5.109}$$

The probability that a bond breaks in an interval $[f, f + df]$ is

$$\frac{d\Phi_N(f)}{df} = -\mathcal{F}_N(f) = N\Phi_1(f)^{N-1} \frac{d\Phi_1(f)}{df} = -N\Phi_1(f)^{N-1}\mathcal{F}_1(f) . \tag{5.110}$$

Putting Eq. (5.43) into Eq. (5.110) we finally obtain

$$\mathcal{F}_N(f) = \mathcal{F}_1(f)|_{v\to Nv}\,. \tag{5.111}$$

Thus based on Eq. (5.45) we derive the following scaling relation for the most probable rupture force f_{max}

$$f_{max}(N) = f_c\left(1 - \left(\frac{\ln(Nv/\dot{f})}{w}\right)^{b_m}\right) \tag{5.112}$$

and based on Eq. (5.44) the mean rupture force

$$\langle f\rangle(N) \simeq f_c\left(1 - \left(\frac{\ln\left(Nv/\dot{f}\right) + \gamma_{EM}}{w}\right)^{b_m}\right)\,. \tag{5.113}$$

The expressions for the survival probability and the rupture probability density are the same as in the single bond case with v replaced by Nv. Therefore, the mean and most probable rupture forces exhibit a scaling as a function of the chain length given by $[\ln(\text{const}N)]^{b_m}$. Thus for any binding potential exhibiting a smooth activation barrier the model based theory predicts a scaling $[\ln(\text{const}N)]^{2/3}$ of the mean and most probable rupture forces in the limit $f/\dot{f} \gg \tau_1^g$.

Limit of very high loading rates

In the opposite limit of very high loading rates, i.e., $f/\dot{f} \ll \tau_1^g$, the force decreases rapidly along the chain. In the extreme limit only the pulled bond contributes to the rupture process, i.e.,

$$\Phi_N(f) = \prod_{n=1}^{N}\Phi_1(f_n(t)) \simeq \Phi_1(f_N(t)=f)\prod_{n=1}^{N-1}\underbrace{\Phi_1(f_n(t)\approx 0)}_{\approx 1} = \Phi_1(f)\,. \tag{5.114}$$

Hence the survival probability of the chain coincides with the one obtained for a single pulled bond. In consequence the mean and most probable rupture forces are given by Eq. (5.44) and Eq. (5.45), respectively.

5.5.2. Force profiles

The remaining unknown input into our theory is the force profile $\tilde{f}(n,f)$. In the following we determine the linearized force profiles for a semiinfinite chain (Fugmann and Sokolov, 2009c) and a chain of fixed length N (Fugmann and Sokolov, 2009a). The assumption of having a semiinfinite chain corresponds to have chain rupture on timescales which are shorter than the longest relaxation time of the chain. This will be the case in very long chains since the relaxation time scales as $\propto N^2$ and becomes very large. In the opposite limit of short chains the boundary will affect the rupture kinetics and has to be taken into account.

Semiinfinite chain

Let us first consider the semiinfinite chain and derive its force profile. The solution of the inhomogeneous heat equation

$$\dot{x}(n,t) = \frac{\kappa}{\gamma}\Delta_n x(n,t) + \frac{\dot{f}}{\gamma} t\delta(n-n_0) \tag{5.115}$$

on an infinite interval ($-\infty < n < \infty$) with an initial condition $x_0(n) = x(n, t=0)$ is in general given by

$$x(n,t) = \int_{-\infty}^{\infty} x_0(n')\mathcal{G}(n,n',t)dn' + \int_0^t \int_{-\infty}^{\infty} \frac{\dot{f}t'}{\gamma}\delta\left(n'-n_0\right)\mathcal{G}(n,n',t-t')dn'dt' \,, \tag{5.116}$$

with the Green's function being the usual heat kernel (Polyanin, 2002)

$$\mathcal{G}(n,n',t) = \sqrt{\frac{\gamma}{4\pi t\kappa}}\exp\left(-\frac{(n-n')^2\gamma}{4\kappa t}\right). \tag{5.117}$$

The solution of (5.116) with $x_0(n) \equiv 0$ and $n_0 = N$ is

$$\begin{aligned} &x(n,t) \\ &= \frac{f}{2\kappa}\left[\frac{4\kappa t/\gamma + (N-n)^2}{3\sqrt{\kappa t\pi/\gamma}}\,\mathrm{e}^{\frac{-(N-n)^2\gamma}{4\kappa t}} + |N-n|\left(1+\frac{(N-n)^2\gamma}{6\kappa t}\right)\left(\mathrm{erf}\left(\frac{|N-n|}{\sqrt{4\kappa t/\gamma}}\right)-1\right)\right]. \end{aligned} \tag{5.118}$$

Then, the force $\tilde{f}(n,t)$ is given by

$$\tilde{f}(n,t) = -2\kappa\nabla_n x\,. \tag{5.119}$$

Since $f = \dot{f}t$ we derive for $n \le N$

$$\tilde{f}(n,f) = f\left[\left(1-\mathrm{erf}\left(\frac{N-n}{\sqrt{4\kappa f/(\gamma\dot{f})}}\right)\right)\left(1+\frac{(N-n)^2\gamma\dot{f}}{2\kappa f}\right) - \frac{N-n}{\sqrt{\kappa\pi f/(\gamma\dot{f})}}\,\mathrm{e}^{-\frac{(N-n)^2\gamma\dot{f}}{4\kappa f}}\right]. \tag{5.120}$$

Within the linear force approximation we obtain

$$\tilde{f}(n,f) \simeq f\left(1-2\sqrt{\frac{\gamma\dot{f}}{\kappa f\pi}}(N-n)\right) \tag{5.121}$$

and with Eqs. (5.99) and (5.106) eventually

$$g(f) = 2\sqrt{\frac{\gamma\dot{f}}{\kappa\pi f}} \quad \text{and} \quad d(f) = -\frac{\sqrt{\gamma\dot{f}}}{\sqrt{\kappa\pi}f^{3/2}}\,, \tag{5.122}$$

which when put into Eq. (5.105) and (5.107) determine the survival probability and bond rupture probability density of the chain, respectively.

Finite chain grafted at a wall

For smaller systems the decrease for the force along the chain is expected to be small, the force propagation is negligible. For very large chain lengths it is expected that bonds, which are far away from the pulled end, experience virtually no force and thus the above presented force profile of the semiinfinite chain is a sufficient input into our theory. Especially for intermediate system sizes—in the case when the time $t_{max} = f_{max}/\dot{f}$ is of the order of the longest relaxation time $\tau_1^g \propto N^2$ of the chain—one might expect a crucial influence of the boundaries on the propagating force profile. Thus, let us now consider a more complicated approach including the influence of the boundary condition $x(n = 0, t) = 0$ (Fugmann and Sokolov, 2009a).

We calculate the amplitude profile in a one-dimensional field with zero amplitude at its boundaries and a δ-function force source at its center. Taking Eq. (5.115) together with the two boundary conditions $x(n = 0, t) = 0$ and $x(n = 2N, t) = 0$ we have a symmetric problem. In fact, we are dealing with an inhomogeneous heat conduction equation with Dirichlet boundary conditions. The initial condition is given by $x_0(n) = x(n, t = 0)$ and its solution reads

$$x(n,t) = \int_0^{2N} x_0(n')\mathcal{G}(n,n',t)dn' + \int_0^t \int_0^{2N} \frac{\dot{f}t'}{\gamma}\delta\left(n' - n_0\right)\mathcal{G}(n,n',t-t')dn'dt' \,, \quad (5.123)$$

with the Green's function being (Polyanin, 2002)

$$\mathcal{G}(n,n',t) = \frac{1}{N}\sum_{k=1}^{\infty} \sin\left(\frac{k\pi n}{2N}\right)\sin\left(\frac{k\pi n'}{2N}\right)\exp\left(-\frac{\kappa k^2\pi^2}{4N^2\gamma}t\right) . \quad (5.124)$$

The solution of Eq. (5.123) is found to be

$$x(n,t) = \frac{\dot{f}}{N\gamma}\sum_{k=1}^{\infty} \sin\left(\frac{k\pi}{2}\right)\sin\left(\frac{k\pi n}{2N}\right)\left(\frac{-1 + \mathrm{e}^{-\kappa t/\gamma\left(\frac{k\pi}{2N}\right)^2} + \kappa t/\gamma\left(\frac{k\pi}{2N}\right)^2}{(\kappa/\gamma)^2\left(\frac{k\pi}{2N}\right)^4}\right) . \quad (5.125)$$

The longest relaxation time of the grafted Rouse chain (see Eq. (2.37)) becomes in the limit of $N \gg 1$

$$\tau_1^g = \frac{4\gamma N^2}{\kappa\pi^2} \,. \quad (5.126)$$

Using this abbreviation we have

$$x(n,t) = \frac{\dot{f}\tau_1^g}{N\gamma}\sum_{k=1}^{\infty} \sin\left(\frac{k\pi}{2}\right)\sin\left(\frac{k\pi n}{2N}\right)\left(\frac{t}{k^2} - \frac{\tau_1^g}{k^4}\left(1 - \exp\left[-\frac{k^2 t}{\tau_1^g}\right]\right)\right) . \quad (5.127)$$

The force at the pulled monomer situated at $n = N$ is $f = \dot{f}t$. However, note that the derivative of $x(n, t)$ for $n \to N$ is defined solely as a limiting value. To by-pass this problem we calculate the force acting on the neighboring bead in terms of the symmetric central

difference quotient

$$\begin{aligned}\tilde{f}(N-1,t) =& \frac{2\kappa\dot{f}\tau_1^g}{N\gamma}\sum_{k=1}^{\infty}\sin\left(\frac{k\pi}{2}\right)\left\{\sin\left(\frac{k\pi\left(N-\frac{1}{2}\right)}{2N}\right)-\sin\left(\frac{k\pi\left(N-\frac{3}{2}\right)}{2N}\right)\right\}\\ &\times\left(\frac{t}{k^2}-\frac{\tau_1^g}{k^4}\left(1-\exp\left[-\frac{k^2t}{\tau_1^g}\right]\right)\right)\,.\end{aligned} \tag{5.128}$$

As for the more simple approach above we linearize the force profile close to the pulled end

$$\tilde{f}(n,f)\simeq f-(f-\tilde{f}(N-1,t=f/\dot{f}))(N-n)=f\left(1-g(f)(N-n)\right)\,. \tag{5.129}$$

Thus we have

$$\begin{aligned}g(f) = 1-&\frac{2\kappa\tau_1^g}{N\gamma}\sum_{k=1}^{\infty}\sin\left(\frac{k\pi}{2}\right)\left\{\sin\left(\frac{k\pi\left(N-\frac{1}{2}\right)}{2N}\right)-\sin\left(\frac{k\pi\left(N-\frac{3}{2}\right)}{2N}\right)\right\}\\ &\times\left(\frac{1}{k^2}-\frac{\dot{f}\tau_1^g}{fk^4}\left(1-\exp\left[-\frac{k^2f}{\dot{f}\tau_1^g}\right]\right)\right)\end{aligned} \tag{5.130}$$

and subsequently $d(f)=dg(f)/df$

$$\begin{aligned}d(f) = -&\frac{2\kappa\tau_1^g}{N\gamma}\sum_{k=1}^{\infty}\sin\left(\frac{k\pi}{2}\right)\left\{\sin\left(\frac{k\pi\left(N-\frac{1}{2}\right)}{2N}\right)-\sin\left(\frac{k\pi\left(N-\frac{3}{2}\right)}{2N}\right)\right\}\\ &\times\left(\frac{\dot{f}\tau_1^g}{f^2k^4}\left(1-\exp\left[-\frac{k^2f}{\dot{f}\tau_1^g}\right]\right)-\frac{1}{fk^2}\exp\left(-\frac{k^2f}{\dot{f}\tau_1^g}\right)\right)\,.\end{aligned} \tag{5.131}$$

Let us now compare the linearized expressions according to

$$\tilde{f}(n,f)=f\left(1-g(f)(N-n)\right)\,, \tag{5.132}$$

with $g(f)$ taken either from Eq. (5.122) (semiinfinite chain) or from Eq. (5.130) (including the boundary condition at the grafted terminal) for a harmonic chain with coupling constant κ. In Fig. 5.17 we compare snapshots of the full force profiles at $f/f_c=0.8$ (solid lines) with the two linearized expressions. The dotted line corresponds to the semiinfinite chain approximation while the dashed line is the solution which takes into account the fixation at the boundary. In panel (a) the force profiles are shown for three different chain lengths ($N=50$, $N=150$, and $N=300$ from the left to the right) and a fixed value of the loading rate $\dot{f}=2\times10^{-6}\,\mathrm{N/s}$. First of all we notice that the force decreases with increasing distance from the pulled end of the chain. As mentioned above the linearized force profiles may become negative. However, as shown in App. C.1, this has no impact on the results of our calculations. Furthermore, the difference between the two linearized force profiles becomes negligible for longer chains. Essentially, we show in App. C.2 that in this limit the expression for $g(f)$ given in Eq. (5.130) approaches Eq. (5.122) which was derived under the assumption that the fixation at the boundary does not affect the profile.

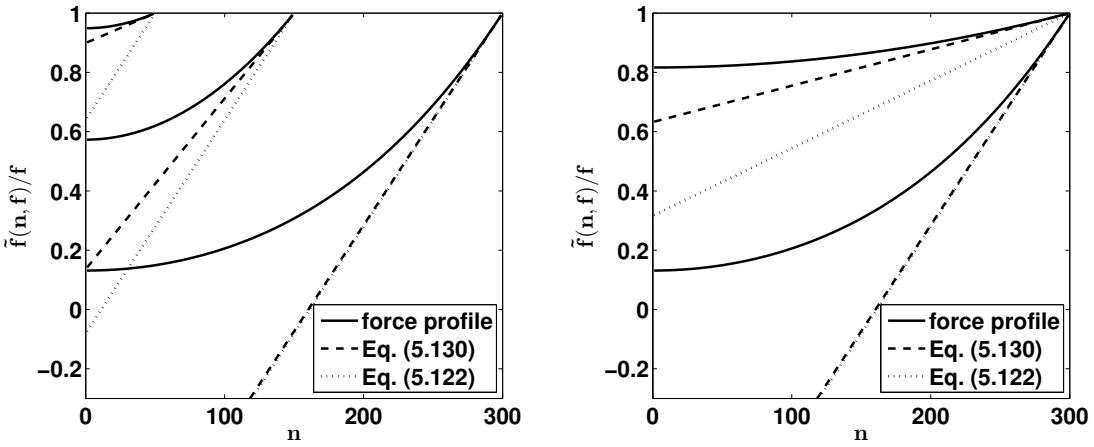

(a) (b)

Figure 5.17.: Comparison of the linearized expressions according to Eq. (5.99) with $g(f)$ taken from either Eq. (5.122) (semiinfinite chain, dotted lines) or from Eq. (5.130) (including the boundary condition at the grafted terminal, dashed lines). Superimposed is the full force profile (solid lines). All force values are given in multiples of the force value at the pulled terminal. Panel (a): Force profiles for three different chain lengths ($N = 50$, $N = 150$, and $N = 300$ from the left to the right) and a fixed value of the loading rate $\dot{f} = 2 \times 10^{-6}\,\mathrm{N/s}$. Panel (b): Force profiles for two different values of the loading rate (upper curves: $\dot{f} = 2 \times 10^{-7}\,\mathrm{N/s}$; lower curves: $\dot{f} = 2 \times 10^{-6}\,\mathrm{N/s}$). The remaining parameter values are $\gamma = 2 \times 10^{-6}\,\mathrm{kg/s}$ and $\kappa = 70\,\mathrm{N/m}$.

For these longer chains the linerization in the vicinity of the pulled end is expected to be sufficient to describe the rupture dynamics of the chain since there, were the force deviates from the linear scaling, it is yet such small that the corresponding bonds do not contribute to the rupture process of the chain. For the intermediate chain length $N = 150$ the linearization is a slightly inaccurate description of the noticeable decrease of the force along the chain. For the shortest chain especially the linear force profile derived for a semiinfinte chain becomes wrong and overestimates the force decrease which is much weaker there compared to the one of the two other chain lengths. Panel (b) shows the force profiles for two different values of the loading rate as given in the caption. For the smaller value of $\dot{f}$ (upper curves) the decrease of the force along the chain is much smaller compared to the one observed for the higher value of $\dot{f}$. In the latter case the linearized force profiles fully cover the range of relevant forces (those values of $\tilde{f}/f$ close to unity). Thus the theory is expected to work well in this parameter region.

Before presenting two examples of chain rupture we briefly discuss a more general approach to calculate the survival probability of the chain analytically.

5.5.3. Alternative calculation of the survival probability of the chain

As mentioned in the beginning of this section the calculation of the survival probability of the chain based on

$$\Phi_N(t) = \exp\left\{\int_0^N \ln\left(\Phi_1(\tilde{f}(n,t))\right) dn\right\} \tag{5.133}$$

relies on the assumption that the survival probability $\Phi_1(\tilde{f}(n,t)$ is given by the single-bond expression derived for a constant loading rate. This enabled us to derive a closed analytical expression for Φ_N as well as the rupture force distribution $\mathcal{F}_N$.

In general we do not need to know the exact form of Φ_1. This survival probability of a single bond located at site $1 \leq n \leq N$ at time t is given by

$$\Phi_1(n,t) = \exp\left[-\int_0^t \nu\left(n,t'\right) dt'\right], \tag{5.134}$$

with the Kramers rate $\nu(n,t')$ given in Eq. (5.28) and a time-dependent force $\tilde{f}(n,t) = \dot{f}t(1-g(t)(N-n))$ according to the linearized force profiles given above. Together with Eq. (5.133) we have

$$\Phi_N(t) = \exp\left[\int_0^N \left(-\int_0^t \nu(n,t')dt'\right) dn\right]. \tag{5.135}$$

We can exchange the integrals. Then, the integral over n can be calculated explicitly and after doing so we are left with

$$\begin{aligned}\Phi_N(t) = \exp\Bigg[-\frac{v}{\dot{f}}\Bigg(&\int_0^t \frac{dt'}{t'g(t')} \exp\left[-w\left(1-\frac{\dot{f}t'}{f_c}\right)^{1/b_m}\right] \\ &- \int_0^t \frac{dt'}{t'g(t')} \exp\left[-w\left(1-\frac{\dot{f}t'(1-g(t')N)}{f_c}\right)^{1/b_m}\right]\Bigg)\Bigg].\end{aligned} \tag{5.136}$$

The remaining integral in the latter expression may be solved numerically. The force at the pulled end depends linear on the time and we can deduce from $\Phi_N(f = \dot{f}t)$ the probability density distribution of the rupture forces

$$\mathcal{F}_N(f) = -\frac{d\Phi_N(f)}{df}. \tag{5.137}$$

In the next paragraphs we study the rupture dynamics of a chain of Morse bonds. We will compare the outcome of the expression (5.137) and our closed form analytical solution given in Eq. (5.107) and will find practically no differences.

5.5.4. Examples

Example 1: Chain of Morse bonds

In Sec. 5.2.2 we considered a single Morse bond loaded at a constant rate. Now we pass to a chain of such bonds, with one end, i.e., at $n = N$, exposed to a monotonically increasing force with loading rate $\dot{f} = \text{const}$. The overdamped Langevin equations of motion of a chain of N particles are [4]

$$\begin{aligned}
\gamma\dot{x}_1 =& -2D_0\alpha\left(1-e^{-\alpha x_1}\right)e^{-\alpha x_1} + 2D_0\alpha\left(1-e^{-\alpha(x_2-x_1)}\right)e^{-\alpha(x_2-x_1)} + \sqrt{2\gamma k_BT}\xi_1 \\
\gamma\dot{x}_n =& -2D_0\alpha\left(1-e^{-\alpha(x_n-x_{n-1})}\right)e^{-\alpha(x_n-x_{n-1})} + 2D_0\alpha\left(1-e^{-\alpha(x_{n+1}-x_n)}\right)e^{-\alpha(x_{n+1}-x_n)} \\
&+ \sqrt{2\gamma k_BT}\xi_n\,, \quad 1<n<N \\
\gamma\dot{x}_N =& -2D_0\alpha\left(1-e^{-\alpha(x_N-x_{N-1})}\right)e^{-\alpha(x_N-x_{N-1})} + \sqrt{2\gamma k_BT}\xi_N + \dot{f}t\,,
\end{aligned} \tag{5.138}$$

with $\{\xi_n\}$ being independent $\delta-$correlated Gaussian white noises. The local extrema of the combined free energy profile are found at

$$x_\pm(n,f) = n\left(\frac{\ln(2)}{\alpha} - \frac{1}{\alpha}\ln\left(1\pm\sqrt{1-\frac{f}{f_c}}\right)\right)\,. \tag{5.139}$$

Since f depends on time the $x_\pm$ are asymptotically reached in the limit of $\dot{f}\to 0$. For finite values of $\dot{f}$ the quasistationary distribution located close to the minima of the metastable potential wells lags behind the value of x_-.

In order to illustrate the overall rupture process we present in Fig. 5.18 a single realization of the Morse chain breakdown. The chain has $N = 10$ bonds. The system is prepared in thermal equilibrium at time $t = 0$ when the force is switched on. In this particular simulation the initial intrinsic barrier height is $\Delta E/k_BT = 87.5$ and rupture is exponentially suppressed. As time goes on (and force increases) the bonds are elongated and the combined activation barrier shrinks. Eventually, before reaching the critical force f_c, the bond connecting the beads $n = 6$ and $n = 7$ breaks.

In principle the location of breakdown is random as long as all bonds are loaded equally. Since there is a force profile along the chain the bonds at the pulled terminal are expected to break preferred. Thus let us have a closer look at the statistics of the probability density of the position of breakdown in the chain. We consider two cases: First, the chain length N is fixed and the loading rate $\dot{f}$ is varied and, second, the loading rate is fixed and the number of monomers in the chain changes.

The first case is depicted in panel (a) of Fig. 5.19. For a small loading rate, i.e., $\dot{f} = 2\times10^{-8}\,\text{N/s}$ (solid line), there is only a very slight decrease of the rupture probability density along the chain. Virtually all bonds contribute equally to the rupture process. Note, that this slight decrease is not solely caused by the delayed force propagation;

[4] As in the single-bond case, we have numerically integrated the set of equations (5.138) by use of a Heun integration scheme. A bond rupture has taken place when a reaction coordinate overcomes the activation barrier. We also tested the dependence of the measured rupture forces upon the variation of the break condition, i.e., the break condition was shifted up to $x_{n+1} - x_n >^! 5l_0$ where irreversible rupture was monitored in all simulation runs, and found a deviation not exceeding 2%.

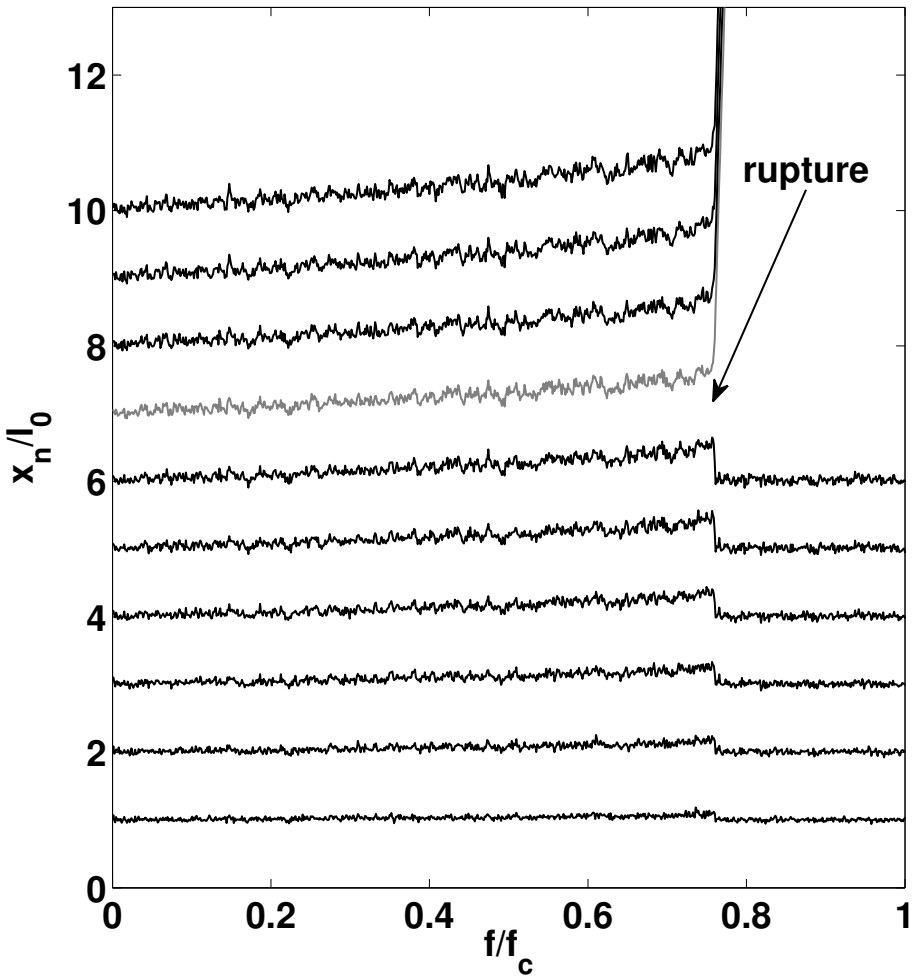

Figure 5.18.: Single realization of Morse chain rupture. Presented are coarse grained data with $\Delta t = 1\,\mu$s. The length of the chain is $N = 10$. The parameter values are $D_0 = 350\,\mathrm{pNnm}$, $k_BT = 4\,\mathrm{pNnm}$, $\gamma = 2\times10^{-6}\,\mathrm{kg/s}$, $\dot{f} = 2\times10^{-6}\,\mathrm{N/s}$, and $\alpha = 10\,\mathrm{nm}^{-1}$ yielding the dimensionless parameter values $v/\dot{f} = 175/(2\pi)$ and $w = 175/3$.

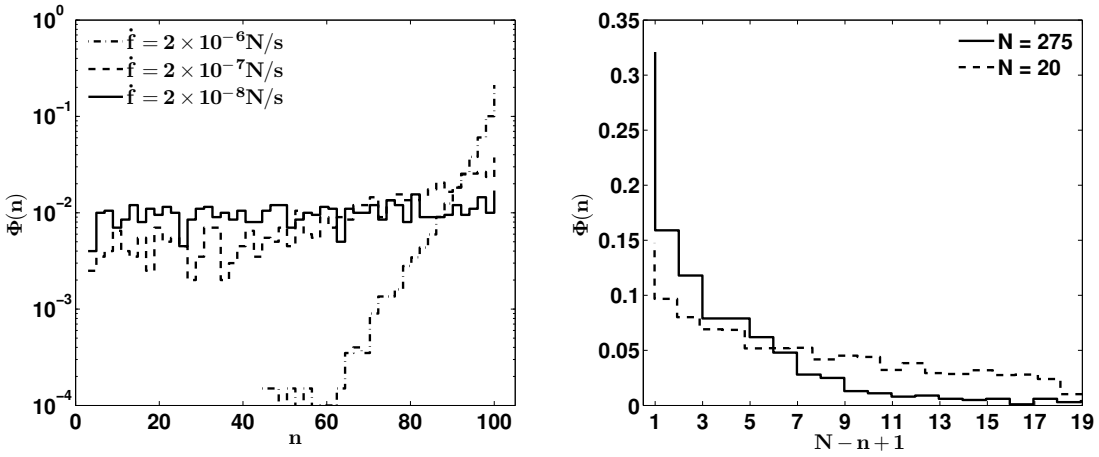

(a) (b)

Figure 5.19.: Probability density of the position of breakdown n. The parameter values are $D_0 = 350\,\mathrm{pNnm}$, $k_BT = 4\,\mathrm{pNnm}$, $\gamma = 2\times10^{-6}\,\mathrm{kg/s}$, and $\alpha = 10\,\mathrm{nm}^{-1}$. Panel (a): The chain length is fixed, $N = 100$, and the value of the loading rates is changed with values given in the legend. Panel (b): The loading rate is fixed $\dot{f} = 2\times10^{-6}\,\mathrm{N/s}$ and the different chain lengths are given in the legend.

for the parameter values given in the caption we can estimate an upper bound for the total force decrease along the chain using Eq. (5.121) and obtain $\Delta f/f|_{f=f_{max}} < 0.08$ which is negligible. Additionally there is a contribution of the non-Markovian coupled dynamics which caused a gradual increase of the mean first passage times towards the grafted terminal of a thermally activated chain in the absence of an external force, see chapter 4. We will neglect this effect in the following since for higher loading rates (dashed and dashed-dotted lines) the force propagation has the predominant impact on the chain breakdown. For $\dot{f} = 2\times10^{-6}\,\mathrm{N/s}$ only half of the chain accounts for the rupture process. Thus the number of bonds which contribute to the rupture process decrease with increasing loading rate as the force propagation is more and more delayed. In panel (b) we present the distribution of the breakdown position for a fixed value of the loading rate and two different values of the chain length N. One readily infers that the probability of a bond breakdown at a given site n decays for a longer chain (solid line) stronger with the distance from the pulled end than it does for a shorter one (dashed line). Thus, although the longer chains offer a larger number of possible breakdown sites, the number of bonds that contribute to the rupture process becomes smaller reaching a constant—loading rate-dependent—value in the limit of a semiinfinite system.

Let us now turn to the scaling of the most probable rupture force f_{max}. In Fig. 5.20 we present the numerically obtained f_{max} as a function of the chain length N for two values of the loading rate $\dot{f}$ (symbols). Superimposed is the most probable rupture force derived from the analytical expression of the rupture probability density $\mathcal{F}_N(f)$ given in Eq. (5.107) together with the linearized force profile from Eq. (5.122) (dashed line), and the theoretical prediction taking into account the grafted chain end, i.e., Eq. (5.107) together with the force profile from Eq. (5.130) (solid line). Furthermore, we depict the

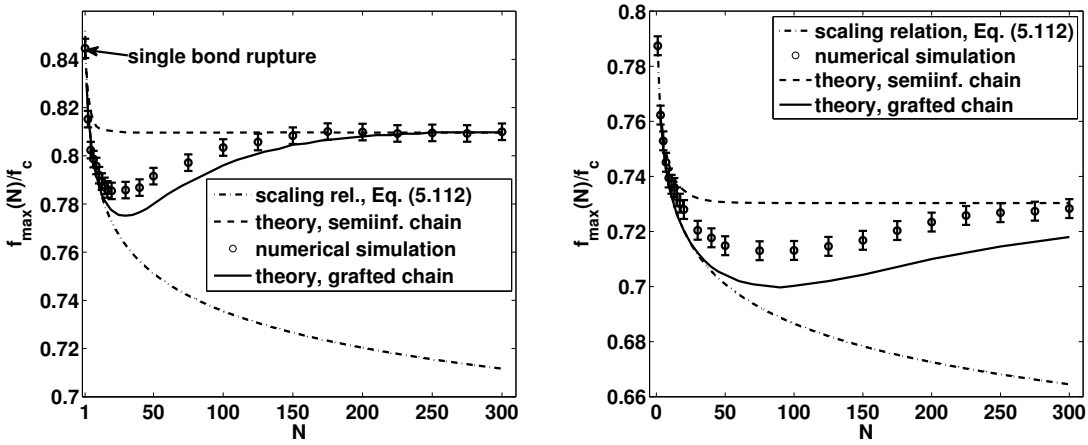

(a) (b)

Figure 5.20.: Most probable rupture force f_{max} as a function of the chain length N. Panel (a): $\dot{f} = 2 \times 10^{-6}\,\mathrm{N/s}$, panel (b): $\dot{f} = 2 \times 10^{-7}\,\mathrm{N/s}$. The remaining parameter values are the same as in Fig. 5.18. Shown is the most probable rupture force derived from the analytical expression of the rupture probability density $\mathcal{F}_N(f)$ given in Eq. (5.107) ($b_m = 2/3$) together with the linearized force profile from Eq. (5.122) (dashed line), and the theoretical prediction taking into account the grafted chain end, i.e., Eq. (5.107) together with the force profile from Eq. (5.130) (solid line). Furthermore, we depict the limiting scaling relation given in Eq. (5.112) (dashed dotted line). Error bars indicate the uncertainty due to the binning of the numerical data.

limiting scaling relation given in Eq. (5.112) (dashed dotted line). For small chain lengths the numerically obtained f_{max} follow the scaling relation given in (5.112) and with further increase of N they reach a minimal value for an intermediate value of N for both presented loading rates $\dot{f}$. The location of the minimum depends on the loading rate and is shifted to a larger length value for smaller $\dot{f}$. The limiting scaling relation is always a lower bound for the most probable rupture force. This is clear since it assumes that all bonds contribute equally to the rupture of the chain what—according to the extreme value statistics—minimizes the most probable rupture force for a given value of N. Deviations from the scaling appear when the chain length grows further. The numerically obtained f_{max} increase and eventually saturate, the latter happens at a smaller value of N for the higher value of the loading rate $\dot{f}$. Thus we observe a non-monotonic scaling of the most probable rupture force as a function of the chain length.

As expected, the f_{max} which are derived from the expression (5.107) assuming a semi-infinte chain (dashed line) fail for small chains but predict the numerical results very well for the larger N. Moreover, the solid line giving the results of Eq. (5.107) together with Eq. (5.130) captures qualitatively the non-monotonic scaling. The shape of the curve of rupture forces is nicely reproduced and in the limit of short and long chains the theory agrees also quantitatively. Furthermore, the chain length which minimizes the most probable rupture force coincides with the one derived from the numerical simulations. Deviations can result from the harmonic approximation in the derivation of the force profile:

The decay of the force profile along the chain for a soft Morse potential is expected to be more pronounced compared to the harmonic chain, so that less bonds contribute to the rupture process. This might explain the shift of the theoretical curve to lower rupture forces compared to the numerical data points.

The overall behavior can be explained as follows. A short chain has only a few bonds that can break. Each of them feels practically the same force f, since the forces acting on the bonds decrease only slightly with their distance from the pulled end, see Fig. 5.19. The longer is the chain, the more breakable bonds are present, however each of them is subjected to a tension which is smaller than f and decays with the chain's length. The interplay between the thermally activated rupture of a single bond and the force distribution along the chain generates a non-monotonic behavior of the typical rupture forces. Note, that the experimentally obtained mean rupture forces in (Embrechts et al., 2008) lead one to assume a quite similar behavior.

The scaling shown in Fig. 5.20 corresponds to a transition from the small-N scaling regime to a saturation for large N. In this limit a proportion of N_s bonds will contribute to the chain rupture and its value depends on the loading rate $\dot{f}$. N_s can be estimated as follows: A single bond rupture is governed by the probability density distribution $\mathcal{F}_1(f)$ and rupture occurs with highest probability at $\tilde{f}(n, f) = f_{max}$ with f_{max} given in Eq. (5.34). The distribution $\mathcal{F}_1(f)$ is strongly skewed to the left, and its variance is given by (Garg, 1995)

$$\sigma_1^2 = \frac{2\pi^2 f_c^2}{27 w^{4/3}} \frac{1}{\left(\ln\left(v/\dot{f}\right)\right)^{2/3}} . \tag{5.140}$$

We can assume that the rupture of a bond hardly occurs if the corresponding force is $f < f_{max} - 2\sigma_1$. The portion of the chain N_s in which the broken bond is localized is then determined by the condition that the force at the bond number $N - N_s$ is $f_{max} - 2\sigma_1$ at the time when the first bond is most probably going to break, i.e., $\tilde{f}(N - N_s, f_{max}) = f_{max} - 2\sigma_1$. Resolving Eq. (5.121) for the corresponding value of $n = N - N_s$ we get

$$N_s\left(\dot{f}\right) = \frac{\sqrt{\frac{2 f_c \kappa \pi^3}{\gamma 27 \dot{f}}}}{\left(\ln\left(v/\dot{f}\right)\right)^{1/3} w^{2/3} \sqrt{1 - \left(\frac{\ln\left(v/\dot{f}\right)}{w}\right)^{2/3}}} . \tag{5.141}$$

Taking the parameter values as in Fig. 5.19 we obtain for $\dot{f} = 2 \times 10^{-8}\,\mathrm{N/s}$ $N_s \simeq 100$, for $\dot{f} = 2 \times 10^{-7}\,\mathrm{N/s}$ $N_s \simeq 35$, and for $\dot{f} = 2 \times 10^{-6}\,\mathrm{N/s}$ we have $N_s \simeq 13$. These values are in reasonable agreement with our numerical findings. Moreover, inserting the value of N_s into the scaling relation of the most probable rupture force (5.112) offers a possibility to estimate the typical rupture force for very long chains and high loading rates, thus in the regime where the rupture force becomes independent of the chain length.

In order to show that the above presented analytical approaches not only predict the value of the most probable rupture force but also the shape of the force probability density function (PDF) of rupture forces we depict in panel (a) of Fig. 5.21 the probability density function of the rupture force f for three different values of the chain length (lines) calculated from Eq. (5.107) with the linearized force profile taking into account the grafted end of the chain (5.129). Superimposed we show the numerically obtained probability

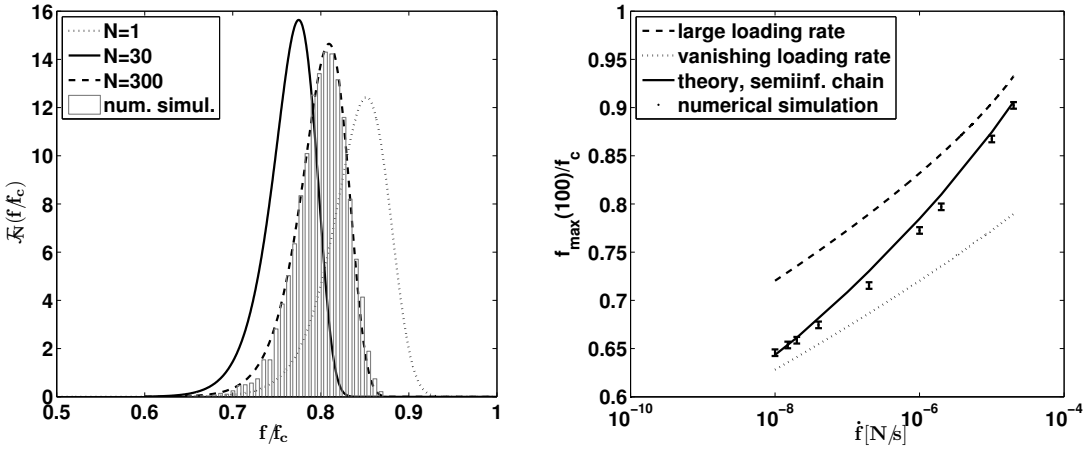

(a) (b)

Figure 5.21.: Panel (a): Distribution of rupture forces $\mathcal{F}_N$ for different chain lengths given in the legend. Lines correspond to Eq. (5.107) ($b_m = 2/3$) with the linearized force profile taking into account the grafted end of the chain (5.129). Superimposed (gray bars) is the numerically obtained distribution for $N = 300$. Panel (b): Most probable rupture force f_{max} as a function of the loading rate $\dot{f}$ for a fixed length of the chain, $N = 100$. All remaining parameter values are the same as in Fig. 5.18. Error bars indicate the uncertainty due to the binning of the numerical data.

distribution for the largest chain length (bars) $N = 300$. In this limit the theory nicely fits to the numerical data. From the curves we deduce that not only the most probable rupture force attains a minimum for some intermediate chain length but also the width of the distribution becomes narrower.

In panel (b) of Fig. 5.21 we present the numerically obtained most probable rupture force f_{max} as a function of the loading rate $\dot{f}$ for a chain of length $N = 100$ (symbols). Superimposed are the most probable rupture force derived from our analytical expression for the rupture force distribution given in Eq. (5.107) (solid line) and its two limiting approximations, either for high loading rates as given in Eq. (5.34) (dashed line) or for vanishing loading rates as given in Eq. (5.112) (dotted line). In the limit of small $\dot{f}$ the most probable rupture force tends to the prediction of Eq. (5.112): Virtually all bonds account for the rupture process of the chain. In the opposite limit of very large loading rates only a few bonds contribute to rupture (in the extreme limit only the one at the pulled end of the chain) and the scaling of f_{max} is given by Eq. (5.34). The crossover behavior is very well reproduced by the theory (Eq. (5.107)). Small deviations appear for the intermediate values of $\dot{f}$ where the exact force profile along the chain plays a role and the linear approximation in Eq. (5.121) gets inaccurate.

Finally, in Fig. 5.22, we compare the outcome of our closed form analytical expression for the probability density of rupture given in Eq. (5.107) (solid line) and the approach taking into account the nonlinear time-dependence of the force profile (symbols), see Eq. (5.137). In both cases we calculated the rupture force probability density distribution for different values of N and deduced the forces corresponding to the maxima. As it is clearly visible,

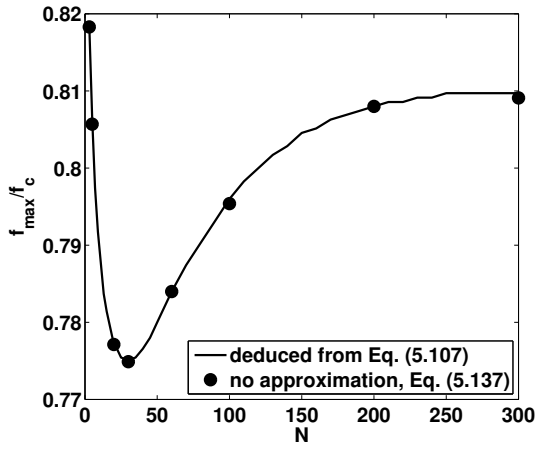

Figure 5.22.: Comparison of our closed form analytical expression for the probability density of rupture given in Eq. (5.107) (solid line) and the approach taking into account the nonlinear time-dependence of the force profile (symbols), cf., Eq. (5.137) with $b_m = 2/3$. All parameter values are the same as in Fig. 5.18.

the symbols cover the solid line. Thus we have shown in turn that the non-monotonic scaling of the rupture forces is mostly influenced by the exponentially decreasing activation rates along the chain and the typical timescale of the force propagation compared to the timescale set by the loading rate $\dot{f}$. The rate of force growth for bonds away from the pulled end is rather unimportant. There might be parameter value sets where a difference between the two approaches is observable, however in the limiting cases of both very high and very low loading rates the approaches have necessarily to coincide since then the force profile and especially its $\dot{f}$-dependence is not an input into our theory. Additionally, since no closed analytical solution is available, solving Eq. (5.137) is much more time-consuming.

Example 2: Chain of bonds described by a double-well potential

In the following we apply our theory to the dynamics of a chain of N bonds described by the DW-potential. We present such a chain to show that the scaling properties of the rupture force which we found are universal and do not depend on the specific choice of the binding potential. The properties of the single double-well activation were presented in section 5.2.2. In contrast to the previous study a barrier crossing of one of the reaction coordinates $x_{n+1} - x_n$ does not cause the breakup of the whole chain. It causes a change of the binding state of a single bond. As the force grows in time the activation of the first bond (first in time, not in space) will be followed by a cascade of bond activations until—finally—all bonds are stretched. The behavior might be compared to the unfolding of protein molecules like titin (Staple et al., 2008; Makarov et al., 2001; Hummer and Szabo, 2003; Oberhauser et al., 2001). It has to be distinguished from the opening process of zipper molecules since there the opening happens in an ordered manner, i.e., the activation of the first bond (closed to the pulled end) is followed by the activation of its neighbor and so on (Evans and Williams, 2002).

The coupled equations of motion are the same as those given in Eq. (5.138) with the

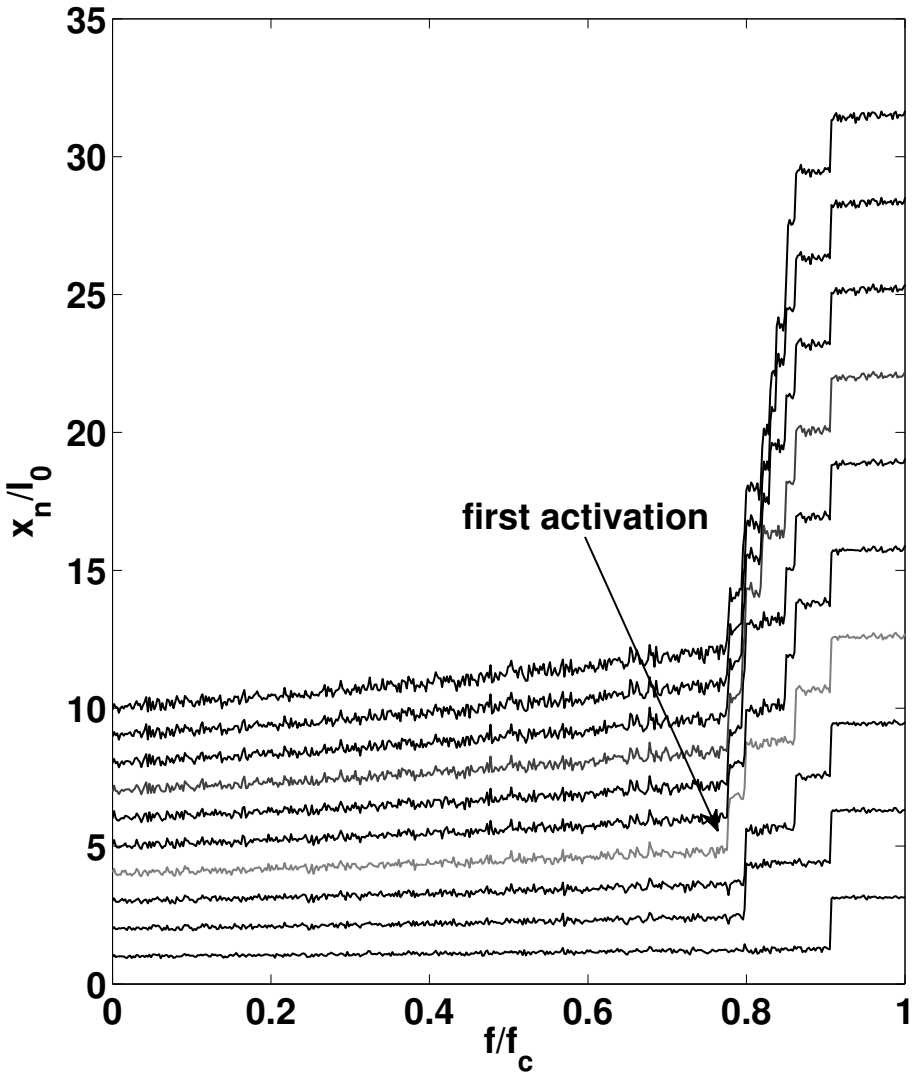

Figure 5.23.: Spatio-temporal evolution of the bead positions x_n in a single pulling experiment. Their location is scaled in multiples of the equilibrium bond length l_0 which can be set to an arbitrary value in the one-dimensional chain. The parameter values are $a = 1.28\,\mathrm{nN/nm^3}$, $b = 1.28\,\mathrm{nN/nm}$, $\dot{f} = 10^{-6}\,\mathrm{N/s}$, and $k_BT = 4\,\mathrm{pNnm}$.

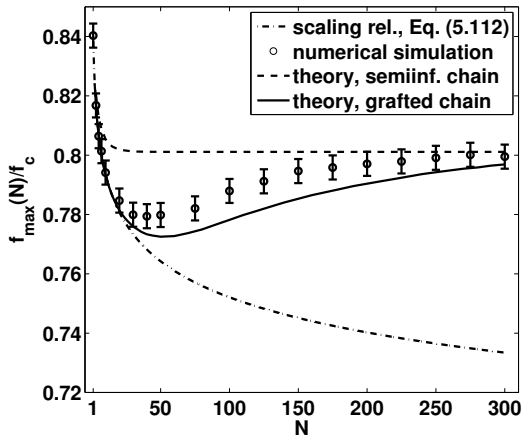

Figure 5.24.: Most probable first activation force f_{max} as a function of the chain length. The parameter values are $a = 1.28\,\mathrm{nN/nm^3}$, $b = 1.28\,\mathrm{nN/nm}$, $\dot{f} = 10^{-6}\,\mathrm{N/s}$, and $k_BT = 4\,\mathrm{pNnm}$. Shown is the most probable rupture force derived from the analytical expression of the rupture probability density $\mathcal{F}_N(f)$ given in Eq. (5.107) ($b_m = 2/3$) together with the linearized force profile from Eq. (5.122) (dashed line), and the theoretical prediction taking into account the grafted chain end, i.e., Eq. (5.107) together with the force profile from Eq. (5.130) (solid line). Furthermore, we depict the limiting scaling relation given in Eq. (5.112) (dashed dotted line). The parameter values of the abbreviations v and w are taken from Eq. (5.61) as in the single bond case. Error bars indicate the uncertainty due to the binning of the numerical data.

forces exchanged for those derived from the combined free energy profile including the DW interaction given in Eq. (5.56). In Fig. 5.23 we show the spatio-temporal evolution of the bead positions x_n. Their locations are scaled in multiples of the equilibrium bond length l_0 which can be set to an arbitrary value in the one-dimensional chain. The initial state of the simulation was generated as follows: First, the bead's position close to the wall was taken from the left half of the equilibrium probability density distribution inside the double-well. The latter distribution was generated by the use of an acceptance-rejection method. Then, the next nearest neighbor's position relative to the first bead was taken again from the same distribution. The procedure was repeated until the bond at the pulled terminal of the chain was reached. Then, after some time, the first bond (bond number 4 in the presented experiment) was activated. After some additional time, further bonds were activated in an unordered manner. The order of activation may change in different realizations. Nevertheless, the larger is the loading rate the higher is the probability that the first activation will happen close to the pulled end. We remark that, although the study of the consecutive activation of bonds might reveal an interesting insight into the coupled dynamics, we focus mainly on the first activation in the chain.

We measured numerically the forces at which the first activation happened for different chain lengths. In the numerical simulations an activation was considered to have taken place when the reaction coordinate $x_{n+1} - x_n$ passed the (force-independent) inflection point behind the activation barrier, i.e., x_c^+. In addition we calculated the most probable

rupture force using the limiting scaling relation given in Eq. (5.112) (dashed-dotted line) and the one obtained from the expression (5.107) with either (5.122) (dashed line) or (5.130) (solid line). The parameter values of the abbreviations v and w are taken from Eq. (5.61) as in the single bond case. Our results are depicted in Fig. 5.24. Like in the Morse chain we observe a non-monotonic dependence of the first activation force f_{max} of the chain length. The limiting scaling relation holds for short chains and yields a lower bound for the measured rupture forces. The most probable rupture force derived from the analytical expression of the rupture probability density $\mathcal{F}_N(f)$ given in Eq. (5.107) together with the linearized force profile from Eq. (5.122) (dashed line) predicts the force in the limit of long chains. The intermediate behavior is qualitatively well reproduced by the same theory taking into account the force profile of the grafted chain (solid line). The scaling behavior of the rupture force turns out to be independent of the model potential and, in fact, to be a result of the typically long relaxation times of the internal modes of a polymer in the viscous environment.

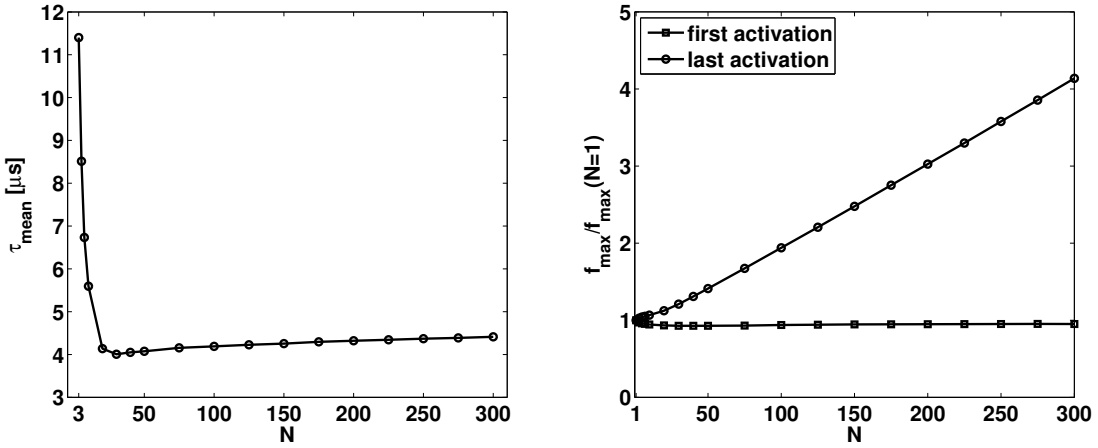

(a) (b)

Figure 5.25.: Panel (a): Mean time of activation of a bond after the first activation event as a function of the total chain length N. Panel (b): Most probable activation force f_{max} as a function of the chain length. Shown is the most probable first and last activation force in multiples of f_{max} for the single bond rupture experiment. The parameter values are the same as in Fig. 5.24.

Let us now briefly discuss the dynamics following the first activation. In Fig. 5.25 we show the mean time of activation after the first activation event, which is defined as

$$\tau_{mean} = \frac{f_{max}(\text{last}) - f_{max}(\text{first})}{(N-1)\dot{f}} \,. \tag{5.142}$$

This time turns out to be maximized for relatively short chains reaching a minimum for intermediate long ones. The location of the latter coincides with the location of the minimum of the most probable rupture forces in Fig. 5.24. For longer chains the time tends to saturate. In panel (b) we show the most probable first and last activation forces

as a function of the chain length. In the limit of long chains f_{max}(last) grows proportional to the system size N, since τ_{mean} becomes a constant. This finding is interesting since in a chain of equally loaded bonds with independent rupture dynamics the times of first and last activation should coincide. The complex interplay between the thermal activation of all the single bonds and the force distribution along the chain which generates the observed behavior goes beyond the scope of the present thesis. However, it underlines the need for a careful interpretation of experimental data when long polymer chains are involved.

5.5.5. Distributed chain lengths

In (Friedsam et al., 2003) the effect of distributed linker lengths on the rupture PDF is discussed, showing that a rectangular length distribution drastically changes the shape of the PDF of the rupture forces. In the following we study how a chain length distribution $\rho(N)$, i.e., a distribution of the number of breakable bonds, alters the rupture dynamics. Let us assume that a hypothetical pulling experiment is repeated several times with chain lengths N which vary from realization to realization of the experiment. Let us further assume that the distribution of chain lengths can be described by a well defined probability density function. Furthermore, we confine ourselves to the small loading rate regime, i.e., we neglect the effects arising from the delayed force propagation and the non-Markovian fluctuations.

For a fixed length the probability is given by $\Phi_N(f) \simeq \Phi_1(f)^N$. The measured survival probability, given the chain lengths are distributed according to some PDF $\rho(N)$, is

$$\langle \Phi_N(f) \rangle_{\rho(N)} = \tilde{\Phi}(f) = \int_0^\infty \Phi_1^N \rho(N) dN \,. \tag{5.143}$$

The probability density is then given by $\tilde{\mathcal{F}}(f) = -d\tilde{\Phi}(f)/df$. In the following we consider exemplary three different PDFs of chain lengths.

Flat length distribution

Let the chain lengths be distributed equally in an interval $[N_{min}, N_{max}]$. The PDF of chain lengths is thus given by

$$\rho(N) = \frac{1}{N_{max} - N_{min}} \Theta\left(N_{max} - N\right) \Theta\left(N - N_{min}\right) \,. \tag{5.144}$$

The survival probability averaged over the distribution of chain lengths is

$$\tilde{\Phi}(f) = \frac{1}{N_{max} - N_{min}} \frac{\Phi_1(f)^{N_{max}} - \Phi_1(f)^{N_{min}}}{\ln(\Phi_1(f))} \,, \tag{5.145}$$

and the probability density for rupture is

$$\begin{aligned} \tilde{\mathcal{F}}(f) = & \frac{\mathcal{F}_1(f)}{N_{max} - N_{min}} \left(\frac{N_{max} \Phi_1(f)^{N_{max}-1} - N_{min} \Phi_1(f)^{N_{min}-1}}{\ln(\Phi_1(f))} \right. \\ & \left. - \frac{\Phi_1(f)^{N_{max}-1} - \Phi_1(f)^{N_{min}-1}}{(\ln(\Phi_1(f)))^2} \right) \,, \end{aligned} \tag{5.146}$$

with $\Phi_1(f)$ given in Eq. (5.31) and $\mathcal{F}_1(f)$ in Eq. (5.32), being the survival probability and the rupture probability density distribution of a single bond, respectively.

In Fig. 5.26, panel (a), we compare the averaged rupture probability density distribution with a distribution for the rupture of a unique chain length corresponding to the mean value of the distribution $\rho(N)$ for three different mean chain lengths. Seemingly the maximum values belonging to the same mean chain length coincide. For the chains with the largest mean length $N = 250$ (dark gray lines) the distributions are almost equal. For the shorter chains (red and blue lines) the averaged distribution is slightly broadened to higher forces while the location of the most probable rupture force remains unchanged. The broadening is the more pronounced the shorter the average length of the chain is. Since the most probable rupture forces scale logarithmically with increasing value of N, the difference in the rupture forces is more pronounced for the shorter chains, their rupture forces deviate from the mean. Since they contribute with the same weight to the average distribution, the latter is shifted slightly to the right.

Gaussian length distribution

Let the chain lengths given by a (truncated) Gaussian distribution

$$\rho(N) = \frac{1}{\sqrt{\pi\sigma^2/2}\left(1+\mathrm{erf}(\mu/\sqrt{2\sigma^2})\right)} \exp\left(-\frac{(N-\mu)^2}{2\sigma^2}\right), \tag{5.147}$$

with $\mu = \langle N\rangle$ the mean and $\sigma^2 = \langle (N-\mu)^2\rangle$ being the width of the distribution. The truncation guarantees $N > 0$. We obtain

$$\tilde{\Phi}(f) = \frac{\Phi_1(f)^\mu \exp\left(\sigma^2/2(\ln(\Phi_1(f)))^2\right)}{1+\mathrm{erf}(\mu/\sqrt{2\sigma^2})}\left(1+\mathrm{erf}\left(\frac{\mu+\sigma^2\ln(\Phi_1(f))}{\sqrt{2\sigma^2}}\right)\right), \tag{5.148}$$

and

$$\begin{aligned}\tilde{\mathcal{F}}(f) =& \frac{\mathcal{F}_1(f)\Phi_1(f)^{\mu-1}\exp\left(\sigma^2/2(\ln(\Phi_1(f)))^2\right)}{1+\mathrm{erf}(\mu/\sqrt{2\sigma^2})} \\ &\times\left\{\sqrt{\frac{2\sigma^2}{\pi}}\exp\left(-\frac{(\mu+\sigma^2\ln(\Phi_1(f)))^2}{2\sigma^2}\right)\right. \\ &\left.+(\mu+\sigma^2\ln(\Phi_1(f)))\left(1+\mathrm{erf}\left(\frac{\mu+\sigma^2\ln(\Phi_1(f))}{\sqrt{2\sigma^2}}\right)\right)\right\}.\end{aligned} \tag{5.149}$$

In Fig. 5.26, panel (b), we compare the averaged rupture probability density distribution with a distribution for the rupture of a unique chain length for two different mean chain length. For the smaller value of μ the averaged distribution is slightly broadened to higher forces while the location of the most probable rupture force remains unchanged. The explanation is the same as for the flat distribution. Since the Gaussian distribution weights length values close to the mean with higher probability the deviations from the single length case are less pronounced compared to the flat distribution.

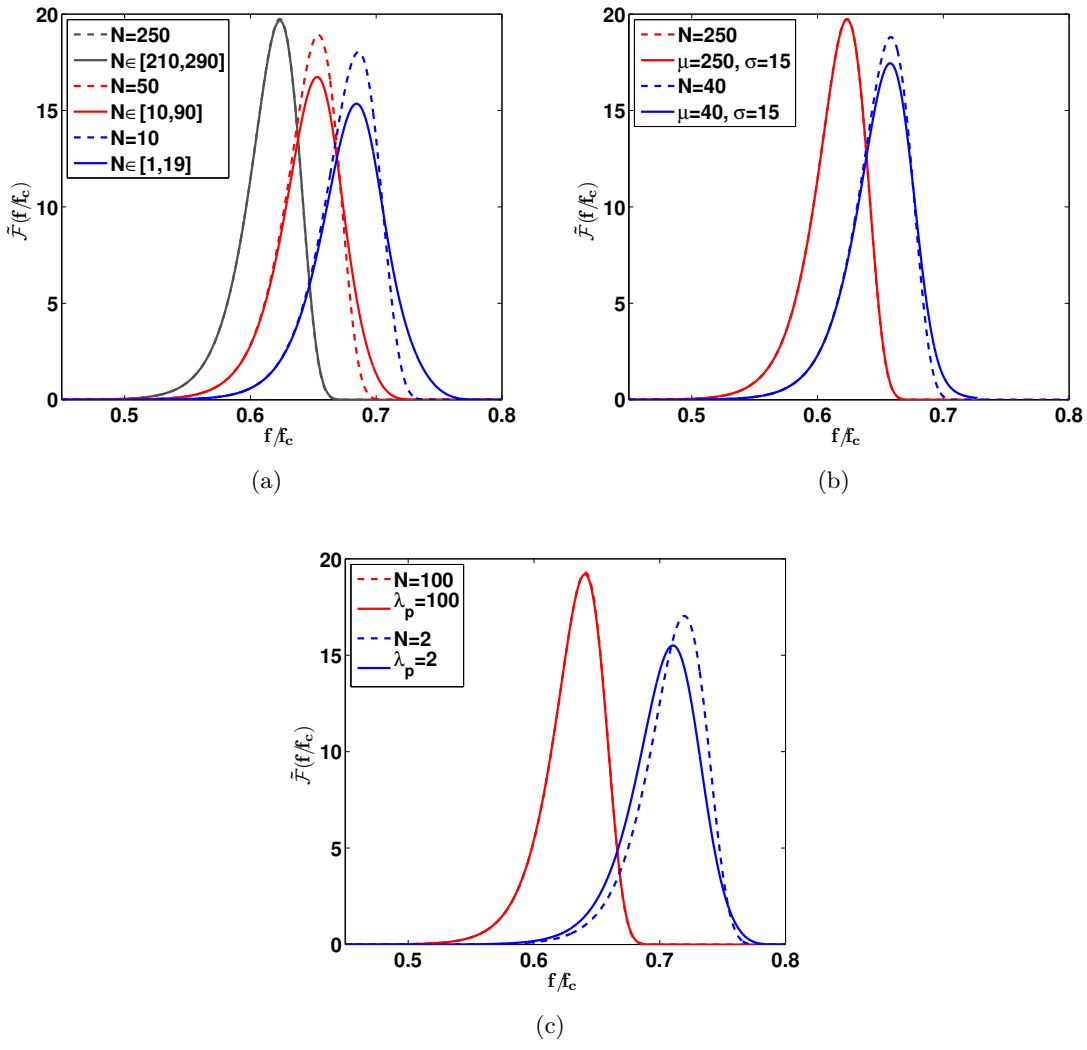

Figure 5.26.: Probability density distribution of the rupture forces f for different lengths distributions. Forces are given in multiples of the critical force f_c. Panel (a): Flat distributions derived from Eq. (5.144) with values of N_{min} and N_{max} as given in the legend, panel (b): Gaussian length distributions derived from Eq. (5.147) with values of the mean μ and the width σ as given in the legend, and panel (c): Poissonian length distributions with $\lambda_p = 2$ and $\lambda_p = 100$. In all figures the distributions for a rupture with a unique chain length corresponding to the mean value of the distribution ρ (as given in the legend) are superimposed (dashed lines). Except for the loading rate $\dot{f} = 2 \times 10^{-8}$ N/s the parameter values are the same as in Fig. 5.18.

Poissonian length distribution

Now we assume the lengths of the chains to be distributed Poissonian

$$\rho(N) = \mathrm{e}^{-\lambda_p} \frac{\lambda_p^{N-1}}{(N-1)!} \quad \text{with} \quad N = 1, 2, 3, \cdots . \tag{5.150}$$

The argument of the distribution is shifted in such way that N counts beginning with $N = 1$. The only parameter fully determining the distribution is λ_p being its mean and variance. We have

$$\tilde{\Phi}(f) = \mathrm{e}^{-\lambda_p} \sum_{N=1}^{\infty} \frac{\lambda_p^{N-1} \Phi_1(f)^N}{(N-1)!} = \Phi_1(f) \exp\left(\lambda_p \left(\Phi_1(f) - 1\right)\right) \tag{5.151}$$

and

$$\tilde{\mathcal{F}}(f) = \mathcal{F}_1(f) \left(1 + \lambda_p \Phi_1(f)\right) \exp\left(\lambda_p \left(\Phi_1(f) - 1\right)\right) . \tag{5.152}$$

In comparison to a distribution obtained for a unique chain length, for a small mean chain length λ_p the averaged distribution is now shifted to smaller values of the forces while its width is slightly larger. This is shown in Fig. 5.26, panel (c). The shift (note that the maximum value of the distribution is shifted, too) is caused by the contribution of longer chains which have smaller rupture forces. However, for the chains with a large mean number of breakable bonds the effect disappears.

To summarize, we have presented length averaged distributions of rupture forces. Length distributions tend to increase the width of the PDF. Since the maximum of the distribution for a single chain length varies logarithmically with N the deviations become smaller for the higher N. Hence we may draw the rather general conclusion, that the distribution of rupture forces obtained in an experiment performed with long chains and small length variance will hardly deviate from the distribution of the corresponding mean length. In turn, an ensemble of short chains with large variance in the chain lengths will cause a broadened and, depending on the length distribution, shifted averaged distribution.

5.6. Summary

We have studied the thermally activated rupture of polymer chains in the presence of a time-dependent force. Based on a detailed presentation of the theoretical description of the force-induced rupture of a single bond we developed an analytical framework predicting the rupture forces of polymer chains which are formed by a huge number of breakable bonds. In particular we focused on the regime of high loading rates where a model-based approximation is valid. Compared to the single bond breaking, the existence of the chain introduces new aspects into the rupture dynamics, one being the delayed force propagation along the chain at higher loading rates. Another one is the impact of non-Markovian fluctuations due to the coupled chain dynamics.

First, we found that the collective non-Markovian fluctuations have a measurable impact on the rupture forces when there is only one breakable link in a long chain of coupled monomers. This effect was studied numerically and qualitatively confirmed by theoretical considerations based on the results derived in the preceding chapter 4. There, we calculated the activation times within the framework of the Wilemski-Fixman approximation. Using

the inverse of these times as the activation rates for a bond under load in the coupled system we were able to predict the probability density distribution of the rupture forces for different chain lengths and therewith the most probable and mean rupture forces.

For large ensembles of breakable bonds linked in series the most dominant impact on the rupture dynamics originates from the force propagation into the chain. For such long chains of breakable bonds we showed that the most probable rupture force f_{max} within the model-based theory decreases with the length of the chain N proportionally to $[\ln(\text{const}N)]^{2/3}$ for short chains and saturates at a value depending on the loading rate for very long ones. In between it can exhibit a non-monotonic behavior: The most probable rupture force attains its minimum for a certain intermediate chain length. The qualitative explanation of the effect involves a complex interplay between the force propagation into the chain and the extreme-value statistics underlying rupture. A theory based on the force profile in a corresponding Rouse chain works well in the limit of short and very long chains (assuming a semiinfinite chain) and we were also able to reproduce a non-monotonic dependence of the rupture force for intermediate chain lengths (assuming the force profile of a grafted harmonic chain).

In the limit of vanishing loading rates we studied the impact of distributed chain lengths on the averaged distribution of rupture forces. We found that the corresponding distribution of rupture forces obtained in an experiment performed with long chains and small variance will hardly deviate from the distribution of the corresponding mean length. Whereas an ensemble of short chains with huge variance in the chain lengths will cause a broadened and depending on the length distribution shifted averaged distribution.

One might conclude, that the force-induced rupture kinetics at high loading rates in a coupled chain system cannot simply be described by the extreme-value statistics governing the independent rupture of bonds in series. On the one hand the force propagation proceeds on a timescale which is given by the longest relaxation time of the chain. Thus, if rupture happens at shorter times, only a part of the chain contributes to the rupture process. On the other hand, on the same timescale, the dynamics of the coupled monomers is non-Markovian. Although we have shown that the force propagation dominates compared to the non-Markovian effects, especially when pulling soft biomolecular bonds at high loading rates—with activation barrier heights which are rather low (only a few k_BT)—the impact of collective fluctuations may also significantly alter the rupture forces. Since the effects found are rather dependent on the different timescales in the system under study than on the specific parameter values they are pertinent to experimental observation.

6. Force-induced rupture of covalent bonds in the DNA molecule

6.1. Introduction

In the following chapter we present an experimental technique allowing for force-induced rupture experiments of covalent bonds under both dynamic and static load. We concentrate mainly on the interpretation of the obtained data which were kindly provided by the experimentalists group of Prof. Rabe (Humboldt University Berlin).

Concerning the application of a static load, usual experimental techniques are restricted to times smaller than approximately one minute (Garcia-Manyes et al., 2009) and therefore cannot be used to reveal the rupture kinetics of covalent bonds with usually very small intrinsic activation rates. In nature many processes involving the breakage of a single covalent bond under stress occur on substantially longer timescales. One example is the degradation of polypeptide chains strained by enzymes which lasts up to a few days (Ciechanover, 2005).

The present experiment employs a recently demonstrated *blowing manipulation* method (Severin et al., 2006) to apply a constant force to a plasmid ds-DNA molecule[1] up to one hour. DNA consists of two long polymers of units called nucleotides with backbones made of sugar and phosphate groups joined together by ester bonds (Dauxois and Peyrard, 2006). These two strands run in opposite directions to each other and are therefore antiparallel. The stretching of polymer loops on a surface is achieved by the interaction of a scanning force microscope (SFM) tip with an ultra-thin liquid layer coating a graphite surface. Plasmid ds-DNA was chosen because its circular shape is particular suitable for this blowing manipulation. Using the same SFM the force-dependent contour lengths of the loops were recorded. The force was calibrated using a structural transition of DNA molecules from the well known double helix B-form to a stress induced S-form. Plasmid ds-DNA molecules are especially suited for such experiments since they are monodisperse and well-defined polymer rings.

Based on the experimental data we estimate analytically the intrinsic parameters of the potential energy landscape of the covalent bonds such as the intrinsic activation rate and the well-to-barrier distance. Calculations rely on the Bell form which was introduced in chapter 5. A comparison of our results with known values obtained by other groups yields a good agreement. The remarkably high value of the derived intrinsic activation rate of a single covalent bond encourages us to speculate about the impact of the surface and the solvent molecules on the rupture process.

The chapter is structured as follows: In the next section we present the experimental set up, explain the blowing technique, and illustrate the rupture process of the DNA loops. In Sec. 6.3 we proceed by calculating the intrinsic activation rate of the weakest covalent

[1] a circular double stranded DNA molecule

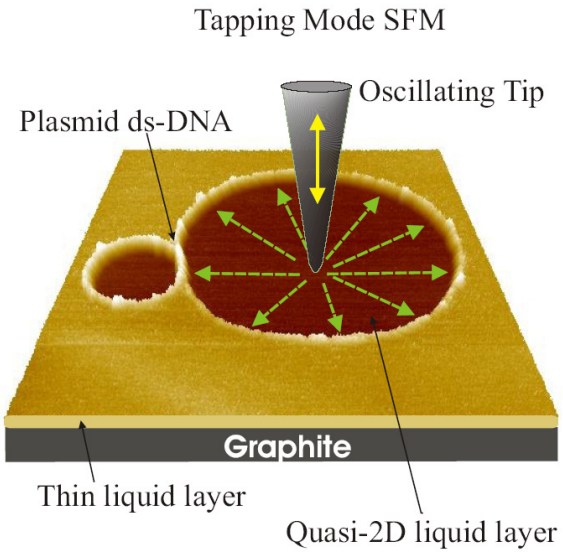

Figure 6.1.: Schematic representation of the experimental set up. A plasmid ds-DNA molecule forms two loops on the surface by self-crossing. Within the first 15 minutes of the experiment they blew into perfect circles. They maintained their shape for the next one hour before the larger loop broke.

bond in the DNA backbone as well as the location of the activation barrier. The first value can be derived without explicit knowledge of the force while the calculation of the location of the transition state enables us to verify the plausibility of the force calibration. Finally, we analyze the time evolution of the cumulative loop size distribution.

6.2. Description of the experiment

We briefly describe the experimental set up. For a detailed description the reader is referred to (Severin et al., 2006; Liang et al.). The surface with the ultra-thin liquid layer was prepared as follows: First, a droplet of chloroform solution of dodecylamine ($C_{12}H_{25}NH_2$) was spin coated onto the graphite surface. Then, a droplet of plasmid ds-DNA (pUC 19, 2686 basepairs (bp), MoBitec GmbH, and Sk 13.3, 1650 bp, MPI for Molecular Genetics Berlin) was applied to the surface and spinned off. The so prepared samples were imaged with a SFM. The sub-monolayer of dodecylamine was used to anchor the hydrophilic DNA molecules on the graphite surface. The alkyl tails of the dodecylamine adsorb on the graphite while its amine groups become positively charged in an aqueous environment and thus attract the negatively charged ds-DNA molecules. On the one hand they immobilize the DNA molecules sufficiently for imaging with tapping mode SFM, on the other hand the long alkyl tails allow for a manipulation of the DNA molecules on the surface.

Once the plasmid ds-DNA is adsorbed on the surface it forms loops of different size by self-crossings. These loops are embedded in a thin liquid film which remains on the surface after spin coating the solvent. The interaction of the SFM tip with the film creates a pressure which shapes the DNA loops to perfect circles. The resulting tangential forces acting

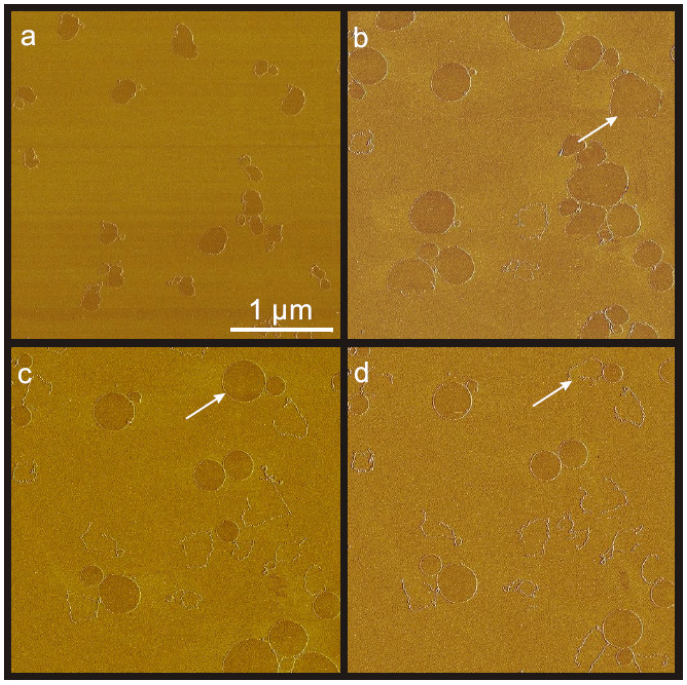

Figure 6.2.: Time evolution of the DNA loops. A series of SFM phase images taken in the same scanning area at different instants in time: a) 3 min, b) 9 min, c) 15 min, and d) 35 min. The difference in the contrast is attributed to the different thickness of the liquid layer in- and outside of the loops.

on the DNA molecules are proportional to the contour lengths of the loops. Thus typically large loops break prior to the smaller ones. Since there is no strain transmission over the DNA strands, loops formed by self-crossing of a single molecule blow independently. The schematic representation of the experimental set up is given in Fig. 6.1. Two loops formed by self-crossing of a single DNA molecule kept increasing their sizes and shaped into perfect round circles during the first 15 minutes after the imaging started. They reached a final extension ratio of 1.2 for the small loop and 1.8 for the larger loop compared to their B-form length, respectively. The latter kept its length and shape during imaging for the next one hour until it broke and the breakage did not affect the other loop. The small loop relaxed to a less stretched form and reduced its extension ratio to 1.1 upon complete evaporation of the thin liquid layer on the surface (not shown). Fig. 6.2, panels (a-d), illustrates a series of SFM phase images taken at the same scanning area of blowing plasmid ds-DNA loops. Initially relaxed loops with a phase contrast between the inside and the outside of the loops were detected on the surface. Their sizes were randomly distributed between a minimum of 150 nm and a maximum of 953 nm which is slightly larger than the B-form contour length of pUC 19 DNA, see Fig. 6.2, panel (a). As imaging continued, all loops increased their sizes and shaped into round circles. The largest loops broke during size increasing such as the one indicated by a white arrow in Fig. 6.2, panel (b). The loops became up to 2.1 times as long as their original lengths. Most loops stabilized in size after 15 minutes (Fig. 6.2, panel (c)). Breakages of the remaining loops were still observed 20 minutes after the size stabilization, such as the loop indicated by a white arrow in Fig. 6.2,

panel (d).

A contrast in the phase image between the inside and the outside of the loops implies the existence of a pressure difference. Since the force acting on a loop is proportional to its length, large loops grew faster than the small ones. The loops continue to grow, while imaging, until the force stretching the molecules becomes balanced by the restoring force of the DNA backbone. Thus, we observe two kinds of breakage: breakage under a dynamic force load (the loop indicated by an arrow in Fig. 6.2, panel (b)) and breakage under a static force load (the loop indicated by an arrow in Fig. 6.2, panels (c) and (d)).

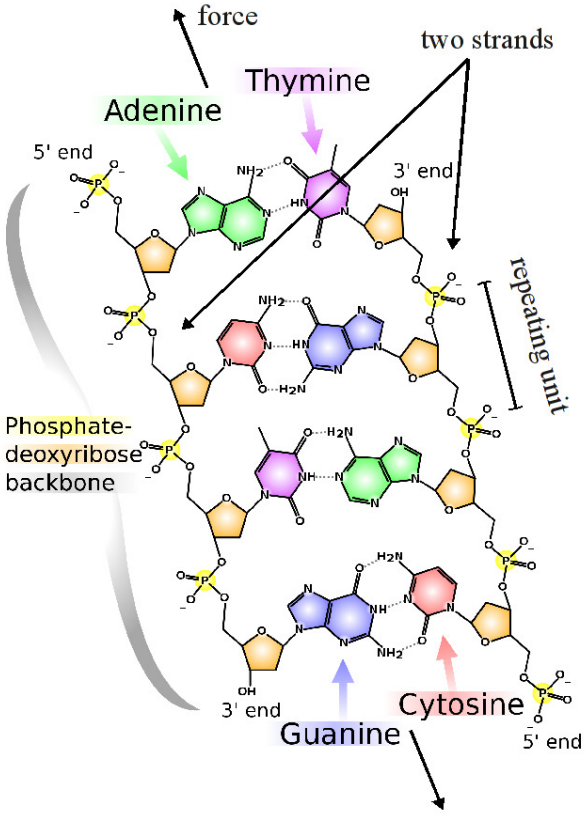

Figure 6.3.: Chemical structure of the ds-DNA. Covalent bonds are represented by solid lines and hydrogen bonds are shown as dotted lines. Arrows indicate the pulling direction. The illustration is taken from `http://en.wikipedia.org/wiki/File:DNA_chemical_structure.svg` where it has been published under the terms of the GNU Free Documentation License.

The circular shape and the difference between the inside and the outside of a blown loop suggests that the process of loop expansion is determined by a difference in the surface pressure Δp_s. Consequently for a loop of size l a tangential force $f = \Delta p_s l/(2\pi)$ forms perfectly circular rings.

The qualitative model explaining the microscopic mechanism of blowing is the following (Severin et al., 2006): One assumes that the liquid film state inside of the loop corresponds to a monolayer and takes for the sake of simplicity the thicker film outside to consist of two molecular layers. The initial formation of the monolayer inside the loop is then attributed

to hammering molecules from the second into the first layer, as well as to punching holes in the layer, which are then filled by the molecules from the second layer and from the SFM tip. Both mechanisms increase the surface of the layer and create additional pressure. The latter mechanism also persists when the monolayer is formed. The explanation of the metastability of the monolayer is based on the assumption of a very high binding energy of the molecules to the graphite surface and somewhat lower binding energy to the SFM tip material, which, however, allows for wetting of the tip by the molecules of the fluid. Therefore, the tip can gather molecules from the second layer of the film outside the loop and bring them to the interior of the circle.

DNA is an extensible molecule and its stretching properties in solution have been widely studied in single molecule manipulation experiments (Cluzel et al., 1996; Smith et al., 1996; Léger et al., 1999). The force-extension curves recorded in these experiments reveal a transition from the known double helix form (B-form) to a novel stress induced (S-form), which occurs at 110 pN and is independent of the force loading rate (Cluzel et al., 1996; Smith et al., 1996; Léger et al., 1999). Although the force is expected to depend on the environment in the present experiment (substrate, solvent and so on), a gap in the size distribution of the DNA loops starting at approximately 520 nm (shown later in Fig. 6.4) is attributed to the force of 110 pN. Using this calibration the forces are linear functions of the loop contour lengths (Liang et al.).

In order to carry out an analysis of the measured data we need to know the chemical structure of the DNA which is shown in Fig. 6.3. During the blowing experiment (arrows indicate the direction of pulling) the hydrogen bonds (dotted lines) are expected to be broken prior to the rupture of the covalent backbone due to their lower activation energy barrier and the structural transition of the double helix. One repeat unit along the DNA backbone involves two $P-O$ and $C-O$ bonds, respectively. Furthermore, there is one $C-C$ bond in the sugar residue[2] and one individual $C-C$ link.

6.3. Analysis

In the following we analyze the experimental data. Albeit the experimental method allows for measurements both in the dynamic as well as in the static loading regime, we concentrate on the latter situation. A possible interpretation of data obtained by dynamic loading is discussed at the end of this chapter. The novelty in the presented measurements is that the static force can be applied for a time ranging up to hours. In the first part we concentrate on the breakage of homopolymer loops. We estimate the intrinsic parameters of the potential energy landscape of the bonds under study and compare the results with known reference values. In the second part we consider polydisperse loops and their degradation process in time.

We remark that in principle the dynamics of the huge ensemble of monomers in the DNA strands is non-Markovian on timescales of the longest relaxation time of the coupled system. In the previous chapters we elaborated how the non-Markovian fluctuations alter the rupture process and showed that the activation rates (the inverse first passage times) are increased towards the center of a chain, especially when the activation energy barriers are low. In the present experimental set up, for symmetry reasons, the activation rates of

[2] 2-deoxyribose, which is a five-carbon ring molecule

i	Plasmid DNA	no. of bp	mean length	mean time
		n_{bp}^i	l_i [nm]	t_i [s]
1	pUC 19 (0 crossings)	2686	1787 ± 78	337 ± 230
2	pUC 19 (1 crossing)	1563	1000 to 1075	876 ± 144
3	sk 13.3	1650	1102 ± 69	762 ± 320

Table 6.1.: List of the measured average molecule lifetimes t_i and rupture lengths l_i in the static load regime for different sets of measurements. Errors indicate the standard deviations. Additionally the number of basepairs n_{bp}^i in the DNA backbone is given.

all bonds have to coincide. The applied forces are low and therefore the activation barrier is high (this is reflected in the very long molecule life times). Hence, the impact of the non-Markovian fluctuations on the escape process is expected to play only a minor role and is therefore neglected in the following.

6.3.1. Derivation of the intrinsic bond parameter values

After a time which depends slightly on the experimental realization and the size of the loop the static regime sets on. Large loops grow faster and attain their stationary contour length earlier. Average loop lifetimes and loop sizes are presented in Tab. 6.1 together with the number of basepairs in the DNA backbone[3].

During the set of measurements labeled with 1 the static regime is reached after 10 min while it is reached after 12 min during the set of measurements labeled with 2 and 15 min during experiment 3. For the DNA loops with zero crossings the number of basepairs is well known from synthesis. The situation is different for the loops with one crossing. Thus, the number of basepairs for the data set 2 (loops with one crossing) is calculated according to $n_{pb}^2 = l_2/l_1 n_{bp}^1$. The latter relation is valid after the B-S transition. From the theoretical point of view one wishes to have a large number of different loop sizes (or different total number of basepairs). As we will outline in the following the ratio of thermal activation rates in the absence of an external load is equal to the ratio of numbers of basepairs, what eventually enables us to calculate the activation rates of individual bonds in the DNA backbone. Thus a huge ensemble of different numbers of basepairs is desirable to minimize measurement uncertainties. However, since the loop length is proportional to the force acting on the bonds inside the loop, short loops with low tangential forces did not break during the measurement and therefore the usable data solely comprise the longest loops.

Focusing on the static load regime, the survival probability Φ_l of the DNA loop with contour length l follows the first order differential equation

$$\frac{d\Phi_l(t)}{dt} = -\nu_l \Phi_l(t)\,, \tag{6.1}$$

with the activation rate ν_l being the inverse loop lifetime in Tab. 6.1. For a single bond in the loop the activation rate ν_1 can be described by the phenomenological Bell form (Bell,

[3]For pUC 19 with 1 crossing the value of the length corresponds to the center of an interval ranging from 1000 nm to 1075 nm which is deduced from the experimental raw data.

1978)

$$\nu_1(f) = \nu_0 \exp\left[\frac{f\Delta x_\pm^0}{k_B T}\right] \tag{6.2}$$

for small applied forces (Friddle, 2008). The thermal activation rate of an unloaded bond ν_0 is increased exponentially upon application of a static force f with $\Delta x_\pm^0$ being the activation barrier well-to-barrier distance. The limited validity of Eq. (6.2) has already been discussed in chapter 5. Referring to Eqs. (5.10) and (5.11) for the binding potential well-to-barrier distance and activation barrier height, respectively, we notice that corrections to the Bell form are of the order $f^2/U''(x_\pm)$. The DNA backbone is formed by covalent bonds for which we expect a high stiffness ($U''(x_\pm) \gg 1$), furthermore, the measured forces are of the order of only a few hundred pN. Thus we may conclude, that the Bell form is indeed valid in this experiment.

In the experiment, the two strands of the double Helix of the ds-DNA are loaded in parallel and therefore the force acting on a single strand is half of the total applied force f. A ds-DNA loop is thus formed by a series of n_{bp} repeat units, each comprising two bonds arranged in parallel. In general, for uncorrelated rupture of N_b bonds in parallel for each level of connectivity $1 \leq n_b \leq N_b$ the failure rate is given by (Evans and Williams, 2002)

$$\nu_{n_b \to n_b - 1} = n_b \nu_0 \exp\left[\frac{f\Delta x_\pm^0}{n_b k_B T}\right], \tag{6.3}$$

and the time to break all bonds is

$$t_{N_b \to 0} = \frac{1}{\nu_0} \sum_{n_b=1}^{N_b} \frac{1}{n_b} \exp\left[-\frac{f\Delta x_\pm^0}{n_b k_B T}\right]. \tag{6.4}$$

In our special case, rupture happens in two consecutive steps, i.e., $N_b = 2$. First, one of the two bonds (both loaded with half of the measured force) breaks. Then, the remaining unbroken bond is loaded with the full force. Since the failure rate of the second step is much higher due to the double force load, the first rupture event and its corresponding time dominates the timescale of DNA loop breakage.

The thermal activation rate ν_l of the whole loop is proportional to the number of weak bonds in the two strands of the double helix which is proportional to the number of basepairs n_{bp} and to the number of weak links per basepair n_w, i.e., $\nu_l \propto 2 n_{bp} n_w$, yielding

$$\nu_l = 2 n_{bp} n_w \nu_0 \exp\left(\frac{f\Delta x_\pm^0}{2 k_B T}\right). \tag{6.5}$$

We assume that among the different covalent bonds in the backbone repeat unit of the DNA strand there is a weakest one. It is rather unimportant which is the weakest link, more important is the fact that there is probably only one per repeat unit, i.e., we set $n_w = 1$ in the following.

Considering two DNA molecules with different values of n_{bp} the ratio of the activation rates is given by

$$\frac{\nu_l^i(f_i)}{\nu_l^j(f_j)} = \frac{t_j}{t_i} = \frac{n_{bp}^i}{n_{bp}^j} \exp\left[\frac{\Delta x_\pm^0}{2 k_B T} \Delta f_{ij}\right], \tag{6.6}$$

i	Plasmid DNA	mean force
		f_i [pN]
1	pUC 19 (0 crossings)	378
2	pUC 19 (1 crossing)	220
3	sk 13.3	233

Table 6.2.: List of the measured rupture forces f_i.

with

$$\Delta f_{ij} = f_i - f_j \,. \tag{6.7}$$

The force is related to the length via

$$\Delta f_{ij} = \eth(l_i - l_j) = \eth \Delta l_{ij} \,, \tag{6.8}$$

where $\eth$ is the force calibration factor which is expected to be the same for the identical experimental conditions. The sets of measurements 1 and 2 were performed under exactly the same experimental conditions. However, as we will see, taking into account measurement 3 leads to almost the same results. The force calibration derived from the data assigns a force of 110 pN to a loop perimeter of 520 nm, thus the calibration factor is $\eth = 11/52\,\mathrm{pNnm}^{-1}$. The derived values of the rupture forces of the DNA loops are listed in Tab. 6.2. They are of the order of a few hundred pN, what is comparable with those (476 pN) obtained in stretching experiments utilizing a receding meniscus (Bensimon et al., 1995). There, the somewhat higher force caused shorter DNA lifetimes of the order of one minute.

Solving Eq. (6.6) for $\Delta x_{\pm}^0$ and inserting the values given in Tabs. 6.1 and 6.2 we obtain for both combinations of data sets, i.e., $i = 1$, $j = 2$ and $i = 1$, $j = 3$,

$$\Delta x_{\pm}^0 = 0.02\,\mathrm{nm} \,.$$

The sets of measurements 2 and 3 coincide within their errors and are thus not suitable for combined calculations. The value of $\Delta x_{\pm}^0$ is a reasonable one for a covalent bond and is consistent with the one derived in (Schwaderer et al., 2008) for a $\mathrm{Si-O}$ bond ($\Delta x_{\pm}^0 = 0.021\,\mathrm{nm}$) and thus gives the correct order of magnitude.

For the calculation of the intrinsic activation rate at zero force we do not need the explicit knowledge of the calibration factor $\eth$. Combining Eqs. (6.5) and (6.6) we obtain an expression for the intrinsic activation rate

$$\nu_0 = \frac{\nu_l^i(l_i)}{2n_{bp}^i} \left(\frac{\nu_l^i(l_i) n_{bp}^j}{\nu_l^j(l_j) n_{bp}^i} \right)^{-l_i/\Delta l_{ij}} \,. \tag{6.9}$$

Inserting the experimental data taken from Tab. 6.1 we obtain

$$\nu_0 = (2.2 \pm 0.1) \times 10^{-7}\,\mathrm{s}^{-1} \,.$$

This corresponds to a remarkably short bond lifetime of less than 53 days. Naively, one would assign a much higher stability to a covalent bond. The results can be extrapolated

to other parameter values and thus be compared to those measured by other groups. Assuming an Arrhenius law with a prefactor of the order of $10^{13}\,\mathrm{s}^{-1}$ (Wang et al., 1990) we deduce an apparent activation barrier height of $\approx 45 k_B T$ which is much smaller compared to the one of an isolated covalent bond (for a $\mathrm{C}-\mathrm{C}$ bond $\approx 140 k_B T$). However, our value is comparable with experimental results of $\mathrm{C}-\mathrm{C}$ bond rupture in ethylene absorbed on a catalytic Pt cluster ($\approx 61 k_B T$, (Wang et al., 1990)). This suggests that the catalytic surface may alter the effective energy landscape of the covalent bond.

Grandbois et al. (Grandbois et al., 1999) loaded a single covalent bond at a constant rate. In such a situation the phenomenological Bell form predicts a typical rupture force as

$$f_{max} = \frac{k_B T}{\Delta x_{\pm}^0} \ln\left(\dot{f}\frac{\Delta x_{\pm}^0}{k_B T \nu_0}\right) . \tag{6.10}$$

Inserting the above calculated values of $\Delta x_{\pm}^0$ and ν_0, furthermore the loading rate from (Grandbois et al., 1999), i.e., $\dot{f} = 10\,\mathrm{nN/s}$, and the thermal energy $k_B T = 4.06\,\mathrm{pNnm}$, corresponding to room temperature, we derive a rupture force of 3.9 nN which is very close to their result being 4.1 nN for a single $\mathrm{C}-\mathrm{C}$ bond.

The forces listed in Tab. 6.2 lie in a range from 220 pN to about 380 pN with lifetimes between 5 and 15 minutes. Stretching experiments of ds-λ-DNA using a receding meniscus brought a lifetime of approximately one minute at a force of $476 \pm 84\,\mathrm{pN}$ (Bensimon et al., 1995). A comparison with our DNA lifetimes should be done with care since the number of basepairs (roughly 48500 for the λ-DNA) differs from our experiment by a factor of the order of 10. However, we can conclude that the values of forces and lifetimes agree well within the range of uncertainty.

In the present experiment forces were considered to lower the activation barrier. We explained why the simple phenomenological Bell model might give a satisfactory description of the underlying kinetics. Beside the assumption of a fixed transition state located at $\Delta x_{\pm}^0$ the model is limited in another sense. The external force highlights one particular direction in the complex high dimensional energy landscape of the molecule. Thus extrapolating our results to zero force makes an interpretation in terms of a well defined covalent bond problematic. Taking into account the catalytic effect of the force (on the one hand lowering energetic barriers and on the other hand changing the conformation of the bond making it easier accessible for reactants) further complicates the analysis as well as taking into account interactions with the substrate. Thus we gather information about an effective bond which nevertheless does not necessarily needs to have a concrete counterpart in the molecule. Therefore, we expect that especially the activation barrier height will differ from the one of an isolated covalent bond.

6.3.2. Cumulative number of bonds for sets of polydisperse loops

So far our analysis concentrated on the breakage of DNA loops with at most one crossing. However, during the measurements the experimentalists recorded the lengths of DNA molecules with multiple crossings, too. For the pUC 19 ds-DNA the experimentally obtained cumulative number of bonds is shown in Fig. 6.4. The upper curves at early times represent the dynamic load regime, while the curves for times exceeding 12 min can be attributed to the static load regime. In contrast to the data we discussed before, the measured data in Fig. 6.4 are a sample taken from an ensemble of polydisperse loops (in

the beginning about 180). Due to crossings they have different numbers of basepairs and thus there is a widespread number of breakable bonds. The thermal activation rates of the loops differ. As time goes on the largest loops break. Their cumulative number shrinks as well as the maximum value of the contour length. The knee at approximately 520 nm designates the structural transition of the ds-DNA which was used for the calibration of the force.

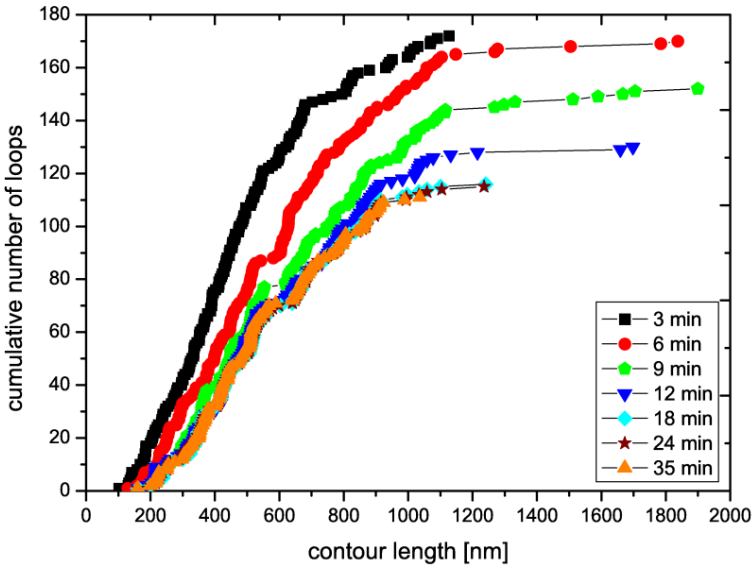

Figure 6.4.: Time development of the cumulative distribution function of loop sizes of pUC 19 ds-DNA. The upper three lines illustrate the growing of the loops and therewith the dynamic load regime. From time $t = 12\,\mathrm{min}$ the static load regime sets on.

In the following we develop a simple model trying to predict the observed decay of the cumulative number of loops under static load. The rupture rate of a DNA loop depends on its lengths in a twofold way: On the one hand, the force acting on the bonds in the loop increases linearly with its length. On the other hand, the number of breakable bonds scales linearly with the loop's contour length. The force increases exponentially the rate while a raise of breakable links causes a linear growth of the loop's activation rate.

We only take into account loop sizes well above the transition length, i.e., $l_t > 600\,\mathrm{nm}$, and describe the length distribution at $t = t_0 = 12\,\mathrm{min}$ (which is taken as initial distribution of the static load regime) by an exponential distribution

$$\rho(l) = p_\rho \exp\left(-p_\rho(l - l_t)\right) . \tag{6.11}$$

We set $1/p_\rho$ equal to the standard deviation of the measured loop lengths with $l > l_t$ at $t = t_0$ (using the mean to estimate $1/p_\rho$ gives almost the same result).

An initially given number of loops with length l decreases following first order kinetics

with a rate ν_l, i.e.,

$$N(l,t) = N(l,t_0)\exp\left[-\nu_l\,(t-t_0)\right] \tag{6.12}$$

and $N(l,t_0) = N_0\rho(l)$. The number of breakable bonds scales linearly with the contour length of the loops as

$$n_{bp} = \frac{n_{bp}^1}{l_1}l\,, \tag{6.13}$$

with the values of n_{bp}^1 and l_1 taken from Tab. 6.1. The activation rate of a loop of size l reads

$$\nu_l = \frac{2n_{bp}^1 l\nu_0}{l_1}\exp\left(\frac{l\delta\Delta x_\pm^0}{2k_BT}\right)\,. \tag{6.14}$$

Eventually the time evolution of loop lengths is governed by

$$N(l,t) = N_0 p_\rho \exp\left(-p_\rho(l-l_t)\right)\exp\left(-\frac{2n_{bp}^1 l\nu_0}{l_1}(t-t_0)\exp\left(\frac{l\delta\Delta x_\pm^0}{2k_BT}\right)\right)\,. \tag{6.15}$$

The cumulative number $\Sigma(l,t)$ of loops up to length l at time t is

$$\Sigma(l,t) = \Sigma_0 + \int_{l_t}^{l} N(l',t)dl'\,, \tag{6.16}$$

with $\Sigma_0 = 71$ being the number of loops with lengths smaller than the transition length l_t

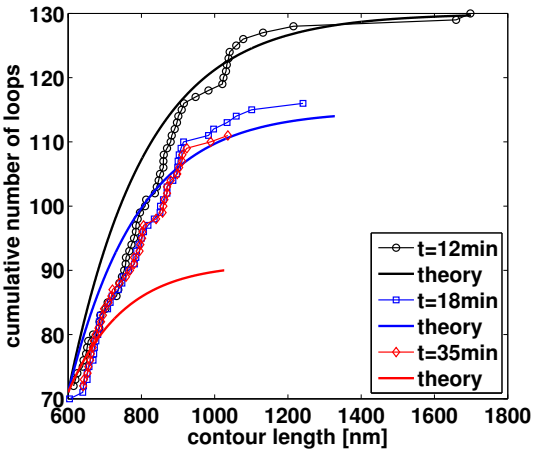

Figure 6.5.: Cumulative number of bonds at different times. We compare the experimentally obtained data (symbols) with the outcome of an analytical approximation according to Eq. (6.16). The parameter values are $N_0 = 59$, $p_\rho = 0.00476\,\mathrm{nm}^{-1}$, $l_t = 600\,\mathrm{nm}$, $\delta\Delta x_\pm^0 = 0.0041\,\mathrm{pN}$, $k_BT = 4.06\,\mathrm{pNnm}$, and $\nu_0 = 2.2\times10^{-7}\,\mathrm{s}^{-1}$.

which does not change during the experiment. In Fig. 6.5 we compare the experimentally obtained data (symbols) with the outcome of an analytical approximation according to Eq. (6.16). For short times $t-t_0$ the calculation shows a good agreement with the experimentally obtained data. The exact form of the cumulative distribution is of course not recovered with the simple exponential ansatz for the initial distribution. As soon as the

largest loops are broken, the theory predicts a further decrease of the cumulative number of loops, while in the experiment this is not observed. Though, the maximum values of the loop contour length are predicted fairly well.

6.4. Summary

Let us summarize our findings. We have analyzed experimental data of the rupture of covalent bonds in ds-DNA loops on a surface in a liquid environment. Although the experimental set up allows for dynamic and static loading we concentrated our analysis on the static part. We were able to calculate the intrinsic activation rate of a covalent bond in the repeat unit of the DNA backbone and found that this rate is by orders of magnitude larger compared to the thermal activation rate of an isolated bond. We attributed this difference to the interaction of the DNA with the surface as well as to small reactants stemming from the liquid environment. In this context force would also act as a catalyst. Such force induced chemical reactions are usually termed mechanochemical reactions, a growing field of intensive research. Even though the extrapolation to the zero force limit yields interesting results which are in need of further studies going beyond the scope of the present thesis, the comparison with the results of other groups shows a nice agreement. It is important to note that our findings are related to the presence of covalent bonds which break upon the application of an external force. The validity of the theory presented here and in the previous chapter (especially the extrapolation to zero force) describing the force-induced rupture of soft biomolecular bonds (as they are found in supramolecular molecules or ligand-receptor pairs) was demonstrated in various experiments (Merkel, 2001; Embrechts et al., 2008; Friddle, 2008).

We confirmed that the force calibration based on the structural B-S transition of the DNA leads to reliable results. Using the calibration we calculated the well-to-barrier distance of the weakest bond in the backbone repeat unit to be $\Delta x_{\pm}^{0} = 0.02\,\mathrm{nm}$ which is typical for covalent bonds. In order to predict the time-evolution of the cumulative loop size distribution we developed a simple analytical description of the breakage of the polydisperse ensemble of loops.

Finally it is worth to remark that the experimental method may also be very suitable for analyzing the regime of dynamic load, since one can study loops loaded at different rates $\dot{f}$ during one realization of the experiment. From the cumulative distribution given in Fig. 6.4 for short times one deduces that the loading rate differs for the different loop sizes, i.e., following a horizontal line the increase in size (and thus in the force) per 3 min timestep is smaller for the shorter loops. One estimates a loading rate of approximately $\dot{f} = 0.1\,\mathrm{pN/s}$ for the largest loops and significantly smaller values for the shorter ones. Since for the latter no rupture was observed they cannot contribute to the rupture statistics.

In the dynamic loading regime useful information on the intrinsic parameters of the breaking bond are derived from the scaling of the rupture force as a function of the loading rate. Hence, one wishes to cover experimentally rupture events happening over a wide range of loading rates. The present experiment does not cover this wide range of loading rates. However, if it became possible to blow longer chains, one would probably observe a broader range of loading rates which results in the breakage of loops of very different size making the experimental technique a powerful tool for analyzing the dynamic breakage of covalent bonds.

7. Summary and concluding remarks

In this work we have addressed the problem of thermal activation and force-induced rupture in polymer chains. A related concern has been the study of the equilibrium relaxation properties of nonlinear polymer chains. In this context we have formulated two main questions in the introduction. Answers have been given in the preceding chapters using analytical calculations as well as numerical simulations.

The first question was, what kind of minimal assumptions about the intramolecular potentials have to be made to build a simple model mimicking the strong internal friction observed in complex realistic experiments and asked how nonlinear interactions alter the equilibrium relaxation behavior of the polymer motion?

We have found that in chains with nonlinear interaction potentials, the relaxation properties of the end-to-end distance and the principal components are essentially those of the harmonic chain, though with shifted correlation times. Whether typical correlation times are decreased or increased depends on the type of nonlinearity. Soft nonlinear potentials increase the correlation times. While these changes are not too large for the single-well potentials, for the double-well ones they can lead to the increase in the relaxation times by orders of magnitude. Thus strong internal friction may be modeled by use of the simple double well potential with effective parameters derived from a more complex original model. The principal components, which have been shown to follow the normal modes of the harmonic chain, independent of the interaction between the beads, can exhibit vastly different kinetics, both with respect to the characteristic times and to the overall scaling. For the double-well potentials the latter can correspond to subdiffusion. To substantiate the validity of our results derived in a simple one-dimensional model, it has been shown numerically that the same behavior can be found in a more realistic three-dimensional polymer chain model.

Thus, soft nonlinearities and especially barriers in the free energy landscape may drastically increase typical equilibrium relaxation times of a polymer chain. Since the motion of the polymer exhibits a non-Markovian behavior on timescales shorter than its longest relaxation time an increase of the latter affects dynamical processes in the chain such as the thermal activation of its bonds.

This leads to the second question which was, how the activation dynamics of bonds is influenced by the presence of the chain and how the thermal stability of a polymer chain is affected by its non-Markovian dynamics?

For the purpose of answering this question, we have considered two experimentally relevant situations. First, the thermal activation of a homopolymer chain which takes place in the absence of an external force, describing chain fragmentation in a liquid environment. In our simple model the dynamics of the intact chain is a Rouse one until a bond breaks and bond breakdown is considered as a first passage problem over a barrier to an absorbing boundary. Within the framework of the Wilemski-Fixman approximation we were able to derive an analytical expression of the mean first passage time. It has been shown that the

fragmentation rate of the chain follows a nonlinear scaling as a function of the number of its breakable bonds. Bond rupture happens with higher probability at free chain ends. Studying the activation times of individual bonds we have focused on the impact of their location in the chain and the length of the latter. We have found that towards the center of the free chain as well as towards the grafted terminal of the fixed chain the activation times increase substantially. In the Markovian limit of high activation barriers the distribution of the fragmentation location in the chain flattens, since the activation rates, being the inverse mean first passage times, become equal along the chain.

Second, we have studied a set up corresponding to the one found in single molecule pulling experiments. A polymer chain is pulled at one of its ends with a force that increases in time while the opposite end is kept fixed. In addition to the non-Markovian fluctuations induced by the coupled dynamics, the delayed force propagation in the chain has an impact on its overall rupture dynamics. We have shown that in large ensembles of breakable bonds the non-Markovian fluctuations play a minor role for the scaling of the rupture forces. However, it has a measurable effect on the rupture forces when there is one breakable link in a long chain of monomers. For such systems we were able to give analytical expressions for the rupture force distribution based on our results derived within the Wilemski-Fixman approximation of first passage times in coupled systems. In long chains of breakable bonds we have found that the most probable rupture force f_{max} exhibits a non-monotonic scaling as a function of the chain length N. For short chains its decrease is proportional to $[\ln(\text{const}N)]^{2/3}$ and it saturates at a value depending on the loading rate for very long ones. In between it can exhibit a non-monotonic behavior: The most probable rupture force attains its minimum for a certain intermediate chain length. The qualitative explanation of the effect involves a complex interplay between the force propagation into the chain and the extreme-value statistics underlying rupture. We were able to derive a theoretical model which reproduces the numerically observed non-monotonic scaling of the rupture force.

Finally we have analyzed experimental data of the rupture of ds-DNA loops on a surface in a liquid environment. We have calculated the intrinsic activation rate of a covalent bond in the repeat unit of the DNA backbone and found that this rate is by orders of magnitude larger compared to the thermal activation rate of an isolated bond. We have attributed this difference to the interaction of the DNA with the surface as well as to small reactants stemming from the liquid environment. In this context force would act as a catalyst. Even though the extrapolation to the zero force limit yields interesting results which are in need of further studies going beyond the scope of the present thesis, the comparison with the results of other groups showed a fairly well agreement. Also, we have calculated the well-to-barrier distance of the weakest bond in the backbone repeat unit and developed an analytical description of the breakage kinetics of a polydisperse ensemble of loops.

In summary, our work shows how the complex dynamics of a coupled chain system alters internal processes such as bond rupture. A complex interplay of extreme-value statistics, internal correlation times, and force loading rates complicates rupture kinetics even in extremely simple chain models. It would be gratifying if this work caused some inspiring ideas to experimentalists or theoreticians for further studies.

Appendices

A. The Rouse normal modes

The connectivity matrix $\mathbb{W}$ of the Rouse model has the following form

$$\mathbb{W} = \begin{pmatrix} (2-\epsilon_1) & -1 & & & 0 \\ -1 & 2 & \ddots & & \\ & \ddots & \ddots & \ddots & \\ & & \ddots & 2 & -1 \\ 0 & & & -1 & (2-\epsilon_2) \end{pmatrix} . \tag{A.1}$$

The values of ϵ_1 and ϵ_2 put constraints on the chain ends. For $\epsilon_1 = \epsilon_2 = 1$ the chain is free, for $\epsilon_1 = 0$ and $\epsilon_2 = 1$ one end is fixed, and for $\epsilon_1 = \epsilon_2 = 0$ both ends are fixed resembling a closed loop. Let us start from a more general point. Consider a tridiagonal matrix

$$\mathbb{W} = \begin{pmatrix} a_N & b_N & & & & 0 \\ c_N & a_{N-1} & b_{N-1} & \ddots & & \\ & \ddots & \ddots & \ddots & & \\ & & & & a_1 & b_1 \\ 0 & & & & c_1 & a_0 \end{pmatrix} . \tag{A.2}$$

Its determinant can be computed by the recursive formula

$$\det \mathbb{W}_N = a_N \det \mathbb{W}_{N-1} - b_N c_N \mathbb{W}_{N-2} \, . \tag{A.3}$$

Thus, we may write

$$\begin{pmatrix} \det \mathbb{W}_N \\ \det \mathbb{W}_{N-1} \end{pmatrix} = \begin{pmatrix} a_N & -b_N c_N \\ 1 & 0 \end{pmatrix} \begin{pmatrix} \det \mathbb{W}_{N-1} \\ \det \mathbb{W}_{N-2} \end{pmatrix} = T_N \begin{pmatrix} \det \mathbb{W}_{N-1} \\ \det \mathbb{W}_{N-2} \end{pmatrix} , \tag{A.4}$$

or in a more compact form

$$\begin{pmatrix} \det \mathbb{W}_N \\ \det \mathbb{W}_{N-1} \end{pmatrix} = \mathbb{T}_N \cdot \mathbb{T}_{N-1} \cdots \mathbb{T}_1 \begin{pmatrix} a_0 \\ 1 \, , \end{pmatrix} , \tag{A.5}$$

with the transfer matrix

$$\mathbb{T}_k = \begin{pmatrix} a_k & -b_k c_k \\ 1 & 0 \end{pmatrix} . \tag{A.6}$$

The chain with both ends fixed

We start with the case $\epsilon_1 = \epsilon_2 = 0$ and the matrix $\mathbb{W}$ has the form

$$\mathbb{W}^1 = \begin{pmatrix} a & -1 & & & 0 \\ -1 & a & \ddots & & \\ & \ddots & \ddots & \ddots & \\ & & \ddots & a & -1 \\ 0 & & & -1 & a \end{pmatrix}, \tag{A.7}$$

with $a = 2$ for a chain with local coupling. Using Eq. (A.3) and the notation $\mathcal{D}_N = \det \mathbb{W}^1_N$ we obtain

$$\mathcal{D}_N(a) = a\mathcal{D}_{N-1}(a) - \mathcal{D}_{N-2}(a)\,, \tag{A.8}$$

together with the initial conditions $\mathcal{D}_0(a) = 1$ and $\mathcal{D}_1(a) = a$. The latter recursion formula is essentially the recursion formula of the Chebyshev polynomials. In fact, the $\mathcal{D}_N(a)$ are the Chebyshev polynomials of the second kind $\mathcal{U}_N(a/2)$ (Nash, 1986). Hence, the solution of Eq. (A.8) is given by

$$\mathcal{D}_N(a) = \mathcal{U}_N(a/2) = \frac{\sin\left((N+1)\,\mathrm{acos}(a/2)\right)}{\sin\left(\mathrm{acos}(a/2)\right)}\,, \tag{A.9}$$

and the eigenvalues of $\mathbb{W}^1$ have to fulfill

$$\mathcal{U}_N\left(\frac{a-\lambda^l_k}{2}\right) = 0\,, \tag{A.10}$$

what gives

$$\lambda^l_k = a - 2\cos\left(\frac{k\pi}{N+1}\right)\,. \tag{A.11}$$

The components of the corresponding eigenvectors follow Eq. (A.8)

$$\mathbf{u}_k(n+1) = \left(a - \lambda^l_k\right)\mathbf{u}_k(n) - \mathbf{u}_k(n-1)\,, \tag{A.12}$$

with the boundary conditions $\mathbf{u}_k(0) = \mathbf{u}_k(N+1) = 0$. The normalized solutions of Eq. (A.12) are

$$\mathbf{u}_k(n) = \sqrt{\frac{2}{N+1}}\sin\left(\frac{nk\pi}{N+1}\right)\,, \tag{A.13}$$

and for $a = 2$ the corresponding eigenvalues read

$$\lambda^l_k = 4\sin^2\left(\frac{k}{N+1}\frac{\pi}{2}\right)\,. \tag{A.14}$$

To summarize, we have calculated the eigenvectors (normal modes) and corresponding eigenvalues (which are proportional to the inverse relaxation times) of a chain whose both ends are fixed.

The chain with one end fixed

Next we consider the connectivity matrix of the following form

$$\mathbb{W}^2 = \begin{pmatrix} a-1 & -1 & & & 0 \\ -1 & a & \ddots & & \\ & \ddots & \ddots & \ddots & \\ & & \ddots & a & -1 \\ 0 & & & -1 & a \end{pmatrix}, \tag{A.15}$$

describing for $a = 2$ a chain with local coupling and, in contrast to the previous situation, only one fixed end. Using Eq. (A.8) we obtain for the determinant of $\mathbb{W}^2$

$$\begin{aligned} \det \mathbb{W}_N^2(a) &= (a-1)\mathcal{D}_{N-1}(a) - \mathcal{D}_{N-2}(a) \\ &= \mathcal{D}_N(a) - \mathcal{D}_{N-1}(a)\,. \end{aligned} \tag{A.16}$$

Demanding $\det \mathbb{W}_N^2(a - \lambda_k^g) = 0$ and using Eq. (A.9) we obtain the equality

$$\sin\left((N+1)\operatorname{acos}\left(\frac{a-\lambda_k^g}{2}\right)\right) = \sin\left(N\operatorname{acos}\left(\frac{a-\lambda_k^g}{2}\right)\right), \tag{A.17}$$

having for $k = 1, \ldots, N$ the nontrivial solutions

$$\lambda_k^g = a - 2 + 4\sin^2\left(\frac{2k-1}{2N+1}\frac{\pi}{2}\right). \tag{A.18}$$

From the recursion formula for the Chebyshev polynomials given in Eq. (A.12) with λ_k^g substituted for λ_k^l the eigenvectors are found to be

$$\mathbf{u}_k(n) = \frac{2}{\sqrt{2N+1}}\cos\left(\frac{(2k-1)(2n-1)}{2N+1}\frac{\pi}{2}\right). \tag{A.19}$$

Since the matrix $\mathbb{W}^2$ becomes the connectivity matrix of a chain fixed at $n = 0$ when the first and last element on the diagonal axis are exchanged, the corresponding normalized eigenvalues are given by substituting $N + 1 - n$ for N and thus

$$\mathbf{u}_k(n) = \frac{2}{\sqrt{2N+1}}\sin\left(2n\frac{2k-1}{2N+1}\frac{\pi}{2}\right). \tag{A.20}$$

The corresponding eigenvalues with $a = 2$ are

$$\lambda_k^g = 4\sin^2\left(\frac{2k-1}{2N+1}\frac{\pi}{2}\right). \tag{A.21}$$

The free chain

Finally we consider the most common case when both ends of the chain are free. In addition to the previous situations the chain's center of mass is allowed to diffuse, hence

the zero mode eigenvector is

$$\mathbf{u}_0 = \sqrt{\frac{1}{N+1}}\,(1,1,\ldots,1)_{N+1}\ . \tag{A.22}$$

The connectivity matrix of the free chain reads

$$\mathbb{W}^3 = \begin{pmatrix} a-1 & -1 & & & 0 \\ -1 & a & \ddots & & \\ & \ddots & \ddots & \ddots & \\ & & \ddots & a & -1 \\ 0 & & & -1 & a-1 \end{pmatrix}\ . \tag{A.23}$$

One can make use of the following coordinate transformation

$$\hat{\mathbb{W}}^3 = \begin{pmatrix} 1 & 1 & & & 0 \\ 1 & -1 & 1 & & \\ 1 & 0 & -1 & \ddots & \\ \vdots & & & \ddots & 1 \\ 1 & 0 & & 0 & -1 \end{pmatrix}\ . \tag{A.24}$$

The matrix $\mathbb{W}^3$ can be transformed to

$$(\hat{\mathbb{W}}^3)^{-1} \cdot \mathbb{W}^3_N(a) \cdot \hat{\mathbb{W}}^3 = \begin{pmatrix} 0 & 0 \\ 0 & \mathbb{W}^1_{N-1}(a)\,. \end{pmatrix}\ . \tag{A.25}$$

Thus using Eq. (A.11) the eigenvalues are

$$\lambda^f_k = a - 2 + 4\sin^2\left(\frac{k}{N}\frac{\pi}{2}\right)\ . \tag{A.26}$$

Furthermore the normalized solutions of Eq. (A.12) read

$$\mathbf{u}_k(n) = \sqrt{\frac{2}{N}}\cos\left(\left(n-\frac{1}{2}\right)\frac{k\pi}{N}\right)\ . \tag{A.27}$$

Changing n for $n+1$ and N for $N+1$ we obtain the eigenvectors for a free chain with beads labeled from $n=0$ to $n=N$

$$\mathbf{u}_k(n) = \sqrt{\frac{2}{N+1}}\cos\left(\left(n+\frac{1}{2}\right)\frac{k\pi}{N+1}\right)\ , \tag{A.28}$$

and the corresponding eigenvalues (with $a=2$)

$$\lambda^f_k = 4\sin^2\left(\frac{k}{N+1}\frac{\pi}{2}\right)\ . \tag{A.29}$$

B. PCA - Eigenvectors of the covariance matrix

The measured data set $\mathbb{X}$ comprises a $N \times M$ matrix, where N is the number of variables and M is the number of samples. The aim is to derive an orthonormal matrix $\mathbb{P}$ with $\mathbb{Y} = \mathbb{P}\mathbb{X}$ such that $\mathbb{C}_{YY} = 1/(M-1)\mathbb{Y}\mathbb{Y}^T$ is diagonalized. The rows of $\mathbb{P}$ are the PCs of $\mathbb{X}$.

We have

$$\begin{aligned} \mathbb{C}_{YY} &= \frac{1}{M-1}\mathbb{Y}\mathbb{Y}^T \\ &= \frac{1}{M-1}(\mathbb{P}\mathbb{X})(\mathbb{P}\mathbb{X})^T \\ &= \frac{1}{M-1}\mathbb{P}(\mathbb{X}\mathbb{X}^T)\mathbb{P}^T \\ &= \frac{1}{M-1}\mathbb{P}(\mathbb{A})\mathbb{P}^T\,. \end{aligned} \tag{B.1}$$

For the symmetric matrix $\mathbb{A}$ it holds that

$$\mathbb{A} = \mathbb{E}\mathbb{D}\mathbb{E}^T\,, \tag{B.2}$$

with $\mathbb{D}$ being a diagonal matrix and the matrix $\mathbb{E}$ which is build from the eigenvectors of $\mathbb{A}$. Choosing $\mathbb{P}$ such that $\mathbb{P} \equiv \mathbb{E}^T$ and substituting it into Eq. (B.1) we have

$$\begin{aligned} \mathbb{C}_{YY} &= \frac{1}{M-1}\mathbb{P}(\mathbb{P}^T\mathbb{D}\mathbb{P})\mathbb{P}^T \\ &= \frac{1}{M-1}(\mathbb{P}\mathbb{P}^{-1})\mathbb{D}(\mathbb{P}\mathbb{P}^{-1}) \\ &= \frac{1}{M-1}\mathbb{D}\,. \end{aligned} \tag{B.3}$$

Here we made use of the fact that for any orthogonal matrix $\mathbb{P}^{-1} = \mathbb{P}^T$.

The choice of the matrix $\mathbb{P}$ diagonalizes $\mathbb{C}_{YY}$. The PCs of $\mathbb{X}$ are the eigenvectors of $\mathbb{A}$ and the rows of $\mathbb{P}$.

C. The force profile of the grafted chain

C.1. Linear approximation and long chains

The linear approximation of the force profile is given by

$$\tilde{f}(n,f) \simeq \begin{cases} f\left(1-g(f)(N-n)\right), & N \leq 1/g(f) \\ 0, & N > 1/g(f), \end{cases} \tag{C.1}$$

with $f(N) \equiv f$ and the function $g(f)$ given in Eq. (5.122). Let us first consider the case when $N \leq 1/g(f)$. Then we have

$$\Phi_N(f) = \Phi_0^N \exp\left\{-\frac{v}{\dot{f}}\int_0^N \exp\left\{-w\left(1-\frac{f}{f_c}\left(1-g(f)n\right)\right)^{1/b_m}\right\}dn\right\} \tag{C.2}$$

and recover Eq. (5.100).

Now we consider the case of large system sizes or high loading rates, i.e., $N > 1/g(f) = \sqrt{\kappa\pi f/(4\gamma\dot{f})}$. The probability function is now given by

$$\begin{aligned}\Phi_N(f) = \Phi_0^N \exp\Bigg\{-\frac{v}{\dot{f}}\Bigg\{\int_0^{1/g(f)} \exp\left\{-w\left(1-\frac{f}{f_c}\left(1-g(f)n\right)\right)^{1/b_m}\right\}dn \\ + \int_{1/g(f)}^N \mathrm{e}^{-w}\,dn\Bigg\}\Bigg\}.\end{aligned} \tag{C.3}$$

Carrying out the integral gives

$$\Phi_N(f) = \Phi_0^N \exp\left\{-\frac{v}{\dot{f}}\left\{\frac{b_m f_c}{w^{b_m} f g(f)}\left[\Gamma\left(b_m, e(f)\right) - \Gamma\left(b_m, w\right)\right] + \left(N-\frac{1}{g(f)}\right)\mathrm{e}^{-w}\right\}\right\}, \tag{C.4}$$

with

$$e(f) = w\left(1-\frac{f}{f_c}\right)^{1/b_m}. \tag{C.5}$$

The probability density function of the rupture forces reads

$$\begin{aligned}\mathcal{F}_N(f) = -\Phi_N(f)\Bigg\{\frac{v b_m f_c}{w^{b_m}\dot{f} f g(f)}\left(\frac{1}{f}+\frac{d(f)}{g(f)}\right)\left[\Gamma\left(b_m, e(f)\right) - \Gamma\left(b_m, w\right)\right] \\ + \frac{d(f)}{g(f)^2}\mathrm{e}^{-w} - \frac{v}{\dot{f} f g(f)}\mathrm{e}^{-e(f)}\Bigg\},\end{aligned} \tag{C.6}$$

with $d(f) = dg(f)/df$. Evaluating Eqs. (C.4) and (C.6) gives practically the same results as those derived from Eqs. (5.105) and (5.107), respectively.

C.2. Linearized force profile in the limit of very long chains

The linearized force profile close to the pulled chain end is given by

$$\tilde{f}(n,f) = f\left(1 - g(f)(N-n)\right) , \tag{C.7}$$

with $f(N) \equiv f$ and the function $g(f)$ which is independent of the system size for the semiinfinite chain. In chapter 5.5.2 we calculated

$$g(f) = g_{si}(f) = \frac{2\sqrt{\gamma \dot{f}}}{\sqrt{\kappa \pi f}} . \tag{C.8}$$

Taking into account the grafted terminal we got

$$\begin{aligned} g(f) = 1 - \frac{2\kappa\tau_1^g}{N\gamma} \sum_{k=1}^{\infty} \sin\left(\frac{k\pi}{2}\right) \left\{ \sin\left(\frac{k\pi\left(N-\frac{1}{2}\right)}{2N}\right) - \sin\left(\frac{k\pi\left(N-\frac{3}{2}\right)}{2N}\right) \right\} \\ \times \left(\frac{1}{k^2} - \frac{\dot{f}\tau_1^g}{fk^4}\left(1 - \exp\left[-\frac{k^2 f}{\dot{f}\tau_1^g}\right]\right)\right) , \end{aligned} \tag{C.9}$$

instead. We proceed to show that the latter expression approaches the one for the semiinfinite chain $g_{si}(f)$ in the limit of $N \to \infty$. Let us first have a look at the trigonometric functions:

$$\begin{aligned} &\sin\left(\frac{k\pi}{2}\right) \left\{ \sin\left(\frac{k\pi\left(N-\frac{1}{2}\right)}{2N}\right) - \sin\left(\frac{k\pi\left(N-\frac{3}{2}\right)}{2N}\right) \right\} = \\ &\sin\left(\frac{k\pi}{2}\right)^2 \left(\cos\left(\frac{k\pi}{4N}\right) - \cos\left(\frac{3k\pi}{4N}\right)\right) - \sin\left(\frac{k\pi}{2}\right)\cos\left(\frac{k\pi}{2}\right)\left(\sin\left(\frac{k\pi}{4N}\right) - \sin\left(\frac{3k\pi}{4N}\right)\right) . \end{aligned} \tag{C.10}$$

The sum over the second term gives zero and we have after some calculus

$$\begin{aligned} g(f) = 1 - \frac{8\kappa\tau_1^g}{N\gamma} \sum_{k=1}^{\infty} \sin\left(\frac{k\pi}{2}\right)^2 \cos\left(\frac{k\pi}{4N}\right) \sin\left(\frac{k\pi}{4N}\right)^2 \\ \times \left(\frac{1}{k^2} - \frac{\dot{f}\tau_1^g}{fk^4}\left(1 - \exp\left[-\frac{k^2 f}{\dot{f}\tau_1^g}\right]\right)\right) . \end{aligned} \tag{C.11}$$

The main contribution will originate from the lowest k values. In the limit of $N \to \infty$ we have $\cos(k\pi/(4N)) \to 1$ and $\sin(k\pi/(4N))^2 \to (k\pi/(4N))^2$. Furthermore we replace the sum over the odd k values by the corresponding integral from 0 to N. Later we take the limit $N \to \infty$ and obtain

$$\begin{aligned} g(f) &= 1 - \frac{\kappa\pi^2\tau_1^g}{4N^3\gamma} \int_0^N \left(1 - \frac{\dot{f}\tau_1^g}{fk^2}\left(1 - \exp\left[-\frac{k^2 f}{\dot{f}\tau_1^g}\right]\right)\right) \\ &= g_{si}(f)\,\mathrm{erf}\left(\frac{\sqrt{\pi}}{g_{si}(f)}\right) - \frac{g_{si}(f)^2}{\pi}\left(1 - \exp\left(-\frac{\pi}{g_{si}(f)^2}\right)\right) . \end{aligned} \tag{C.12}$$

Since $g_{si}(f)$ is by definition small the error function approaches 1 and the second term can be neglected compared to the first one, thus

$$g(f) \to g_{si}(f)\,. \tag{C.13}$$

With these results we have shown that in the limit of very long chains the linearized force profiles coincide.

Nomenclature

Abbreviations .....

ACF ..... autocorrelation function, page 16

AFM ..... atomic force microscope, page 71

BFP ..... biomembrane force probe, page 71

DFS ..... dynamic force spectroscopy, page 71

DNA ..... deoxyribonucleic acid, page 1

DW-potential ..... double-well potential, page 15

FJC ..... freely jointed chain, page 6

GGS ..... generalized Gaussian structure, page 10

PC ..... principal component, page 22

PCA ..... principal component analysis, page 31

PDF ..... probability density function, page 116

Q-potential ..... quartic potential, page 23

T-potential ..... Toda potential, page 23

Functions .....

$\beta(x) = \Gamma(x)'/\Gamma(x)$ ..... digamma function, page 24

$\delta(x)$ ..... Dirac delta function, page 6

$\Gamma(m, x) = \int_x^\infty y^{m-1}\,\mathrm{e}^{-y}\,dy$ ... incomplete Gamma function, page 104

$\Gamma(x) = \int_0^\infty y^{x-1}\exp(-y)dy$ .. Gamma function, page 24

$\Theta(x) = \int_\infty^x \delta(y)dy$ ..... Heaviside step function, page 105

Symbols and Variables ...

α ..... stiffness parameter of the Morse potential, page 15

η ..... fluid viscosity, page 10

γ ..... friction constant, page 9

γ_{EM} ..... Euler-Mascheroni constant, page 24

κ ..... coupling constant, page 9

λ_k ..... eigenvalue corresponding to the eigenvector $\mathbf{u}_k$, page 11

μ ..... mean value, page 18

ν ..... rate, page 44

ν_0 ..... activation rate at zero force, page 77

Ω ..... area in phase space bounded by $\partial\Omega$, page 43

Φ ..... survival probability, page 43

ϕ ..... (auto) correlation function, page 16

Ψ ..... distribution of the polymer conformation, page 6

ψ ..... distribution function, page 6

ψ_{eq} ..... equilibrium distribution, page 49

ρ ..... density distribution function, page 30

σ ..... variance, page 18

$\Sigma(l,t)$ ..... cumulative number of loops of size l at time t, page 137

τ_k^f ..... relaxation time of mode k in the free Rouse chain, page 12

τ_k^g ..... relaxation time of mode k in the grafted Rouse chain, page 13

τ_{mfp} ..... mean first passage time, page 43

Θ_n ..... bond angle, page 38

ξ ..... Gaussian white noise, page 9

Ξ_n ..... torsional angle, page 38

$\eth$ ..... force calibration factor, page 134

a, b ..... parameters of the quartic potential, page 15

a_f, b_f ..... fitting parameters, page 65

b_m ..... scalar parameter, page 80

$\hat{C}$ ..... numerical coefficient, page 68

$\mathbb{C}$ ..... covariance matrix, page 31

$\mathcal{D}$ ..... determinant, page 144

D ..... noise strength, page 23

$d(f)$ ..... derivative of $g(f)$ with respect to f, page 104

D_0 ..... dissociation energy of a Morse bond, page 15

$e(f)$ ..... barrier height of the effective cubic potential, page 104

$\dot{f}$ ..... force loading rate, $f = \dot{f}t$, page 73

$\mathcal{F}$ ..... probability density distribution, page 43

f ..... force, page 73

f_{max} ..... most probable rupture force, page 77

$\mathcal{G}$ ..... conditional probability, propagator, page 16

$g(f)$ ..... linear decrease of the force along the chain, page 103

H ..... Hermite polynomial, page 17

I ..... abbreviation for an integral expression, page 104

J ..... probability flux, page 46

K ..... sink strength of the sink $\mathcal{Q}$, page 52

k ..... mode number, page 11

k_B ..... Boltzmann constant, page 8

$\mathcal{L}$ ..... Fokker-Planck operator, page 17

l ..... vector DNA loop size, page 130

l_0 ..... bond length, page 6

$\mathbb{M}$ ..... mobility tensor, page 9

N ..... number of bonds in the polymer, number of DNA loops in Ch. 6, page 6

n_w ..... number of weak links per DNA repeat unit, page 133

n_{bp} ..... number of basepairs in the ds-DNA, page 132

Δp_s ..... surface pressure difference, page 130

$\mathbb{P}_{kk'}$ ..... projection of the k-th principal component on the k'-th normal mode, page 33

pop ..... population, page 46

$\mathcal{Q}$ ..... sink function, page 52

$q(f)$ ..... correcting prefactor, page 95

$\mathbf{R}$ ..... 3D Cartesian coordinates of a bead, page 6

$\mathbf{r}$ ..... 3D bond vector, page 6

$\mathbf{r}_{ete}$ ..... end-to-end vector/distance, page 6

$\mathbb{S}$ ..... surface, page 66

S ..... abbreviation, page 104

s ..... coordinate in Laplace space, page 53

Δt ..... timestep, page 35

$\mathbb{T}$ ..... transfer matrix, page 143

T ..... temperature, page 8

t ..... time, page 9

$\mathbf{u}_k$ ..... k-th normalized eigenvector, page 11

$\mathcal{U}$ ..... Chebyshev polynomials of the second kind, page 144

U ..... interaction potential, page 9

v ..... parameter, $\tilde{v} = v/\dot{f}$ dimensionless, page 79

$\mathbb{W}$ ..... connectivity matrix, page 9

w ..... dimensionless apparent barrier height, page 79

$\Delta x_{\pm}$ ..... well-to-barrier distance, page 75

$\mathbf{X}_k$ ..... normal coordinate along the mode k, page 11

$\mathfrak{X}$ ..... single trajectory, page 18

x ..... Cartesian coordinate, page 13

x_+ ..... local potential maximum, page 13

x_- ..... local potential minimum, page 13

x_c ..... inflection point, page 75

Bibliography

N. S. Allen and M. Edge. *Fundamentals of Polymer Degradation and Stabilization*. Elsevier Applied Science, New York, 1966.

A. Ashkin. Optical trapping and manipulation of neutral particles using lasers. *Proc. Natl. Acad. Sci. U.S.A.*, 94(10):4853–4860, 1997. doi: 10.1073/pnas.94.10.4853.

V. Barsegov, G. Morrison, and D. Thirumalai. Role of internal chain dynamics on the rupture kinetic of adhesive contacts. *Phys. Rev. Lett.*, 100(24):248102, 2008. doi: 10.1103/PhysRevLett.100.248102.

GI Bell. Models for the specific adhesion of cells to cells. *Science*, 200(4342):618–627, 1978. doi: 10.1126/science.347575.

D. Bensimon, A. J. Simon, V. Croquette, and A. Bensimon. Stretching DNA with a receding meniscus: Experiments and models. *Phys. Rev. Lett.*, 74(23):4754–4757, 1995. doi: 10.1103/PhysRevLett.74.4754.

O. Berger, O. Edholm, and F. Jähnig. Molecular dynamics simulations of a fluid bilayer of dipalmitoylphosphatidylcholine at full hydration, constant pressure, and constant temperature. *Biophys. J.*, 72(5):2002–2013, 1997. doi: 10.1016/S0006-3495(97)78845-3.

M. K. Beyer and H. Clausen-Schaumann. Mechanochemistry: The mechanical activation of covalent bonds. *Chem. Rev.*, 105(8):2921–2948, 2005. doi: 10.1021/cr030697h.

K. Binder and W. Paul. Monte Carlo simulations of polymer dynamics: Recent advances. *Journal of Polymer Science: Part B*, 35(1):1–31, 1997. doi: 10.1002/(SICI)1099-0488(19970115)35:1<1::AID-POLB1>3.0.CO;2-\#.

G. Binnig, C. F. Quate, and C. Gerber. Atomic force microscope. *Phys. Rev. Lett.*, 56(9):930–933, 1986. doi: 10.1103/PhysRevLett.56.930.

R. B. Bird, O. Hassager, R. C. Armstrong, and C. F. Curtiss. *Dynamics of Polymeric Fluids, Vol. 2, Kinetic Theory*. John Wiley and Sons, New York, 1977.

W. H. Carothers. Studies on polymerization and ring formation. I. An introduction to the gerneral theory of condensation polymers. *J. Am. Chem. Soc.*, 51(8):2548–2559, 1929. doi: 10.1021/ja01383a041.

J. J. López Cascales and J. García de la Torre. Simulation of polymer chains in elongational flow. Kinetics of chain fracture and fragment distribution. *The Journal of Chemical Physics*, 97(6):4549–4554, 1992. doi: 10.1063/1.463899.

H.-Y. Chen and Y.-P. Chu. Theoretical determination of the strength of soft noncovalent molecular bonds. *Phys. Rev. E*, 71(1):010901, 2005. doi: 10.1103/PhysRevE.71.010901.

Q. Chen, R. Groote, H. Schönherr, and G. J. Vancso. Probing single enzyme kinetics in real-time. *Chemical Society Reviews*, 38(9):2671–2683, 2009. doi: 10.1039/B903638E.

Z. Cheng and S. Redner. Scaling theory of fragmentation. *Phys. Rev. Lett.*, 60(24): 2450–2453, 1988. doi: 10.1103/PhysRevLett.60.2450.

A. Ciechanover. Proteolysis: From the lysosome to ubiquitin and the proteasome. *Nat. Rev. Mol. Cell. Biol.*, 6(1):79–86, 2005. doi: 10.1038/nrm1552.

A. Ciferri. *Supramolecular polymers*. CRC Press, 2000. ISBN 0824702522.

P. Cluzel, A. Lebrun, C. Heller, R. Lavery, J.-L. Viovy, D. Chatenay, and F. Caron. DNA: An extensible molecule. *Science*, 271(5250):792–794, 1996. doi: 10.1126/science.271.5250.792.

A. E. Cohen and W. E. Moerner. Principal-components analysis of shape fluctuations of single DNA molecules. *Proc. Natl. Acad. Sci. U.S.A.*, 104(31):12622–12627, 2007. doi: 10.1073/pnas.0610396104.

P. Cordier, F. Tournilhac, C. Soulie-Ziakovic, and L. Leibler. Self-healing and thermoreversible rubber from supramolecular assembly. *Nature*, 451(7181):977–980, 2008. doi: 10.1038/nature06669.

A. Cressman, Y. Togashi, A. S. Mikhailov, and R. Kapral. Mesoscale modeling of molecular machines: Cyclic dynamics and hydrodynamical fluctuations. *Phys. Rev. E*, 77(5): 050901, 2008. doi: 10.1103/PhysRevE.77.050901.

S. Cui, C. Albrecht, F. Kühner, and H. E. Gaub. Weakly bound water molecules shorten single-stranded DNA. *J. Am. Chem. Soc.*, 128(20):6636–6639, 2006. doi: 10.1021/ja0582298.

D. Das and S. Sabhapandit. Accurate statistics of a flexible polymer chain in shear flow. *Phys. Rev. Lett.*, 101(18):188301, 2008. doi: 10.1103/PhysRevLett.101.188301.

T. Dauxois. *Dynamique Non Lineaire et Mecanique Statistique d'un Modelle d'ADN*. PhD thesis, L'université de Bourgogne, 1988.

T. Dauxois and M. Peyrard. *Physics of Solitons*. Cambridge University Press, New York, 2006. ISBN 0-521-85421-0.

T. Dauxois, M. Peyrard, and C. R. Willis. Localized breather-like solution in a discrete Klein-Gordon model and application to DNA. *Physica D*, 57(3-4):267–282, 1992. doi: 10.1016/0167-2789(92)90003-6.

P. G. de Gennes. Coil-stretch transition of dilute flexible polymers under ultrahigh velocity gradients. *The Journal of Chemical Physics*, 60(12):5030–5042, 1974. doi: 10.1063/1.1681018.

P. G. de Gennes. *Scaling Concepts in Polymer Physics*. Cornell University Press, London, 1979.

P. G. de Gennes. Kinetics of diffusion-controlled processes in dense polymer systems. I. Nonentangled regimes. *The Journal of Chemical Physics*, 76(6):3316–3321, 1982. doi: 10.1063/1.443328.

C. L. Dias, M. Dubé, F. A. Oliveira, and M. Grant. Scaling in force spectroscopy of macromolecules. *Phys. Rev. E*, 72(1):011918, 2005. doi: 10.1103/PhysRevE.72.011918.

M. Doi. Diffusion-controlled reaction of polymers. *Chem. Phys.*, 9(3):455–466, 1975. doi: 10.1016/0301-0104\%2875\%2980083-8.

M. Doi. *Introduction to Polymer Phyics*. Oxford University Press, Oxford, 1996.

M. Doi and S. F. Edwards. *The Theory of Polymer Dynamics*. Oxford University Press, Oxford, 1986.

J. K. Dreyer, K. Berg-Sørensen, and L. Oddershede. Quantitative approach to small-scale nonequilibrium systems. *Phys. Rev. E*, 73(5):051110, 2006. doi: 10.1103/PhysRevE.73.051110.

O. Dudko, A. E. Filippov, J. Klafter, and M. Urbakh. Dynamic force spectroscopy: A Fokker-Planck approach. *Chem. Phys. Lett.*, 352(5-6):499–504, 2002. doi: 10.1016/S0009-2614(01)01469-5.

O. K. Dudko, A. E. Filippov, J. Klafter, and M. Urbakh. Beyond the conventional description of dynamic force spectroscopy of adhesion bonds. *Proc. Natl. Acad. Sci. U.S.A.*, 100(20):11378–11381, 2003. doi: 10.1073/pnas.1534554100.

O. K. Dudko, G. Hummer, and A. Szabo. Intrinsic rates and activation free energies from single-molecule pulling experiments. *Phys. Rev. Lett.*, 96(10):108101, 2006. doi: 10.1103/PhysRevLett.96.108101.

O. K. Dudko, G. Hummer, and A. Szabo. Theory, analysis, and interpretation of single-molecule force spectroscopy experiments. *Proc. Natl. Acad. Sci. U.S.A.*, 105(41):15755–15760, 2008. doi: 10.1073/pnas.0806085105.

W. Ebeling and I. M. Sokolov. *Statistical Thermodynamics and Stochastic Theory of Nonequilibrium Systems*. World Scientific Publishing Co. Pte. Ltd., Singapore, 2005.

A. Embrechts, H. Schönherr, and G. J. Vancso. Rupture force of single supramolecular bonds in associative polymers by AFM at fixed loading rates. *J. Phys. Chem. B*, 112 (25):7359–7362, 2008.

T. Engel. *Firing Statistics in Neurons as Non-Markovian First Passage Time Problem*. PhD thesis, Humboldt-Universität zu Berlin, 2006.

E. Evans. Probing the relation between force-lifetime-and chemistry in single molecular bonds. *Annu. Rev. Biophys. Biomol. Struct.*, 30(1):105–128, 2001. doi: 10.1146/annurev.biophys.30.1.105.

E. Evans and K. Ritchie. Dynamic strength of molecular adhesion bonds. *Biophys. J.*, 72 (4):1541, 1997. doi: 10.1016/S0006-3495(97)78802-7.

E. Evans and K. Ritchie. Strength of a weak bond connecting flexible polymer chains. *Biophys. J.*, 76(5):2439–2447, 1999.

E. Evans and P. Williams. Course 4: Dynamic force spectroscopy. In H. Flyvbjerg, F. Jülicher, P. Ormos, and F. David, editors, *Physics of Bio-Molecules and Cells*, pages 145–204, 2002. doi: 10.1007/3-540-45701-1_4.

E. Evans, K. Ritchie, and R. Merkel. Sensitive force technique to probe molecular adhesion and structural linkages at biological interfaces. *Biophys. J.*, 68(6):2580–2587, 1995. doi: 10.1016/S0006-3495(95)80441-8.

M. Fixman. Simulation of polymer dynamics. II. Relaxation rates and dynamic viscosity. *The Journal of Chemical Physics*, 69(4):1538–1545, 1978. doi: 10.1063/1.436726.

E. L. Florin, V. T. Moy, and H. E. Gaub. Adhesion forces between individual ligand-receptor pairs. *Science*, 264(5157):415–417, 1994. doi: 10.1126/science.8153628.

P. Flory. *Principles of Polymer Chemistry*. Cornell University Press, 1953. ISBN 0801401348.

P. Flory. *Statistical Mechanics of Chain Molecules*. Interscience, 1969. ISBN 0470264950.

R. W. Friddle. Unified model of dynamic forced barrier crossing in single molecules. *Phys. Rev. Lett.*, 100(13):138302, 2008. doi: 10.1103/PhysRevLett.100.138302.

R. W. Friddle, P. Podsiadlo, A. B. Artyukhin, and A. Noy. Near-equilibrium chemical force microscopy. *J. Phys. Chem. C*, 112(13):4986–4990, 2008. doi: 10.1021/jp7095967.

C. Friedsam, A. K. Wehle, F. Kühner, and H. E. Gaub. Dynamic single-molecule force spectroscopy: Bond rupture analysis with variable spacer length. *J. Phys.: Condens. Matter*, 15(18):1709, 2003. doi: 10.1088/0953-8984/15/18/305.

S. Fugmann and I. M. Sokolov. Non-monotonic dependence of the polymer rupture force on molecule chain length. *Europhys. Lett.*, 86(2):28001, 2009a. doi: 10.1209/0295-5075/86/28001.

S. Fugmann and I. M. Sokolov. Internal friction and mode relaxation in a simple chain model. *The Journal of Chemical Physics*, 131(23):235104, 2009b. doi: 10.1063/1.3274678.

S. Fugmann and I. M. Sokolov. Scaling of the rupture dynamics of polymer chains pulled at one end at a constant rate. *Phys. Rev. E*, 79(2):021803, 2009c. doi: 10.1103/PhysRevE.79.021803.

S. Fugmann and I. M. Sokolov. Thermally activated breakdown in a simple polymer model. *Phys. Rev. E*, 81(3):031804, 2010. doi: 10.1103/PhysRevE.81.031804.

S. Fugmann, D. Hennig, S. Martens, and L. Schimansky-Geier. Deterministic escape of a dimer over an anharmonic potential barrier. *Physica D*, 237(24):3179–3185, 2008a. doi: 10.1016/j.physd.2008.08.008.

S. Fugmann, D. Hennig, L. Schimansky-Geier, and P. Hänggi. Deterministic escape dynamics of two-dimensional coupled nonlinear oscillator chains. *Phys. Rev. E*, 77(6): 061135, 2008b. doi: 10.1103/PhysRevE.77.061135.

S. Garcia-Manyes, L. Dougan, C. L. Badilla, J. Brujić, and J. M. Fernández. Direct observation of an ensemble of stable collapsed states in the mechanical folding of ubiquitin. *Proc. Natl. Acad. Sci. U.S.A.*, 106(26):10534–10539, 2009. doi: 10.1073/pnas.0901213106.

C. W. Gardiner. *Handbook of stochastic methods for physics, chemistry, and the natural sciences*. Springer, Berlin, 2004.

A. Garg. Escape-field distribution for escape from a metastable potential well subject to a steadily increasing bias field. *Phys. Rev. B*, 51(21):15592–15595, 1995. doi: 10.1103/PhysRevB.51.15592.

A. Ghosh, D. I. Dimitrov, V. G. Rostiashvili, A. Milchev, and T. A. Vilgis. Thermal breakage and self-healing of a polymer chain under tensile stress. *The Journal of Chemical Physics*, 132(20):204902, 2010. doi: 10.1063/1.3427245.

M. Grandbois, M. Beyer, M. Rief, H. Clausen-Schaumann, and H. E. Gaub. How strong is a covalent bond? *Science*, 283(5408):1727–1730, 1999. doi: 10.1126/science.283.5408.1727.

R. Granek and J. Klafter. Fractons in proteins: Can they lead to anomalously decaying time autocorrelations? *Phys. Rev. Lett.*, 95(9):098106, 2005. doi: 10.1103/PhysRevLett.95.098106.

A. A. Gurtovenko and A. Blumen. *Generalized Gaussian Structures: Models for Polymer Systems with Complex Topologies*, volume 182. Springer Berlin Heidelberg, 2005. doi: 10.1007/b135561.

O. Hallatschek, E. Frey, and K. Kroy. Propagation and relaxation of tension in stiff polymers. *Phys. Rev. Lett.*, 94(7):077804, 2005. doi: 10.1103/PhysRevLett.94.077804.

P. Hänggi, P. Talkner, and M. Borkovec. Reaction-rate theory: Fifty years after Kramers. *Rev. Mod. Phys.*, 62(2):251, 1990. doi: 10.1103/RevModPhys.62.251.

B. C. Hathorn, B. G. Sumpter, and D. W. Noid. On the distribution of fragment sizes in the fragmentation of polymer chains. *Macromol. Theory Simul.*, 10(6):587–591, 2001. doi: 10.1002/1521-3919(20010701)10:6<587::AID-MATS587>3.0.CO;2-P.

D. Hennig. Formation and propagation of oscillating bubbles in DNA initiated by structural distortions. *Eur. Phys. J. B*, 37(3):391–397, 2004. doi: 10.1140/epjb/e2004-00071-7.

D. Hennig and J. F. R. Archilla. Stretching and relaxation dynamics in double stranded DNA. *Physica A*, 331(3-4):579–601, 2004. doi: 10.1016/j.physa.2003.09.053.

D. Hennig, S. Fugmann, L. Schimansky-Geier, and P. Hänggi. Self-organized escape of oscillator chains in nonlinear potentials. *Phys. Rev. E*, 76(4):041110, 2007. doi: 10.1103/PhysRevE.76.041110.

G. Hummer and A. Szabo. Kinetics from nonequilibrium single-molecule pulling experiments. *Biophys. J.*, 85(1):5–15, 2003. doi: 10.1016/S0006-3495(03)74449-X.

S. Izrailev, S. Stepaniants, M. Balsera, Y. Oono, and K. Schulten. Molecular dynamics study of unbinding of the avidin-biotin complex. *Biophys. J.*, 72(4):1568, 1997. doi: 10.1016/S0006-3495(97)78804-0.

M. Jacobsen. Laplace and the origin of the Ornstein-Uhlenbeck process. *Bernoulli*, 2(3): 271–286, 1996. doi: 10.2307/3318524.

M. S. Z. Kellermayer, S. B. Smith, H. L. Granzier, and C. Bustamante. Folding-unfolding transitions in single titin molecules characterized with laser tweezers. *Science*, 276(5315): 1112–1116, 1997. doi: 10.1126/science.276.5315.1112.

B. S. Khatri and T. C. McLeish. Rouse model with internal friction: A coarse grained framework for single biopolymer dynamics. *Macromolecules*, 40(18):6770–6777, 2007. doi: 10.1021/ma071175x.

A. Kitao and N. Go. Investigating protein dynamics in collective coordinate space. *Current Opinion in Structural Biology*, 9(2):164–169, 1999. doi: 10.1016/S0959-440X(99)80023-2.

A. Kolb, C. M. Marques, and G. H. Fredrickson. Flow effects in the polymer cyclization reaction. *Macromol. Theory Simul.*, 6(1):169–180, 1997. doi: 10.1002/mats.1997.040060112.

S. C. Kou and X. S. Xie. Generalized Langevin equation with fractional Gaussian noise: Subdiffusion within a single protein molecule. *Phys. Rev. Lett.*, 93(18):180603, 2004. doi: 10.1103/PhysRevLett.93.180603.

H. Kramers. Brownian motion in a field of force and the diffusion model of chemical reactions. *Physica*, 7(4):284, 1940. doi: 10.1016/S0031-8914(40)90098-2.

W. Kuhn and H. Kuhn. Bedeutung beschränkt freier Drehbarkeit für die Viskosität und Strömungsdoppelbrechung von Fadenmoleküllösungen. I. *HelV. Chim. Acta*, 28(1):1533, 1945. doi: 10.1002/hlca.6602801218.

W. Kuhn and H. Kuhn. Bedeutung beschränkt freier Drehbarkeit für die Viskosität und Strömungsdoppelbrechung von Fadenmoleküllösungen. II. *HelV. Chim. Acta*, 29(1):71, 1946. doi: 10.1002/hlca.19460290114.

F. Kühner and H. E. Gaub. Modelling cantilever-based force spectroscopy with polymers. *Polymer*, 47(7):2555, 2006. doi: 10.1016/j.polymer.2005.12.090.

S. Kumar and M. S. Li. Biomolecules under mechanical force. *Physics Reports*, 486(1-2): 1–74, 2010. ISSN 0370–1573. doi: 10.1016/j.physrep.2009.11.001.

J. S. Langer. Statistical theory of the decay of metastable states. *Ann. Phys. (N.Y.)*, 54 (2):258, 1969. doi: 10.1016/0003-4916(69)90153-5.

C. F. Lee. Thermal breakage of a discrete one-dimensional string. *Phys. Rev. E*, 80 (031134):1–6, 2009. doi: 10.1103/PhysRevE.80.031134.

N.-K. Lee and D. Thirumalai. Pulling-speed-dependent force-extension profiles for semi-flexible chains. *Biophys. J.*, 86(5):2641–2649, 2004. doi: 10.1016/S0006-3495(04)74320-9.

J. F. Léger, G. Romano, A. Sarkar, J. Robert, L. Bourdieu, D. Chatenay, and J. F. Marko. Structural transitions of a twisted and stretched DNA molecule. *Phys. Rev. Lett.*, 83 (5):1066–1069, 1999. doi: 10.1103/PhysRevLett.83.1066.

J. E. Lennard-Jones. On the determination of molecular fields. II. From the equation of state of a gas. *Proc. R. Soc. Lond. A*, 106(738):463–477, 1924. doi: 10.1098/rspa.1924.0082.

H. Liang, N. Severin, S. Fugmann, I. M. Sokolov, and J. P. Rabe. Time-dependent rupture of single ds-DNA chains. in preparation.

A. E. Likthman and C. M. Marques. First-passage problem for the Rouse polymer chain: An exact solution. *Europhys. Lett.*, 75(6):971–977, 2006. doi: 10.1209/epl/i2006-10206-6.

H.-J. Lin, H.-Y. Chen, Y.-J. Sheng, and H.-K. Tsao. Bell's expression and the generalized Garg form for forced dissociation of a biomolecular complex. *Phys. Rev. Lett.*, 98(8):088304, 2007. doi: 10.1103/PhysRevLett.98.088304.

Y.-H. Lin. *Polymer viscoelasticity: basics, molecular theories, and experiments*. World Scientific Publishing Co. Pte. Ltd., Singapore, 2003.

G. Madras, J. M. Smith, and B. J. McCoy. Thermal degradation of poly([alpha]-methylstyrene) in solution. *Polymer Degradation and Stability*, 52(3):349–358, 1996a. doi: 10.1016/0141-3910(95)00242-1.

G. Madras, J. M. Smith, and B. J. McCoy. Degradation of poly(methyl methacrylate) in solution. *Ind. Eng. Chem. Res.*, 35(6):1795–1800, 1996b. doi: 10.1021/ie960018b.

D. E. Makarov, P. K. Hansma, and H. Metiu. Kinetic Monte Carlo simulation of titin unfolding. *The Journal of Chemical Physics*, 114(21):9663–9673, 2001. doi: 10.1063/1.1369622.

C. W. Manke and M. C. Williams. Internal viscosity of polymers and the role of solvent resistance. *Macromolecules*, 18(10):2045–2051, 1985. doi: 10.1021/ma00152a042.

R. Mannella. A gentle introduction to the integration of stochastic differential equations. In J. A. Freund and T. Pöschel, editors, *Stochastic Processes in Physics, Chemistry, and Biology*, volume 557 of *Lecture Notes in Physics, Berlin Springer Verlag*, page 353, 2000.

S.-J. Marrink, O. Berger, P. Tieleman, and F. Jähnig. Adhesion forces of lipids in a phospholipid membrane studied by molecular dynamics simulations. *Biophys. J.*, 74(2):931, 1998. doi: 10.1016/S0006-3495(98)74016-0.

E. D. McGrady and R. M. Ziff. ''Shattering'' transition in fragmentation. *Phys. Rev. Lett.*, 58(9):892–895, 1987. doi: 10.1103/PhysRevLett.58.892.

F. G. Mehler. Reihenentwicklung nach Laplaceschen Funktionen höherer Ordnung. *Journal für Mathematik*, 6:161–176, 1866.

R. Merkel. Force spectroscopy on single passive biomolecules and single biomolecular bonds. *Phys. Rep.*, 346(5):343–385, 2001. doi: 10.1016/S0370-1573(00)00103-4.

H. Morawetz. Schwierigkeiten bei der Durchsetzung des Polymerbegriffs - ein Essay. *Angewandte Chemie*, 99(2):95–100, 1987. doi: 10.1002/ange.19870990204.

A. G. Moreira and C. M. Marques. The role of polymer spacers in specific adhesion. *The Journal of Chemical Physics*, 120(13):6229–6237, 2004. doi: 10.1063/1.1651088.

P. M. Morse. Diatomic molecules according to the wave mechanics. II. Vibrational levels. *Phys. Rev.*, 34(1):57–64, 1929. doi: 10.1103/PhysRev.34.57.

J. L. Mynar and T. Aida. Materials science: The gift of healing. *Nature*, 451(7181): 895–896, 2008. doi: 10.1038/451895a.

P. L. Nash. Chebyshev polynomials and quadratic path integrals. *J. Math. Phys.*, 27(12): 2963, 1986. doi: 10.1063/1.527275.

G. Neuert, C. H. Albrecht, and H. E. Gaub. Predicting the rupture probabilities of molecular bonds in series. *Biophys. J.*, 93(4):1215, 2007. doi: 10.1529/biophysj.106.100511.

T. Neusius, I. Daidone, I. M. Sokolov, and J. C. Smith. Subdiffusion in peptides originates from the fractal-like structure of configuration space. *Phys. Rev. Lett.*, 100(18):188103, 2008. doi: 10.1103/PhysRevLett.100.188103.

A. F. Oberhauser, P. K. Hansma, M. Carrion-Vazquez, and J. M. Fernandez. Stepwise unfolding of titin under force-clamp atomic force microscopy. *Proc. Natl. Acad. Sci. U.S.A.*, 98(2):468–472, 2001. doi: 10.1073/pnas.021321798.

J. A. Odell, A. Keller, and Y. Rabin. Flow-induced scission of isolated macromolecules. *The Journal of Chemical Physics*, 88(6):4022–4028, 1988. doi: 10.1063/1.453855.

R. W. Pastor, R. Zwanzig, and A. Szabo. Diffusion limited first contact of the ends of a polymer: Comparison of theory with simulation. *The Journal of Chemical Physics*, 105 (9):3878–3882, 1996. doi: 10.1063/1.472208.

A. D. Polyanin. *Handbook of Linear Partial Differential Equations for Engineers and Scientists*. Chapman & Hall/CRC, 2002.

L. A. Pontryagin, A. Andronov, and A. Vitt. On the statistical treatment of dynamical systems. *Zh. Eksp. Teor. Fiz.*, 3:165–180, 1933.

M. Rief, M. Gautel, F. Oesterhelt, J. M. Fernandez, and H. E. Gaub. Reversible unfolding of individual titin immunoglobulin domains by AFM. *Science*, 276(5315):1109–1112, 1997. doi: 10.1126/science.276.5315.1109.

D. Rigby and R.-J. Roe. Molecular dynamics simulation of polymer liquid and glass. I. Glass transition. *The Journal of Chemical Physics*, 87(12):7285–7292, 1987. doi: 10.1063/1.453321.

H. Risken and T. Frank. *The Fokker-Planck Equation*. Springer-Verlag, Berlin, 1996.

Prince E. Rouse. A theory of the linear viscoelastic properties of dilute solutions of coiling polymers. *The Journal of Chemical Physics*, 21(7):1272–1280, 1953. doi: 10.1063/1.1699180.

J.-P. Ryckaert and A. Bellemans. Molecular dynamics of liquid n-butane near its boiling point. *Chem. Phys. Lett.*, 30(1):123–125, 1975. doi: 10.1016/0009-2614(75)85513-8.

P. Samori. *Scanning Probe Microscopies Beyond Imaging*. Wiley-VCH, Weinheim, 2006. ISBN 3-527-31269-2.

P. Schwaderer, E. Funk, F. Achenbach, J. Weis, C. Bräuchle, and J. Michaelis. Single-molecule measurement of the strength of a siloxane bond. *Langmuir*, 24(4):1343–1349, 2008. doi: 10.1021/la702352x.

U. Seifert, W. Wintz, and P. Nelson. Straightening of thermal fluctuations in semiflexible polymers by applied tension. *Phys. Rev. Lett.*, 77(27):5389–5392, 1996. doi: 10.1103/PhysRevLett.77.5389.

P. Senet, G. G. Maisuradze, C. Foulie, P. Delarue, and H. A. Scheraga. How main-chains of proteins explore the free-energy landscape in native states. *Proc. Natl. Acad. Sci. U.S.A.*, 105(50):19708–19713, 2008. doi: 10.1073/pnas.0810679105.

N. Severin, W. Zhuang, C. Ecker, A. A. Kalachev, I. M. Sokolov, and J. P. Rabe. Blowing DNA bubbles. *Nano Lett.*, 6(11):2561–2566, 2006. doi: 10.1021/nl061989b.

S. Sills and R. M. Overney. Creeping friction dynamics and molecular dissipation mechanisms in glassy polymers. *Phys. Rev. Lett.*, 91(9):095501, 2003. doi: 10.1103/PhysRevLett.91.095501.

R. Simha. Kinetics of degradation and size distribution of long chain polymers. *Journal of Applied Physics*, 12(7):569–578, 1941. doi: 10.1063/1.1712939.

S. B. Smith, Y. Cui, and C. Bustamante. Overstretching B-DNA: The elastic response of individual double-stranded and single-stranded DNA molecules. *Science*, 271(5250):795–799, 1996. doi: 10.1126/science.271.5250.795.

I. M. Sokolov. Cyclization of a polymer: First-passage problem for a non-Markovian process. *Phys. Rev. Lett.*, 90(8):080601, 2003. doi: 10.1103/PhysRevLett.90.080601.

J. Spanier, J. Myland, and K. B. Oldham. *An Atlas of Functions*. Springer, New York, 2008. ISBN 0387488065.

G. Srinivas, K. L. Sebastian, and B. Bagchi. Time-dependent survival probability in diffusion-controlled reactions in a polymer chain: Beyond the Wilemski–Fixman theory. *The Journal of Chemical Physics*, 116(16):7276–7282, 2002. doi: 10.1063/1.1466832.

D. B. Staple, S. H. Payne, A. L. C. Reddin, and H. J. Kreuzer. Model for stretching and unfolding the giant multidomain muscle protein using single-molecule force spectroscopy. *Phys. Rev. Lett.*, 101(24):248301, 2008. doi: 10.1103/PhysRevLett.101.248301.

T. Strunz, K. Oroszlan, R. Schafer, and H.-J. Güntherodt. Dynamic force spectroscopy of single DNA molecules. *Proc. Natl. Acad. Sci. U.S.A.*, 96(20):11277, 1999. doi: 10.1073/pnas.96.20.11277.

J. Sung, J. Lee, and S. Lee. Theory of intrapolymer excimer-formation kinetics. *The Journal of Chemical Physics*, 118(1):414–424, 2003. doi: 10.1063/1.1525801.

A. Szabo, K. Schulten, and Z. Schulten. First passage time approach to diffusion controlled reactions. *The Journal of Chemical Physics*, 72(8):4350–4357, 1980. doi: 10.1063/1.439715.

C.-C. Tang, Y.-P. Chu, and H.-Y. Chen. Lifetime of ligand-receptor clusters under external force. *Phys. Rev. E*, 76(6):061905, 2007. doi: 10.1103/PhysRevE.76.061905.

J. Tang and S.-H. Lin. Distance versus energy fluctuations and electron transfer in single protein molecules. *Phys. Rev. E*, 73(6):061108, 2006. doi: 10.1103/PhysRevE.73.061108.

Y. Togashi and A. S. Mikhailov. Nonlinear relaxation dynamics in elastic networks and design principles of molecular machines. *Proc. Natl. Acad. Sci. U.S.A.*, 104(21):8697–8702, 2007. doi: 10.1073/pnas.0702950104.

A. L. Tournier and J. C. Smith. Principal components of the protein dynamical transition. *Phys. Rev. Lett.*, 91(20):208106, 2003. doi: 10.1103/PhysRevLett.91.208106.

Z. Tshiprut and M. Urbakh. Exploring hysteresis and energy dissipation in single-molecule force spectroscopy. *The Journal of Chemical Physics*, 130(8):084703, 2009. doi: 10.1063/1.3077867.

Z. Tshiprut, J. Klafter, and M. Urbakh. Single-molecule pulling experiments: When the stiffness of the pulling device matters. *Biophys. J.*, 95(6):L42–L44, 2008. doi: {10.1529/biophysj.108.141580}.

G. E. Uhlenbeck and L. S. Ornstein. On the theory of the Brownian motion. *Phys. Rev.*, 36(5):823–841, 1930. doi: 10.1103/PhysRev.36.823.

M. Urbakh, J. Klafter, D. Gourdon, and J. Israelachvili. The nonlinear nature of friction. *Nature*, 430(6999):525, 2004. doi: 10.1038/nature02750.

M. C. Wang and G. E. Uhlenbeck. On the theory of the Brownian motion II. *Rev. Mod. Phys.*, 17(2-3):323–342, 1945. doi: 10.1103/RevModPhys.17.323.

P.-K. Wang, C. P. Slichter, and J. H. Sinfelt. Similaritles and differences in the C-C bond scission of ethylene and acetylene on supported Ir and Pt clusters. *J. Phys. Chem.*, 94 (3):1154–1157, 1990. doi: 10.1021/j100366a028.

G. Wilemski and M. Fixman. Diffusion-controlled intrachain reactions of polymers. I. *The Journal of Chemical Physics*, 60(3):866–877, 1974a. doi: 10.1063/1.1681162.

G. Wilemski and M. Fixman. Diffusion-controlled intrachain reactions of polymers. II. *The Journal of Chemical Physics*, 60(3):878–890, 1974b. doi: 10.1063/1.1681163.

R. M. Ziff. Kinetics of polymer degradation. *Macromol.*, 19(10):2513–2519, 1986. doi: 10.1021/ma00164a010.

B. H. Zimm. Dynamics of polymer molecules in dilute solution: Viscoelasticity, flow birefrigence and dielectric loss. *J. Chem. Phys.*, 24(2):269–278, 1956. doi: 10.1063/1.1742562.

List of Publications

- H. Liang and N. Severin and **S. Fugmann** and I. M. Sokolov and J. P. Rabe
  Time-dependent rupture of single ds-DNA chains, in preparation

- **S. Fugmann** and I. M. Sokolov
  Thermally activated breakdown in a simple polymer model, Physical Review E 81, 031804 [2010], doi: 10.1103/PhysRevE.81.031804

- **S. Fugmann** and I. M. Sokolov
  Internal friction and mode relaxation in a simple chain model, The Journal of Chemical Physics 131, 235104 [2009], doi: 10.1063/1.3274678

- **S. Fugmann** and I. M. Sokolov
  Non-monotonic dependence of the polymer rupture force on molecule chain length, Europhysics Letters 86, 28001 [2009], doi: 10.1209/0295-5075/86/28001

- **S. Fugmann** and I. M. Sokolov
  Scaling of the rupture dynamics of polymer chains pulled at one end at a constant rate, Physical Review E 79, 021803 [2009], doi: 10.1103/PhysRevE.79.021803

- D. Hennig, **S. Fugmann**, L. Schimansky-Geier, and P. Hänggi
  When it helps to be purely Hamiltonian: Acceleration of rare events and enhanced escape dynamics, Advances in Solid State Physics 48, [2009],
  doi: 10.1007/978-3-540-85859-1_19

- S. Martens, D. Hennig, **S. Fugmann**, and L. Schimansky-Geier
  Resonancelike phenomena in the mobility of a chain of nonlinear coupled oscillators in a two-dimensional periodic potential, Physical Review E 78, 041121 [2008], doi: 10.1103/PhysRevE.78.041121

- **S. Fugmann**, D. Hennig, S. Martens, and L. Schimansky-Geier
  Deterministic escape of a dimer over an anharmonic potential barrier, Physica D 237, 3179 [2008], doi: 10.1016/j.physd.2008.08.008

- D. Hennig, S. Martens, and **S. Fugmann**
  Transition between locked and running states for dimer motion induced by periodic external driving, Physical Review E 78, 011104 [2008], doi: 10.1103/PhysRevE.78.011104

- **S. Fugmann**, D. Hennig, L. Schimansky-Geier, and P. Hänggi
  Deterministic escape dynamics of two-dimensional coupled nonlinear oscillator chains, Physical Review E 77, 061135 [2008], doi: 10.1103/PhysRevE.77.061135

- D. Hennig, **S. Fugmann**, L. Schimansky-Geier, and P. Hänggi
  Role of energy exchange in the deterministic escape of a coupled nonlinear oscillator chain, Acta Physica Polonica B 39, 1001 [2008]

- D. Hennig, **S. Fugmann**, L. Schimansky-Geier, and P. Hänggi
  Self-organized escape of oscillator chains in nonlinear potentials, Physical Review E 76, 041110 [2007], doi: 10.1103/PhysRevE.76.041110

Danksagung

Ich möchte an dieser Stelle die Gelegenheit nutzen und all jenen danken, die mich während meines Physikstudiums und der anschließenden Arbeit am Institut für Physik begleitet und unterstützt haben.

Zu aller erst gilt mein herzlicher Dank meinem Betreuer Prof. Sokolov, der immer ein offenes Ohr für Fragen hatte und mit seinen vielen Anregungen sehr zum erfolgreichen Gelingen dieser Arbeit beigetragen hat. Sein enger Kontakt zu Prof. Klafter und Prof. Urbakh und die sich daraus ergebenen Anregungen habe die Arbeit sehr bereichert. Ebenso danken möchte ich Prof. Schimansky-Geier für seine Unterstützung und sein Vertrauen in meine Arbeit.

Bei Hua Liang, Dr. Nikolai Severin und Prof. Rabe möchte ich mich für die inspirierende Zusammenarbeit bedanken.

Bei Steffen Martens, PD Dr. Dirk Hennig, Jessica Strefler und Dr. Sten Rüdiger möchte ich mich für das sicher nicht leichte Korrekturlesen dieser Arbeit bedanken. Ihre vielen hilfreichen Kommentare haben mit zum Gelingen der Arbeit beigetragen.

Die stets freundliche Atmosphäre in den Arbeitsgruppen “Statistische Physik und Nichtlineare Dynamik” und “Theorie Stochastischer Prozesse” lässt mich gerne an die vergangenen Jahre zurückdenken.

Nicht zuletzt gilt mein Dank dem Sonderforschungsbereich 555 “Komplexe Nichtlineare Prozesse” für viele anregende Seminare und die finanzielle Unterstützung meiner Arbeit. Der Sonderforschungsbereich hat es mir ermöglicht, interessante Einblicke in verschiedenste interdisziplinäre Forschungszweige zu gewinnen. Dafür bin ich sehr dankbar.

Nicht vergessen möchte ich natürlich meine Familie und meine Freunde, auf deren Rückhalt ich immer bauen konnte und die mir auch abseits der Physik viel Freude bereitet haben.

Selbständigkeitserklärung

Ich erkläre, dass ich die vorliegende Arbeit selbständig und nur unter Verwendung der angegebenen Literatur und Hilfsmittel angefertigt habe.

Berlin, den 08.06.2010 Simon Martin Fugmann